Experimental and Finite Element Analysis of Wind Induced Displacement of a Dual axis Photovoltaic solar trackers

By

Bukola Adeleke

A thesis submitted to the

Faculty of Graduate and Postdoctoral studies

in partial fulfilment of the requirements for the degree of Master of

Applied Science in Civil Engineering

uOttawa

Department of Civil Engineering

Faculty of Engineering

University of Ottawa

Ottawa, Ontario, Canada

Acknowledgement

Firstly, I would like to express my sincere gratitude to my supervisor Prof. Dragomirescu for the continuous support of my masters' programme, for her patience, motivation, and immense knowledge. Honestly, her guidance helped me in all time of research and writing of this thesis. Also I appreciate her contributions of time, ideas, and funding to make my experience productive and stimulating.

I would like to present my gratitude to Dr. Joan Haysom, and the entire research team of SunLab at the University of Ottawa as well, who released the tracker for the execution of my experiment and taught me the operation system of the tracker.

Equally important, many thanks go to my parents who raised me with a love of science and supported me in all my pursuits. My deepest gratitude also goes to my caring lovely wife for her indispensable support both physically and spiritually. Moreover, I would like to thank my family for all their love and encouragement.

Above all, I wholeheartedly thank all mighty God for giving me the vision, power, spirit and endurance to complete this interesting research.

Abstract

Photovoltaic (PV) solar panels and trackers represent one of the most common renewable energy technology which converts sunlight radiation into electrical energy. The solar trackers specifically are more complex structures because they involve mechanical devices, a supporting slender structure, and photovoltaic modules mounted and positioned on top of the supporting structure. Solar trackers are mounted on mobile supports or racks, in order to enable the rotation and tilt of the PV which thus maintains their optimum exposure to the incident sunlight. Solar trackers support structures should be designed for wind resistance during the operation and at stow position for its life span and this became a concern considering the new tendency of installing the solar trackers on the rooftop of low-rise or medium-rise buildings. The current research focused on performing site measurements of the wind-induced displacement for a dual-axis solar tracking system installed on the roof of the Mann Parking building of the University of Ottawa, for different azimuth, elevations.

The supporting structure of the solar tracker was instrumented with 16 strain gauges and the strains developed in the metal truss members were measured during the months February 2015 and March 2015. The tracker was rotated and tilted at different angles through the duration of the experiment and the strains observed on each structural element were recorded. In order to estimate deflections of the supporting structure for wind speeds higher than the ones measured, a finite element (FE) model of the solar tracker was created and static analysis was performed for different inclinations using the SAP 2000 structural software. The experimental results were in agreement with the FE simulation results as the stresses obtained ranged between 1.02×10^7 Pa and 7.88×10^7 Pa. Lower attack angles between 45° and 60° were found to have significant effect on the elements of the solar tracker irrespective of the wind load magnitude. Operational attack angles between 65° and 75° were found to be safer positions as obtained displacements and stress analysis result showed that the supporting structure of the solar tracker was stable for wind speeds between 0 m/s and 33m/s in Ottawa region.

List of symbols

A_{ref}	Reference area (m^2) (Eq 2.1)
ASCE	American Society of Civil Engineer
A_D	Drag induced area (m^2)
A_L	Lift induced area (m^2)
C	Damping (Eq 2.4)
C_f	Force coefficient (no unit) (Eq.2.1)
C_i	Correction factor (no unit) (Eq 3.3)
CFD	Computational fluid dynamics
CPV	Concentrated photovoltaic
C_L	Lift Coefficient (no unit)
C_D	Drag coefficient (no unit))
F_D	Drag force (N)
F_L	Lift force (N)
F_W	Wind force (N)(Equation 2.1)
FEA	Finite Element Analysis
G.F	Gauge factor (unitless)
K_o	Corrected gauge factor (no unit) (Eq 3.4)
K	Stiffness matrices of structure (Eq 2.5)
L	Length of the lead wire (Eq 3.3)
PV	Photovoltaic

q_p	Velocity pressure (m/s)(Eq .2.1)
R	Nominal gauge resistance (ohms) (Eq 3.4)
U1, U2, U3	Translational, Horizontal, transverse and vertical displacement (m)
P	Air density (kg/m^3) (Eq 2.1)
x	Displacement (m) (Eq 2.5)
$\dot{x}$	Velocity (m/s) (Eq 2.5)
$\ddot{x}$	Acceleration ($^{m}/_{s^2}$) (Eq 2.5)
r	Total lead wire resistance(ohms/m)(Eq.3.3)
$\mu\epsilon$	Micro strain
V_r	Excitation voltage (no unit)
V_o	Voltage output (mv)(Eq.3.2)
V_i	Voltage input (mv) Eq.3.2)
V_p	Peak wind velocity (m/s)(Eq.2.2)
σ	Stress (Pa)(Eq 3.5)
γ	Young modulus of material (Pa) Eq.3.5.)

List of Contents

List of Figures

List of Tables

Chapter 1 Introduction

1.1 Background

The concerns regarding the ever consumption consume of energy reported in various fields of industry and construction, led to great developments in the way we produce and collect energy from the available sources. Nowadays energy can be classified under two major categories as renewable and non-renewable energy depending on the resources used to generate it [1]. It is considered renewable when the energy source can be derived from natural resources which can be naturally replenished within a human lifespan, while the non-renewable energy source is considered when this cannot not be recovered fast enough for future use [2]. Non-renewable fossil fuel, such as coal and oil, is known to be the traditional technological means of generating energy mainly for electricity in some part of the world; the technological process which occurs primarily by burning the fossil fuel was set-up in 1882 in Eastern New York and its usage has been gradually increasing on a daily basis with the developments brought by the industrial revolution [2].Thus, coal became the principal source of energy production and recently it was revealed that 40% of the electricity used in the world is still generated by burning coal, which causes problematic climate changes. The fossil fuels plant using coal releases up to 11 billion ton of carbon dioxide into the atmosphere on yearly basis [3].The massive release of greenhouse gases into the atmosphere indirectly claims the life of approximately 150,000 people by famine, malaria and non-availability of fresh water. Consequently, 114 thermal plants were shut down in U.S.A. and England, countries which initiated a reduction of the greenhouse gases emissions by reducing to one fourth the number of their power plants that operate on coal and fuel, in order to purify the energy production system from non-renewable energy sources. A study conducted by the Ontario government in 2005 revealed that the annual health damages caused by burning coal amounted to $3.0 billion; thus Ontario proposed to face out the last coal-fired generation plant by 2014 and proceed to cleaner sources of energy [4]. Among the renewable sources, solar energy has gained substantial interest as it produces high amounts of energy with lower technology investment cost and without creating any global environmental hazard. Producing electricity from solar energy is catalyzed through the installation of photovoltaic systems. Photovoltaic systems generate electrical

power by converting solar radiation into electricity using semiconductors that exhibit the photovoltaic effects [5] thus the photovoltaic (PV) technology directly converts sunlight into electricity. PV solar panels produce reliable and long term energy collection when installed under a fixed angle, without any moving components and without generating any environmental pollution. However, PV panels and arrays reach the optimum direction of sun only once in a day which greatly limits its energy efficiency.

The development of the photovoltaic solar trackers came to minimize the effect of greenhouse gas emission and to optimize the collection and production of electricity by solar energy [6]. The PV solar trackers can be described as devices designed as elevated supporting structures for the photovoltaic modules such as group of panels, which can rotate and tilt so that they follow the direction of the sun in such a way that the modules are aligned perpendicular to the sunlight at all times during the day and thereby maximizing the energy collection efficiency as compared to the fixed PV solar systems [7]. The supporting structure of the tracker is employed to tilt the solar modules in order to minimize the azimuthal angle between the incoming light and the photovoltaic module [8].

1.2 Research Motivation

Solar trackers are generally simply supported slender constructions with large installation platforms on which the PV solar modules for solar energy collection are mounted; these are outdoor structures mainly designed to resist their own dead load, snow load and wind load, the later representing the dominant loading. Until present the solar trackers were mounted at ground level, however recent initiatives of installing solar trackers on medium-rise and high-rise building's roof-tops have been reported. With the altitude the magnitude of the wind speed is also increasing, thus wind loading for such structures becomes a real concern. Also the wind load is time-dependent and also depends on the wind speed magnitude and direction, but also is related to the shape and position of the solar tracker platform. Currently, there are no design codes and professional specifications that focus directly on the wind-resistance of the PV solar tracker installed on a roof-top, and accurate determinations of wind load on trackers when these are inclined at different angles with respect to wind direction are not yet formulated. Because the codes do not provide appropriate recommendations for the wind load estimation of solar tracker, this has resulted in under-designed support structures for the solar trackers that they may lead to failure. A

typical example of failure was found in Northern Vermont, where a PV tracker installed for only four months failed after the occurrence of a windstorm, as shown in Figure 1 [9].

Figure 1.1: Damaged of ground mounted PV tracker in Northern VT, U.S.A. [9]

As specified by the international building code (IBS) in section 101.3, the photovoltaic panels must be structurally designed to meet earthquake, wind and life safety requirements [10]. However, no requirement is mentioned regarding solar tracker stability. Therefore photovoltaic systems designers must carefully consider the estimation of the critical wind loading in the analysis of the photovoltaic solar trackers as this is usually an outdoor structure. The structural analysis of the solar tracker supporting structure presents a number of challenges, as the existing design codes and official tracker standards do not provide sufficient guidelines on how wind load should be calculated and which assumption should be applied [10]. Minimum design loads criteria for building and other structures, as presented in ASCE-07, Eurocode and US 2009 International building code, do not relate specifically to solar trackers because not sufficient studies have been performed for measuring the actual forces on the solar trackers already installed in the field, at the terrestrial level or on buildings' roof-top. Therefore it is of vital importance that photovoltaic solar trackers are properly designed and remain within the safe limits during their life span, but especially during windstorm events the load concentration should not exceed the structural capacity of the structure.

1.3 Aims and Objectives

The current research project is carried out to ascertain the structural stability and integrity of the dual axis solar tracker mounted on the roof of the Mann Parking building in the University of Ottawa campus, during the operation and at stow position and under the action of the time-dependent wind load at different angles of attack. Therefore this study aims at achieving the following goals:

- To measure the weather characteristics between fall 2014 and winter 2015, in order to commutate the static and dynamic wind forces to be applied on the solar tracker, i.e. to obtain the dominant wind direction, wind speed record, temperature and air humidity and density.
- To install strain sensors at selected critical elements of the dual axis solar tracker to measure the strain values and to determine the stresses on the supporting frame of the solar tracker, where the instrumented specimen presented extreme high records of induced wind forces.
- To develop a Finite Element Model of the solar tracker with the aid of SAP 2000 structural software and to determine the structural response of the tracker supporting structure for the applied wind forces, at the critical wind directions with respect to different elevation and azimuth angles ranging from 45° to 78°. The FEM results will be compared with the measurements performed during the fall 2014 to winter 2015 on this structure.
- To determine the critical response of the solar tracker, several cases will be performed by employing the FE model, for extreme wind loads determined by wind speeds much higher than those recorded in Ottawa during the fall 2014 to winter 2015 period. Thus the effect of the fluctuating wind speed on the structure will be determined.

1.4 Thesis Layout

The motivation of the performed experiment and of the FE simulations was highlighted in Chapter 1, along with the purpose of this study of clarifying the critical response of photovoltaic solar trackers under various wind loadings. Description of the solar tracker types, its components and functioning mechanisms were reviewed in Chapter 2. Also, in Chapter 2 different standards and design codes were reviewed, along with the wind tunnel tests and procedures for investigating the structural stability and energy collection performance of photovoltaic solar trackers were fully

described. Moreover the effect of the inclination angles of solar tracker, under the action of wind loads were also was reviewed. The comparison performance of different types of the solar trackers was also described in details in Chapter 2.

Chapter 3 concentrates on the experimental determination of wind induced displacement of the solar tracker where all the equipment employed was thoroughly described. The procedural steps involved in the experimental setup were also highlighted in detail together with the obtained results. The weather data obtained from the Ottawa International Airport was also discussed in regard to the accuracy of the experiment.

Chapter 4 presents the finite element modeling of the photovoltaic solar tracker, its objectives and the assumptions considered in the simulation. The FEM model draws types of elements used with respect to boundary conditions to be calibrated with the data obtained from the solar tracker specimen instrumented with 16 strain gauge sensors, which collect data for time lag of two minutes. Also, to estimate the air humidity, the air density and the effect of the inclination angles on modeling the lift and drag forces, several formulations were considered, as explained in Chapter 4.

Chapter 5 presents the governing functions for the static and dynamic wind loading applied to each member of the PV solar tracker. Finally the outcomes of simulation were presented and were compared in terms of displacements, stresses and forces developed along the critical members of the supporting structure. The data measured by the strain sensors installed at particular points on the tracker elements surface were reported and compared with the FE model results.

The conclusions of both FE analysis and experimental results and also the recommendations for future research work regarding the wind effect estimation of solar trackers are presented in Chapter 6.

Chapter 2 Literature review

2.1 Photovoltaic Solar Trackers

In photovoltaic technology applications, the solar trackers serves as mobile mechanical devices that track the sun across the sky on a daily basis, thus enhancing the collection of the available solar irradiance to be converted to solar electricity by the solar PV modules they support. The solar trackers could be categorised as standard Photovoltaic trackers and Concentrated Photovoltaic trackers depending on the number and orientation of the tracker axes, actuation architecture, drive type, intended application, vertical support and foundation type [11].

2.1.1 Standard Photovoltaic (PV) Module Tracker

The standard PV trackers use basic silicon cells for the panels the support which enhances the performance of the entire photovoltaic system as it increases the amount of energy produced from a fixed amount of power generating capacity. Also the standard tracker has the main function of reducing the angle of incidence between the incoming sunlight and the Photovoltaic module, thus it provides power generation of 99.6% as the tracker accuracy is $\pm 5^0$ [11].

2.1.2 Concentrated Photovoltaic (CPV) Module tracker

Concentrated photovoltaic solar tracker ensures proper alignment of the CPV optical elements they carry, with the sun's direct beam; the alignment is done with a higher degree of accuracy than the Standard PV trackers.

Depending on the number of axes and orientation of the primary axis, the photovoltaic solar trackers could also be categorised as single-axis and dual-axis trackers. The former has one degree of freedom which acts as an axis of rotation and the latter has two degree of freedom as axes of tilt (elevation) and rotation (azimuth) [11]. The single-axis tracker implementation includes: horizontal single axis tracker, vertical single-axis tracker and inclined single-axis tracker as shown in Figures 2.1 a), b) and c). The Dual-axes tracker implementation can be found as vertical primary dual-axis, horizontal primary dual-axis and inclined primary dual-axis trackers as represented in Figures 2.2 a) and b).

Figure 2.1 (a): Horizontal Single axis tracker [11]

Figure 2.1(b) Vertical Single axis tracker [11]

Figure 2. 1(c) Inclined Single-axis tracker [11]

Figure 2.2 (a): Horizontal Primary dual axis Tracker [11]

Figure 2.2 (b): Vertical Primary Dual axis Tracker [11]

The vertical primary dual-axes tracker is the most common structure which allows the azimuth-elevation mobility of the solar tracker. As shown in Figure 2 .2 b), the 0^0 azimuth is always pointing to north, and 90^0 azimuth is always pointing to east; for the elevation, the angle of 0^0 occurs when a vector normal to the module face points to the horizon and the elevation angle of 90^0 occurs when the module faces the sky, thus assumed almost parallel with the wind direction. The current study employed the above convention however some wind tunnel studies performed

on flat structures inclined in regard to the wind direction have assumed the opposite elevation angles; thus special attention was paid when referencing the drag and lift coefficients referenced from the available literature.

2.2. Major Components of the Solar Trackers

2.2.1 Actuation and Control

The actuation and control devices, for the solar tracker, exist in two forms: distributed actuation and gauge actuation. In the former, the tracker axis of rotation is independently actuated and controlled, while the latter employs multiple axes of rotation driven simultaneously with a single actuation system [11].

2.2.2 Drive Train

The drive train of the solar tracker enhances the transfer of the mechanical payload interface .The drive train includes; gears, motors, actuators, hydraulic rams, transmission and linkages. The solar trackers are controlled based on three different drives namely as; Electric drive, Hydraulic drive and Passive drive [11].

- Electric drive: In this type of drive, AC motors and DC brushless motors are interfaced with gear box to create the rotational motion of the tracker.
- Hydraulic drive: This dwells on the usage of a pump to generate hydraulic pressure being transferred to hydraulic motor through valves, pipes, and hoses. The rotary motion to drive the tracker axis was produced by adjusting the mechanical advantage.
- Passive drive: In this type of drive, the tracker axis is driven with the aid of differential fluid pressure.

2.3 Structural Foundation Characteristics of a Solar Tracker

Trackers are structural systems that support the weight of the Photovoltaic Modules installed at the top, increase the power output performance, and resist the eventual external forces, especially the wind loads induced by high and fluctuating wind speed. These are outdoors electro-mechanical devices exposed mainly to harsh environment-induced forces, thus the solar trackers need an adequate foundation design for the supporting structure of the trackers so that these would be able

to withstand any form of wind and snow loads, irrespective of the direction and the additional weight of the frame and of the PV solar panels they carry. A safety margin coefficient should be taken into consideration for taking into account the dynamic effect of the loads and of the rotating / tilting motion of the tracker. The solar tracker foundations depend on the proposed site location and soil conditions, if they have terrestrial mount. Moreover, the trackers could be supported by a steel pole which directly transfers the loads from PV solar panels to the foundation or supported on the Carousel-like mounted tracker type, that transfer loads through rings attached to foundation at multiple points. Trackers foundation could be penetrating into the mounting surface or non-penetrating foundation [11]. For the roof mounted solar trackers, mainly the Carousel-type mount is found with a non-penetrating foundation consisting on one massive block of concrete, or several smaller blocks anchored symmetrically on the circular rake structure at the base of the tracker and thus offering sufficient counterbalancing weight to withstand the higher wind or snow loads applied at the top of the structure.

2.3.1 Penetrating Foundation

The penetrating foundation is usually applied for terrestrial-mounted solar trackers and it consists of pile foundation, which transfers the loads to a deeper and stronger layer of soil or bedrock, so as to prevent the uplift forces. This type of foundation is employed when a photovoltaic system is proposed to be sited in the vicinity of a river or in an area where the bearing capacity of the soil is below the specified standard. However, it is common for the ground-mounted and water-mounted applications. The design and the construction of this type of foundation for the solar trackers, depends on the geological terrain of the proposed site.

2.3.2 Non-Penetrating Foundation

Ballasted foundation is one of the most common types of non-penetrating foundation, which is found for the ground-mounted and roof solar tracker applications. The ground –mounted systems with non-penetrating foundation are probably the simplest combination for installing the solar tracker and can be found on a larger scale when compared to other types of installations such as on building roof or on parking structures such as the solar tracker system analysed in the current study.

2.4. Review of Design Codes and Standards

Wind loads must be carefully considered in the analysis of photovoltaic solar tracker because these are outdoor structures exposed to harsh environment and extreme wind loading can easily dominate the design conditions. When the current research was initiated, the analysis of the structure itself presented a number of challenges because the existing design codes and the solar trackers standards do not provide sufficient guidelines on how the wind load should be calculated and which assumptions should be applied. The "Minimum design loads for building and other structures" code (ASCE-07), Euro code and US 2009 International building code do not relate specifically to solar trackers and this could result to situations when such structures could be faulty designed. The main concern is the structural stability of the solar tracker slender frame support structure, therefore it is very important that the photovoltaic trackers remain safe during windstorm events and the loading combinations does not exceed the structural capacity.

2.5 Analytical Comparison of Wind Action on Photovoltaic Solar Tracker Model

2.5.1 Eurocode (EN 1991-1-4)

Solar trackers are structures functioning outside the enclosed facilities because they need the full exposure to sunlight; therefore this necessity compels the proper evaluation of the snow, rain, seismic, self-weight and wind induced loads. The latter is the major concerns for the structural engineers, due to lack of research and documentation investigating the structural response of the solar trackers under the effect of extreme wind events. Several design codes and standards specified certain procedures of determining the wind loads on general structures and Photovoltaic Panels can be classified as flat structures belonging to the cladding component of the building. Euro code (EN 1991-1-4) presents the procedural calculation steps for estimating the wind loads [12]. According to the Eurocode 1, the wind action on a structure or on a structural element, having a height less than 15 m, could be determined by the expression shown below:

$$F_w = C_f q_p A_{ref} \qquad \text{[Eq .2.1]}$$

Where c_f denotes the force coefficient; q_p denotes the velocity pressure; A_{ref} is the reference area of the structural element and the velocity induced pressure is mathematically expressed as :

$$q_p = \frac{1}{2} * \rho * v_p^2 \qquad \text{[Eq .2.2]}$$

Where v_p is the peak wind velocity and ρ is the air density which depends on the altitude, temperature and biometric pressure to be expected during the wind storms. The recommended value for ρ is 1.25 kg/m^3.The wind pressure acting on the external e surface, or on the internal i surface, shall be determined by following expression:

$$w_{pe,i} = q_p c_{pe,i} \qquad \text{[Eq.2.3]}$$

Where $c_{pe,i}$ is the pressure coefficient for the external e and internal i surface.

Mono pitch roof canopy are similar to Photovoltaic tracker whereby the force coefficient were emphasized. The only drawback for using this assumption is that the force coefficient for maximum tilt angles are ranging between 0^0 and 30^0 are as shown in Table 2.1, however the investigated solar tracker had tilt angles of up to 78° Moreover, a signboard structure was considered for the approximately vertical position with off-ground height z_e larger than h/4 as shown in figure 2.3, which is closer to the solar tracker configuration with higher tilt angles. The force coefficient for this latter model was 1.80.

Table 2.1: C_p values for Monopitch Canopies [12]

Tilt angles α				
	0°	10°	20°	30°
$c_{f,max}$	0.5	1.2	1.7	2.2
$c_{f,min}$	–0.6	–1.5	–2.2	–3.0

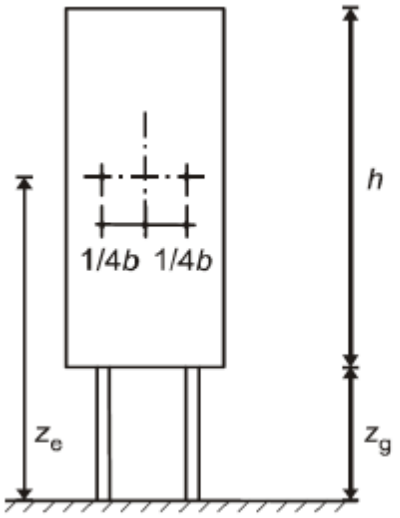

Figure 2.3: Signboards notation [12]

2.5.2 Russian Standard

The Russian standard presents a modeled shed roof similar to the canopy presented in the Eurocode. The pressure distribution had values recommended for the sheds roof angles ranging between 10^0 and 30^0, as shown in table 2.2 and these angles did not cover the entire interval of tilt angle needed for the wind action model in the case of the solar tracking Photovoltaic platform [5]. Figure 2.4 shows the pressure distribution on sheds roofs [12].

Table 2.2: Pressure coefficient values for sheds roofs [12]

α	Wind case	c_{p1}	c_{p2}
10°	I	1.4	0.4
	II	1.3	0.2
20°	I	1.8	0.5
	II	1.4	0.3
30°	I	2.2	0.6
	II	1.6	0.4

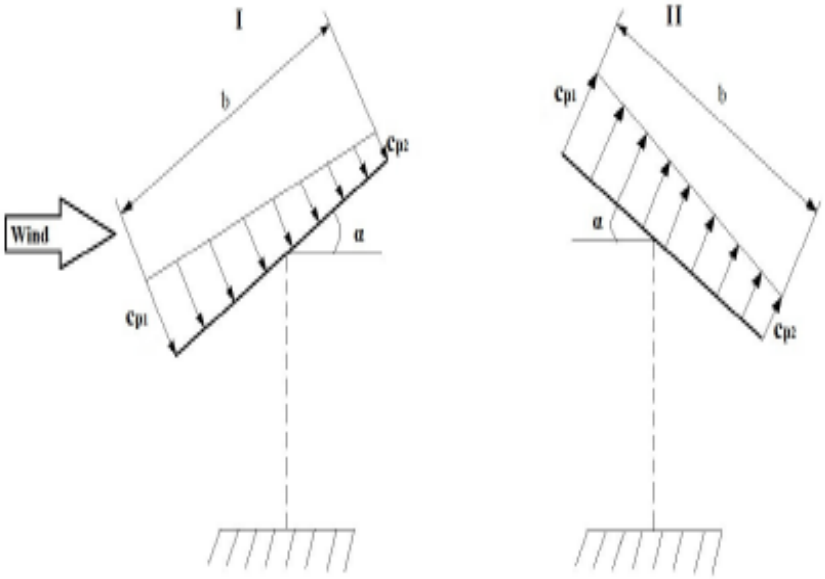

Figure 2.4: Pressure distribution on the sheds roofs [12].

2.5.3 American Standard (ASCE 7)

American Society of Civil Engineering published the minimum design loading criteria for structures, ASCE 7. For the wind loading, the presented modeled cases of monoslope roofs, shown in Figure 2.5, indicated pressure coefficients for the roof tilt angles of up to maximum 45°. The table 2.3 below shows the load cases pressure coefficient values for the monosloped free roofs where the positive values depict a net downward acting wind action and the negative values depict a net upward acting wind action [12].

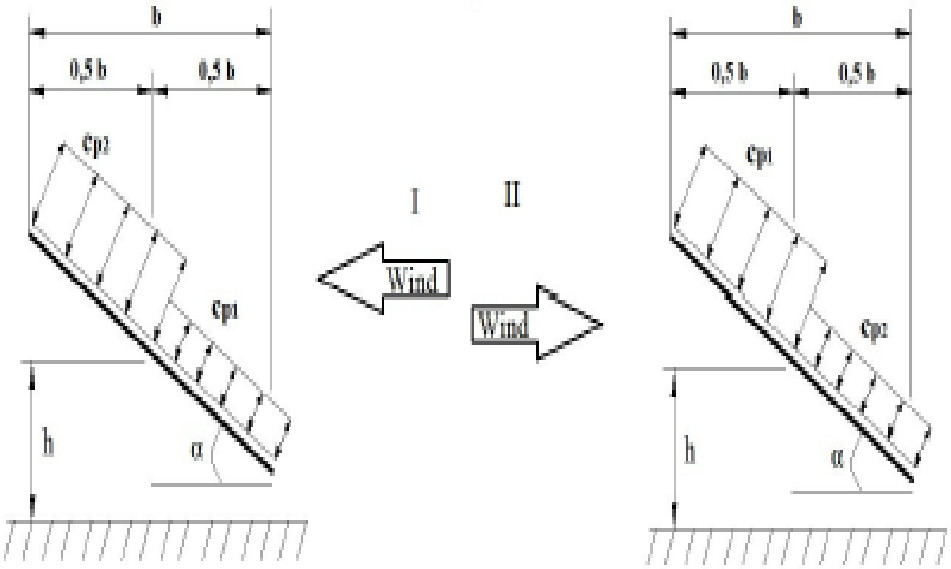

Figure 2.5: Pressure distribution on monoslope free roofs [12].

Table 2.3.Pressure coefficient values for monoslope free roofs [12].

α	Load case	Wind case I		Wind case II	
		c_{p1}	c_{p2}	c_{p1}	c_{p2}
0°	max	1.2	0.3	1.2	0.3
	min	–1.1	–0.1	–1.1	–0.1
15°	max	1.3	1.6	–0.9	–1.3
	min	1.8	0.6	–1.9	0
30°	max	2.1	2.1	–1.8	–1.8
	min	2.6	1	–2.5	–0.5
45°	max	2.2	2.5	–1.6	–1.8
	min	2.6	1.4	–2.3	–0.7

2.5.4 Spanish Standard

Wind action on inclined open surfaces was considered to have similar properties with the current solar tracking system for the Photovoltaic platforms, thus having the pressure coefficients for

different wind directions (front and back) and the wind attack angles α , within the tilt angle range of 0^0 to 90^0 as shown in table 2.4 below. Figure 2.6 depicts the wind direction and the wind attack angles for both wind directions, front and back.

Table 2.4: Pressure coefficient for inclined Open surface [12]

Symbol	Value						
α (degrees)	0	10	20	30	40	50	60-90
c_{p1}	0	0.8	1.2	1.6	1.6	1.4	1.2
c_{p2}	0	0	0.4	0.8	0.8	1.0	1.2

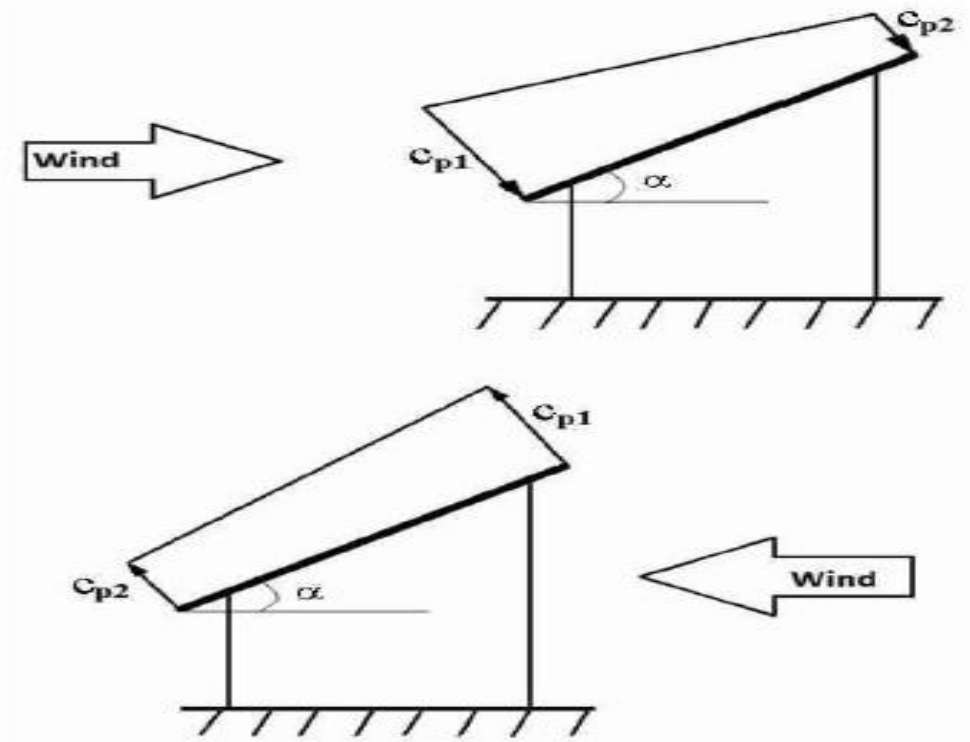

Figure 2.6: Pressure coefficients and distribution diagram on inclined open surfaces [12].

2.6 Limitations of the Design Codes

Certification of the design process for the PV systems installation becomes a great challenge as uncertainty arises in the analysis of the structural loads and the safety and sufficiency of such constructions are not adequately addressed in any of the national or international design codes or standard. ASCE -07 [13] is the design standard for the wind loads induced on structures but it does not provide sufficient guidance to the design professionals and the industrial companies in charge with assessing the PV Installation. Also, the ASCE-07, Eurocode, Russian codes and other design standards lack information about: the design process for the PV solar modules oriented at an inclined angle to the roof they are installed on, the specific geometry of the roof-mounted PV systems and trackers. Alternative experimental facilities proposed to overcome the aforementioned challenges by proposing wind tunnel testing which should be conducted for any rooftop PV system installations, as this presents the closest picture of the pressure equalization, dynamic loads on PV modules, interactions with the air flow around the building and the transmissions of the loads to the structure.

2.7 Wind Tunnel Tests and Analytical Studies

Structural engineers designing photovoltaic solar trackers are always challenged with accurate estimation of wind loads as building code procedures are based on the general assumptions which are usually, but not always conservative and do not always provide accurate wind loading the estimation due to exposure condition, directional shapes, torsion, aerodynamics interactions and load combination. For the detailed wind load definition, the wind tunnel tests are employed [14] The wind tunnels are simulating the boundary wind layer and the effect of the wind speed on the scaled models of the structure investigated for better establishing the providing reliable pressure distribution data for the surface of the solar tracker or other outdoors structures, thus assisting with a better estimation of the design wind loads; thereby the experimental procedures overcome the limitations of the design codes and of the insufficient analytical procedures. Bogg and Lepage (2006) [14] highlighted the procedural steps for a typical wind-tunnel test for the purpose of evaluation structural loading on outside structures as follows:

- In the wind tunnel, the natural wind environment must be simulated to include the mean wind speed and the turbulence profile and localized effect of the nearby buildings.

- Construction of the scaled models of the structures to be tested must respect the geometrical scale of the prototype building or structure and the test with the appropriate instrumentation must be carried out under the simulated environment in order to determine its behaviour.
- Analysis and interpretation of the observed experimental results with regards to the structural dynamic properties of the tested structure should be performed to obtain the static-equivalent and dynamic loads and accelerations.

For the analytical method of estimating the structural response of a structure under the effect of wind forces, there are two types of models for predicting the wind loads on structure: the aeroelastic and aerodynamic models [14]. The former considers the motion-dependent excitation term while the latter did not, as shown in equations 2.4 and 2.5 respectively:

$$m\dot{x} + c\dot{x} + kc = P(t, x, \dot{x}) \quad \text{[Eq.2.4]}$$

$$m\ddot{x} + c\dot{x} + kx = P(t) \quad \text{[Eq 2.5]}$$

Where the m, $\ddot{x}$,$\dot{x}$,x ,c and k denote the mass, acceleration (m/s^2) (,velocity (m/s) ,displacement (m), damping and the stiffness matrices of the structure respectively.

A very limited number of research papers were reported for the solar trackers under the effect of wind or other loading. Libra and Poulek (1980) [15] investigated the stability of the solar tracker they modeled, subjected to wind speeds of 160 km/hr in a wind tunnel facility, which has the testing room of 3 m diameter, at the Aircraft Research and Testing Institute in Prague. The PV solar tracker was positioned in four different positions relative to the direction of the wind which are: perpendicular to the front part of the tracker, perpendicular to the back of the tracker, perpendicular to the lateral side of the tracker, and sideways to the back side of the tracker with the tilt angle of 45°. For each of the positions tested, the wind speed was gradually increased until 160 km/hr each time maintaining the value constant for 3 minutes. The experimental results showed that the solar tracker was stable and had very small vibrations during the test while the wind speed pattern maintained a smooth flow even when wind speed test was increased to 180 km/hr for a short period of time. The pressures at the surface of the PV solar tracker were not measured.

Robert et al.(2010) [16] presented the estimated drag, lift forces and the overturning moments as wind loads on different solar energy collector support systems by employing the numerical Computation Fluid Dynamics (CFD) models such as; k-epsilon, RNG and K-Omega algorithms. The results of the CFD models were compared with the direct force measurement tests obtained from wind tunnel experiments. The RNG and K-Omega models had reasonable agreement with results for the measured lift and drag loads, while the k-epsilon model failed to estimate the drag coefficients at the second tile position. The results generated by the numerical CFD models are in good agreement with the wind tunnel smoke visualization reported by the same authors.

Swagat (2011) [17] performed a wind tunnel experiment for studying the wind effects on a ground mounted photovoltaic solar tracker; the tests were carried out at Wind Engineering and Fluid Laboratory, at Colorado State University. Their findings focused on the parametric investigation of the system porosity, the inclination angles, the wind direction and the arrangement of the PV solar panels of the tracker system. The wind induced forces and the overturn moments measured in the wind tunnel were compared with wind loads recommended by the ASCE-7-05 and were found to be in reasonable agreement.

Hernandez et al.(2009) [18] carried out an aerodynamic study on a prototype photovoltaic solar tracker located in Italy, for the purpose of identifying its performance under the required wind design loads, in accordance with the Spanish Building Code of Practise. The maximum wind speed chosen was based on the comparison between the established Spanish Building Code requirements and recorded wind speed data at the solar tracker site. The design wind speed was used in estimating the dynamic pressure P, on the PV solar module with respect to the varied angle of inclinations ranging from 0^0 to 70^0 at intervals of 10^0 using the expression below:

$$\rho = c_i \frac{v^2}{16} \qquad \text{[Eq .2.6]}$$

Where c_i (i=1,2) is the dynamic pressure coefficient which depends on inclination angle of the panel and the direction of the winds as shown in Table 2.5 and Figure 2. 7 respectively.

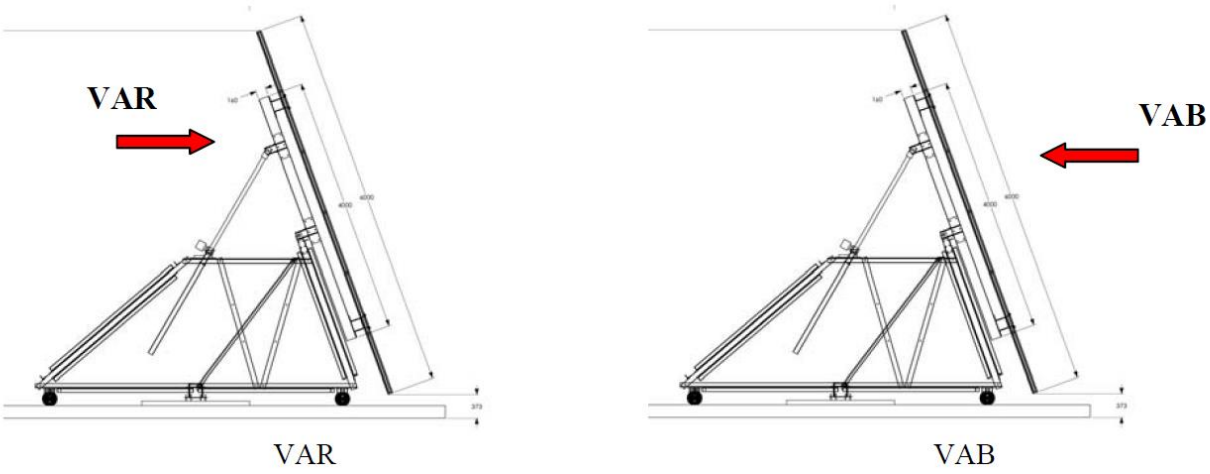

Figure 2. 7: 3D View and lateral elevation of a solar tracker [13]

Table 2. 5 Values of coefficients C1 and C2 [13]

Incidence angle of wind	Leading Edge C1	Trailing Edge C2
70°	1.2	1.2
60°	1.2	1.2
50°	1.4	1.0
40°	1.6	0.8
30°	1.6	0.8
20°	1.2	0.4
10°	0.8	0.0
0°	0	0

A Finite Element Model (FEM) of the same solar tracker was developed for seven different positions of tracker and was studied for several load combinations as part of the ultimate and serviceability limit states. The FE analysis results revealed that the inclination angle above 10^0 produced unacceptable slope at the lateral sides of the solar tracker against the design recommended values for outdoors structures, as shown in Table 2.6. Moreover, the stresses obtained between 30^0 and 50^0 were above the stipulated stress values in the Spanish building code

as shown in Table 2.7 which shows that the configuration was inadequate and the solar tracker positioned at tilt angles of 30^0 to 50^0, in this sense was structurally unsafe.

Table 2.6 Slope on lateral sides [18]

Angle of panel	Maximum slope (°)	Node	Maximum allowable slope (°)
0°	0.40	259	1
10°	0.937	259	1
20°	1.303	259	1
30°	1.665	259	1
40°	1.639	259	1
50°	1.515	259	1
60°	1.38	259	1
70°	1.317	259	1

Table 2.7 Maximum Von Mises Stress [18]

Angle of panel	Maximum stress (MPa)	Upper limit of stress (MPa)
0°	116.7	275
10°	183.1	275
20°	242.3	275
30°	307.4	275
40°	301.7	275
50°	275.8	275
60°	247.7	275
70°	240.5	275

Abdulrahim et al. (2013) [19] presented the assessment of the critical loadings and the member sizing for the design of the structural support used for a solar tracking bi-focal collector, comprising of a rotating shaft, steel support structure for two solar collectors and the support frame which allows the azimuth rotation of the shaft and the overall rotation of the solar collector. The support structure was designed in accordance with American institute of steel construction (AISC) and the structural members were carefully analysed using the powerful structural software RISA

3D. The study focused more on the analysis of the rotating shaft and the estimated wind loads were used as a perquisite in the model of a triangular element stiffness matrix for a 2-dimensional stress formulation of the Finite Element Model. The assessment provides the stresses, which were found to be within the allowable limits and with this regards, the solar tracking system was estimated as adequately designed in terms of the stability and durability of the structure.

Solar tracker neither provides electricity nor converts solar energy to electricity but increases the efficiency of Photovoltaic module by orienting the module to face sunlight directly. However, the power efficiency of PV module could be greatly reduced if there is a tracking error due to structural deformation of the tracking system, mechanical clearance of reduction gears and set-up error. In other to eliminate the aforementioned tracking error source, critical assessment of structural stability of a solar tracker with a pedestal support structure and deformation-induced tracking error need to be greatly considered. Chih and Chen (2014) [20] presented field investigation of the gravity effects on the structural deformation of a tracker by installing two strain gauges at selected locations on the tracker and the strain changes were determined with the aid of a strain meter. The field measurements were validated by using the developed Finite Element model of the tracker and the obtained result from finite element analysis were found to be in agreement with the strain measured at the two locations, as shown in figure 3.2. The Photovoltaic module used for this study consists of 9 flat panels, each having 60 Photovoltaic cells (Fig. 2.8).

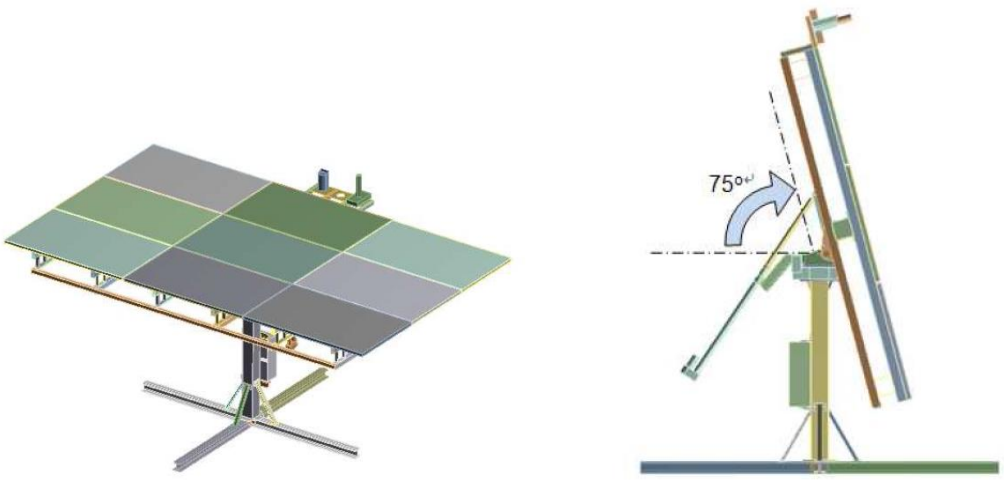

Figure 2. 8: FEA model of the tracking PV system at elevation angle of 0° and 75° [20]

In other to avoid damages crated to the system by the potential resonance of the structure, the natural frequency of the PV system inclined at various angles were recorded as shown in Table 2.8 for the purpose of selecting the optimum site for the installation of such solar trackers. The maximum misalignment of the solar radiation reported in Figure 2.10 was 0.275^0 at the elevation angle of 15^0. Since the obtained maximum misalignment was lower than 5^0 which is considered 99.5% of the maximum power generation, it shows that the solar tracker is structurally stable under the gravity effects as the misalignment is negligible

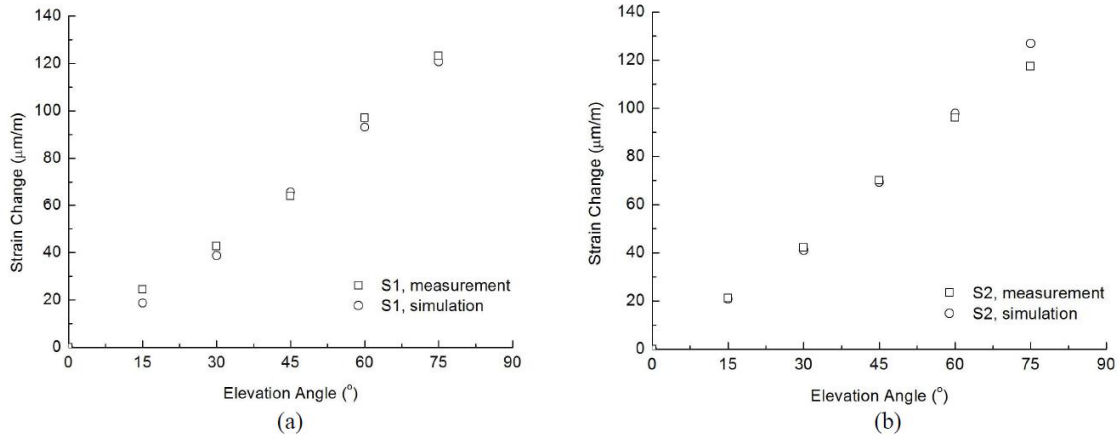

Figure 2.9 Comparison of simulated and measured strain changes at locations [20]

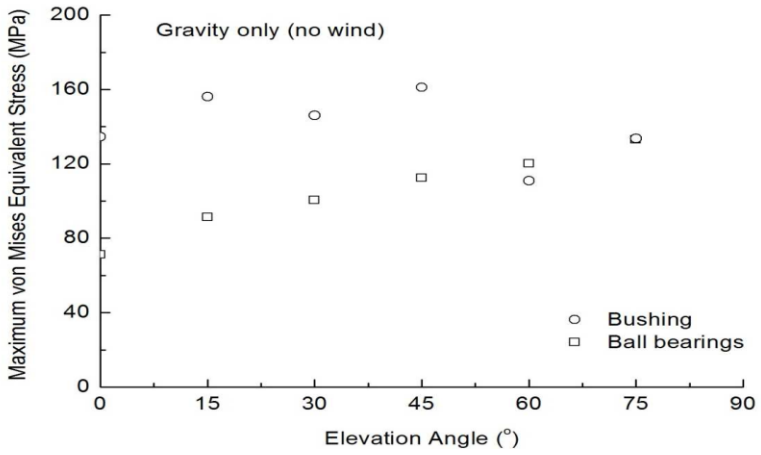

Figure 2.10 (a) Maximum von Mises equivalent stresses in the bushing and ball bearings [20]

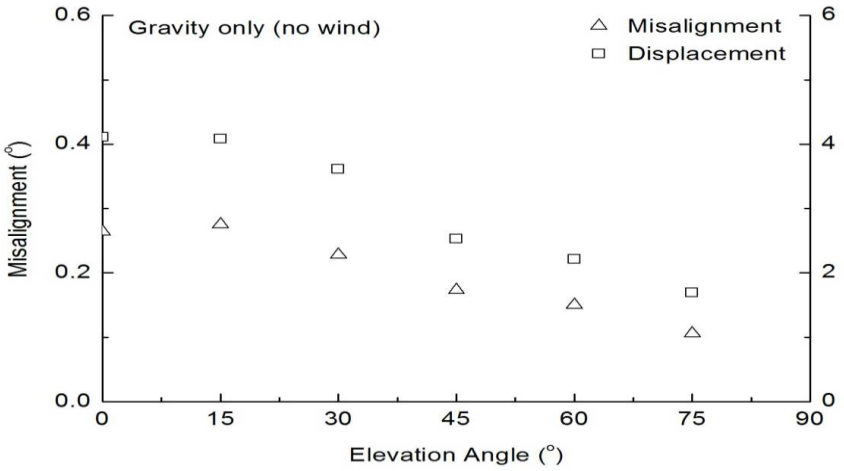

Figure 2.10(b): Maximum misalignment and displacement of PV modules [20]

Table 2.8 Natural frequency of the given PV system at various elevation angles [20]

Mode	Natural frequency (Hz)					
	0°	15°	30°	45°	60°	75°
First	3.85	4.06	4.06	4.07	4.03	4.23
Second	4.20	4.54	4.13	4.13	4.14	4.79
Third	6.32	6.02	4.90	4.83	4.83	5.95
Fourth	6.59	8.90	9.15	8.93	8.70	9.24
Fifth	10.1	9.34	9.22	9.78	9.41	9.70
Sixth	11.4	9.89	10.7	10.7	10.7	11.4

2.8 Performance evaluation of the Photovoltaic solar trackers systems in Canada

Mostafa et al. (2012) [21] studied and compared the performance of four different configurations of Photovoltaic solar trackers systems in Montreal, Canada during three typical days: clear summer, clear winter and overcast with respect to array irradiation as shown in Figures 2.11 a, b and c) The configuration setup ranges from horizontally fixed, fixed at latitude angles, single axis azimuth tracking at 55^0 tilt angle and dual axis tracking system. Each system comprises of 48 number of PV module. The system was also simulated and analysed on daily, monthly and annual

bases using PVSOL Pro, which is a software which helps planning the optimum placement of the PV solar systems, for achieving the best solar energy collection. As shown in table 2.9, the simulation results showed that there was increase in the array radiation of 16.8%, 50.1% and 55.7% for the tilted fixed, azimuth tracking and dual axis tracking arrays accordingly, as compared to horizontally fix array. Dual axis tracker outperformed the other 3 configurations as it received 55.7% more solar radiation and generated 71% more electricity than the horizontal system, over the period of one year. However, all the systems had equal irradiation opportunities during the cloudy day but dual axis tracker has less performance during the cloudy day unless it is positioned horizontally in the overcast conditions.

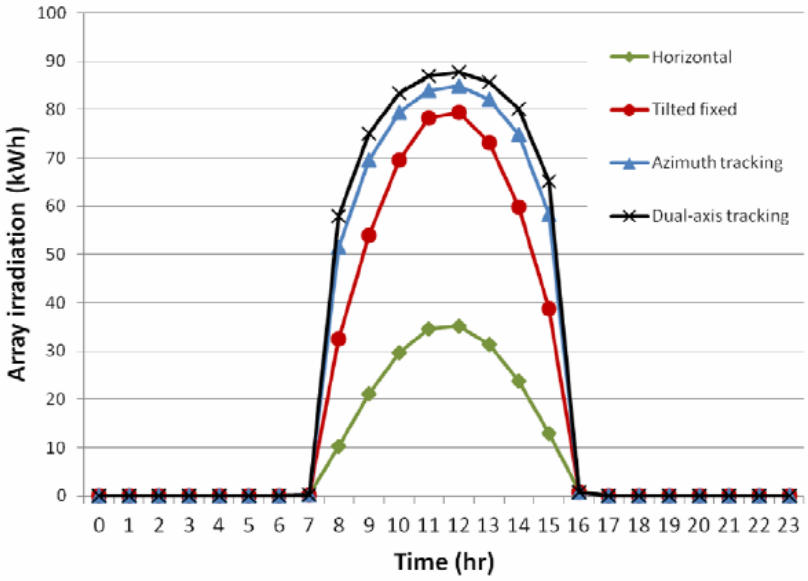

Figure 2.11 (a): Array irradiation in a clear winter day [21].

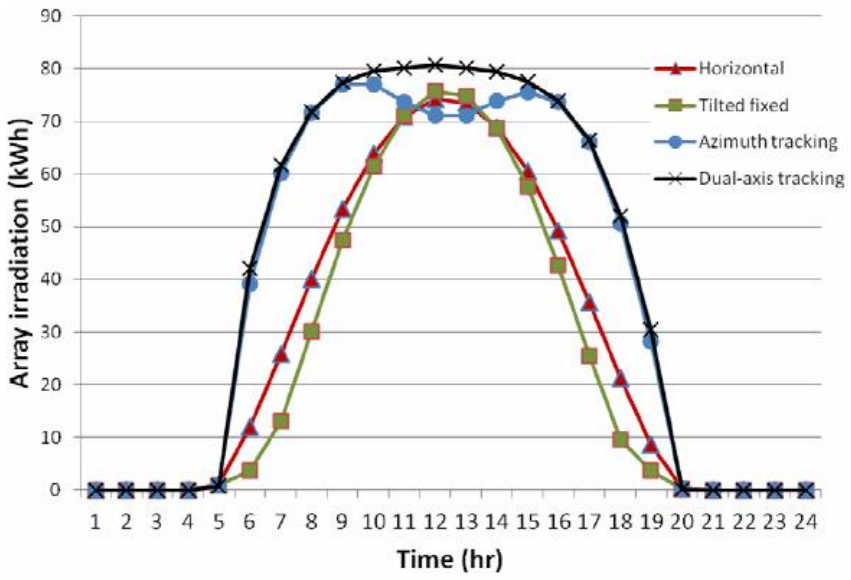

Figure 2.11(b): Array irradiation in a clear summer day [21]

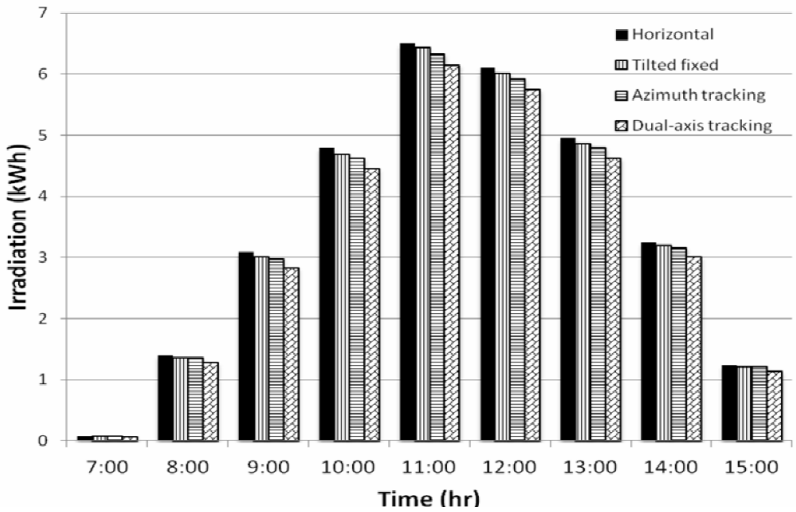

Figure 2.11 (c): Array irradiation in an overcast day [21].

Table 2.9: Overal comparison of PV systems efficiency [21].

Array	Annual irradiation (MWh)	Energy production (MWh)	Efficiency (%)	Cloudy day irradiation (kWh)	A Clear winter day irradiation (kWh)	A Clear summer day irradiation (kWh)
Horizontal fixed	104.5	11.6	11	31.4	200.6	659
Tilted fixed	122.1	14.3	11.7	30.8	486.4	586
Azimuth tracking	156.9	19.1	12.2	30.4	585.7	910
Dual-axis tracking	162.7	19.9	12.2	29.3	623.8	954

Helwa et al. (2010) [22] practically investigated the power evaluation and efficiency of four different solar tracking systems over a period of one year. The focus was to determine the accuracy of the tracker for the solar panel installed. The four tracking system used in the study were: a tracker system tilted at angle 40^0 horizontally facing south, a tracker system inclined at 33^0 horizontally, a rotating system tilted at 6^0 parallel to the north-south direction and the dual axis system (Azimuth-elevation tracker).The result of this study showed that tracking the solar system around a tilted axis increased its annual solar radiation by 11% over a fixed-tilt system, while the combination of tilted-axis tracker and the soft concentration received 57% more annual solar radiation input and produced 31% more output power than the fixed-tilt system. Moreover, tracking along two axes generated 30% more power output over a fixed-tilt system. Also the studied revealed that fact that the accuracy of the solar tracker depends on the number of axis at which it rotates.

Restueke et al. (2012) [23] carried out a comprehensive annual performance study on a fixed photovoltaic system and a system with dual-axis tracker located at Mugla University in Turkey. The studied was performed between April 2010 and March 2011 as shown in Table 2.10, the result of the studied showed that dual axis tracking PV system produced 15,076 Kwh/year of electricity while the fixed system produced electricity of only 11,526KWh/year. The result indicated that the double axis tracker yielded more energy gain as compared to the fixed PV system on a monthly basis throughout the year. In order to authenticate the field measurements, both systems were simulated using the existing site condition and the simulation results were in good agreement with the measured values having only 5% difference as shown in Figure 2.12

Table 2.10 Monthly yielded and energy gain of double axis tracking PV system [23]

Month	Fixed (kW h/month)	Double axis tracking (kW h/month)	Gain (%)
April-10	157.65	209.32	32.78
May-10	166.80	229.90	37.83
June-10	144.80	206.26	42.45
July-10	152.67	209.92	37.50
August-10	152.67	209.92	37.50
September-10	165.16	215.63	30.55
October-10	107.61	131.12	21.85
November-10	92.48	113.10	22.31
December-10	41.45	49.40	19.19
January-11	53.49	62.56	16.97
Feburary-11	78.29	92.50	18.14
March-11	147.75	181.11	22.57

Salah (2003) [24], studied the effect of four different tracking systems with respect to the voltage-current characteristics and power generation of flat Plate Photovoltaic Module. The experimental study was carried out at renewable energy laboratory of applied science of Aman Jordan University on May 29th 2002 between 7:30.a.m and 4:30.p.m at hourly interval. Five identical FPPV modules were mounted on four tracking surfaces: two axes, one axis vertical, one axis east-west and one axis north-south and each of the above mentioned tracking system was compared with fixed system tilted at 32^0 to the south. The experimental result as shown in Table 2.11 depicted that tracking surfaces produced more daily energy collection of 43.87%,37.53%,34.43% and 15.29% for the two axes tracking, east-west tracking, vertical tracking and north-south tracking, respectively as compared to the fixed system. Moreover, the voltage-current relationships for different tracking systems compared with fixed system at different shaded horizontal temperatures were shown in Figures 2.13 a) to c) which present the area under the curves for each tracking system and fixed system. From Figures 2.13 a) to c), the later shows lowest area under the curve which shows that other tracking system produced more power generation as they have large area under the curves.

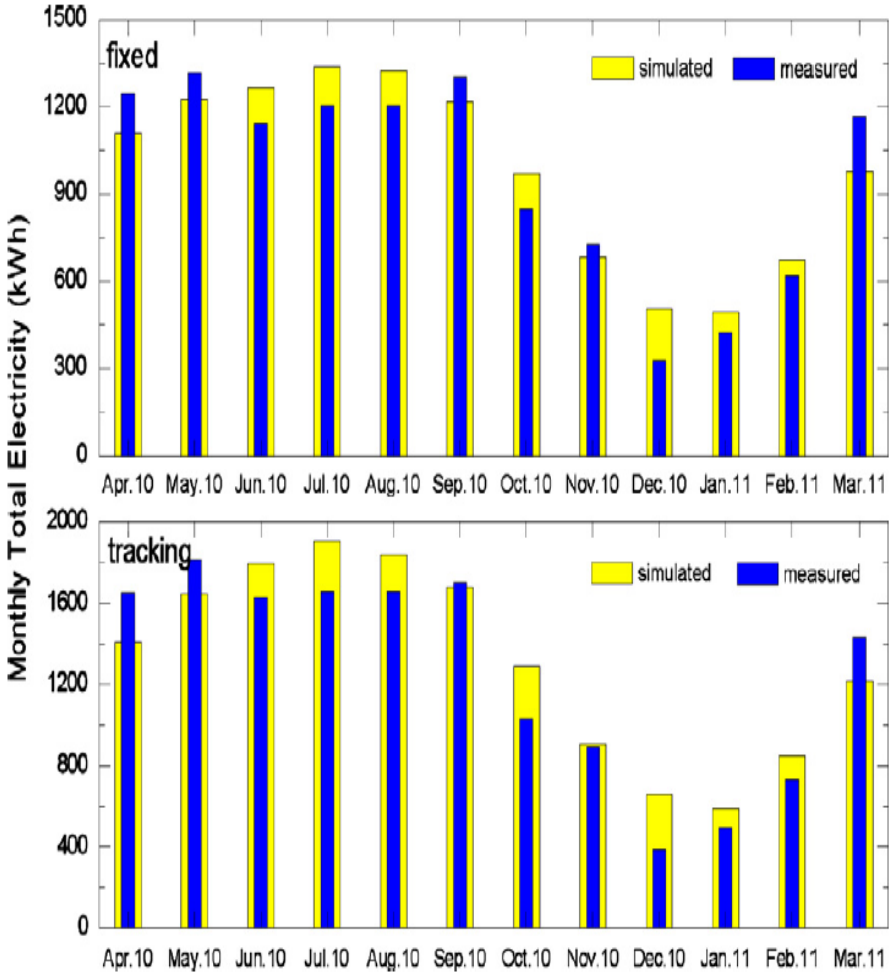

Figure 2.12: Simulation and measured energy difference for fixed and Tracking PV system [23]

Table 2.11: The measured maximum power at the output of FPPV on 29 May 2002 [24]

Time	P_{out} (W)				
	2-axes	N–S	Vertical	E–W	Fixed
7:30 am	29.6	10.4	20.7	26.6	6.7
8:30 am	30.6	17.7	27.9	29.2	11.5
9:30 am	30.3	24.6	29.6	28.9	19.6
10:30 am	31.0	29.6	29.6	28.9	25.3
11:30 am	30.6	28.9	28.9	28.9	27.6
12:30 pm	30.6	29.6	29.9	29.2	26.2
1:30 pm	31.0	30.3	31.3	30.0	27.2
2:30 pm	29.2	27.9	28.2	28.6	25.9
3:30 pm	29.6	25.9	28.2	29.2	21.3
4:30 pm	29.2	17.7	27.6	28.9	18.4
Average (W)	30.17	24.26	28.19	28.84	20.97
Power gain (%)	43.8722	15.2891	34.4301	37.5298	–

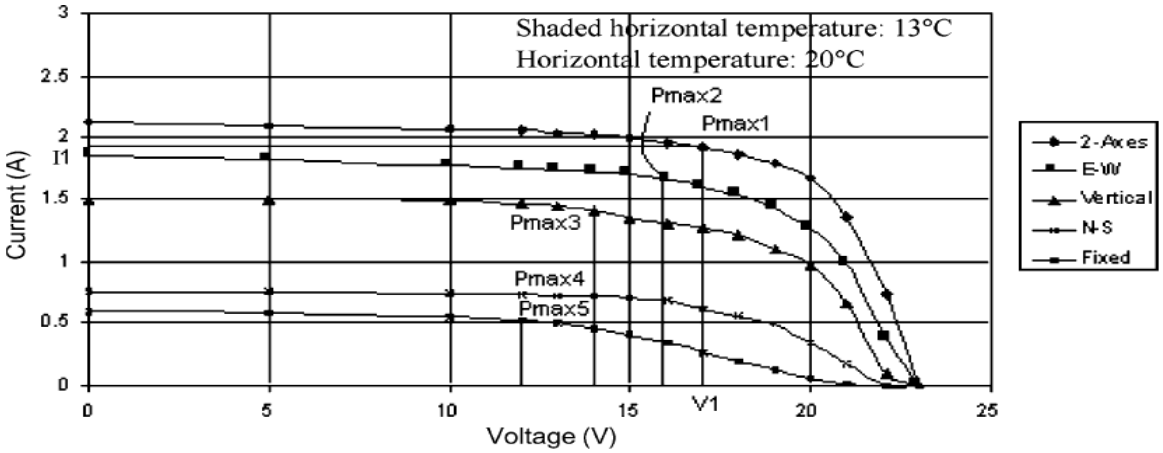

Fig. 2.13(a). The voltage–current characteristics for different tracking systems compared with fixed one at 7:30 am local time [24]

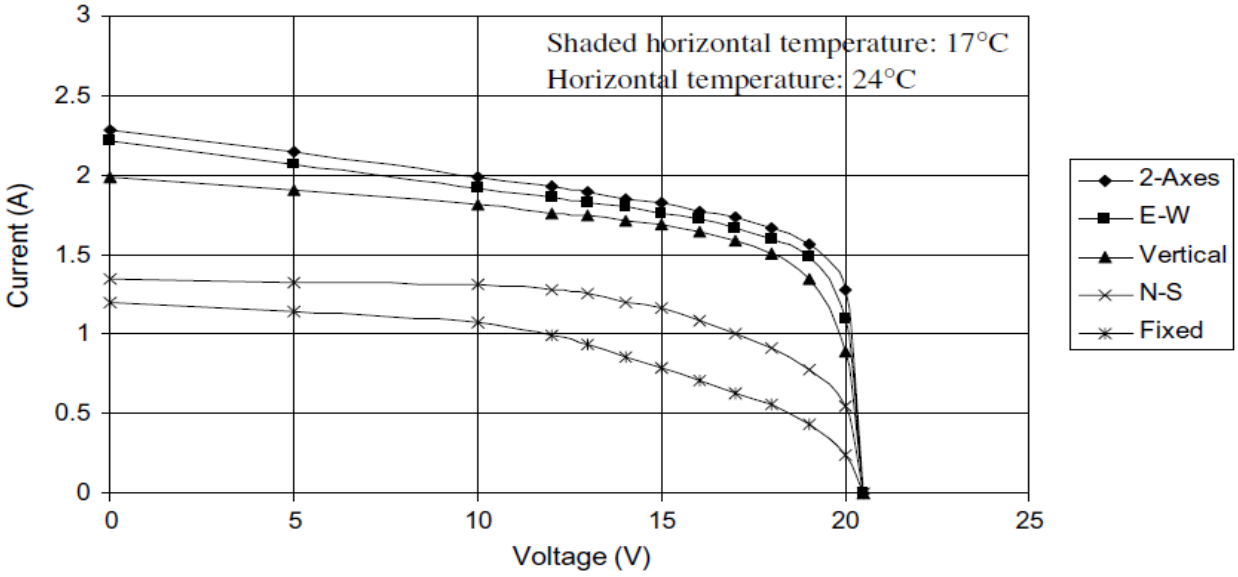

Fig.2.13 (b). The voltage–current characteristics for different tracking systems compared with fixed one at 8:30 am local time [24]

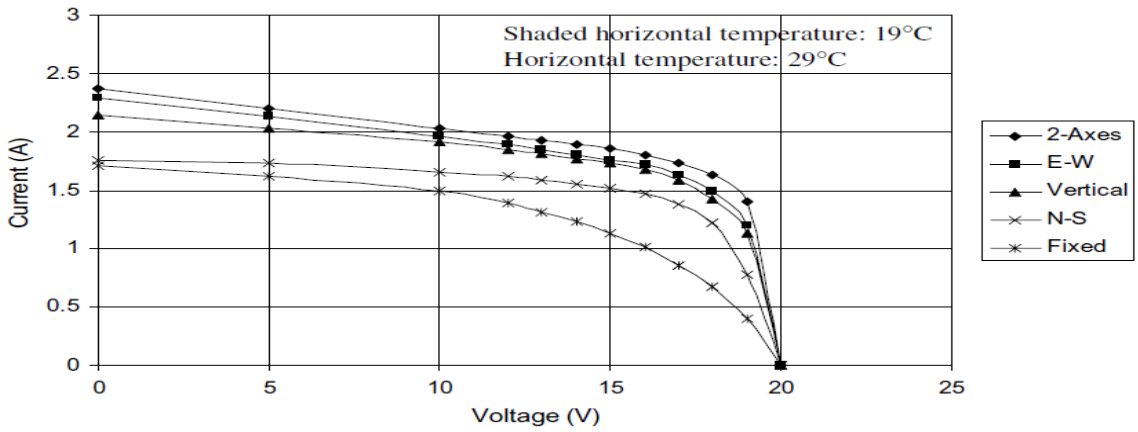

Fig. 2.13(c). The voltage–current characteristics for different tracking systems compared with fixed one at 9:30 am local time [24].

Chapter 3 Experimental setup

3.1 Description of the Solar Tracker

The dual axis steel solar tracker installed on the Mann Packing building of the University of Ottawa, is primarily designed to withstand strong winds and heavy storms; thus the supporting structure consists of 12 precast concrete blocks each weighting approximately 1 tone, placed at the bottom circular frame. The A shaped legs of the tracker are seated on two steel bars which are connected to the circular frame by four rollers, technically positioned so that the entire structure can rotate up to 360°, in order to orient the two rows of poly-crystalline photovoltaic panels of 15.5 kg directly towards the direction of the sun, thereby increasing the PV performance in capturing the daily solar energy. The solar tracker is made of three different parts the upper part, the main body and the bottom part. The upper part consists of an aluminum frame on which the four poly-crystalline photovoltaic panels are mounted and a circular steel beam supporting the frame, which are vital structural elements for the overall functionality of the entire solar tracker. The aluminum frame is connected to the PV solar panels module on both lower and upper edges of the solar panel as shown in Figure 3.1, to provide structural support to the PV solar panel module .There are two elements supporting each of the solar panel rows, forming four horizontal arms denoted as 'K1', 'K2','K'3 and 'K4' for the purpose of identifying them during the analytical investigation which is presented in detail in chapter four of this thesis. The other top part is the circular steel beam made which carries the PV solar panels modules installed on the aluminum frame, and rotates the PV modules at angles between 45° and 78° The circular steel beam is denoted as element 'M' in the following chapters. The main body of the solar tracker is formed by the truss upright frame made of steel, resembling two A-shaped legs, connecting the top circular steel beam, element "M" symmetrically at 500 mm to the bottom rack of the tracker denoted as element 'A'. The solar tracker was installed on the Mann Parking building of the University of Ottawa by the SUNLab research team, from the Electrical Engineering Department of the University of Ottawa. The entire solar tracker structure was raised at 50 cm above the roof finished level (FRL) as shown in Figure 3.1, for enabling the removal of snow during the winter season and to complete the water drainage whenever it rains. For measuring the wind effect on the structure, the solar tracker specimen was instrumented with 2 bi-axial strain gauge sensors, designed to

measure the strain in two dimensions and 12 uniaxial strain gauge sensors designed to measure the strain in one direction respectively.

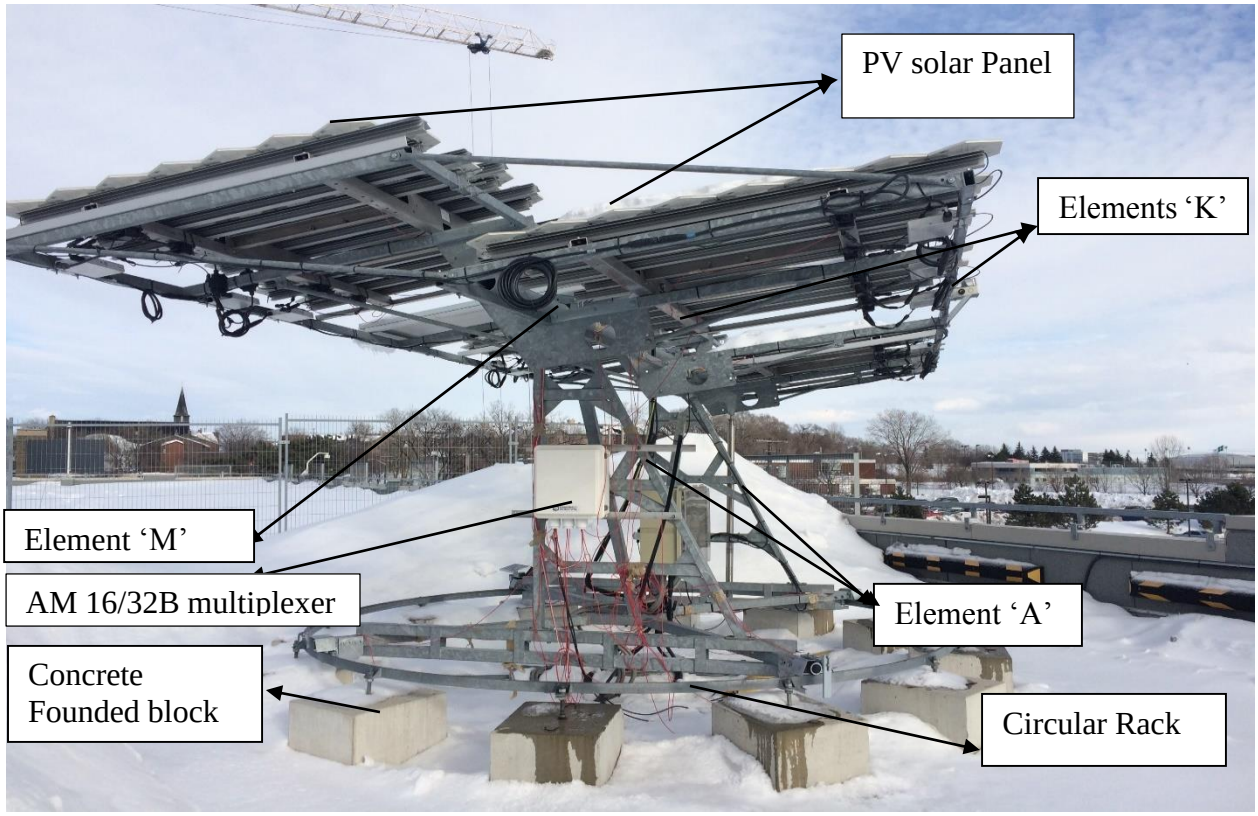

Figure 3.1 Dual Axis solar tracker installed on Mann Parking building, University of Ottawa

The strain gauges sensors were placed on the supporting steel or aluminum elements of the supporting structure and not on the surface of the actual PV solar panel module, because this would interfere with the function of the solar tracker and with the collection of solar energy.

3.2 Experimental setup

The solar trackers are slender metal structures supporting one or more modules of PV solar panels which are generally placed outdoors therefore are exposed to environmental loads the most important being the wind storm load and the snow accumulation load. An accurate estimation of the aforementioned loads on the solar trackers become a great challenge among structural engineers, as the current design code does not specifically any related wind load estimation procedure for such structures. Several standards exist [11, 12, and 13] only for ground and roof

mounted PV solar panels, but the solar trackers contain elevated solar panels for which no design specifications are stipulated. In the light of the lack of design guidelines and recommendations for solar trackers, this research presents the experimental measurements and determination of the wind-induced displacement of the dual axis solar tracker installed on the roof of the Mann Parking building of the University of Ottawa, which is a medium-rise building of four floors, and compares the experimental results with the outcomes obtained from the finite element analysis of the same structure, which was discussed in chapter four. However, due to the limitation of recording devices and data acquisition system channels, only some locations along the supporting frame of the solar tracker were instrumented as follows: element 'M' was instrumented with two biaxial and two uniaxial strain gauge sensors, placed at 100cm interval along the M bar; elements 'K' which represent the four edge frames of the solar panels, were instrumented with four uniaxial strain gauge sensors each placed at 50 cm from the corner, where a higher displacement is expected due to the slender structure of the panel plates; element 'A' was instrumented with four uniaxial strain gauge sensors, each placed 60cm below the actuator , and the bottom frame of the rotating rack was instrumented with two biaxial sensors, placed on the front segment of the frame at 50 cm intervals. Figures 3.2 a) and b) below schematically presents the solar tracker elements 'A' to 'L' and the location of the strain gauge sensors installed on the tracker elements

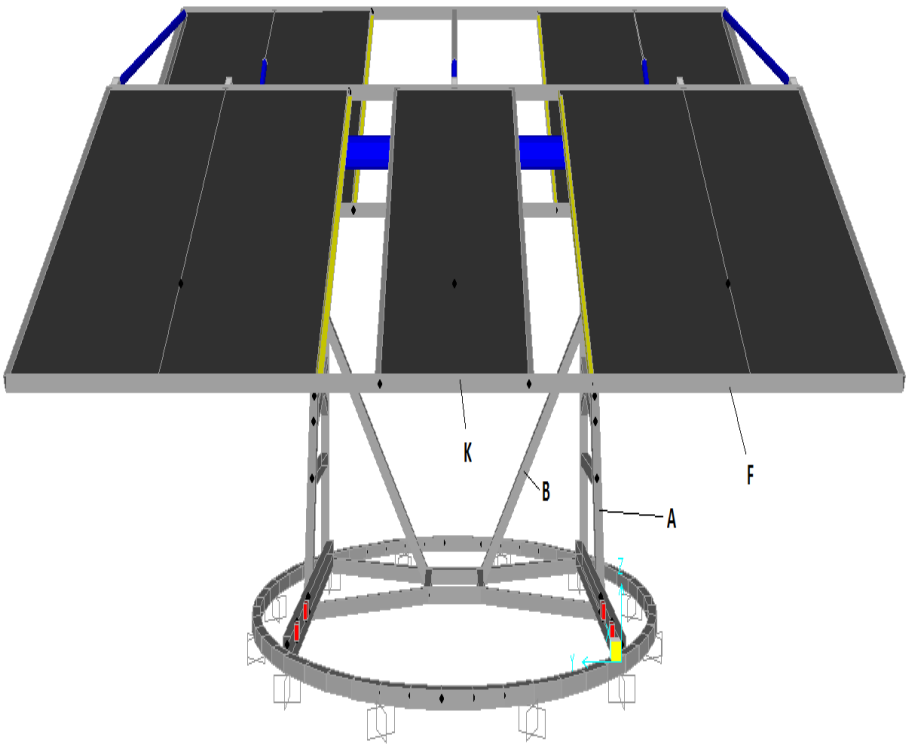

Figure 3.2 a) Solar tracker elements

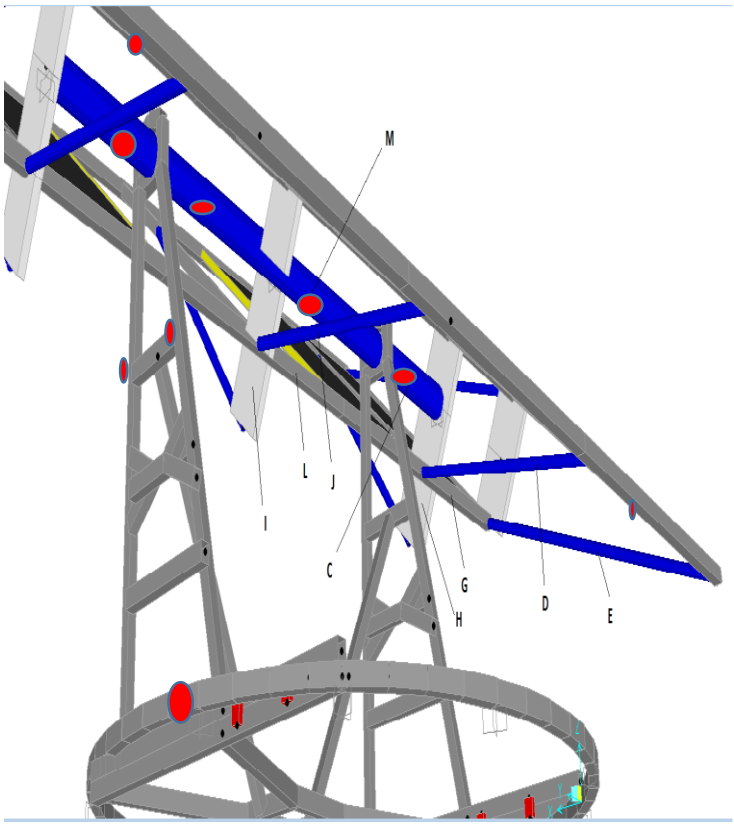

Figure 3.2 b) Strain gauge sensors location

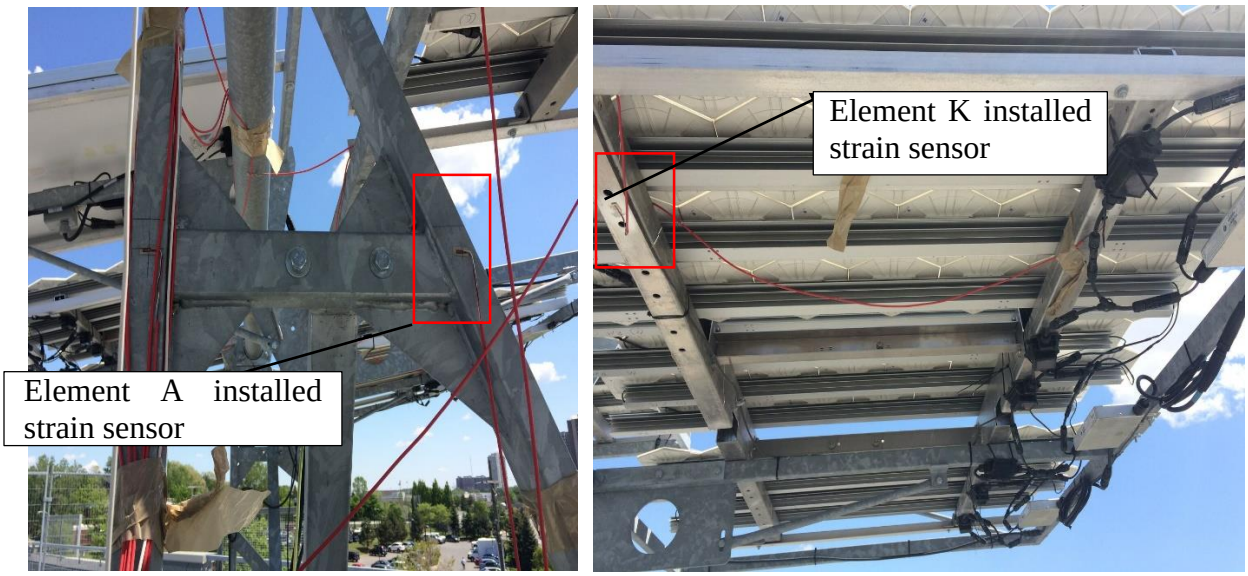

Figure 3.3 Installed strain gauge on a) Element A, and b) Element K

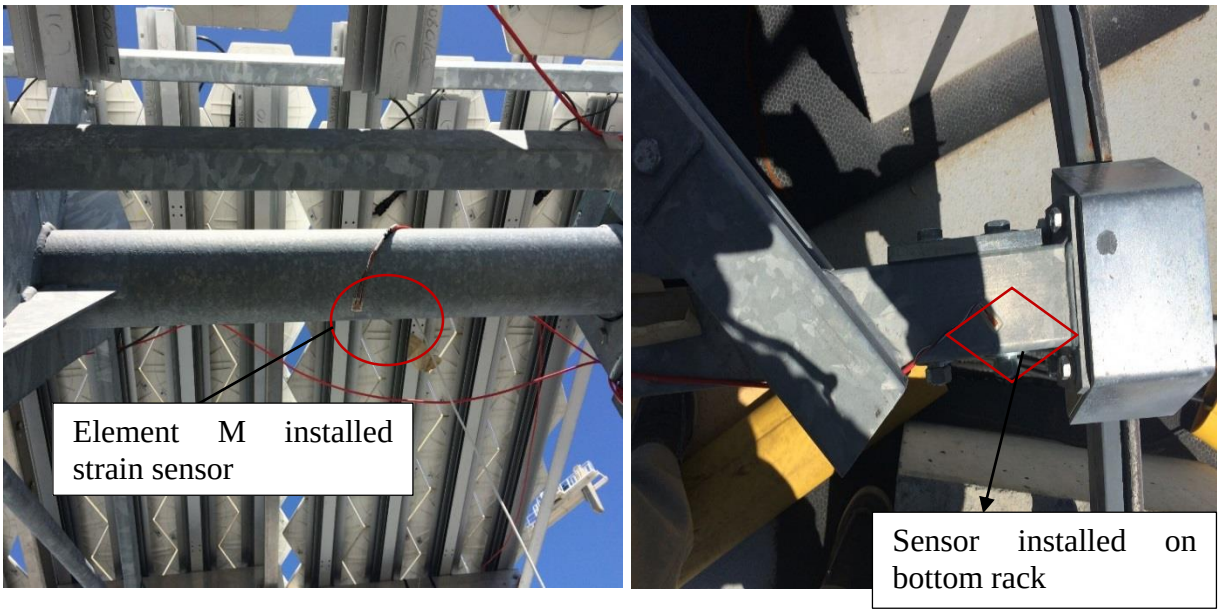

Figure 3.3 Installed strain gauge on c) Element M and d) the circular rack.

Figures 3.3 a), b) and c) present the details of the actual solar tracker instrumented along the members A, K, M and the bottom rack. These members were selected for the morning measurements because they were considered to be the most critical members (member K) with the highest exposure to wind loadings, or the most stable parts of the supporting structure (members A, M and bottom frame).

In total the complete experimental devices setup consisted of: 16 strain gauges of 120 OHMS WFLA-3-11, four terminal blocks on which the Wheatstone bridge connection was set with 120 ohms resistors, an AM 16/32B multiplexer and a CR 1000 Campbell data logger.

3.2.1 Strain gauges sensors

The strain gauges are defined as sensors with an integrated circuit whose resistance changes with the applied load [25]. Measuring the change in resistance and converting it to the strain values leads to the determination of the stress induced by the load to the material on which this is applied. In the current research, the strain gauge sensors were employed for measurement of the strain on the dual axis steel tracker because the steel and aluminum materials of the solar tracker are compatible with the mechanical properties recommended by the strain gauge manufacturer, as

shown in Table 3.1. The WFLA-3-11 strain gauge utilised is an "F Series water proof strain gauge with a pre-attached vinyl lead wire. The entire sensor is coated with a flexible and transparent epoxy resin, for an easier installation of the strain gauge onto the steel solar tracker. This is a single element having 0.08 mm^2 integral vinyl lead wire and the total lead wire resistance per meter is of 0.44 Ω with gauge factor of approximately 2.1.

Table 3.1 Mechanical Properties of Strain gauge [25]

Main Test Material	Metal
Operating Temperature	0° to +80°C
Compensation range	+10° to +80°C
Bonding Adhesive	CN,P-2
Material Backing	Epoxy
Material Element	Cu-Ni alloy foil
Strain limit	3%[3000× 10^{-6}]
Fatigue life at room temperature	1× 10^{6}[$\pm$1500 $*$ 10^{-6}]
Type	WFLA
Gauge length[mm]	3
Gauge width[mm]	1.7
Backing width[mm]	8
Backing length[mm]	17
Backing thickness[mm]	1.5
Resistance[Ω]	120
Lead wire pre-attached	3-wire 5m
Type name of the lead wire	-5LT

3.2.2. Wheatstone Bridge Terminal Block

The multicomponent MC 24323 terminal block is made of brass, and consists of 2 rows and 20 electrical poles as shown in Figure 3.4. The terminal block allows connection of 3 fixed resistors of 120 ohms each, connected together in series with the fourth resistor representing the installed strain gauge sensor, as a variable resistor thus form a 4 wire Wheatstone bridge on the terminal blocks. The electrical connection was performed by pining the wired resistors to the metal part of the terminal block by the aid of several short screws. On one terminal block a number of 2 Wheatstone bridges can be accommodated, thus for the entire experimental setting of 16 strain gauges, an amount of eight terminal blocks were used. Each strain gauge sensor requires one

Wheatstone bridge connection for reading the proper resistance values. Table 3.2 presents the technical information of the MC 24323 terminal block used.

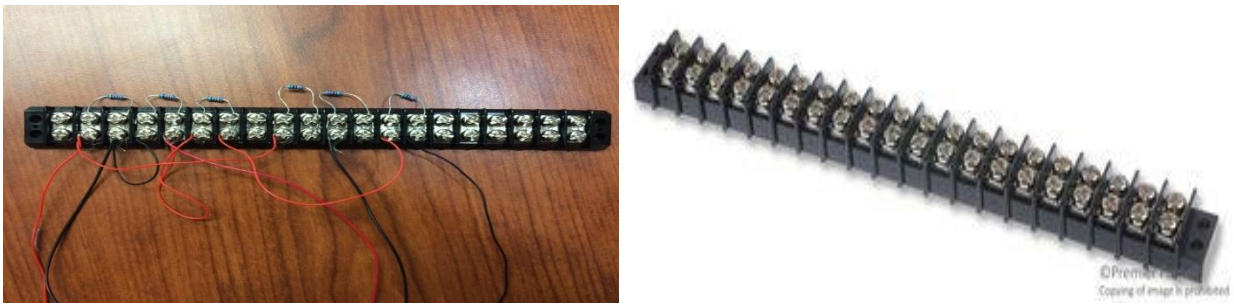

Figure 3.4 (a) Wheatstone bridge set-up on terminal block. (b)Terminal block without Wheatstone bridge. [26]

Table 3.2 Technical description of Terminal block [26]

Connector type	MC 24323 Terminal block
Block Contact Material	Brass
Number of positions	20
Number of rows	2
Rated current	20 A
Rated Voltage	300 V
Wire size AVG Maximum	14 AWG
Wire size AVG Minimum	22 AWG

The resistors used to complete the Wheatstone bridges were the MF 50 series of 120 ohms metal film resistor, as shown in Figure 3.5, which is characterised by stable performance in various environments, with low noise, voltage coefficient, temperature coefficient range and superior moisture protection, and with measurement tolerance of $\pm$1% [26].

Figure 3.5 MF 50 R120 resistor [26]

3.2.3. AM 16/32B Multiplexer

The CR 1000 datalogger was shared with the SUNLab research team; therefore only two input channels were available for sampling the 16 strain gauge sensors installed. Thus the AM 16/32 multiplexer (Fig. 3.6 a)) was used for reading the signal from all the 16 strain gauges with a time lapse of 2 sec and transmitting the output to one single channel on the CR 1000 datalogger. For avoiding the exposure to harsh environment, the AM 16/32 multiplexer was housed in 102 mm × 239 mm× 46 mm water proof anodized aluminum enclosure, which has the purpose of reducing the temperature gradients across the device terminal strips [27]. Provided the mounting taps as shown in Figure 3.5 the multiplexer was connected to the MC 24323 terminal blocks to which the device installed on the tracker's main body were attached. As shown in Figure 3.6 (b), the wiring connections to the device were made between the top panel terminal and the four terminals located on the left hand side of the mode switch button, referred to as control terminals, which allowed for the connection between the power-control terminals of the AM 16/32 multiplexer and the CR 1000 datalogger. Four ODD and EVEN COM terminals located on the right hand side of the mode switch, known as the measurement terminals that conveyed the shielded multiplexed sensor signals intended for the datalogger analogue inputs, while the remaining 16/32 terminals are meant for sensor shield connection depending on the mode switch whether 2× 32 or 4× 16 is selected for measuring 32 sensors or only 16 sensor respectively [27]. The AM 16/32 multiplexer was employed in the experiment because of its compatibility with strain gauge sensors, the terminal blocks, and the CR1000 data logger and due to its ability to multiplex sixteen groups of for lines at a time. Equally important, the AM 16/32 multiplexer was used to increase the number of the measured sensors as the datalogger could not scan more than 4 sensors in 4× 16 mode. Also, its operational temperature ranging between -55°C and +85° were clear advantages which allowed for its use in all-weather conditions during the fall, winter, spring and summer seasons.

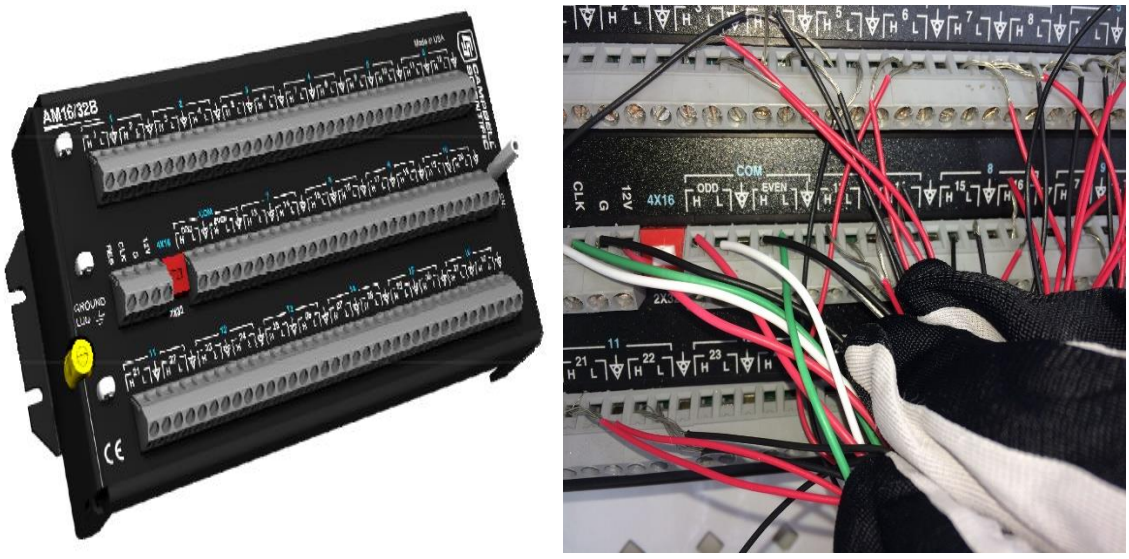

Figure 3.6a) AM 16/32 multiplexer, b) Wiring between multiplexer, datalogger and sensors [27]

The time sampling was regulated from another control line that determined how the channel selection was accomplished, and this allows the AM 16/32 multiplexer to operate in two different modes depending on the RESET settings to HI or LO. Ground on the device was connected to the null ground using 8 AWG Cable to prevent surge dissipation which might propagate on the sensor shield lines. The devices functionally operate on 12V DC power supply directly connected to the data logger battery.

3.2.3.1. Measurement terminals

The measurement terminals consist in the ODD and EVEN COMM terminals located on the right hand side of the panel switch of the AM 16/32 multiplexer which was connected by two 4 CBL cable to the measurement terminals on the CR 1000 together in 4× 16 mode as shown in figure 3.6 [28]. The common terminal located next to the COM ODD and COM EVEN terminals was used to bus other 16 terminals in order to provide a path to the null ground of the sensor cable shields.

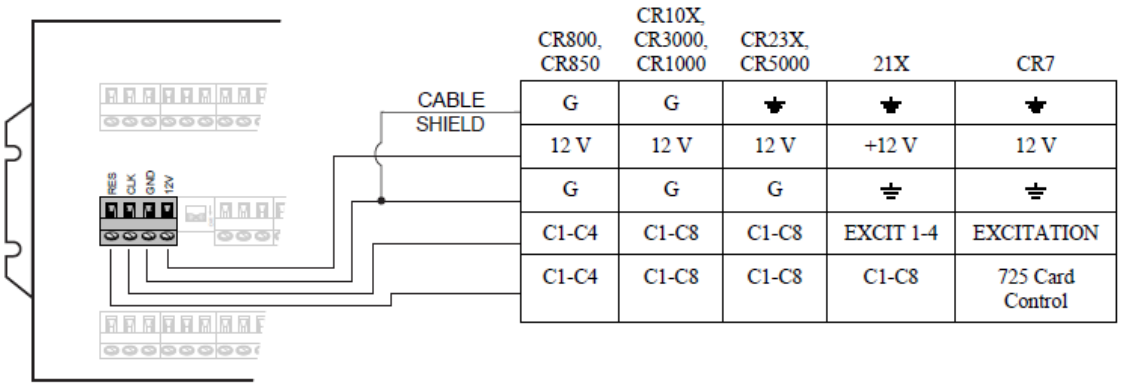

CR800, CR850	CR10X, CR3000, CR1000	CR23X, CR5000	21X	CR7
G	G	⏚	⏚	⏚
12 V	12 V	12 V	+12 V	12 V
G	G	G	⏚	⏚
C1-C4	C1-C8	C1-C8	EXCIT 1-4	EXCITATION
C1-C4	C1-C8	C1-C8	C1-C8	725 Card Control

Figure 3.7 a) Connection between 16/32B and Data logger Power/control terminal using cable 4CBL [28]

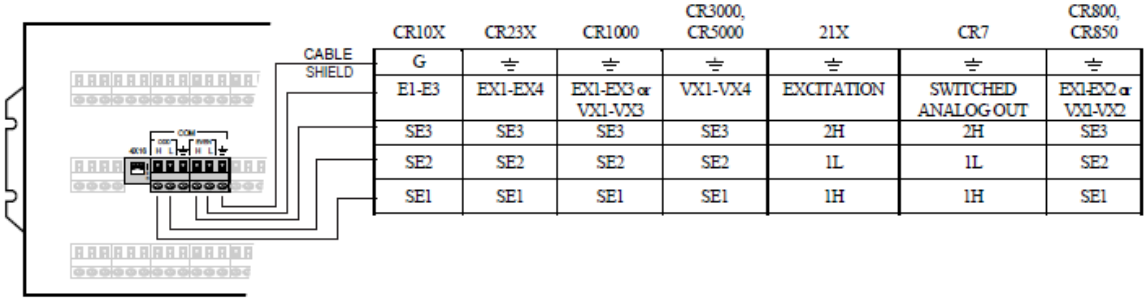

CR10X	CR23X	CR1000	CR3000, CR5000	21X	CR7	CR800, CR850
G	⏚	⏚	⏚	⏚	⏚	⏚
E1-E3	EX1-EX4	EX1-EX3 or VX1-VX3	VX1-VX4	EXCITATION	SWITCHED ANALOG OUT	EX1-EX2 or VX1-VX2
SE3	SE3	SE3	SE3	2H	2H	SE3
SE2	SE2	SE2	SE2	1L	1L	SE2
SE1	SE1	SE1	SE1	1H	1H	SE1

Figure 3.7b) Connection between 16/32B and Data logger measurement terminal using cable 4CBL [28]

The sensor input terminals consist of four simultaneously enabled terminals numbered as 1H ,1L ,2H ,2L which in 4 by 16 mode, continues until 16 set is numbered as 31H, 31L, 32H, 32L. The ODD NUMBERS represent COM ODD TERMINALS and EVEN NUMBERS denotes COM EVEN TERMINALS. When the AM 16/32 multiplexer receives time pulses from the data logger, each set of terminal is switched into contact mode with the COM terminals.

3.2.4 . CR 1000 Datalogger

CR 1000 datalogger is a data acquisition system used to measure the strain gauge sensors through the electrical signal they release. The sampling is performed every 2 minutes and th sensors are read with a time lag of 2 seconds, thus the reduced statistical data to is stored in the device and

later transferred to a computer. The CR 1000 datalogger consists of 8 analogue input differential (DE) or 16 Single ended (SE) individually configured input channels, able to measure up to ±5V and 3 analogue output switched voltage channels VX1-VX3 which are sequentially active during the measurement. Figure 3.8 presents the labelled schematic diagram of CR 1000 which is powered by the PS 200 rechargeable battery, connected to a solar panel as re-charging source. A CR Visual Basic code was written and loaded into CR 1000 to enable it to read and store the data incoming from the AM 16/32 multiplexer. The device was programmed to scan all the 16 strain gauge sensors connected to the AM 16/32 multiplexer with a time lag of 2 seconds. The copy of the Visual Basic code is presented in detail Appendix A.

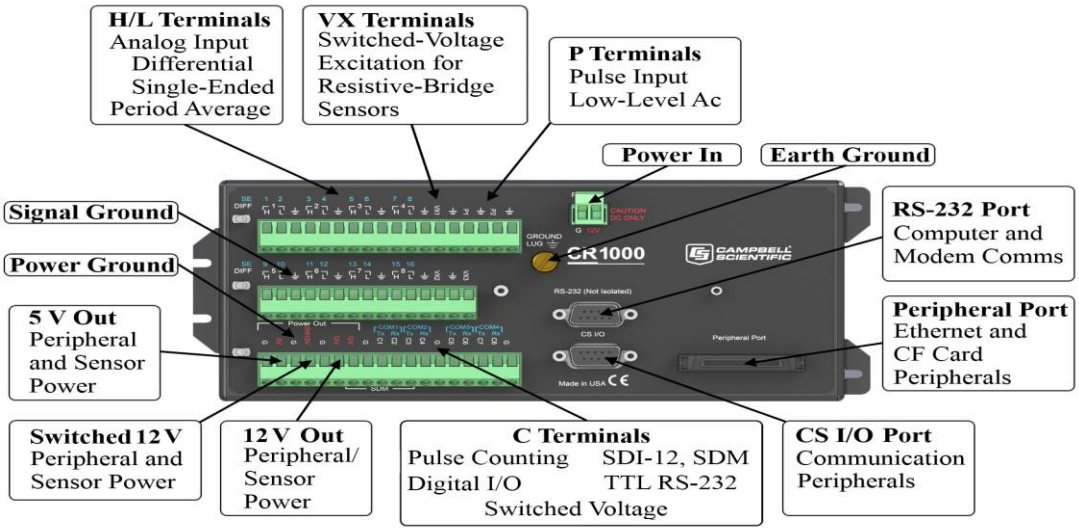

Figure 3.8 CR 1000 Data Logger connection schematics [28]

3.3 Installation of the strain –gauge sensors

Proper installation of the strain gauge sensors is very important for the experimental results accuracy. The procedural steps followed in accordance with the sensor manufacturer manual were as follows:

Surface Preparation: The contact surfaces of the steel tracker elements on which the gauges were bonded, were thoroughly cleaned by removing all the grease, rust and paint and the surface was smoothly finished with 180 abrasive paper specified for steel structures.

Fine Cleaning: The bonding surfaces were cleaned with white towel slightly soaked in acetone.
Adhesive Application: One drop of adhesive was applied to the back of each strain gauge base and adhesive nozzle was used to spread the adhesive over the back surface uniformly and thinly.
Bonding: Strain gauges were carefully bonded to the cleaned surface and the sheets of polyethylene were used to cover the gauges by pressing them on the sensor for 30 seconds.

3.4. Strain Measurement

The electrical signal incoming from the strain gauge sensors must be converted to the strain values by following the calculation procedure recommended for the Wheatstone bridge connection. The strain measurements involves quantities larger than a few mill units of strain ($\varepsilon \times 10^{-3}$). As a result, it is of paramount importance to actually measure the smallest variations in the resistance recorded by the strain gauges, to obtain the required strain measurements. A quarter Wheatstone bridge consisting of four arm resistors: 3 fixed resistors of 120 ohms each, and a strain gauge sensor all arranged in series in a diamond-like setup and connected to the terminal block as shown in figure 3.9(a). The resultant two input and two output terminals from the Wheatstone bridge were connected to the sensor input terminals on the AM 16/32B multiplexer, with the recommended input voltage of 450 mv as programmed in CR 1000 datalogger. Whenever the tracker was rotated and inclined at certain angles using the Golden Sun software, as it will be detailed in the later sections, the output voltage for each strain gauge was measured and recorded at time intervals of two second between 9.a.m and 5.p.m daily, during the January - March 2015 by CR 1000. The measurements were stopped at 5 p.m. because the solar tracker had to be returned to the stow position (78° tilt angle) each evening, for safety reasons.

The obtained output voltage was used to compute the strain from each of the strain gauge sensors installed on the solar tracker's structural elements using the following formulation [29]:

$$\mu\varepsilon = \frac{4*10^6 V_r}{GF(1+2V_r)} \qquad \text{[Eq.3.1]}$$

Where GF denotes the gauge factor which is approximately 2.1 as specified by the sensor manufacturer and V_r is the ratio of output voltage to the input voltage which is expressed as [25]:

$$V_r = 0.001\frac{V_o}{V_i}$$ [Eq.3.2]

Where 0.001 is the source zero from the configuration code, Vo is the output voltage and Vi is the input voltage (450mv)as shown in figure 3.9(b)

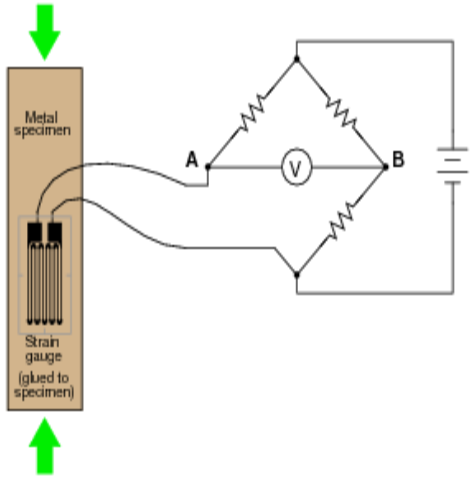

(a)

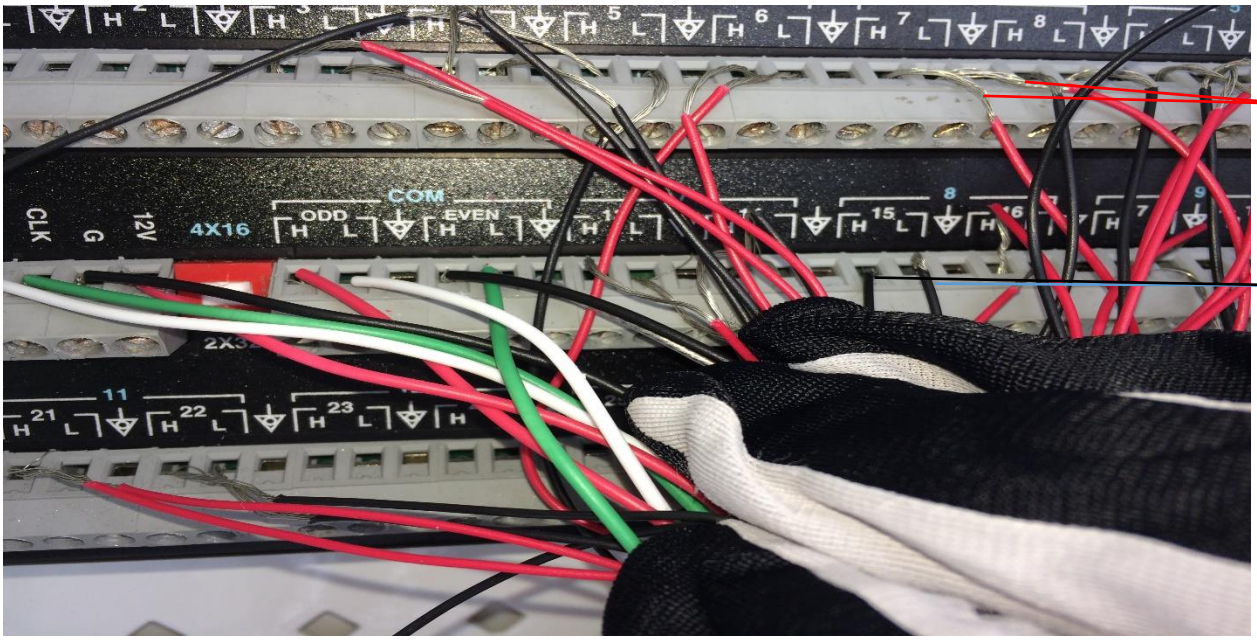

(b)

Figure 3.9 a) Quarter Wheatstone bridge b) with Vx and Vo[30]

The strain measurements had to be corrected for several factors, as recommended by the manufacturer. The first error correction is due to the resistance changes in the lead wire connecting the sensors to the multiplexer, error caused by the influence of temperature changes and the lead wire desensitization. The lead wire error was rectified by introducing the correction gauge factor for the 2-wire quarter Wheatstone bridge with the correction coefficient of the lead wire as given in equation 3 [25]:

$$C_l = \frac{R}{R+rL} \qquad \text{[Eq.3.3]}$$

Correction gauge factor (K_0) is expressed as:

$$K_0 = C_l K \qquad \text{[Eq 3.4]}$$

Where R is the nominal gauge resistance (120 Ω), r denotes total resistance per meter of lead wire ($0.44\ \frac{\Omega}{m}$), L is the length of lead wire (5m) and K is the initial gauge factor value recommended by the gauge manufacturer, which is 2.1, therefore the final correction gauge factor is:

$$K_0 = \frac{120}{120+(0.44*5)} * 2.1 = 2.062$$

Therefore, the recorded output voltages were corrected using the above correction gauge factor of 2.062.

3.5. Computation of strain

The computation of the strain measurements of Sensor 1 for which the electrical signal was recorded at 2 minutes time interval is detailed below to show the procedure for the strain calculation.. The modified gauge factor, initial zero voltage and source zero from configuration code were used in the computation.

$$\mu\varepsilon = \frac{-4*10^6*V_r}{GF(1+2*V_r)}$$

$$\mu\varepsilon = \frac{4*10^6*0.001*\left(\frac{205.75-120}{450}\right)}{2.062*(1+(2*0.001)*(\frac{205.75-120}{450})} = 375.65$$

For exemplification, Tables 3.3. and 3.4. below present the recorded output voltage, and the corresponding calculated micro strain values, for the first 8 stain gauge sensors during the first 20 minutes of the 10:00 a.m. hour, for the day of 10 February 2015.

Table 3.3 Recorded output voltage by datalogger (CR 1000) for Sensors 1 to 8

Time step	1	2	3	4	5	6	7	8
10/02/2015 10:00	212.26	211.72	211.45	211.31	211.18	211.18	210.91	210.91
10/02/2015 10:02	211.85	211.18	211.18	211.18	210.91	210.91	210.64	210.64
10/02/2015 10:04	212.26	211.72	211.45	211.18	211.18	211.18	210.91	210.91
10/02/2015 10:06	212.26	211.45	211.45	211.18	211.18	210.91	210.91	210.64
10/02/2015 10:08	211.72	211.18	210.91	210.91	210.64	210.64	210.37	210.23
10/02/2015 10:10	211.17	210.63	210.36	210.36	210.09	210.09	209.82	209.82
10/02/2015 10:12	210.88	210.07	210.07	209.80	209.53	209.53	209.26	209.13
10/02/2015 10:14	210.33	209.79	209.52	209.52	209.25	208.98	208.98	208.98
10/02/2015 10:16	210.05	209.51	209.24	209.24	208.97	208.97	208.70	208.43
10/02/2015 10:18	209.51	208.97	208.97	208.70	208.56	208.43	208.29	208.16
10/02/2015 10:20	209.77	209.23	208.96	208.96	208.69	208.56	208.42	208.42

Table 3.4 Corresponding strain value for sensors 1 to 8

Time step		2	3	4	5	6	7	8
10/02/2015 10:00	394.24	391.93	390.78	390.20	389.62	389.62	388.47	388.47
10/02/2015 10:02	392.50	389.62	389.62	389.62	388.46	388.46	387.31	387.31
10/02/2015 10:04	394.23	391.92	390.77	389.61	389.61	389.61	388.46	388.46
10/02/2015 10:06	394.23	390.77	390.77	389.61	389.61	388.46	388.46	387.30
10/02/2015 10:08	391.92	389.61	388.45	388.45	387.30	387.30	386.15	385.57
10/02/2015 10:10	389.59	387.28	386.13	386.13	384.97	384.97	383.82	383.82
10/02/2015 10:12	388.35	384.89	384.89	383.74	382.58	382.58	381.43	380.85
10/02/2015 10:14	386.00	383.69	382.54	382.54	381.39	380.23	380.23	380.23
10/02/2015 10:16	384.81	382.51	381.35	381.35	380.20	380.20	379.04	377.89
10/02/2015 10:18	382.48	380.17	380.17	379.02	378.44	377.86	377.29	376.71
10/02/2015 10:20	383.61	381.30	380.15	380.15	379.00	378.42	377.84	377.84

The stress analyses of each sensors of the elements was performed using the Hooke's law presented in equation 3.5.The element stress solely depends on the young modulus of materials made of and the wind induced micro strain .Only element 'K' was made of aluminium while other elements were made of steel. This material different have great impact on the stress analysis of the element

as aluminium element has lower stress values as compared to steel element .Young modulus for aluminium and steel elements as obtained from [37] are 6.9E+09 and 2.0E+11Pa respectively. Sensors1 to 6 produced stress at 2 minutes time lag for element 'M', element 'K' yielded sensor stresses 7 to 10 ,11 to 14 correspond to stress on element A and last two sensors produced stresses on the circular rack as presented in table 3.5 below;

$\sigma = \gamma * \mu\epsilon$ [Eq 3.5]

Table 3.5: Corresponding stresses value for sensors 1 to 8

Time step	1	2	3	4	5	6	7	8
10/02/2015 10:00	7.88E+07	7.84E+07	7.82E+07	7.80E+07	7.79E+07	7.79E+07	2.68E+07	2.68E+07
10/02/2015 10:02	7.85E+07	7.79E+07	7.79E+07	7.79E+07	7.77E+07	7.77E+07	2.67E+07	2.67E+07
10/02/2015 10:04	7.88E+07	7.84E+07	7.82E+07	7.79E+07	7.79E+07	7.79E+07	2.68E+07	2.68E+07
10/02/2015 10:06	7.88E+07	7.82E+07	7.82E+07	7.79E+07	7.79E+07	7.77E+07	2.68E+07	2.67E+07
10/02/2015 10:08	7.84E+07	7.79E+07	7.77E+07	7.77E+07	7.75E+07	7.75E+07	2.66E+07	2.66E+07
10/02/2015 10:10	7.79E+07	7.75E+07	7.72E+07	7.72E+07	7.70E+07	7.70E+07	2.65E+07	2.65E+07
10/02/2015 10:12	7.77E+07	7.70E+07	7.70E+07	7.67E+07	7.65E+07	7.65E+07	2.63E+07	2.63E+07
10/02/2015 10:14	7.72E+07	7.67E+07	7.65E+07	7.65E+07	7.63E+07	7.60E+07	2.62E+07	2.62E+07
10/02/2015 10:16	7.70E+07	7.65E+07	7.63E+07	7.63E+07	7.60E+07	7.60E+07	2.62E+07	2.61E+07
10/02/2015 10:18	7.65E+07	7.60E+07	7.60E+07	7.58E+07	7.57E+07	7.56E+07	2.60E+07	2.60E+07
10/02/2015 10:20	7.67E+07	7.63E+07	7.60E+07	7.60E+07	7.58E+07	7.57E+07	2.61E+07	2.61E+07

3. 6 Photovoltaic dual axis Tracker Control System

The wind induced loading on flat structures such as the PV solar panels modules are very much influenced by the position of such structure with regard to the wind direction. Therefore the current experiment has focused on measuring the strains and stresses induced to the supporting structure of the PV solar panels modules inclined (elevation) at angles between 45° and 78° and rotated (azimuth) at angles between 30° and 210°. Each day a different inclination / rotation angles

combination was tested by changing the elevation and azimuth angles of the solar tracker. Accurate changes in the angle degrees were possible by using the Golden Sun tracker software developed by the Sun Lab research group at the University of Ottawa, which has two main tabs for remotely operating the tracker. The first tab is the Status tab which contains the calculated and measured angle data for comparison purposes (Fig. 3.10 a)); thus eventual errors could be easily detected if there was much difference between the desired angle and the angle achieved by the solar tracker. Figure 3.10 b)) shows the Golden Sun software window controlling the parking tab that resets the tracker to the horizontal position of 78°. The software works together with the Electric motor mechanism installed under the rack of the solar tracker, that controls the motion of the tracker and the control box which enhances the azimuth and the rotation operation of the solar tracker.

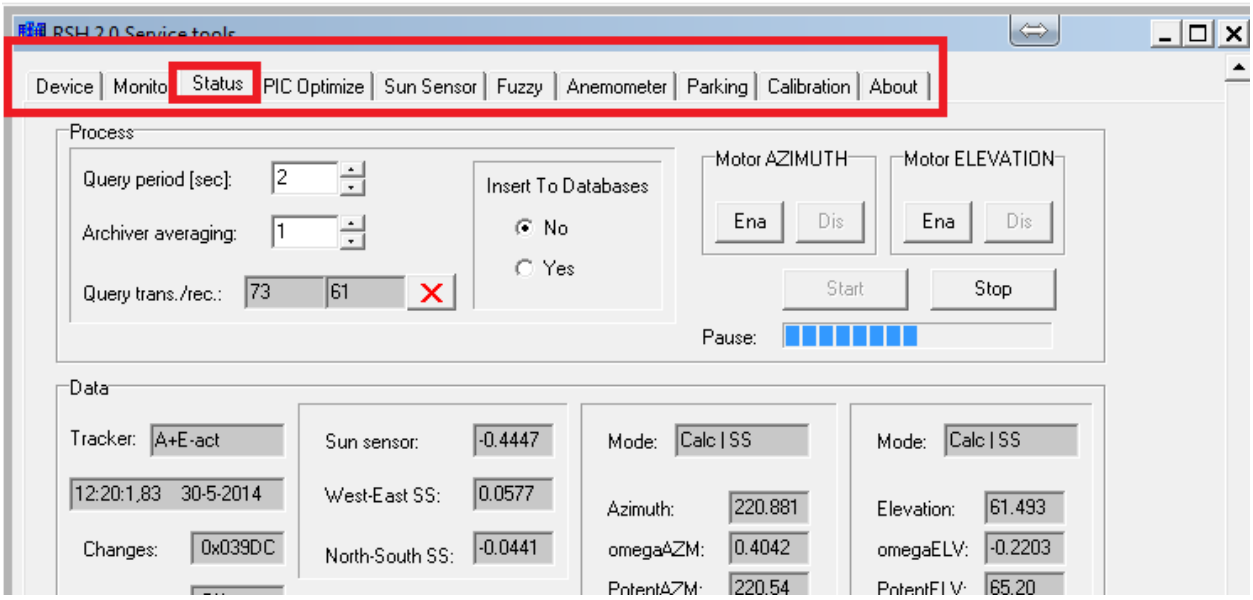

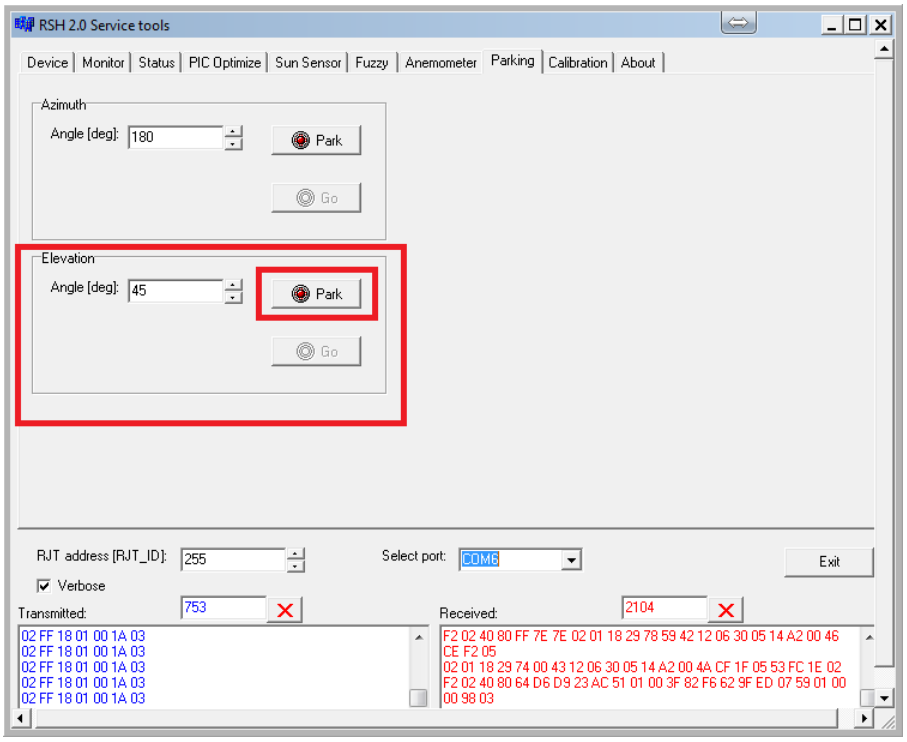

Figure 3.10.Features of the Golden Sun tracker software a) Azimuth and elevation angles control window b) Stow position angle (78°) control window [30]

Each morning the solar tracker was placed in the elevation/azimuth position required for the experiment by the aid of the Golden Sun software, the motor controlled by the software was disengaged manually for avoiding any accidental command re-writing which would displace the solar tracker from the tested position. At 5:00 p.m. the experiment is considered finished and the motor control box was re-connected to the software transmission commands. Also during each night the solar tracker was placed with the PV solar panels modules almost horizontal, at stow position of 78°, because this is considered as the neutral position, which is less affected by the wind speed intensity and direction. The procedural steps followed for performing the experiment, and for varying the inclination and the rotation angles of the solar tracker on a daily basis during the Winter 2015 season are described as follows:

Morning (9.a.m) Tracker during Operation

- The elevation motor was loosened with the spanner.
- The control box was turned on.

- The elevation angles were changed using the Golden Sun tracker software installed on an off-site computer.
- The elevation motor was tightened manually, so that the software cannot re-write the commands and the angles cannot be changed during that day.
- The control box was turned off, for disconnecting the transmission connection with the Golden Sun software.

Evening (5.p.m) Tracker at stow position

- The elevation motor was loosened with the spanner.
- The control box was turned on.
- The elevation angles were changed to stow position (78°) using the Golden Sun tracker software installed on the off-site computer.
- The elevation motor was tightened.
- The control box was turned off.

By positioning the solar tracker for different elevation and azimuthal angles Cases 1-30° to Case 7-120°, were categorized, each representing elevation angles of 45, 50, 60, 65, 70, 75 at one rotation angle, as detailed in Table 3.4. Thus a total of 49 cases were investigated for the investigated operational angles of the solar tracker between 9:00 a.m. and 5:00 p.m. daily. The stow position depicts the safe angle for the tracker and it should be always employed during the night, when the devices cannot be controlled manually. However because the data acquisition system was still running, several cases and comparisons will provided based on the data measured for the stow position (78°).

Table 3.6 Investigated Tracker Inclination and rotating angles.

Cases	Inclination (elevation) angle (°)	Rotation (azimuth) angle(°)
Case 1-30°	45, 50, 55, 60, 65, 70, 75	30
Case 2-60°	45, 50, 55, 60, 65, 70, 75	60
Case 3-90°	45, 50, 55, 60, 65, 70, 75	90
Case 4-120°	45, 50, 55, 60, 65, 70, 75	120
Case 5-150°	45, 50, 55, 60, 65, 70, 75	150
Case 6-180°	45, 50, 55, 60, 65, 70, 75	180
Case 7-210°	45, 50, 55, 60, 65, 70, 75	210

3.7 Weather data

The preparation of the experiment started in Fall 2014, however the first measurements were collected in Winter 2015. Also along with the strain measurements for the structure the weather data, such as wind speed intensity and direction, temperature, air humidity and density, were required in order to develop the estimations for the wind loading encountered at the solar tracker site for each case. Unfortunately, the anemometer equipment which measures the wind data at the solar tracker site, installed on the Mann Parking roof, was faulty during the Fall – Winter 2015 period and as a result, the weather data at the site station was not available for this experiment. Alternatively, the weather data from Ottawa Macdonald-Cartier International Airport, Ontario were obtained as this was more reliable when compared to any other source [41]. The weather station at the airport is situated in open terrain, at 2 m above the ground, while the solar tracker from the Mann Parking building are situated on the roof at less than 10 m (reference height in wind speed profiles) above the ground. Also the Mann Parking building is located on the corner of the King Edward St. and Mann Ave. and does not have other buildings in the vicinity therefore it can be considered as open terrain. Wind speed data from the Mann weather station were recorded for September 2014, prior to conducting the solar tracker testing, and the hourly averages were compared with the data reported from the Macdonald Cartier Airport weather station. Differences lower than 10% were noticed, therefore the wind speed data was considered acceptable for calculating the wind loading for the finite element analysis. Thus the weather data recorded for February, March and April 2015 on daily basis with the aid of equipment known as LUFFT WS 501 was used in the current study. This equipment measures ambient temperatures, atmospheric pressure, wind speed, relative humidity, wind direction and global horizontal sun irradiation. the maximum temperature, maximum wind speed, maximum relative humidity between month of February and April were used in estimating the drag and lift forces for the static analysis of the solar tracker, while the time-dependent signal of the recorded parameters were used for time-history analysis loading for the FE analysis.. The variation of the maximum, mean and minimum temperatures for the months of February 2015 and March 2015 are shown in Figure 3.11 a), b) and c) below.

a)

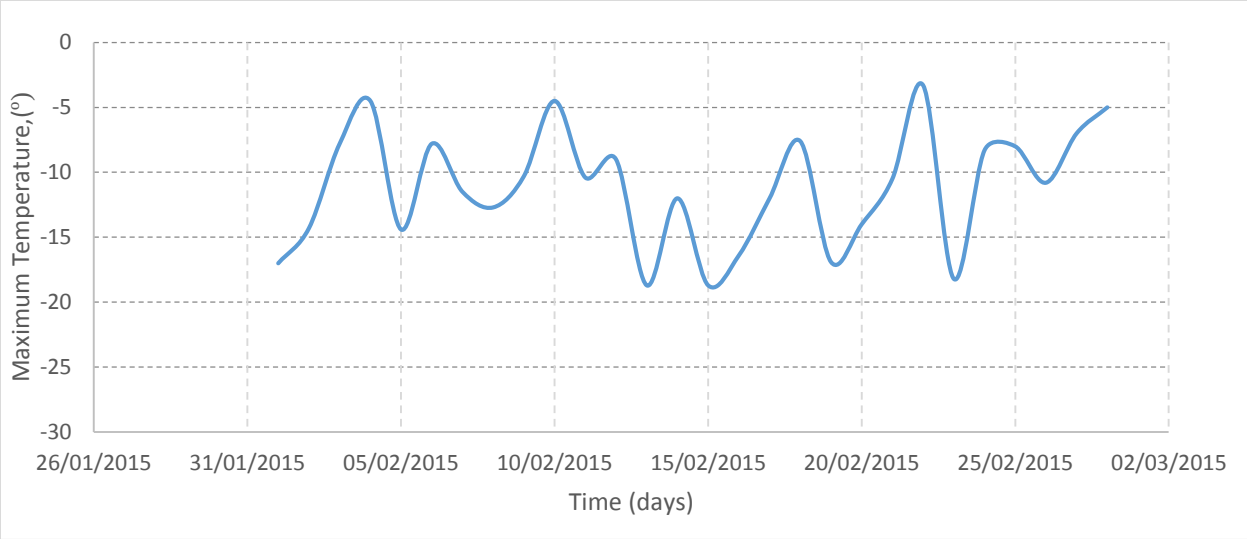
0
-5
-10
-15
-20
-25
-30
Maximum Temperature,(°)
26/01/2015
31/01/2015
05/02/2015
10/02/2015
15/02/2015
20/02/2015
25/02/2015
02/03/2015
Time (days)

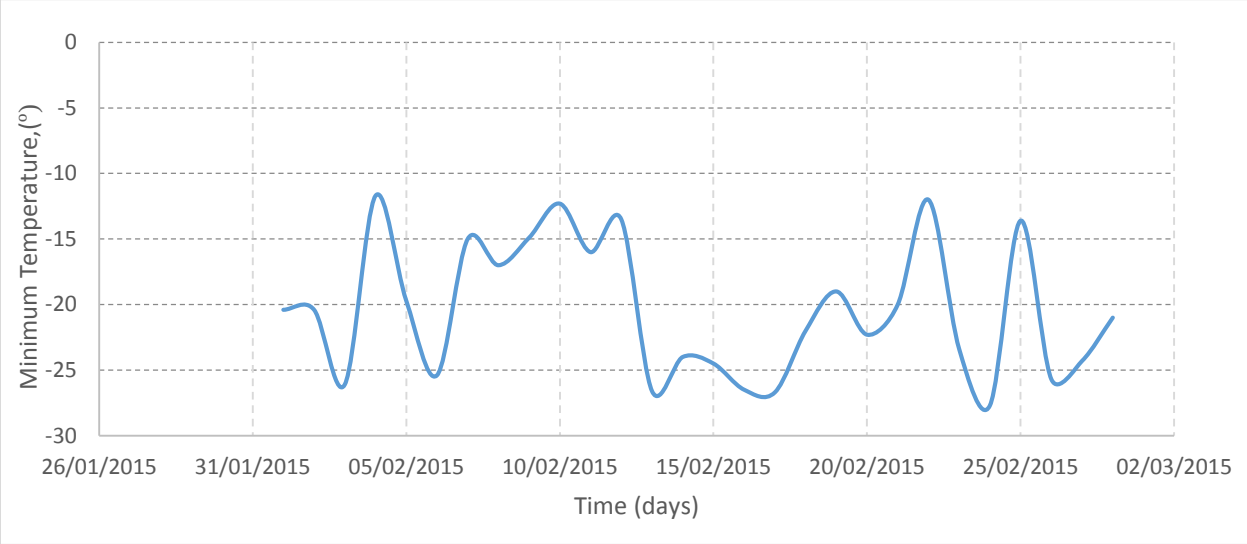
0
-5
-10
-15
-20
-25
-30
Minimum Temperature,(°)
26/01/2015
31/01/2015
05/02/2015
10/02/2015
15/02/2015
20/02/2015
25/02/2015
02/03/2015
Time (days)

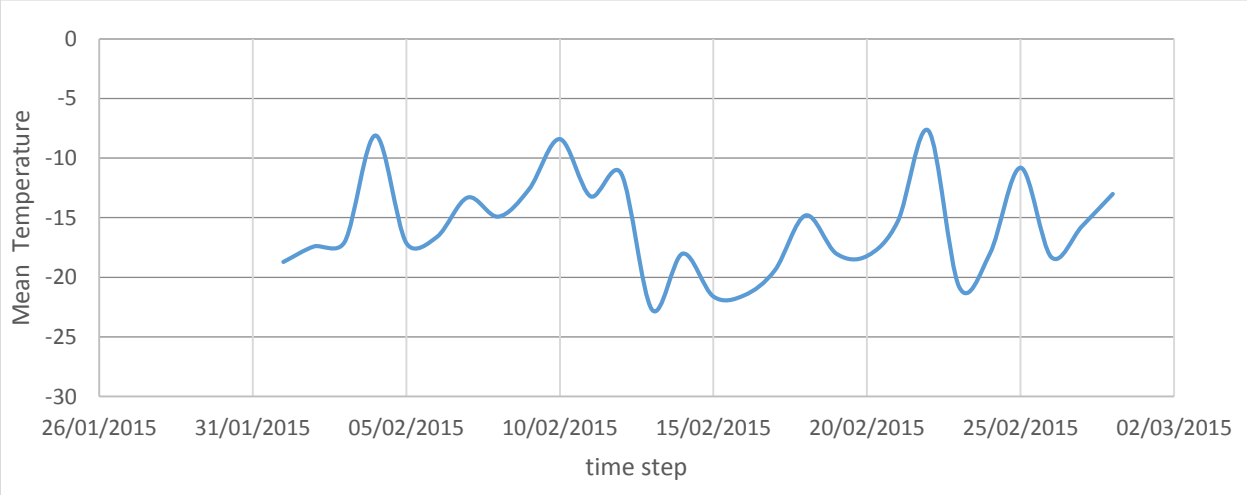
0
-5
-10
-15
-20
-25
-30
Mean Temperature
26/01/2015
31/01/2015
05/02/2015
10/02/2015
15/02/2015
20/02/2015
25/02/2015
02/03/2015
time step

b)

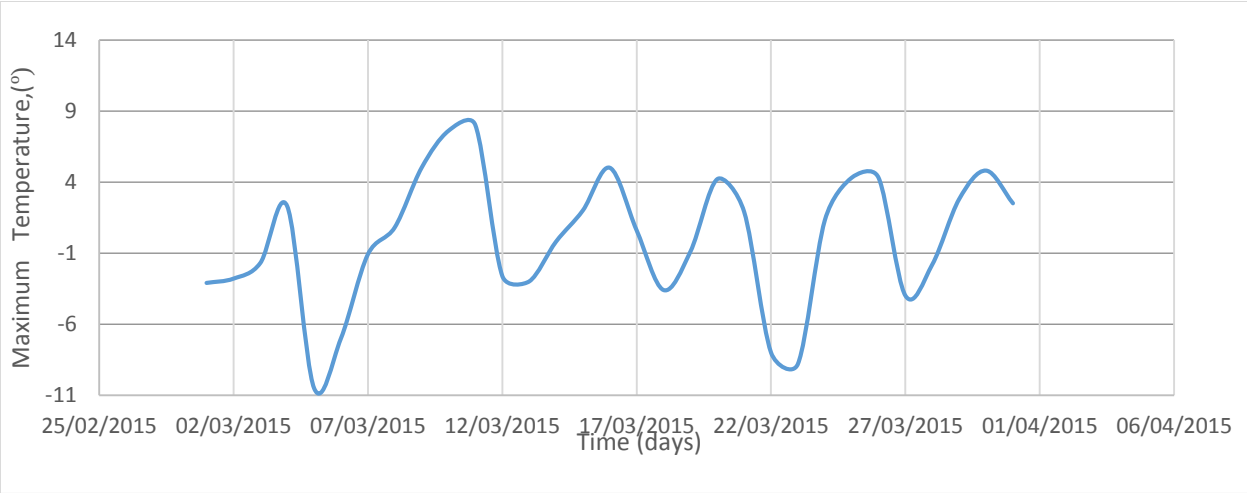
14
9
4
-1
-6
-11
Maximum Temperature,(°)
25/02/2015
02/03/2015
07/03/2015
12/03/2015
17/03/2015
22/03/2015
27/03/2015
01/04/2015
06/04/2015
Time (days)

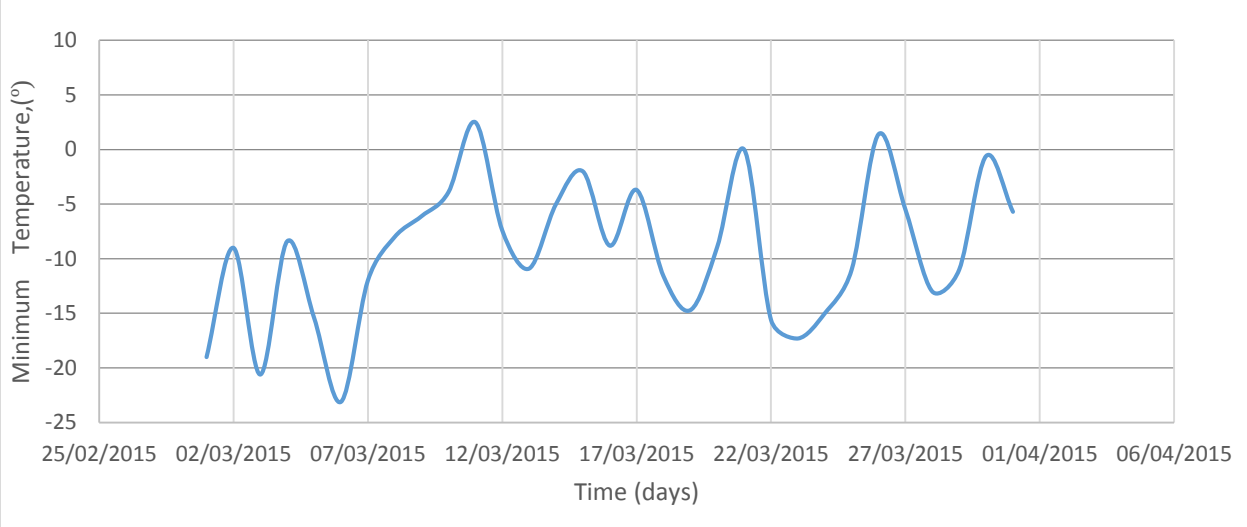
10
5
0
-5
-10
-15
-20
-25
Minimum Temperature,(°)
25/02/2015
02/03/2015
07/03/2015
12/03/2015
17/03/2015
22/03/2015
27/03/2015
01/04/2015
06/04/2015
Time (days)

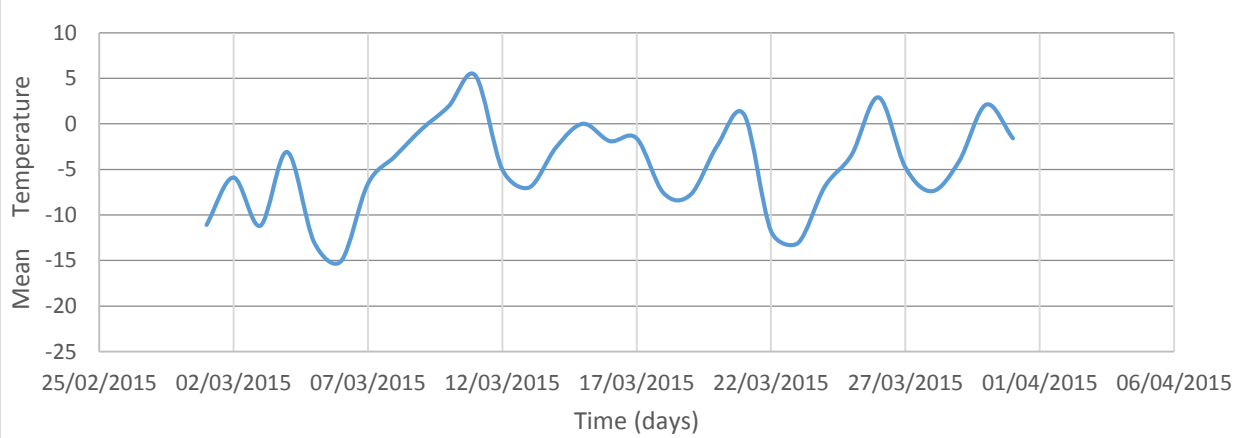
10
5
0
-5
-10
-15
-20
-25
Mean Temperature
25/02/2015
02/03/2015
07/03/2015
12/03/2015
17/03/2015
22/03/2015
27/03/2015
01/04/2015
06/04/2015
Time (days)

c)

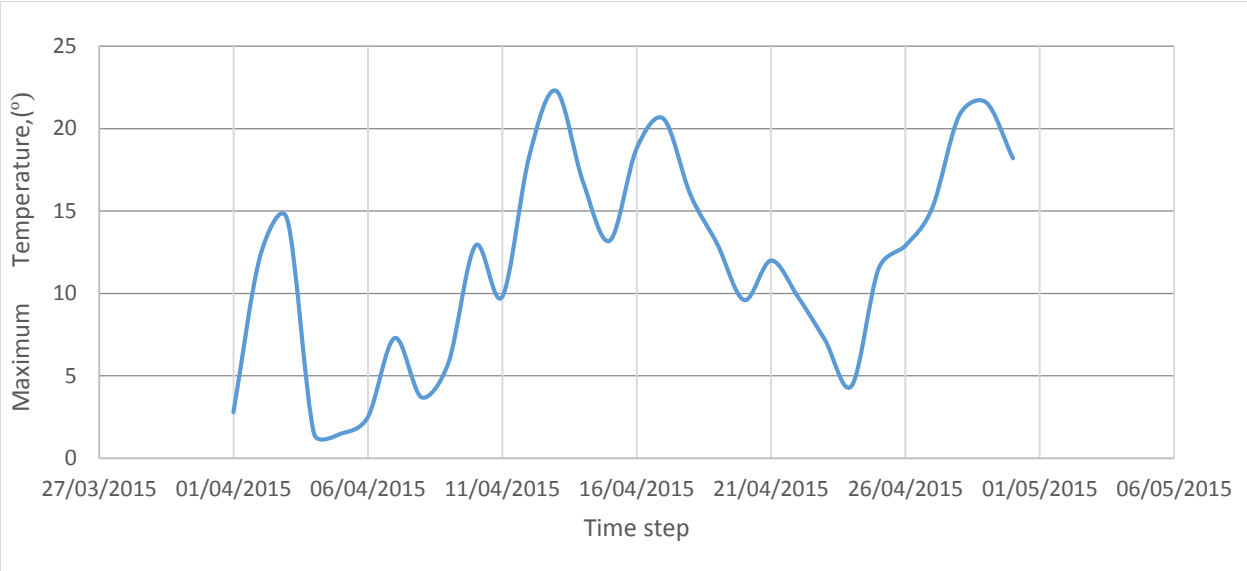
Maximum Temperature,(°)
25
20
15
10
5
0
27/03/2015
01/04/2015
06/04/2015
11/04/2015
16/04/2015
21/04/2015
26/04/2015
01/05/2015
06/05/2015
Time step

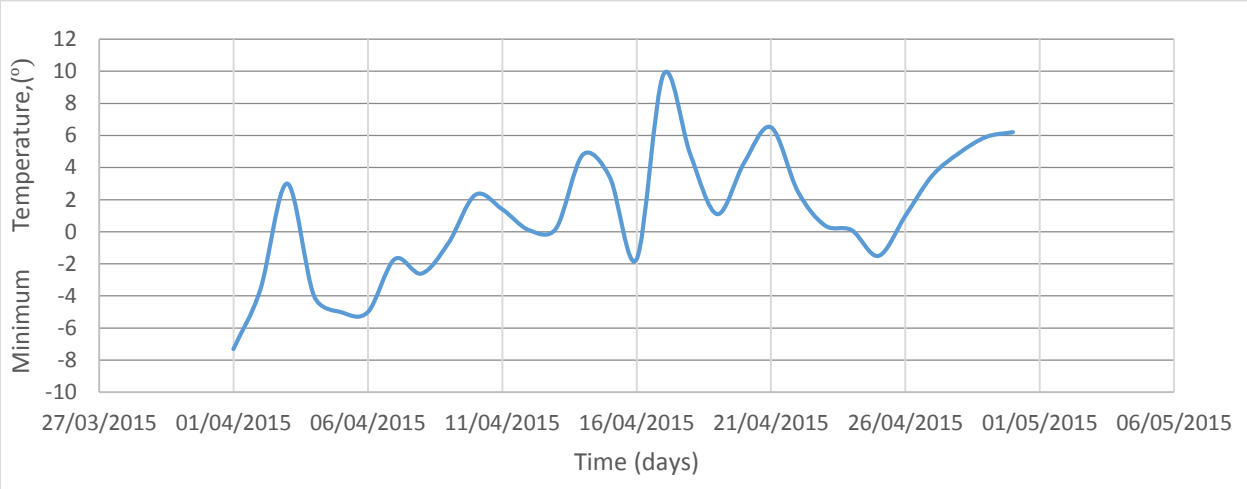
Minimum Temperature,(°)
12
10
8
6
4
2
0
-2
-4
-6
-8
-10
27/03/2015
01/04/2015
06/04/2015
11/04/2015
16/04/2015
21/04/2015
26/04/2015
01/05/2015
06/05/2015
Time (days)

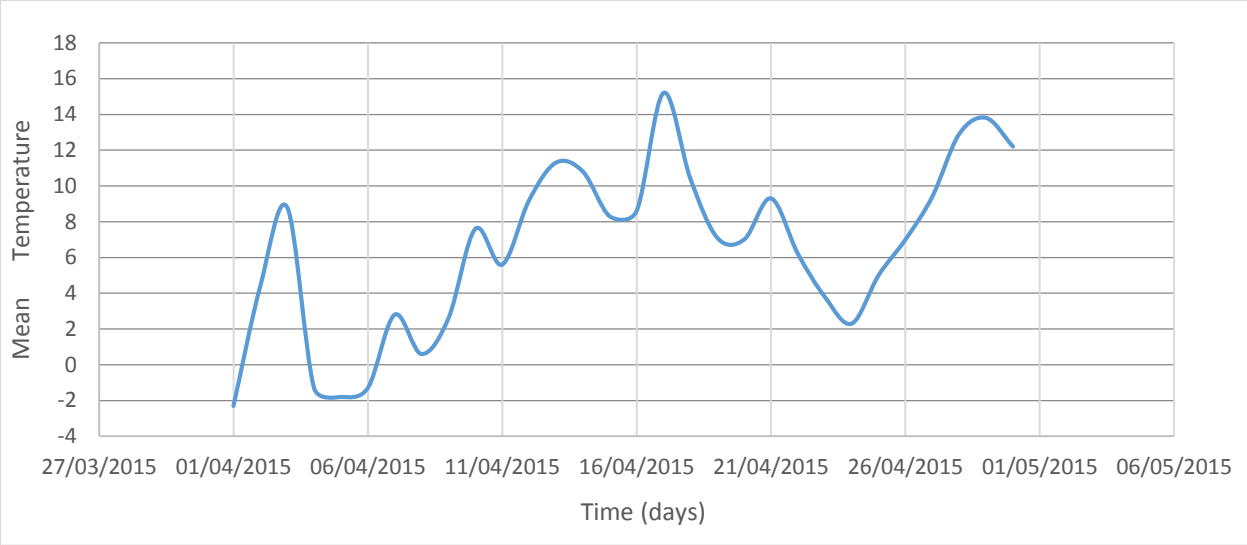

Figure 3.11 .Maximum, minimum and mean temperatures (^{0}C) for a) February 2015 b) March 2015 c) April 2015 [41]

Another weather parameter that is very important for the computation of the wind induced drag and lift forces on tracker, is the relative humidity of the air. The maximum value of the relative humidity for the month of February 2015 was recorded on February 2nd as 91%, while the minimum value of the above mentioned parameter occurred on February 27th with a value of 33 %. However, the maximum values increased for the month of March 2015 reaching a value of 97% on March 17th and the minimum value reduced to 22% on March 31st. The maximum air relative humidity values recorded were used for determining the air dry density using equation 4.7, . Also the daily periodic variation of the relative humidity for both months of February and March 2015 are presented below in Figures 3.12 a) and b).

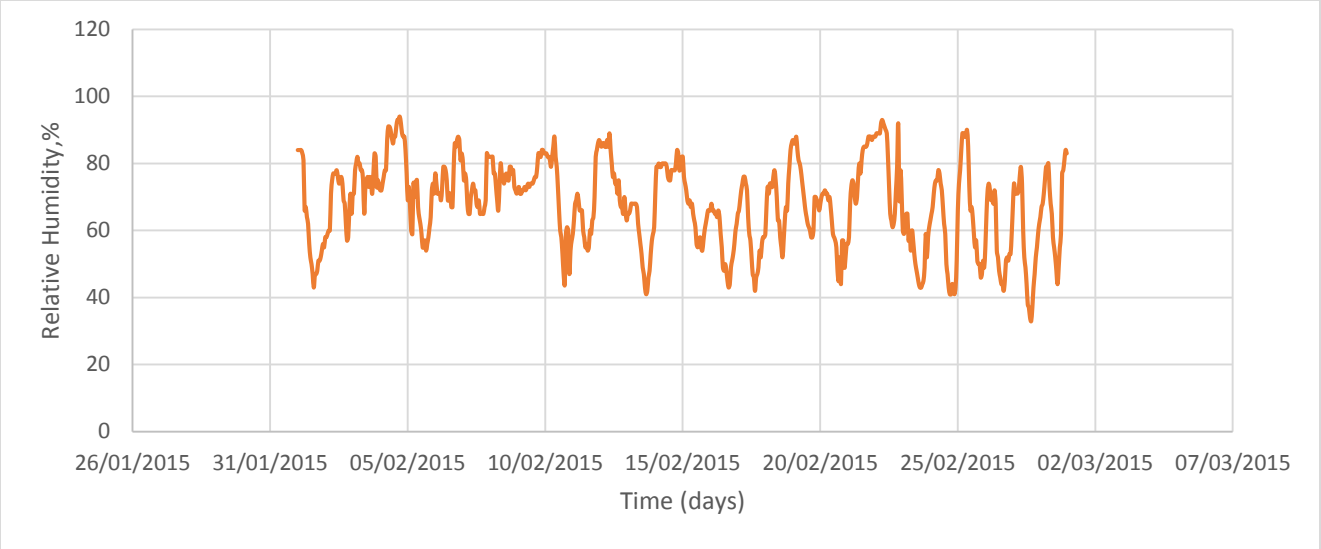

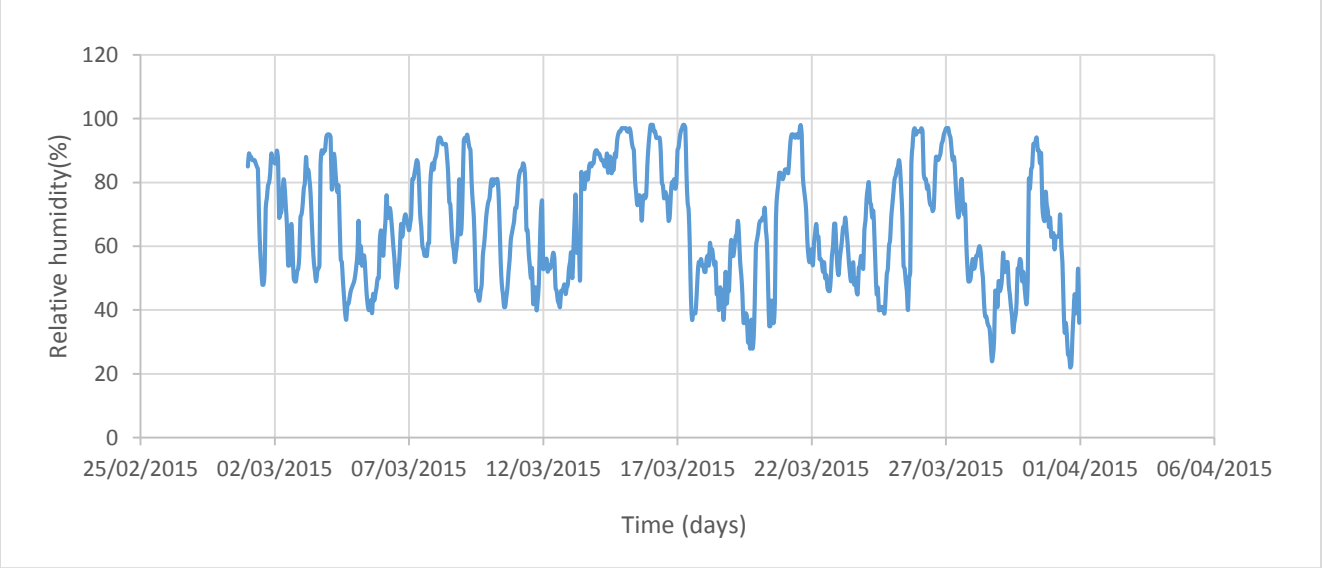

Figure 3.12. Relative humidity variation (%) for a) February 2015 b) March 2015

The maximum air pressure values were recorded on February 28th, March 1st and March 12th 2015 as 102.54 KPa, 102.32 KPa and 102.27 K Pa respectively. On the other hand, the minimum values of the air pressure were recorded on February 25th and March 30th as 98.80 KPa and 98.53 KPa accordingly. The air pressure trend for February and March 2015 period are presented in Figures 3.13 a) and b) respectively.

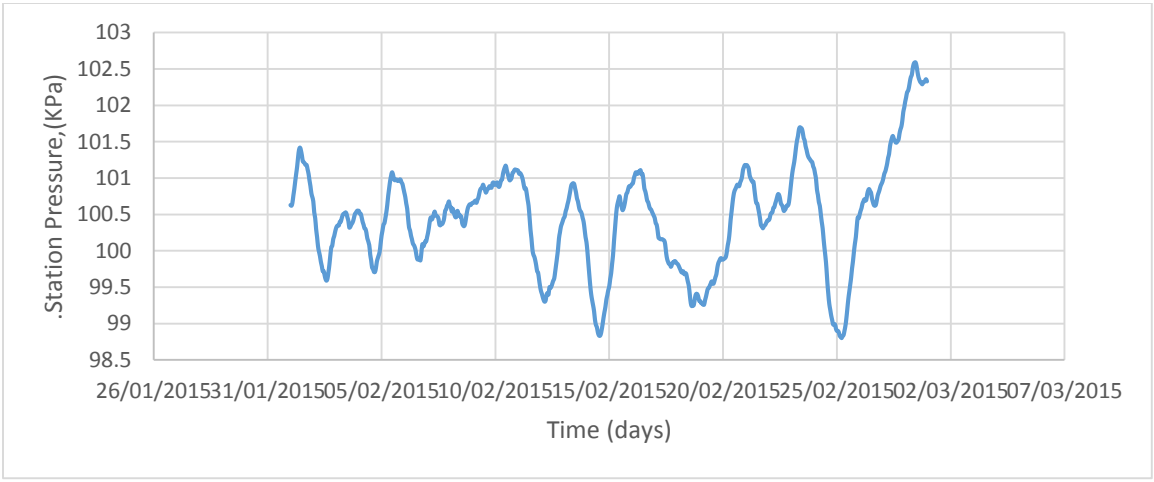

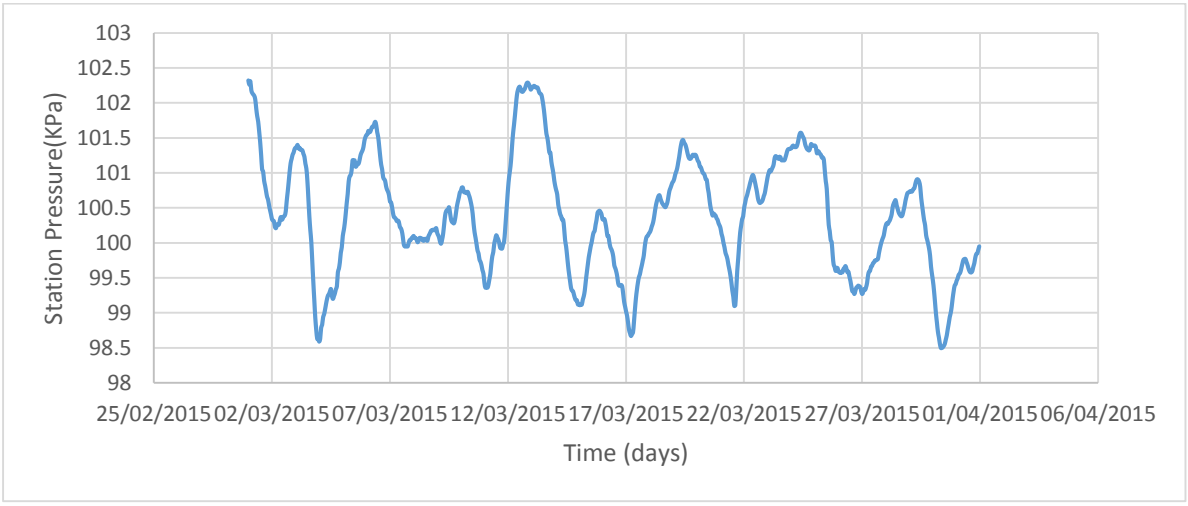

Figure 3.13 Amplitude of a variable periodic air-pressure (KPa) for a) February 2015, b) March 2015

The last weather parameter directly influencing the wind-induced loadings on the solar tracker is the wind speed. The maximum wind speed was recorded on February 15th and March 17th as 11.39 m/s and 16.11m/s respectively. The minimum values recorded were found to be 0 m/s and 0.27 m/s on multiple days: February 7th, February 4th , March 3rd and March 13th 2015. Since the critical response of the tracker is of interest and of most concern, the maximum wind speed recorded on March 17th was employed when determining the static wind lift and drag loads for the static analysis of the solar tracker, while the entire wind speed record was used for the time

history analysis performed on the FE model of the solar tracker. Figures 3.14 a) and b) present two different records for the hourly average of the wind speeds, for both months of February and March 2015.

a)

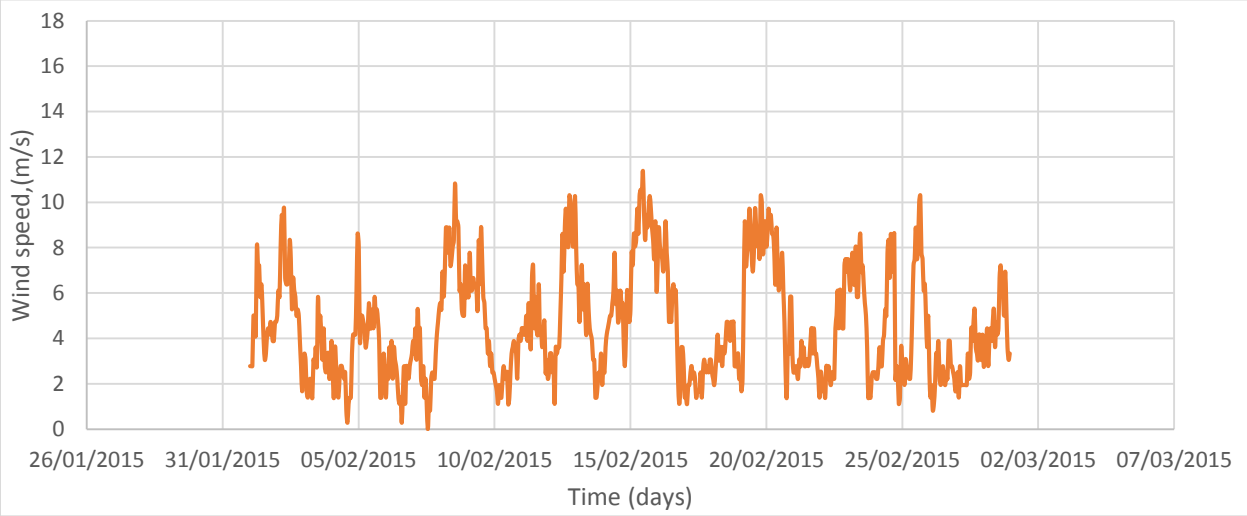

b)

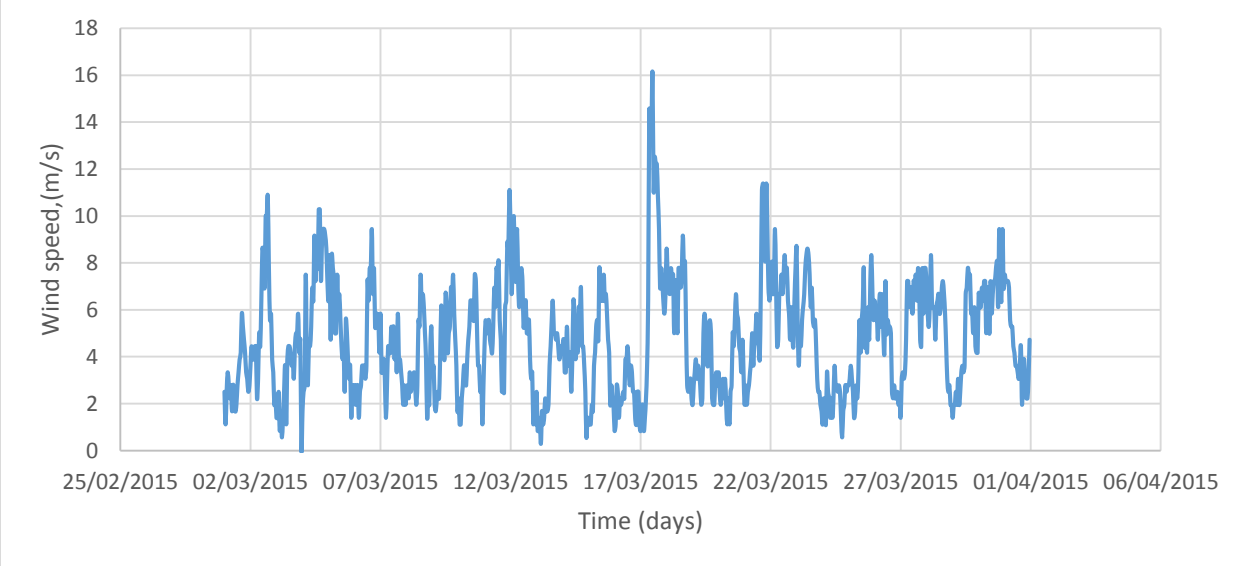

Figure 3.14 Wind speed intensity variation (m/s) for a) February 2015 and b) March 2015

Wind load is a variable dynamic load acting on the surface of the structural elemental directly exposed to the incoming wind speed; also the magnitude of the dynamic loading depends on the

element geometry and the direction of the applied load as detailed in the previous section. In other to accurately analyse the solar tracker structure, the wind speed direction at which wind is considered dominant for short periods of time, was considered during the application of the drag and lift loads to the structure. Based on the data recorded for both months, the wind direction was considered dominant along four different directions; north-west, south-east, north-east and south-west directions which are correspond to direction angles of 270^0-360^0, 0^0-90^0, 90^0-180^0 and 180^0-270^0 as mentioned. The dual axis solar tracker instrumented was able to rotate in all the directions to follow the movement of the sun, thereby increasing the efficiency of the energy collection by the installed solar PV module, but it does not predict the direction of the dominant wind speed which could cause great damage to the structure itself. Thus wind speed direction was obtained at hourly interval on daily basis, from the weather station at the Ottawa International Airport for February 2015 and March 2015. Figure 3.13 below, shows that in February 2015, the wind speed was dominant in north-west direction, which was between 270^0 and 360^0. In March 2015, the wind speed was dominant between 180^0 and 270^0 on the south-west direction.

The weather data parameters presented above were used for determining the magnitude of the wind-induced drag and lift loads on different structural elements of the solar tracker, as it will be explained in detail in Chapter 4, where the FE analysis is presented. The wind speed direction was used for interpreting the dominant angles of attack for the investigated FEM of the solar tracker and for choosing the azimuth / elevation angle combinations which would reflect the dominant exposure angles encountered at the site where the solar tracker is installed.

a)

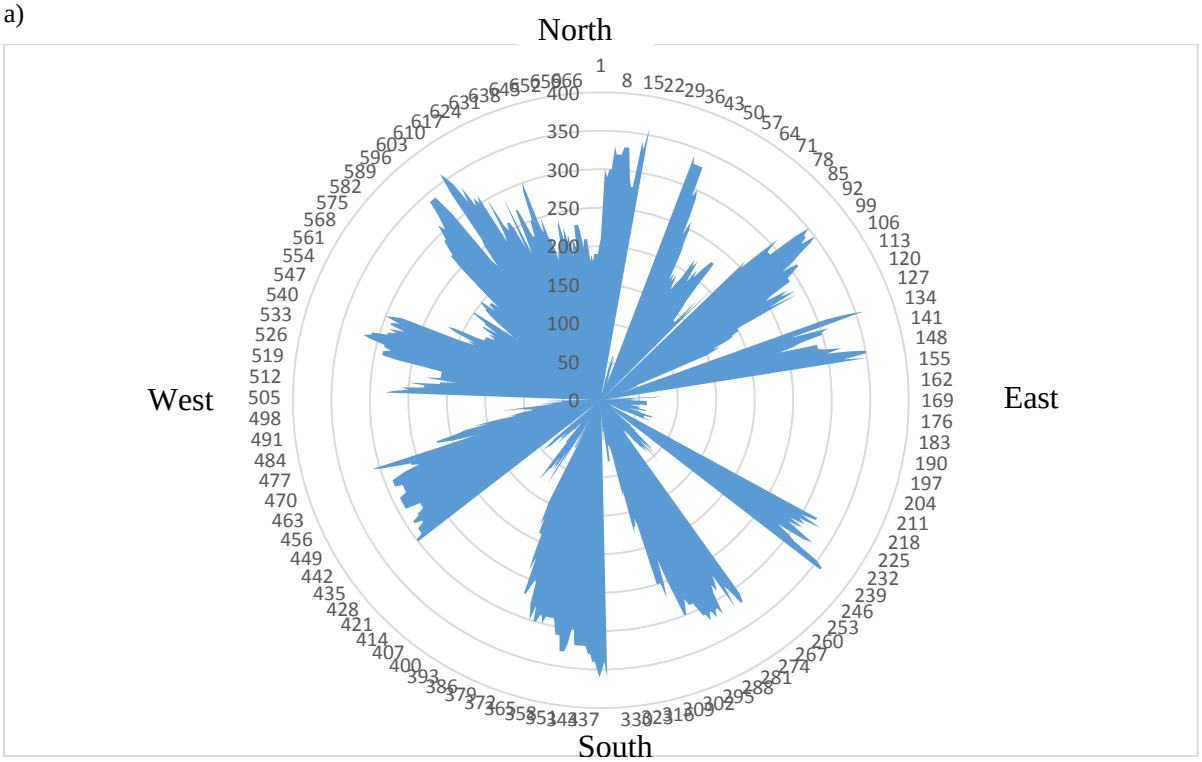

b)

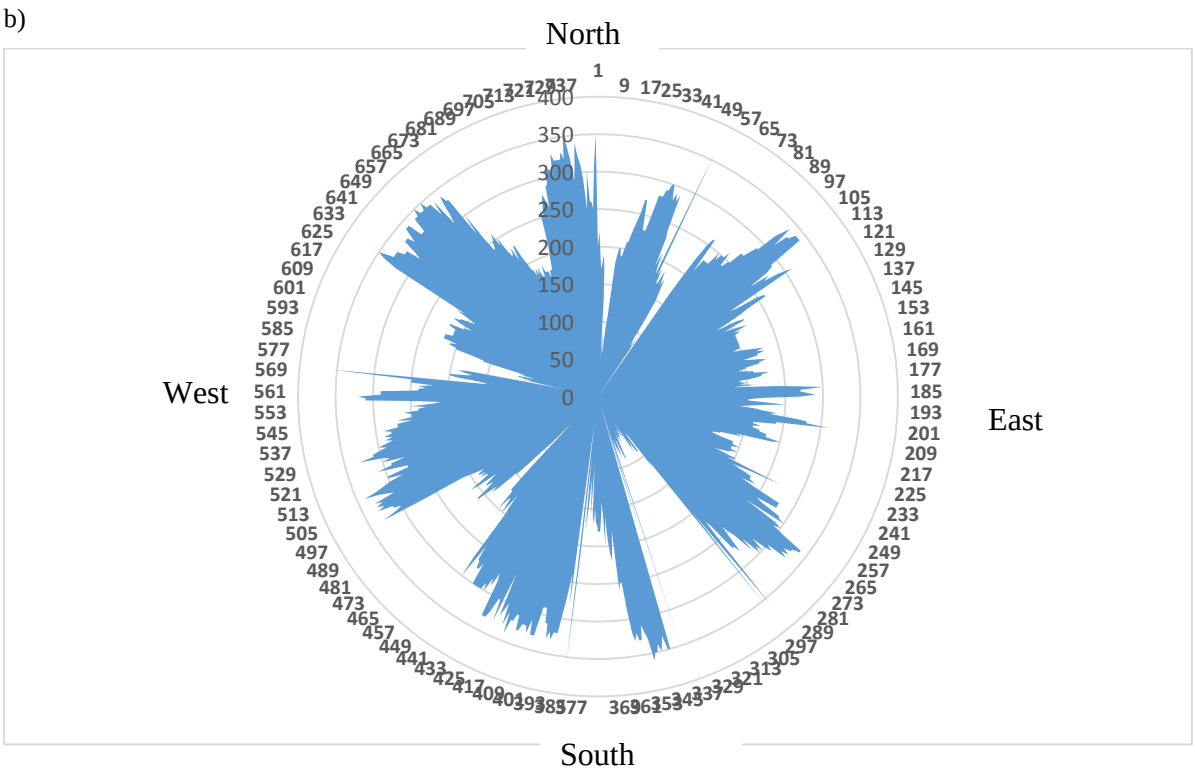

Figure 3.15 Wind speed direction for a) February 2015 and b) March 2015

Chapter 4 Finite Element Modelling

4. 1 Finite Element Analysis

Finite element method (FEM) is one of the numerical techniques employed in structural engineering problems, for estimating the solutions of the response differential equations, based on the initial values and on the boundary conditions. The finite element analysis involves dividing the complicated structures which must be investigated, into smaller elements that can be solved in relation to each other. In other words, the FEM fundamentals involves breaking the structure to be studied into a finite number of pieces, forming subdomains called elements, then reconnecting these elements at nodes, with certain constrains or even fixations so that the elements can hold together and can simulate the response of the entire structure together. This analysis process develops results from a set of simultaneous algebraic equations. FEM is a reliable method of finding displacements and stresses at defined coordinate known as nodes. Moreover, the FEM it is a powerful tool to calculate the dynamic properties of the investigated structure [42]. Furthermore, employing FEM saves substantial amount of time by simulating numerous loading scenarios with the aid of computers, thus reducing the time and the expenses related to performing experiments and in-situ measurements for determining the effect of the same loading cases for a given structure. Nowadays, finite element methods are widely used in structural and stress analysis, thermal analysis, dynamic analysis and fluid dynamic analysis.

4.2. Objectives of the Finite Element Analysis

The primary objective of performing the finite element analysis for the solar tracker model, was to obtain the wind-induced displacements of the solar tracker through the static analysis of the wind loading and to compare the results with experimental results A second objective was to check the structural stability of dual axes solar tracker under the action wind speeds much higher than the maximum wind speed of 16.11 m/s recorded during the winter 2015 season. Thus wind speeds of up to 33 m/s were employed for determining the structural response of the component members of the solar tracker and the eventual critical displacement for the entire supporting frame was discussed.

4.3 General Steps involved in finite element method

The order and details of the general steps undertaken for performing the finite element analysis of the dual axis solar tracker are presented below.

- Building the geometry of the structural model: the exact dimensions of the dual axis solar tracker installed on the Mann Parking building were used for creating the structural model to be investigated by the aid of the commercial software SAP 2000. The location and connections of the sub-elements of this structure were also employed as close as possible to the geometry of the prototype. During the model construction, some very parts which were very small were simplified and were integrated in the bigger adjacent elements, thus such assumption could not affect the analytical results.
- Selection of the element types: for each of the elements composing the geometry of the solar tracker model, different types of structural elements, available in SAP 2000 for element development, were selected. Each of these was used for a specific purpose, depending on the type of modeling. For example, the main structural elements used for the solar tracker modeling were the frame -truss element was employed because it could be used for braces, trusses and slender elements composing the supporting frame of the tracker. Also this frame element was used for most of the short connecting elements. Nodes were formed at each connecting points of the line elements thereby, each element had six degree of freedom at each node, consisting of translational and rotational displacements. The actual solar panel module installed at the top of the supporting structure was modeled as multiple shell elements, connected to each other, and supported at the edges by frame-truss members. A total of thirteen frame elements were created representing the geometry of the solar tracker
- Model mesh generation: in order to estimate the response of the structure at various locations within the structure, division in smaller elements was required which was achieved by meshing the structural model. Three global Cartesian coordinate system namely the X, Y and Z directions, was employed for representing connecting elements in the longitudinal direction X, in transverse direction Y and Z in vertical direction.
- Application of loads and Boundary conditions an estimated maximum wind load in horizontal and vertical direction, corresponding to the drag and lift wind forces, were

applied to all elements of the tracker as distributed loads, thereafter being transferred from the applied loads to the nodes. The bottom part of the tracker (circular rack) was fixed to the precast concrete blocks and the top part (Element M) was hinged to the main frame (element A) .The displacements at each element nodes were determined based on the static analysis. A time-history analysis was also performed by employing the wind loads as time dependent variable loadings, directly determined from the measured wind speed, as detailed in the following sections.

4.4 Photovoltaic Solar Tracker Modeling

A finite element model of the dual axis solar tracker was fully developed to simulate the experimental findings. The Finite Element analysis relays on selecting the proper element type to predict the actual behaviour of the tracker. The structural elements were defined by: material type, element type, nodal points, geometry, degrees of freedom and nodal forces [42]. In this study the Line element of frame type along with the shell element were used for different parts of the solar tracker model**.** In order to accurately investigate the structural stability of the solar tracker under the action of natural wind-induced drag and lift forces, the steel supporting structure was divided into 13 elements as presented in the previous section, these elements were modeled and analysed at various elevation angles ranging from 45° to 75° and rotation angles from 30º to 210º. Depending on shape of the frontal element, the direction of wind, air density and the drag and lift load coefficients the loading cases were estimated. Both static and dynamic analysis was performed using the structural analysis software SAP 2000. For achieving a belter model of the dual axis tracker, the material properties of different members and the exact geometry of the structure were introduced in the software.

4.4.1 Frame-Line Element

The frame-line element was mostly used in the development of the dual axis tracker model for the truss elements of the structure, by connecting two nodes together at ends. The cross-section and the material type was different, however the same frame-line structural element was used for all the elements: the upper part, the frame body and the circular rack of the solar tracker, as shown in Figure 4.1except for the solar panel These elements activated all six degree of freedom on both connected nodes [42].

The material properties of the frame components were selected as per the respective steel and aluminium materials used for the construction of the solar tracker support frame, as shown in Table 4.1 below.

Table 4.1 Material properties used for the frame elements

Object Type	Material	Total Weight (N)	Number of elements
Frame	Steel	19,736.36	156
Frame	Aluminum	703.64	4

4.4.2 Shell Element

A total of nine shell elements were used to model the Photovoltaic solar panel module which is installed on top of the solar tracker support structure under two rows. The PV panel is fabricated as a sandwich containing up to five layers of different types of material such as glass, silicon cells, connected together by the aid of adhesive layers known as Ethylene Vinyl Acetate (EVA) layers The first (lower) row has a total of five PV panels and the second (upper) row has only four PV panels and the same configuration was maintained for the Finite element model. Each shell element has four nodes.

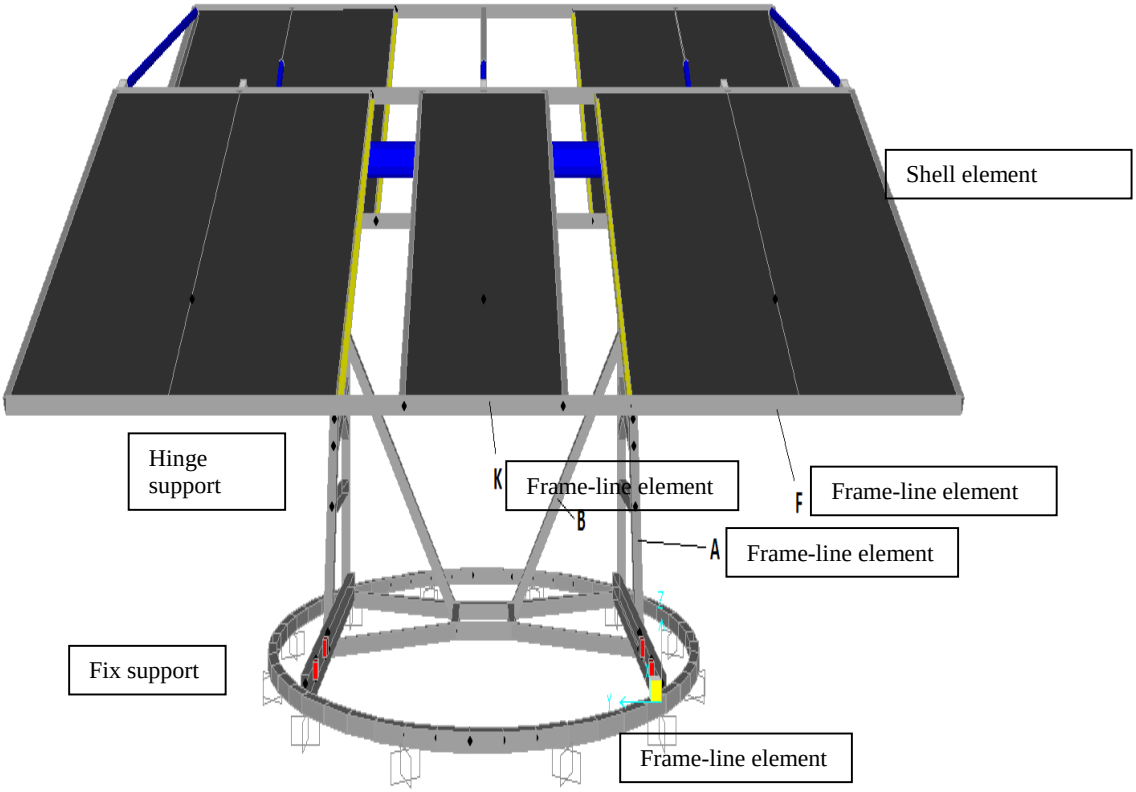

Figure 4.1 Finite Element Model of the solar tracker and the elements details

4.4.3 Boundary Conditions

The boundary conditions have a great impact on the accuracy of the finite element analysis as it sets the limitations to the problem**.** The solar tracker was modeled in such way that the circular rack at the bottom is fixed at 12 points, every 30º, to simulate the precast concrete blocks installed at the base of the solar tracker. The two vertical legs of the solar tracker are simply supported by the bottom frame, which is fixed connected to the circular rack. The upper part of the solar tracker consisting of beam elements was hinged to the top of the frame for enabling the PV modules to incline and rotate.

The overall finite element model of the solar tracker shown in the Figure 4.2 consists of 156 structural elements, 169 nodes and a total number of 1,014 degree of freedom. The location of the nodes is very important because the displacement under static and time-history loading was obtained at the nodes while the stresses were averaged for the surface of the elements.

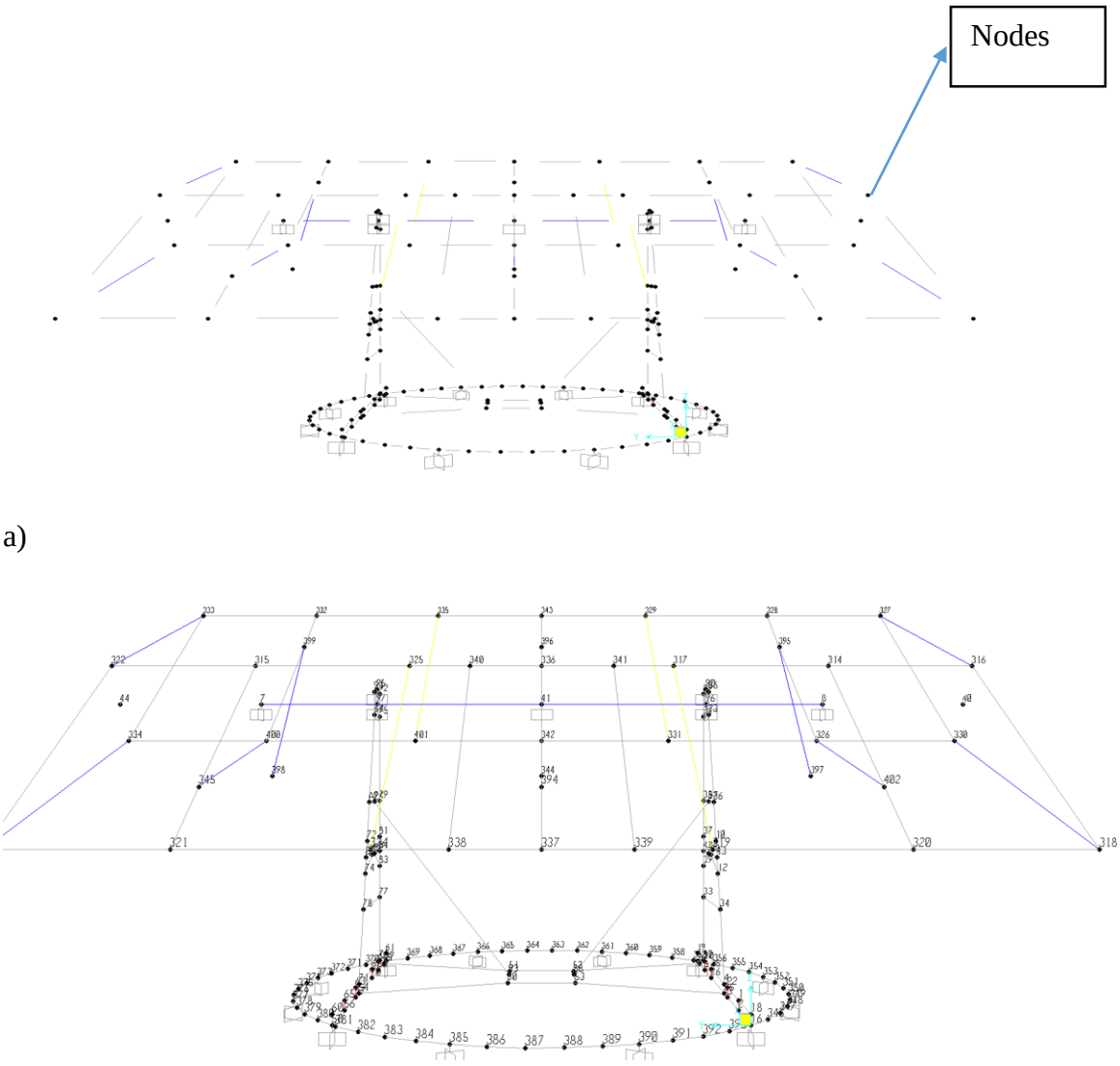

Figure 4.2: Nodes of the finite element model of the solar tracker

4.5. Modal Analysis

The study of the dynamic properties of a particular structure with reference to the vibrational excitation is described by performing the modal analysis. The vibration analysis is employed to find the periods at which the structure will resonate, considering the given total mass, damping and stiffness of the investigated structure. This can be accomplished either through analytical, numerical or experimental techniques. Modal analysis can be carried out in two different ways,

either by Eigenvector or by Ritz-vector methods [42]. The former method is analysed to determine the undamped vibration mode shapes and frequency of the structural system. It provides an engineering design safety criterion so that the period of vibration obtained does not coincide with the natural frequency of the proposed structure. Modal analysis of the finite element model of the solar tracker was performed aiming at determining the natural frequency, the damping factors and the mode shapes of the first vibration modes of the structure. These vibration modes would be the most excited by external dynamic loadings, especially if the period or the frequency of the loading would be very close to one of the natural frequencies of the structure.

In the current study the first 12 vibration modes of the solar tracker structure were established to avoid damage caused by resonance in response to increased attack angles and wind load. These show the relative shape of the modes of vibration where the mass matrices of the selected structural elements are used either to determine the concentrated masses at nodes or the distributed mass as part of the element. In general the natural vibration modes represent an excellent insight into the behaviour of the structure. Contrarily, the Ritz analysis outperform the Eigenvector method as it determines the modes that are excited by a particular loading and provides more reliable results when used for response-spectrum or time history analysis focusing on modal superposition [42]. The physical interpretation of the Eigenvalues and the Eigenvectors are the natural frequencies and the corresponding mode shapes of the investigated structure.

The dynamic properties of the structure include the natural vibration mode or the mode shape, the natural frequency or the period and modal participation factors, and all these parameters depend on the structure properties, type of material, and the boundary conditions employed in the modal analysis.

The natural vibration mode corresponds to the free vibration in damped system. First, second and up to n^{th} mode represent the order in which the least energy is required to deform the structure. Natural periods describe the time it takes for the structure to freely vibrate into a corresponding natural mode for which one full cycle is mathematically expressed as [42]**:**

$$T=1/f \text{ (s)} \qquad \text{[Eq.4.1]}$$

The modal participation factor corresponds to the ratio of the influence of a specific mode to the total dynamic response of the structure. The mode shape is described as an expected displacement of the structure under the vibrational excitation and it depends on both the shape and structural properties of the structure and the involved boundary conditions of the structure [42].

Modal analysis can be presented using the general equation of motion as shown in equation 4.2 below [42]:

$$[M]\{\ddot{U}\} + [C]\{\dot{U}\} + [K]\{U\} = \{F(t)\} \quad \text{[Eq.4.2]}$$

Assuming the free vibration, thus ignoring the forcing term on the other side of the equation, the above equation becomes Equation 4.3..However,the condition does not hold in SAP 2000 as forcing term was included in the equation for the modal analysis performed by the software. So, the equation stays the same as equation 4.2

$$[M]\{\ddot{U}\} + [C]\{\dot{U}\} + [K]\{U\} = \{0\} \quad \text{[Eq.4.3]}$$

Assuming the harmonic motion, the above equation is modified as:

$$[K] - w^2[M]\{U\} = \{0\} \quad \text{[Eq.4.4]}$$

The roots of the equation are w^2 , the eigenvalues, where i ranges from 1 to the number of degrees of freedom assumed for which the corresponding displacement vectors are {U} .

4.6. Time history analysis

Time history analysis employs directly the time record of the input load which is combined to give the response for each time step. The applied load depends on the time step. The Time history analysis dwells on dynamics equilibrium equation expressed in equation 4.5 as [42]:

$$M\ddot{U}(t) + C\dot{U}(t) + KU(t) = r(t) \quad \text{[Eq.4.5]}$$

Where

K is the stiffness matrix

C is the damping

M is the diagonal mass matrix

U represents the displacement, (m)

$\dot{U}$ is the velocity, (m/s)

$\ddot{U}$ represents the acceleration, (m/s^2)

Time history analysis was performed at discrete time steps of 18,800 for better results and the displacement and the reaction forces of the solar tracker were presented over the time interval during the loading application and after the application of the wind forces.

4.7. Wind loading modelling

As discussed in the previous chapter, the accurate estimation of the wind loading acting on the PV solar tracker depends on important weather parameters such as: wind speed, air pressure, air density, element area directly under the action of loads and wind direction, but also on the lift and drag coefficients and the shape of the structural element. The weather characteristics were considered individually for every day of the months February 2015 and March 2015, as presented section 3.7 for the computation of the drag and lift components of the wind forces, as time dependent record.

4.7.1 Computation of the air density

The air density is one of the parameters that need to be carefully obtained for determining the drag and lift wind forces. This parameter changes with the variation in temperature, relative humidity, and depends on the open air stream pressure from the weather data of the examined site. According to international standard atmosphere, the value of air density at sea level for 15^0C is approximately 1.225 kg/m^3. However, this is not the exact value considered in the current study based on the weather data recorded between February and March 2015. As Table 4.2 below presents, the recorded weather data for the day of 1st February 2015, shows extreme and high temperatures during the day when the solar tracker was at stow position (78^0).

Table 4.2: Recorded weather data in February 2015

Date/Time	Year	Month	Day	Temp (°C)	Relative Humid (%)	Station Pressure (kPa)
01/02/2015 0:00	2015	2	1	-14.3	84	100.63
01/02/2015 1:00	2015	2	1	-13.9	84	100.62
01/02/2015 2:00	2015	2	1	-14.5	84	100.66
01/02/2015 3:00	2015	2	1	-15.3	84	100.76
01/02/2015 4:00	2015	2	1	-17.1	83	100.85
01/02/2015 5:00	2015	2	1	-18.1	81	100.96
01/02/2015 6:00	2015	2	1	-16.9	66	101.06
01/02/2015 7:00	2015	2	1	-18.5	67	101.16
01/02/2015 8:00	2015	2	1	-19.4	64	101.29
01/02/2015 9:00	2015	2	1	-19.5	62	101.39
01/02/2015 10:00	2015	2	1	-19.4	56	101.42
01/02/2015 11:00	2015	2	1	-19	52	101.38
01/02/2015 12:00	2015	2	1	-18.4	50	101.31
01/02/2015 13:00	2015	2	1	-18.1	47	101.23
01/02/2015 14:00	2015	2	1	-17.5	43	101.22
01/02/2015 15:00	2015	2	1	-18	47	101.2

According to ideal gas law, the density of dry air could be estimated based on the temperature and pressure as [31]:

$$\rho_d = \left(\frac{p}{T * R_d}\right) \quad \text{[Eq. 4.6]}$$

Where:

$\rho_d is\ the\ air\ density(\ ^{kg}/_{m^3})$

p is the absolute pressure (Pascal)

T is the absolute temperature K, ($273.15+C^0$)

R_d is the specific gas constant for dry air ($\frac{J}{kg*^0K}$)

The above expression is only valid for dry air at the standard conditions. For practical purpose, the extreme low temperature value was considered for the moist air density computation. Neglecting the small errors as a result of non-ideal gas compressibility and the vapour pressure measurements not made over liquid water, W.H Brassiere et al [31] presented humid air density expression as:

$$\rho_{humid\ air\ density} = \left(\frac{p}{R_d * T}\right) * \left(1 - \frac{0.378e}{p}\right) \quad \text{[Eq.4.7]}$$

Where

$\rho_{humid\ air\ density}$ is the density of humid air, kg/m^3

P is the absolute pressure $= P_d + P_v$, Pascal

R_d is the specific gas constant for dry air which is equal to $287.04(\frac{J}{kg*^0K})$

E is the pressure of water vapour (Partial pressure), Pascal

T is the air temperature, ^{0}K

According to W. H. Brustsaere [31] and to the U.S. National weather agency [32], the air density could be computed with reference to the relative humidity given in equation 4.8 below:

$$\text{RH}\ \frac{e}{e_s} \quad \text{[Eq.4.8]}$$

Where e and e_s are expressed as:

$$e = 6.11 * 10^{(\frac{7.5*T_d}{237.7+T_d})} \quad \text{[Eq 4.9]}$$

$$e_s = 6.11 * 10^{\frac{7.5*T}{(237.7+T)}} \quad \text{[Eq 4.10]}$$

Where RH is the relative humidity

e_s is the saturated vapour pressure (partial pressure)

T is Air temperature, ^{0}C

$T_d\ is$ Dewpoint temperature, ^{0}C

These procedural steps described the determination of the air density at critical recorded temperature of -26^{0}C, the relative humidity of 92% with air pressure of 102.47 KPa:

- Saturated vapour pressure computation :

$$e_s = 6.11 * 10^{\frac{7.5*T}{(237.7+T)}} = e_s = 6.11 * 10^{\frac{7.5*(-26)}{(237.7-26)}} = 0.7327 \text{ Pascal} \quad \text{[Eq.4.11]}$$

- Partial pressure of water vapour computation with respect to relative humidity percentage :

$$\text{RH} = \frac{e}{e_s} \quad \text{[Eq.4.12]}$$

$$\text{e} = e_s * RH = \frac{92*0.7327}{100} = 0.6741 \text{Pa}$$

- Density of humid air density :

$$\rho_{humid\ air\ density} = \left(\frac{p}{R_d * T}\right) * \left(1 - \frac{0.378e}{p}\right) \quad \text{[Eq.4.13]}$$

$$\rho_{humid\ air\ density} = \left(\frac{102478}{287.04(273.15-26)}\right) * \left(1 - \frac{0.378*0.6741}{102478}\right)$$

$$\rho_{humid\ air\ density} = 1.444\ ,^{kg}/_{m^3}$$

Table 4.3 below shows the density of humid air obtained at different temperatures, time intervals, humidity and recorded air pressure.

Table 4.3: Computed air density data for February 2015

Date/Time	Temp (°C)	Relative Humidity (%)	Station Pressure (kPa)	Es	E	Air Density ($kg/m^{3)}$
01/02/2015 0:00	-14.3	84	100.63	2.0228	1.6992	1.3544
01/02/2015 1:00	-13.9	84	100.62	2.0904	1.7559	1.3521
01/02/2015 2:00	-14.5	84	100.66	1.9898	1.6714	1.3558
01/02/2015 3:00	-15.3	84	100.76	1.8624	1.5644	1.3614
01/02/2015 4:00	-17.1	83	100.85	1.6020	1.3297	1.3722
01/02/2015 5:00	-18.1	81	100.96	1.4719	1.1922	1.3790
01/02/2015 6:00	-16.9	66	101.06	1.6293	1.0753	1.3740
01/02/2015 7:00	-18.5	67	101.16	1.4225	0.9531	1.3840
01/02/2015 8:00	-19.4	64	101.29	1.3168	0.8428	1.3906
01/02/2015 9:00	-19.5	62	101.39	1.3055	0.8094	1.3926
01/02/2015 10:00	-19.4	56	101.42	1.3168	0.7374	1.3924
01/02/2015 11:00	-19	52	101.38	1.3629	0.7087	1.3897
01/02/2015 12:00	-18.4	50	101.31	1.4347	0.7174	1.3855
01/02/2015 13:00	-18.1	47	101.23	1.4719	0.6918	1.3827
01/02/2015 14:00	-17.5	43	101.22	1.5488	0.6660	1.3794
01/02/2015 15:00	-18	47	101.2	1.4845	0.6977	1.3818

Therefore the highest value for the air density during the first day of February 2015 was 1.392 kg/m^3, which is higher than the standard values of approximately 1.225kg/m^3 .When determining the wind loading time history, all the computed values of the air density were taken into account for different time steps.

The photovoltaic tracker orients the solar panels at different angles of inclination, depending on the latitude of the site. Instability of the tracker structure could occur as a result of the interfering of external loads such as wind load. The wind load is applied to the structure in two different forms the along wind component representing the drag force and the across-wind component representing the lift force [33] as shown in Figure 4.5 below. Whenever the structure is inclined in regard to the main wind direction, the drag and lift components are obtained by decomposing the wind loading under the two main directions: horizontal and vertical directions. This procedure was considered in the current study, when applying the static drag and lift forces to the members of the solar tracker.

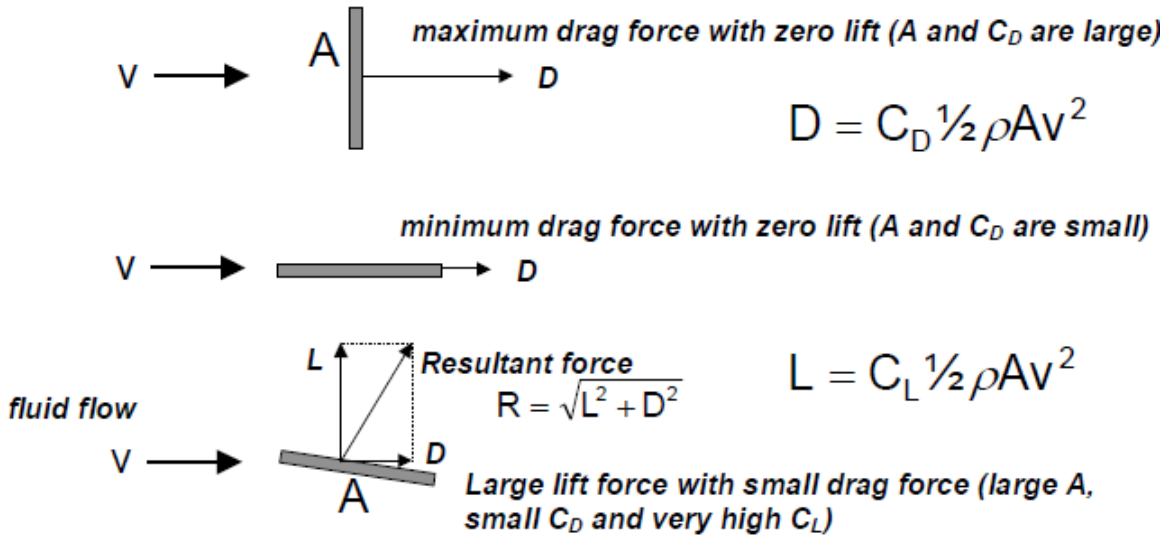

Figure 4.3: Drag and lift forces acting on a body [33].

4.7.2 Drag Force

Drag force is the wind force component along the direction of flow. According to Buckingham's π theorem [34], drag force is mathematically expressed as:

$$F_D = \frac{1}{2}\rho V^2 C_D A_D \qquad \text{[Eq .4.14]}$$

Where

F_D *is the Drag force* (N),

ρ is the air density, kg/m^3

V denotes the wind speed, m/s, and

A_D is the area of the element projected on the drag direction in m^2

C_D is the drag coefficient .

As shown in the above equation 4.12, the drag force depends on the shape of the structural element under the action of wind load, air density, drag coefficient and the square of the wind speed [35]. Drag force acting on the solar tracker exists in two forms: the frictional component and the applied

pressure drag [36].The former surfaces when the panels are close to horizontal, while the latter dominates when the panel is positioned close to vertical.

4.7.3 Lift Force

Lift forces is described as mechanical force that acts opposite to the direction of motion [35]. It depends on air density, square of wind speed of the locality, structural surface area under the action of lift force, shape of the structure, element angle of inclination to the flow and the lift coefficient [35]. Lift force acting on a structure is expressed as;

$$F_L = \frac{1}{2}\rho V^2 C_L A_L \qquad \text{[Eq.4.15]}$$

F_L Is the Lift force (N)

C_L is the lift coefficient and

A_L, m^2 denotes the area of the structural element projected on the lift force direction.

4.7.4 Drag and Lift Coefficients

Drag and lift forces are produced when a body is positioned in the flow of direction. Figure 4.6 presents an ideal case where the pressure of the fluid is acting on a given area ∂A on the body surface and is denoted by P; the force P acts normal to ∂A, and τ is the frictional stress acting tangentially to ∂A. The integration of the pressure for the entire body surface of the components in the direction of the flow U; the pressure stress is referred to as the pressure drag and the integration of the frictional stresses is referred to as the frictional drag as expressed by equations 4.14 and 4.15 accordingly [44].

$$D_p = \int_A^{90} PdAcos\theta \qquad \text{[Eq.4.16]}$$

$$D_f = \int_A^{90} \tau dAsin\theta \qquad \text{[Eq.4.17]}$$

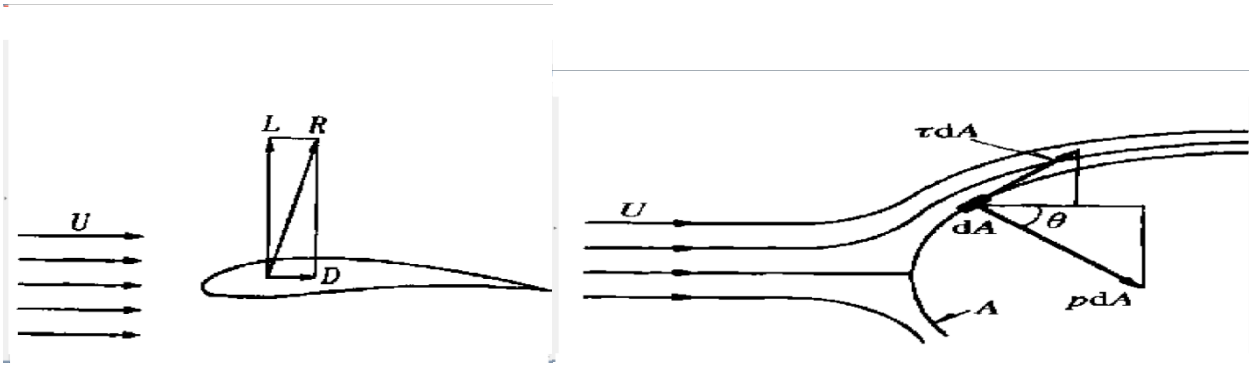

Figure 4.4 A body under drag load ‘D’ and lift load ‘L’ [44]

The summation of both pressure and frictional drag components resulted into the total drag acting on a body whose proportions vary with the shape of the body.

The drag coefficient depends on several parameters: shape of the body, flow Reynolds number, Froude number, Mach number and the surface roughness. Also this is a function of the body shape, inclination angle flow condition, density of air and drag force [35]. Thus it is difficult to obtain the value of the drag coefficient theoretically, so the best way to determine the drag coefficient is either by conducting wind tunnel test or by employing the mathematical expressions shown in equation 4.16, as a ratio of the lift force to the force produced by the dynamic pressure multiplied by the area.

$$C_D = \frac{F_D}{\rho A \frac{V^2}{2}} \qquad \text{[Eq 4.18]}$$

According to engineering toolbox [37], Table 4.4 presents various drag coefficient for common body shapes resulting from a series of wind tunnel experiments.

Also, Sandraey [38] presented the drag coefficients for a number of symmetrical shapes at low wind speeds as shown in table 4.5.

Table 4.4: Drag coefficients for some common shapes [37].

Type of Object	Drag Coefficient, C_d	Frontal Area, A (ft^2)
Laminar flat plate (Re=106)	0.001	
Turbulent flat plate (Re=106)	0.005	
Streamline body	0.04	$\pi / 4\ d^2$
Airplane wing, normal position	0.05	
Long stream-lined body	0.1	
Airplane wing, stalled	0.15	
Hollow semi-sphere facing stream	0.38	
Solid Hemisphere	0.42	$\pi / 4\ d^2$
Sphere	0.5	
Cube	0.8	s^2
Bike racing	0.88	3.9
Thin Disk	1.1	$\pi / 4\ d^2$
Solid Hemisphere flow normal to flat side	1.17	$\pi / 4\ d^2$
Squared flat plate at 90 °	1.17	
Wires and cables	1.0 - 1.3	
Hollow semi-cylinder opposite stream	1.2	
Hollow semi-sphere opposite stream	1.42	
Long flat plate at 90 °	1.98	
Rectangular box	2.1	

Table 4.5 Drag coefficient values for various geometries and shapes [38]

No	Body	Status	Shape	C_D
1	Square rod	Sharp corner		2.2
		Round corner		1.2
2	Circular rod	Laminar flow		1.2
		Turbulent flow		0.3
3	Equilateral triangular rod	Sharp edge face		1.5
		Flat face		2
4	Rectangular rod	Sharp corner 	L/D = 0.1	1.9
			L/D = 0.5	2.5
			L/D = 3	1.3
		Round front edge 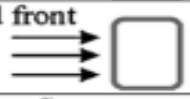	L/D = 0.5	1.2
			L/D = 1	0.9
			L/D = 4	0.7
5	Elliptical rod 	Laminar flow	L/D = 2	0.6
			L/D = 8	0.25
		Turbulent flow	L/D = 2	0.2
			L/D = 8	0.1
6	Symmetrical shell	Concave face	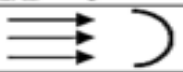	2.3
		Convex face		1.2
7	Semicircular rod	Concave face		1.2
		Flat face		1.7

No	Body	Laminar/turbulent	Status	C_D
1	Cube	Re > 10,000		1.05
2	Thin circular disk	Re > 10,000		1.1
3	Cone ($\theta = 30°$)	Re > 10,000		0.5
4	Sphere	Laminar $Re \leq 2\times10^5$		0.5
		Turbulent $Re \geq 2\times10^6$		0.2
5	Ellipsoid	Laminar $Re \leq 2\times10^5$		0.3-0.5
		Turbulent $Re \geq 2\times10^6$		0.1-0.2
6	Hemisphere	Re > 10,000	Concave face	0.4
		Re > 10,000	Flat face	1.2
7	Rectangular plate	Re > 10,000	Normal to the flow	1.1 - 1.3
8	Vertical cylinder	$Re \leq 2\times10^5$	L/D = 1	0.6
			$L/D = \infty$	1.2
9	Horizontal cylinder	Re > 10,000	L/D = 0.5	1.1
			L/D = 8	1
10	Parachute	Laminar flow		1.3

4.7.4.1 Lift Coefficient

Lift coefficient varies with the change in angle of attack and it could be either generated by wind tunnel tests or determined by mathematical derivation, as presented in equation 4.17 [35]. After performing a series of wind tunnel experiments, Sandia National Laboratory reported the evolution of the lift and drag coefficients, as a function of the angle of attack as shown in figure 4.7 a) and b), for different Re numbers. Also figure 4.8 shows the variation of the lift coefficient for both negative and positive angles of attack, for the airfoil shaped body (NACA 0015).

$$C_L = \frac{F_L}{\rho A \frac{V^2}{2}} \qquad \text{[Eq.4.19]}$$

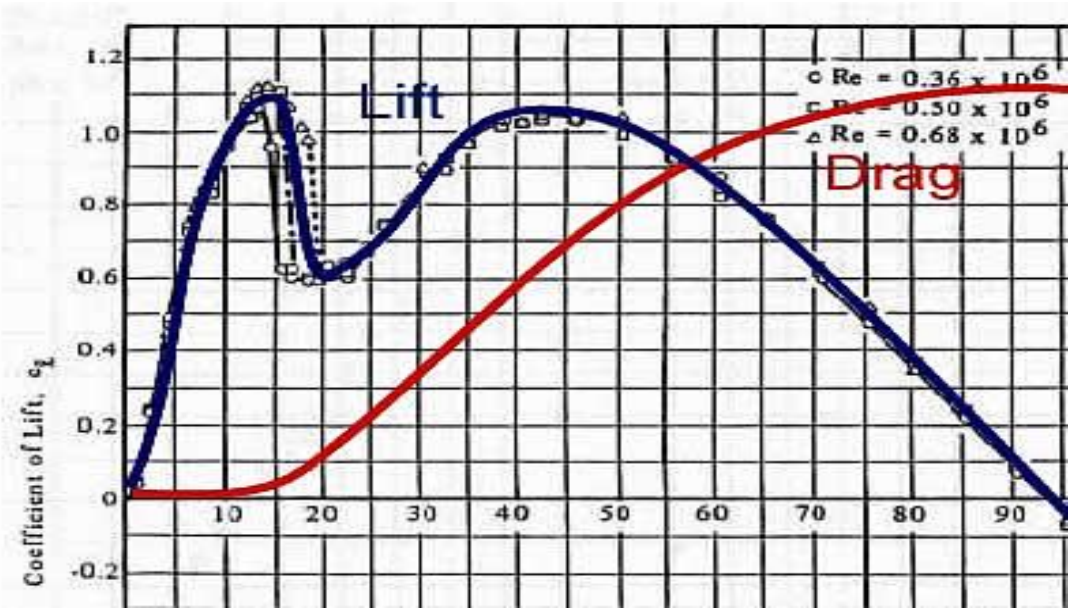

Figure 4.5 a) Evolution of Lift and Drag coefficients [39]

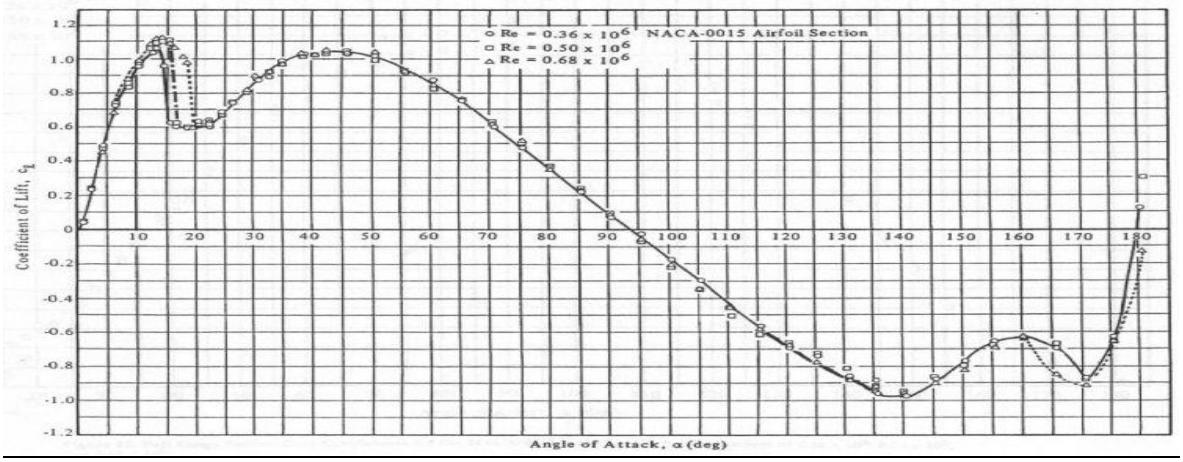

Figure 4.5b) Evolution of Lift coefficient for NACA airfoil [40]

In this study, comparison was made between the drag and lift coefficients presented in Tables 4. and 4.5 above, in order to select the proper values for the structural members of the solar tracker. Thus the tracker frame elements A, B, F, G, H, I, K, L which are rectangular truss elements, the box shape was selected which, as per Sandarcy [38] has the drag and lift coefficients of 2.2. The tracker elements C, D, E, J, M, which are round steel bars, the circular shape was selected and the corresponding drag and lift coefficients of 1.2 were used. For the shell element of the PV solar panel, the drag coefficient of 0.8 was used [37,43], when this is at stow position, 78° (almost parallel with the flow) and a drag coefficient of 1.98 when the PV solar panels are placed perpendicular to the wind speed (0° in the current study). Since the critical response of the tracker at the maximum drag and lift load are of interest, the higher values were used for the estimation of drag and lift forces as shown in Table 4.6 and 4.7 below. Moreover, the lift and drag coefficients for the solar panel were determined using Figure 8 below because it is directly related to the thin flat element [43].The figure presents coefficients of flat panel based on the angle of attack.

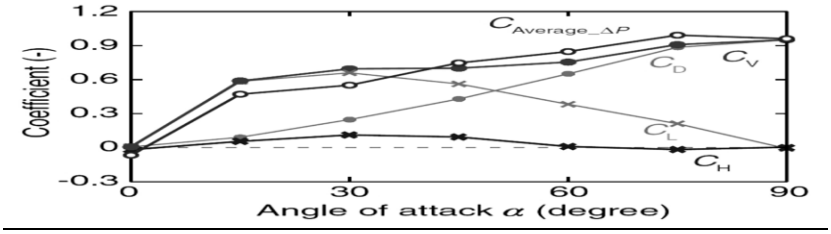

Figure 4.6 Relationship between inclination angle and Coefficients for thin plate [43]

Table 4.6: Induced Drag and Lift Area using Sandracy Drag Coefficient and NACA Coefficient

Element Identity	Element Type	Drag Coefficient [37]	NACA	Angle of Attack	Nominal Area for Drag Coeff (m^2)	Nominal Area for Drag Coeff (m^2)
A	Square, sharp corner	2.2	0.4	0^o	1.89m× 0.061	0.061×0.061
B	Square, sharp corner	2.2	0.4	0^o	1.5443m× 0.061m	1.5443m× 0.061m
C	Circular	1.2	0.4	78^o	0.15×0.8291×sin 78^o	0.15×0.8291×cos 78^o
D	Circular	1.2	0.4	78^o	1.642×0.05×0.9781	1.642×0.05×cos78^o
E	Circular	1.2	0.4	78^o	2.219m×0.05m× Sin 78°	2.219m×0.05m× cos 78°
F	Square, sharp corner	2.2	0.4	78^o	2.0879m×0.061m×Sin 78°	2.0879m×0.061m×cos 78°
G	Square, sharp corner	2.2	0.4	78^o	2.0879m×0.061m×Sin 78°	2.0879m×0.061m×cos 78°
H	Square, sharp corner	2.2	0.4	78^o	0.3048m×0.061m × sin 78°	0.3048m×0.061m × cos 78°
I	Square, sharp corner	2.2	0.4	78^o	0.3048m×0.061m × sin 78°	0.3048m×0.061m × cos 78°
J	Circular	1.2	0.4	78^o	1.642×0.05×0.9781	1.642×0.05×cos78^o
K	Square, sharp corner	2.2	0.4	78^o	1.8471m×0.061m×Sin 78°	1.8471m×0.061m×Cos 78°
L	Square, sharp corner	2.2	0.4	78^o	1.8471m×0.061m×Sin 78°	1.8471m×0.061m×Cos 78°
M	Circular	1.2	0.4	78^o	2.3531m×0.15m×Sin 78°	2.3531m×0.15m×Cos 78°
PV panel plate	Plate	0.8	0.4	78^o	2.1m× sin 78°	2.1m× cos 78°
PV panel plate	Plate	0.8	0.0	0^o	2.1×sin 0°	2.1 ×cos 0°

Just for comparison, if the chart for the airfoil shape section is used, then the drag and lift coefficients for different members are as presented in Table 4.7

Table 4.7: Induced Drag and Lift Area using NACA design chart

Element Identity	Element Type	Nasa Drag Coefficient	Nasa Lift Coefficient	Angle of Attack	Nominal Area for Drag Coeff (m^2)	Nominal Area for Lift Coeff (m^2)
A	Box	1.1	0.4	0^o	1.89m× 0.061	0.061×0.061
B	Box	1.1	0.4	0^o	1.5443m× 0.061m	1.5443m× 0.061m
C	Circular	1.1	0.4	78^o	0.15×0.8291×sin 78^o	0.15×0.8291×cos 78^o
D	Circular	1.1	0.4	78^o	1.642×0.05×0.9781	1.642×0.05×cos78^o
E	Circular	1.1	0.4	78^o	2.219m×0.05m× Sin 78°	2.219m×0.05m× cos 78°
F	Box	1.1	0.4	78^o	2.0879m×0.061m×Sin 78°	2.0879m×0.061m×cos 78°
G	Box	1.1	0.4	78^o	2.0879m×0.061m×Sin 78°	2.0879m×0.061m×cos 78°
H	Box	1.1	0.4	78^o	0.3048m×0.061m × sin 78°	0.3048m×0.061m × cos 78°
I	Box	1.1	0.4	78^o	0.3048m×0.061m × sin 78°	0.3048m×0.061m × cos 78°
J	Circular	1.1	0.4	78^o	1.642×0.05×0.9781	1.642×0.05×cos78^o
K	Box	1.1	0.4	78^o	1.8471m×0.061m×Sin 78°	1.8471m×0.061m×Cos 78°
L	Box	1.1	0.4	78^o	1.8471m×0.061m×Sin 78°	1.8471m×0.061m×Cos 78°
M	Circular	1.1	0.4	78^o	2.3531m×0.15m×Sin 78°	2.3531m×0.15m×Cos 78°

4.8 Static analysis of drag with respect to angle of attack.

The static drag and lift forces were determined for each of the members of the PV solar tracker. An example of the calculation performed for determining the nominal area of the element which is directly exposed to the wind direction, considering the elevation (tilt) and azimuth (rotation) angles are presented for the circular, square and flat plate elements of the tracker. Also the induced drag and lift forces obtained using the drag and lift coefficient as presented in Tables 4.6 and 4.7 above were determined for each individual element. Calculation details for all the elements are presented in Appendix C.

Nominal areas for drag and lift forces:

- **Element A (Square section with sharp corners)**

Drag Area of element A= Length × breadth

1.89m× 0.061= 0.1153m^2

Lift Area of Element A= Length × breadth

0.061×0.061=0.0037m^2

The angle of attack does not affect this element because it does not move like upper parts of the tracker.

- **Element C(Circular beam)**

  Projected Area of Element C

  Diameter of the element=0.15m

  Length of the element = 0.8291m

  Angle of attack =78°

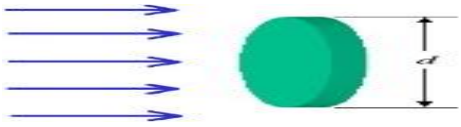

  Projected Lift Area = 0.15×0.8291×cos 78^0 = 0.026m^2

  Projected Drag Area= 0.15×0.8291×sin 78^0 = 0.12m^2

- **Element H**

Length of the element=0.3048m

Width of the element=0.061m

Angle of attack=78°

Projected Lift Area of the element=0.3048m×0.061m × cos 78°

$0.004m^2$

Projected Drag Area of the element=0.3048m×0.061m × sin 78°

$0.018m^2$

- **Element L**

Length of the element=1.8471m

Width of the element =0.061m

Angle of attack=78°

Projected Lift Area=1.8471m×0.061m×Cos 78°

$0.023m^2$

Projected Drag Area=1.8471m×0.061m×Sin 78°

$0.110m^2$

- **Element M(Circular Beam)**

Length of the element=2.3531m

Diameter of the beam=0.15m

Angle of attack=78°

Projected Lift Area=Length × diameter × cos78°

2.3531m×0.15m×cos 78°= $0.073m^2$

Projected Drag Area=2.3531m×0.15m×sin 78°=0.3453m^2

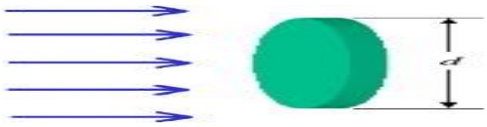

4.9 Static analysis of Drag with Respect to the Wind Speed and Air density

As discussed in the previous section, the maximum wind speed and the humid air density are part of the parameters needed to compute the wind loads. The analysis below shows how the drag and lift forces were computed for each element, considering the nominal areas and the measured wind speed and air density, for each of the recorded signals, during the period of February 2015 to March 2015.

Drag force:

$F_{DA}=\frac{1}{2}C_{DA}\rho A_{DA}V_{max}^2$=1/2× 2.2× 0.1153× ρV_{max}^2 [Eq 4.20]

$F_{DB}=\frac{1}{2}C_{DB}\rho A_{DB}V_{max}^2$=1/2× 2.2×1.5443 × ρV_{max}^2 [Eq 4.21]

$F_{DC}=\frac{1}{2}C_{DC}\rho A_{DC}V_{max}^2$=1/2× 1.2×0.12m × ρV_{max}^2 [Eq 4.22]

$F_{DJ}=\frac{1}{2}C_{DJ}\rho A_{DJ}V_{max}^2$=1/2× 1.2× 0.080× ρV_{max}^2 [Eq 4.23]

$F_{DK}=\frac{1}{2}C_{DK}\rho A_{DK}V_{max}^2$=1/2× 2.2×0.110 × ρV_{max}^2 [Eq 4.24]

$F_{DL}=\frac{1}{2}C_{DL}\rho A_{DL}V_{max}^2$=1/2× 2.2× 0.110× ρV_{max}^2 [Eq 4.25]

$F_{DM}=\frac{1}{2}C_{DM}\rho A_{DM}V_{max}^2$=1/2× 1.2×0.3453 × ρV_{max}^2 [Eq.4.26]

4.10. Static analysis of Lift Forces with Respect to Wind Speed and Air density:

$F_{LA}=\frac{1}{2}C_{LA}\rho A_{LA}V_{max}^2$=1/2× 2.2×0.0037 × ρV_{max}^2 [Eq.4.27]

$F_{LB}=\frac{1}{2}C_{LB}\rho A_{LB}V_{max}^2$=1/2× 2.2×0.094 × ρV_{max}^2 [Eq .4.28]

$F_{LC}=\frac{1}{2}C_{LC}\rho A_{LC}V_{max}^2$=1/2× 1.2× 0.026× ρV_{max}^2 [Eq.4.29]

$F_{LJ}=\frac{1}{2}C_{LJ}\rho A_{LJ}V_{max}^2$=1/2× 1.2× 0.017× ρV_{max}^2 [Eq.4.30]

$F_{LK}=\frac{1}{2}C_{LK}\rho A_{LK}V_{max}^2$=1/2× 2.2×0.023 × ρV_{max}^2 [Eq.4.31]

$F_{LL}=\frac{1}{2}C_{LL}\rho A_{LL}V_{max}^2$=1/2× 2.2×0.023× ρV_{max}^2 [Eq.4.32]

$F_{LM}=\frac{1}{2}C_{LM}\rho A_{LM}V_{max}^2$=1/2× 1.2× 0.073× ρV_{max}^2 [Eq 4.33]

The maximum loads determined for each element were calculated and were presented in Table 4.8 and 4.9 for the period of February 2015 and March 2015. For the static analysis, the recorded maximum wind speed of 16.11 m/s with the measured humid air density of 1.44 kg/m^3 as calculated in the above sections, were used to compute the resultant maximum drag and lift loads of 68.78 N and 34.33 N respectively as shown in table 4.9. However, the recorded hourly wind speed, with the corresponding humidity and air density were used for determining the time dependent drag and lift forces which were employed in the time-history analysis of the solar tracker elements, as shown in table 4.9 and 4.10. Figure 4.6 shows the variation and the maximum monthly drag and lift loads on each element.

Table 4.8 Element Maximum Drag and Lift loads for February 2015.

ELEMENTS	MAXIMUM DRAG LOAD (N)	MAXIMUM LIFT LOAD (N)
A	23.12	0.74
B	18.85	18.85
C	13.12	2.84
D	8.75	1.86
E	11.81	2.52
F	25.06	5.21
G	25.06	5.21
H	3.61	0.80
I	3.61	0.80
J	8.75	1.86
K	22.06	4.61
L	22.06	4.61
M	37.77	7.98

Table 4.9: Element Maximum drag loads and lift loads for March 2015.

ELEMENT	MAXIMUM DRAG LOAD[N]	MAXIMUM LIFT LOADS[N]
A	42.11	1.35
B	34.33	34.33
C	23.90	5.18
D	15.94	3.39
E	21.51	4.58
F	45.65	9.50
G	45.65	9.50
H	6.57	1.46
I	6.57	1.46
J	15.94	3.39
K	40.17	8.40
L	40.17	8.40
M	68.78	14.54

The estimated wind load and the recorded wind speeds were used to finally generate the drag and lift loads for the tracker elements A to E, at stow position as shown in Tables 4.10. The drag and lift forces for the rest of the elements are represented in Appendix C.

Table 4.10: Drag forces for elements ‘A’ to ‘E’ at stow position (78°) using Maximum Wind Speed and air density for each time lag

Date/Time	Wind speed(m/s)	Air Density	A	B	C	D	E
01/02/2015 0:00	2.7778	1.3544	1.3254	1.0806	0.7524	0.5016	0.6772
01/02/2015 1:00	2.7778	1.3521	1.3232	1.0788	0.7512	0.5008	0.6761
01/02/2015 2:00	2.7778	1.3558	1.3268	1.0817	0.7532	0.5022	0.6779
01/02/2015 3:00	5.0000	1.3614	4.3166	3.5191	2.4505	1.6336	2.2054
01/02/2015 4:00	5.0000	1.3722	4.3508	3.5471	2.4699	1.6466	2.2229
01/02/2015 5:00	4.1667	1.3790	3.0365	2.4756	1.7238	1.1492	1.5514
01/02/2015 6:00	8.0556	1.3740	11.3080	9.2190	6.4194	4.2796	5.7775
01/02/2015 7:00	7.2222	1.3840	9.1556	7.4642	5.1975	3.4650	4.6778
01/02/2015 8:00	7.2222	1.3906	9.1999	7.5003	5.2227	3.4818	4.7004
01/02/2015 9:00	5.8333	1.3926	6.0100	4.8997	3.4118	2.2745	3.0706
01/02/2015 10:00	6.3889	1.3924	7.2085	5.8769	4.0922	2.7281	3.6830
01/02/2015 11:00	5.2778	1.3897	4.9096	4.0026	2.7871	1.8581	2.5084
01/02/2015 12:00	3.8889	1.3855	2.6575	2.1665	1.5086	1.0057	1.3578
01/02/2015 13:00	3.0556	1.3827	1.6374	1.3349	0.9295	0.6197	0.8366
01/02/2015 14:00	3.3333	1.3794	1.9438	1.5847	1.1035	0.7357	0.9931
01/02/2015 15:00	4.1667	1.3818	3.0426	2.4805	1.7272	1.1515	1.5545

The time-history of the wind-induced drag and lift loads for the most critical elements, for which the higher wind loads were obtained in Table 4.10 are presented below, while the time history of the drag and lift forces for the rest of the elements were included in Appendix C.

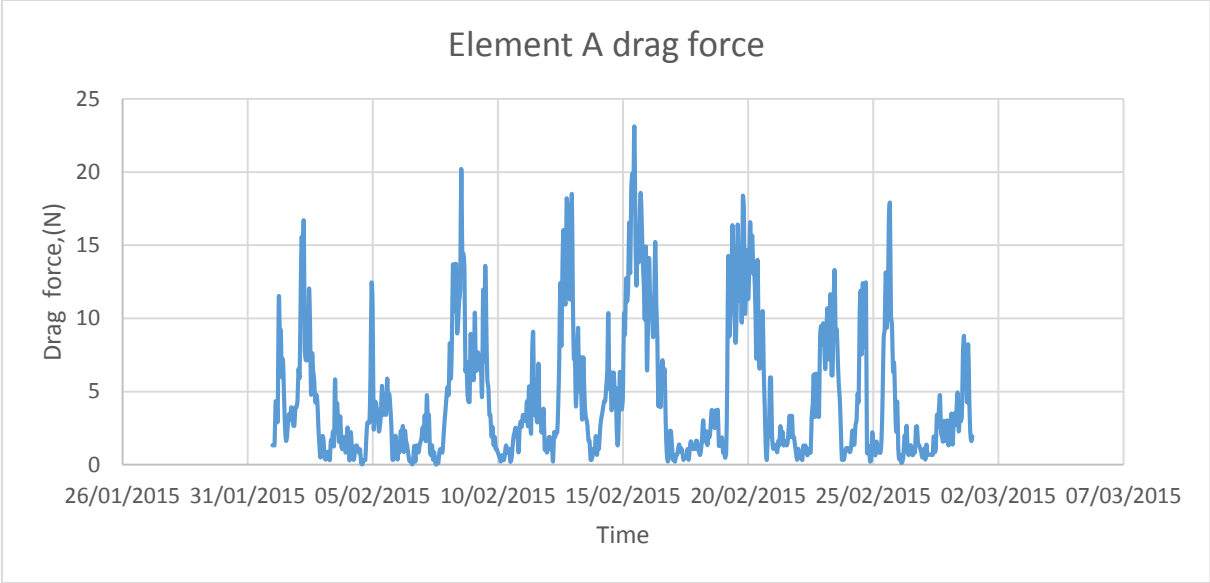
Element A drag force
Drag force,(N)
25
20
15
10
5
0
26/01/2015
31/01/2015
05/02/2015
10/02/2015
15/02/2015
20/02/2015
25/02/2015
02/03/2015
07/03/2015
Time

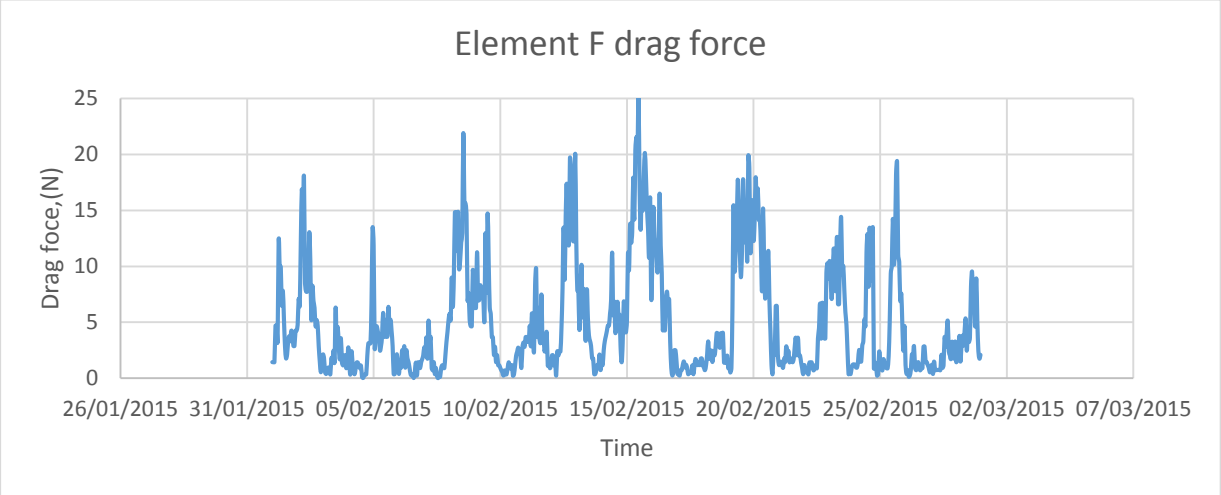
Element F drag force
Drag foce,(N)
25
20
15
10
5
0
26/01/2015
31/01/2015
05/02/2015
10/02/2015
15/02/2015
20/02/2015
25/02/2015
02/03/2015
07/03/2015
Time

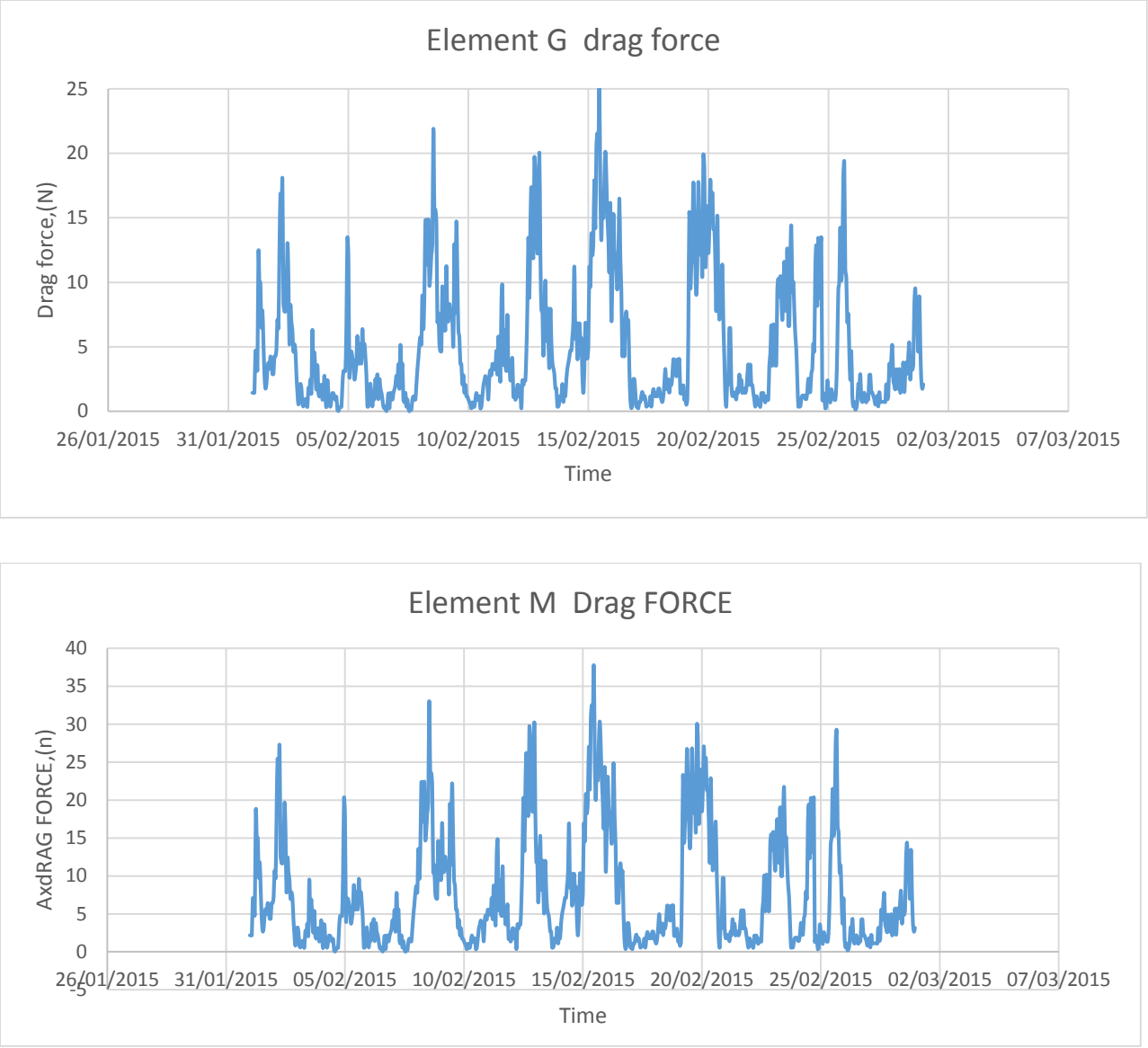

Figure 4.7 Time-history of the drag force on tracker element in February 2015.

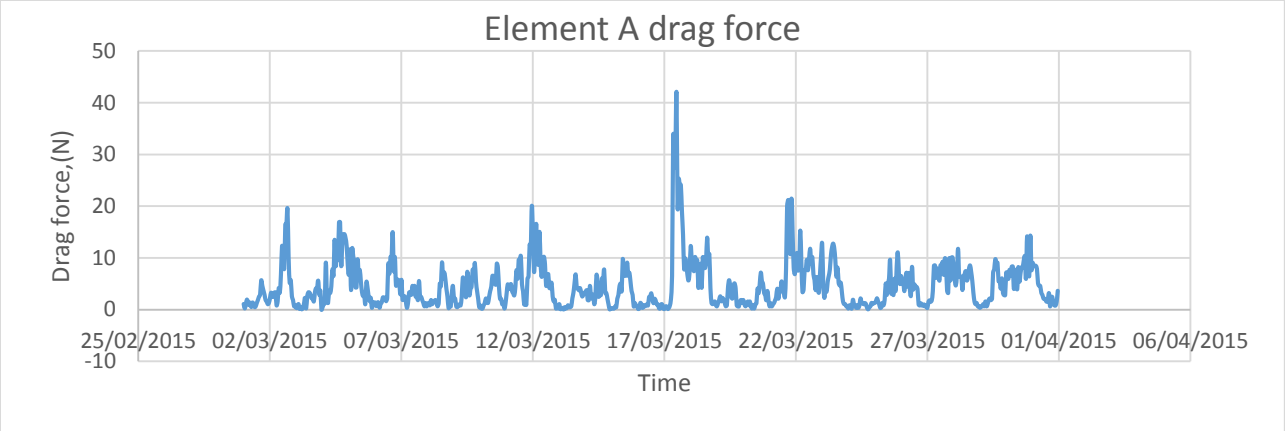
Element A drag force
Drag force,(N)
50
40
30
20
10
0
-10
25/02/2015
02/03/2015
07/03/2015
12/03/2015
17/03/2015
22/03/2015
27/03/2015
01/04/2015
06/04/2015
Time

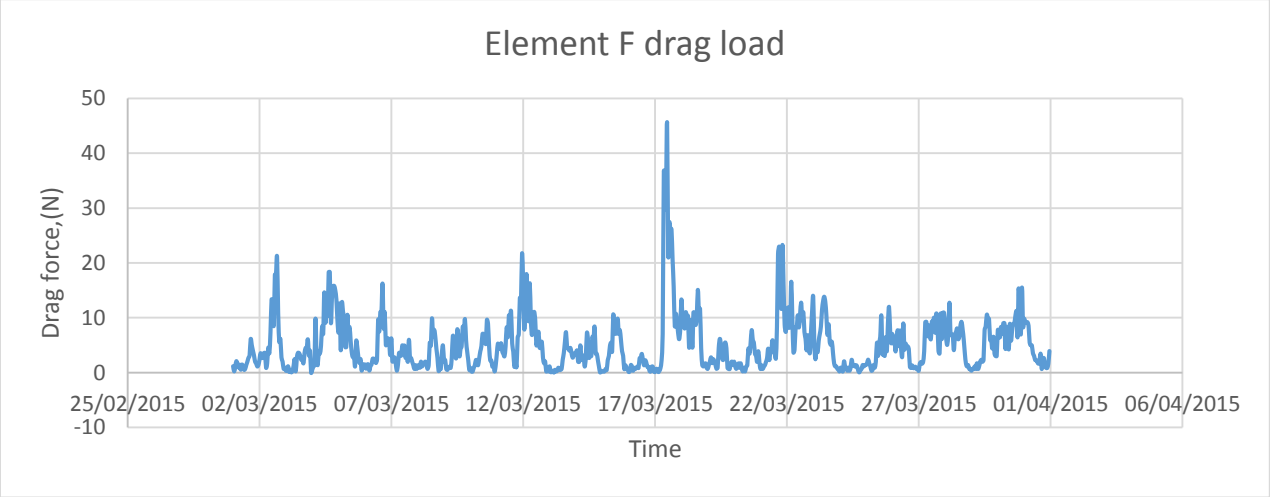
Element F drag load
Drag force,(N)
50
40
30
20
10
0
-10
25/02/2015
02/03/2015
07/03/2015
12/03/2015
17/03/2015
22/03/2015
27/03/2015
01/04/2015
06/04/2015
Time

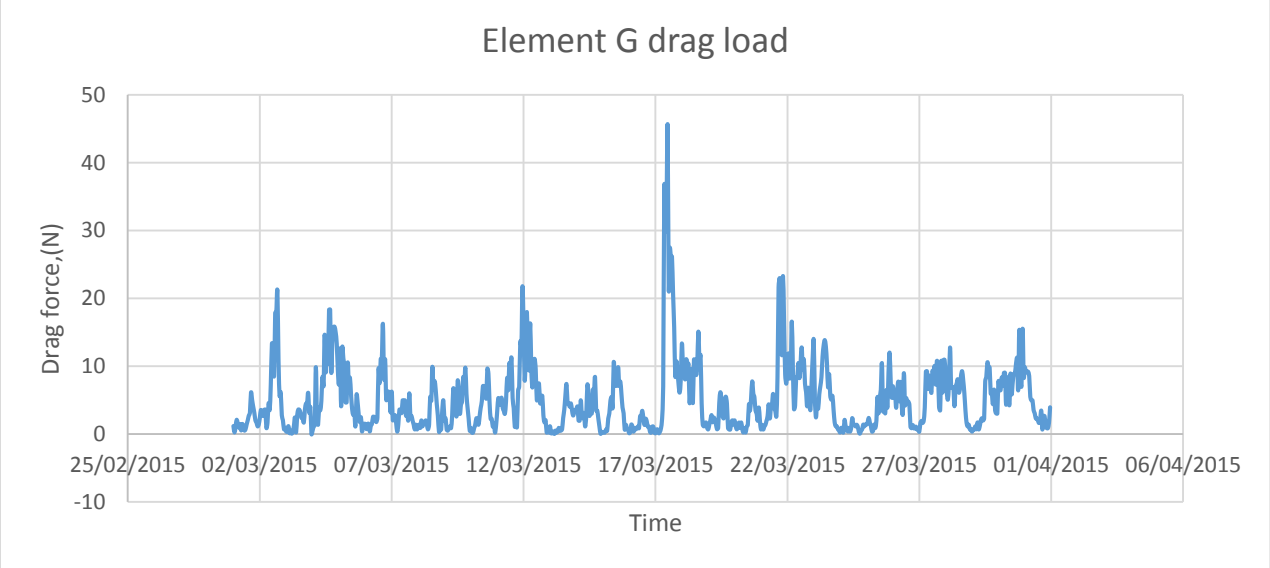
Element G drag load
Drag force,(N)
50
40
30
20
10
0
-10
25/02/2015
02/03/2015
07/03/2015
12/03/2015
17/03/2015
22/03/2015
27/03/2015
01/04/2015
06/04/2015
Time

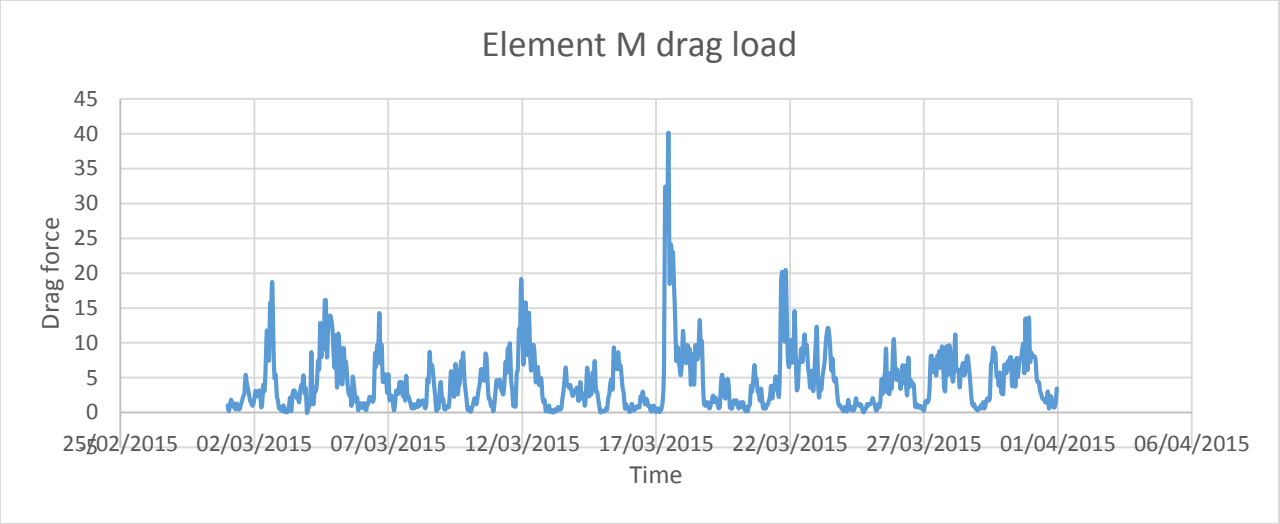

Figure 4.8 Time-history of the drag force on tracker elements in March, 2015.

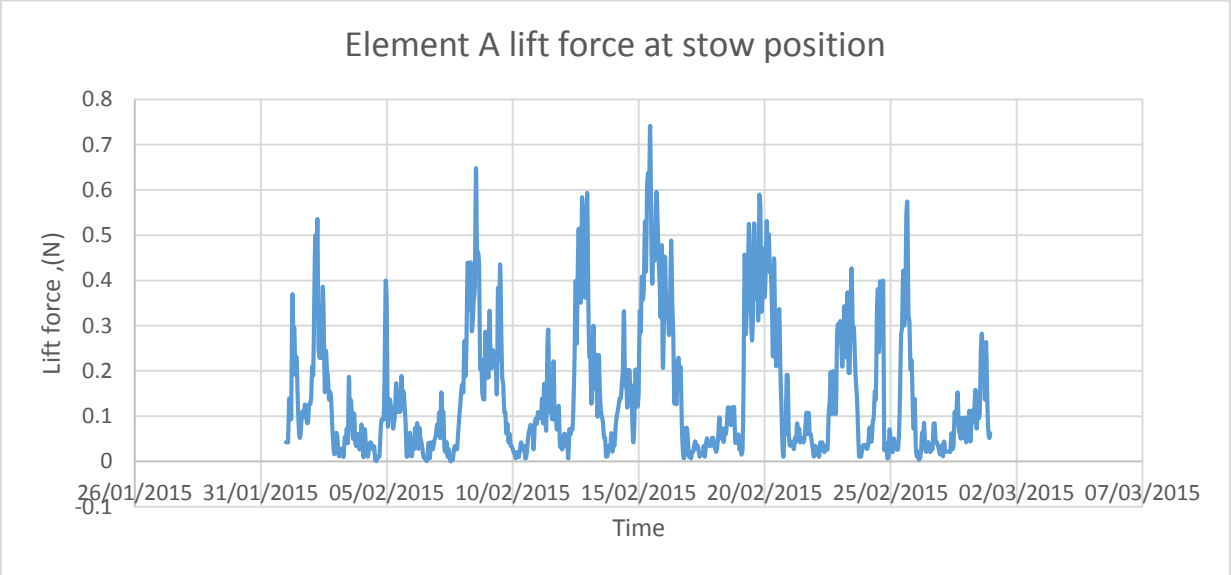

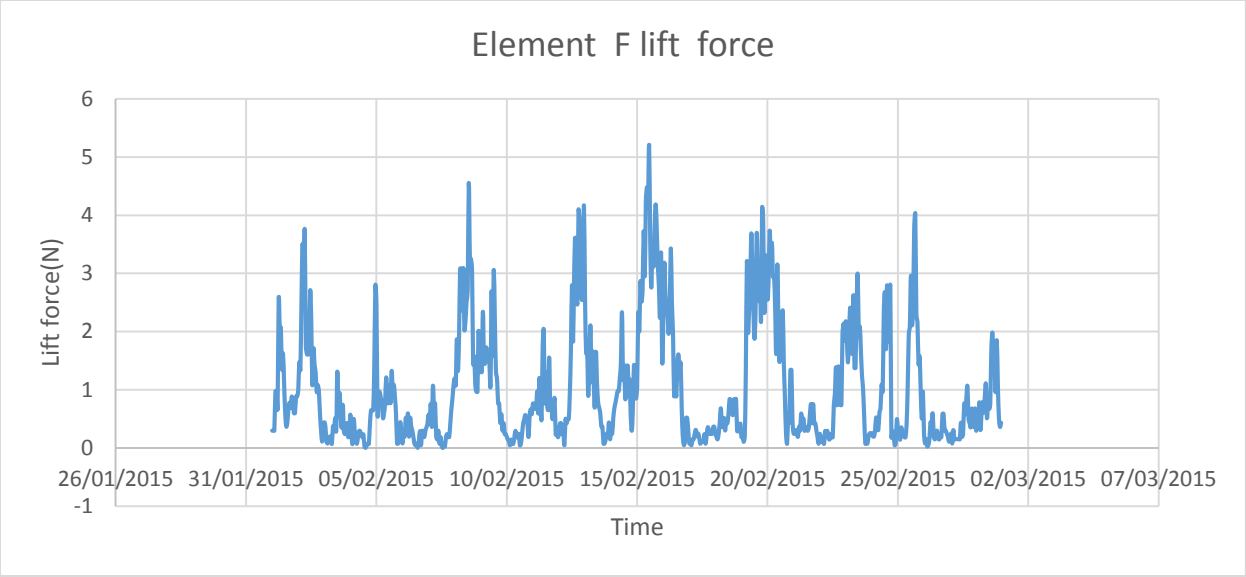
Element F lift force
Lift force(N)
6
5
4
3
2
1
0
-1
26/01/2015
31/01/2015
05/02/2015
10/02/2015
15/02/2015
20/02/2015
25/02/2015
02/03/2015
07/03/2015
Time

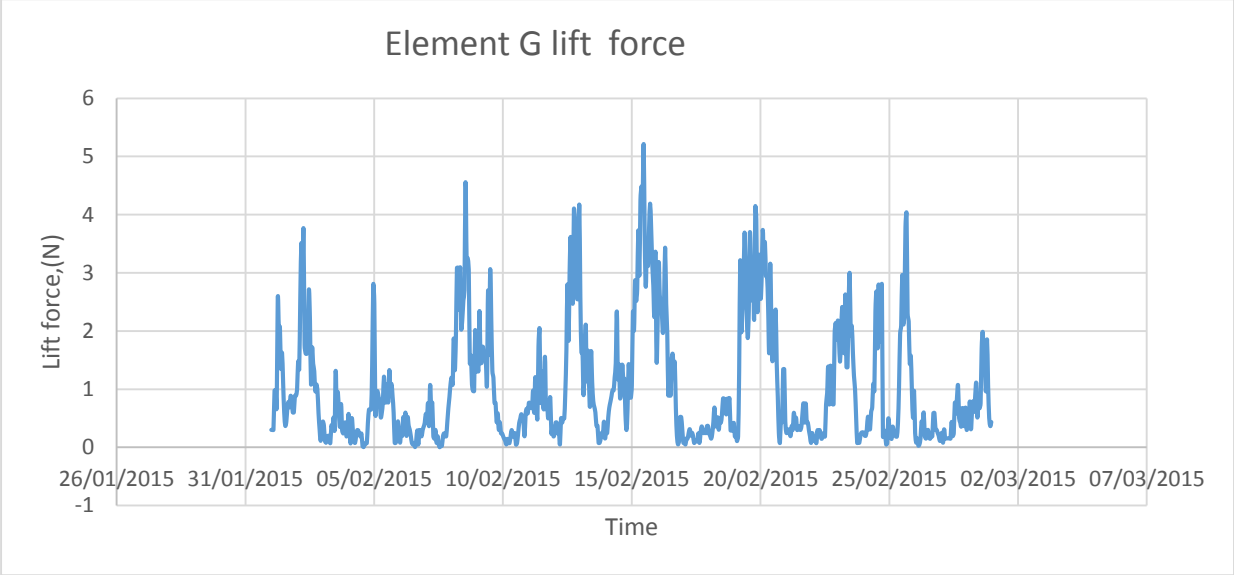
Element G lift force
Lift force,(N)
6
5
4
3
2
1
0
-1
26/01/2015
31/01/2015
05/02/2015
10/02/2015
15/02/2015
20/02/2015
25/02/2015
02/03/2015
07/03/2015
Time

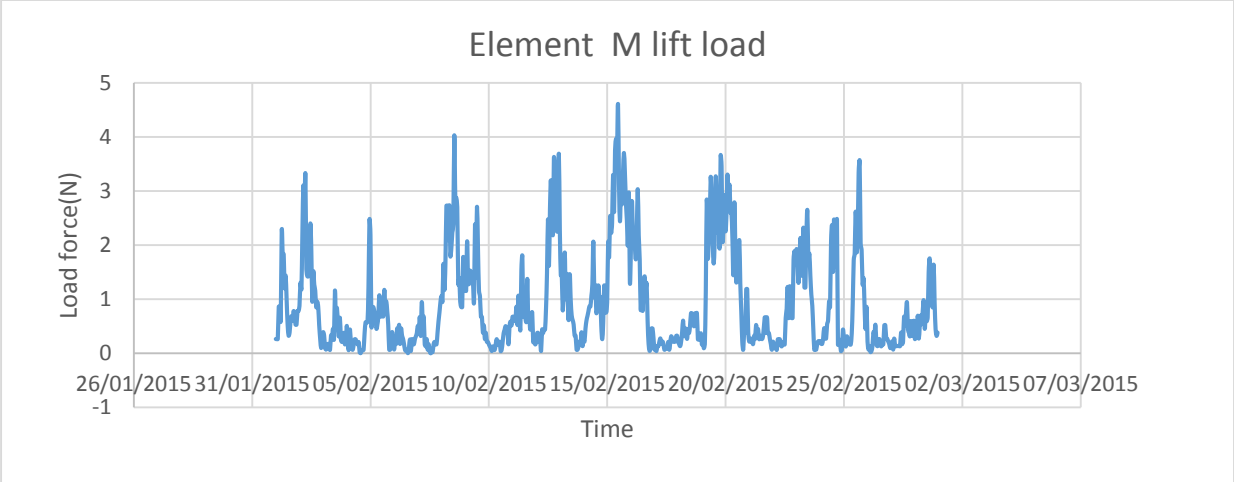

Figure 4.9 Time-history of the lift load on tracker elements in February, 2015.

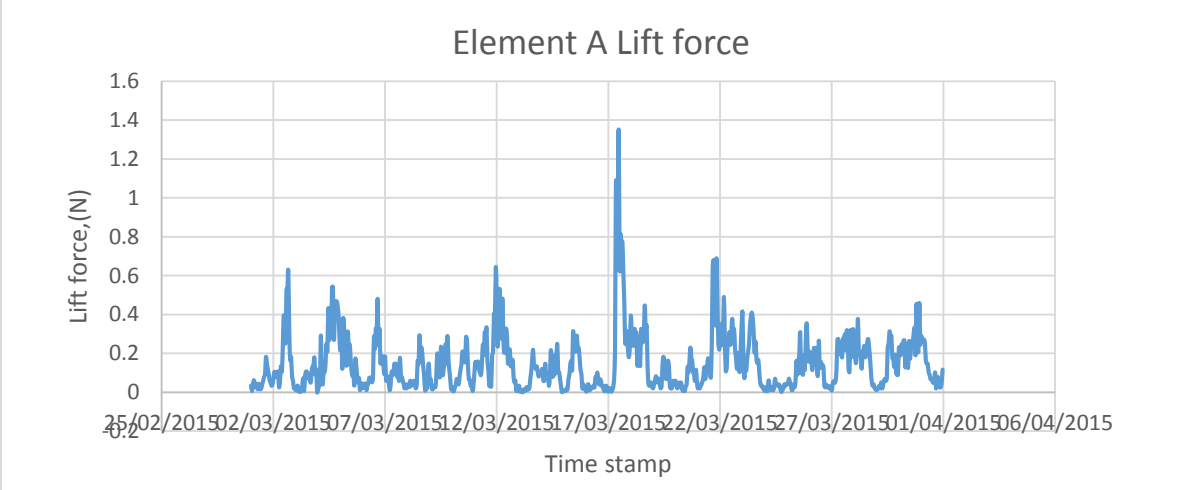

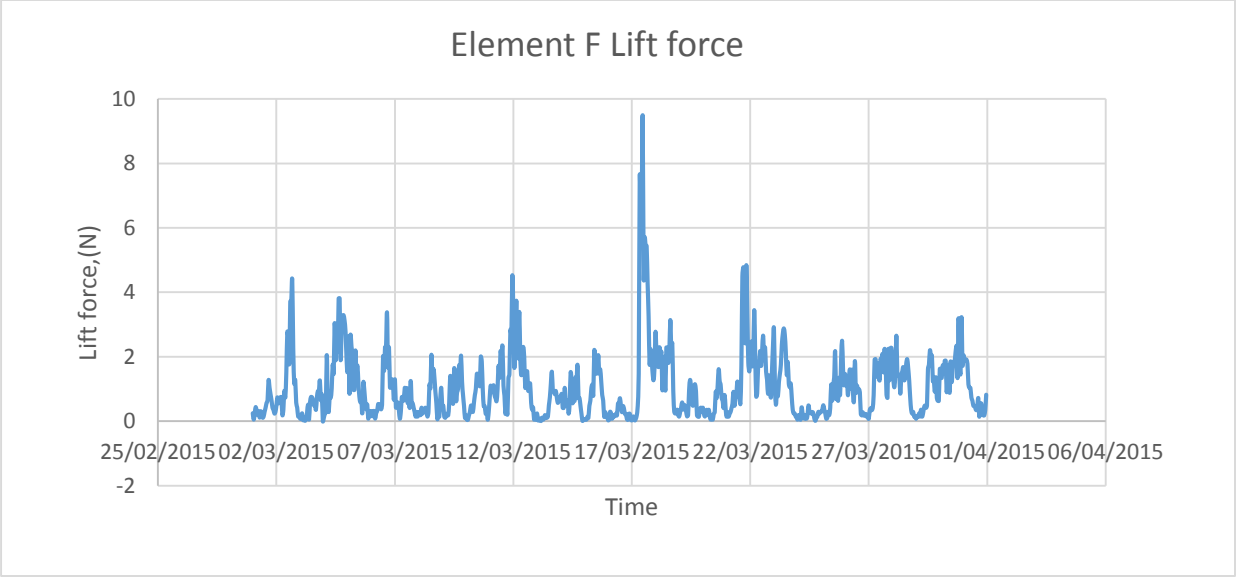
Element F Lift force
10
8
6
4
2
0
-2
Lift force,(N)
25/02/2015
02/03/2015
07/03/2015
12/03/2015
17/03/2015
22/03/2015
27/03/2015
01/04/2015
06/04/2015
Time

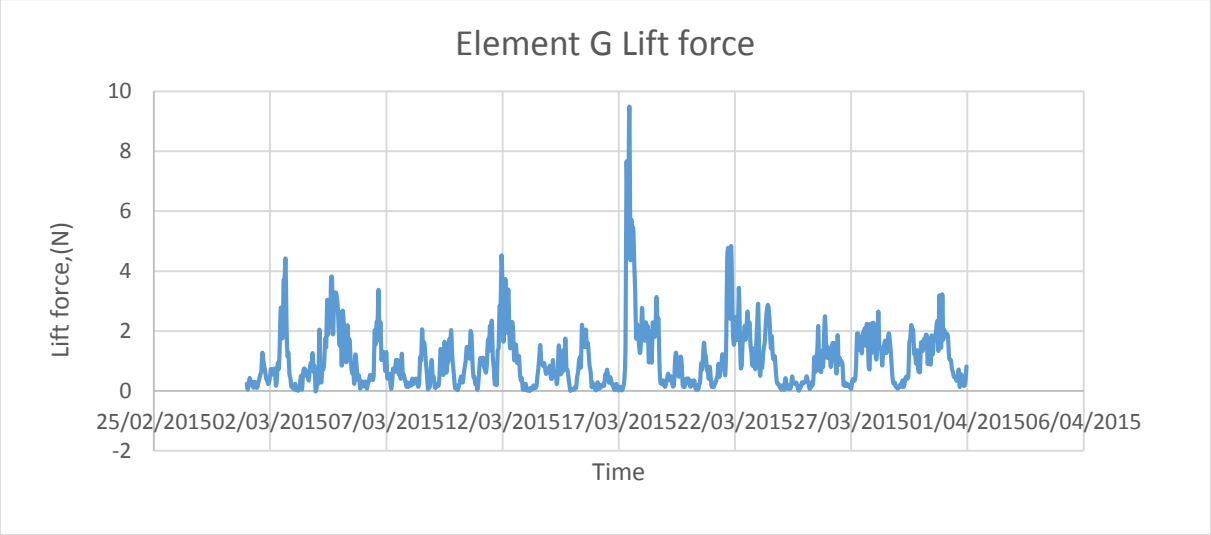
Element G Lift force
10
8
6
4
2
0
-2
Lift force,(N)
25/02/2015
02/03/2015
07/03/2015
12/03/2015
17/03/2015
22/03/2015
27/03/2015
01/04/2015
06/04/2015
Time

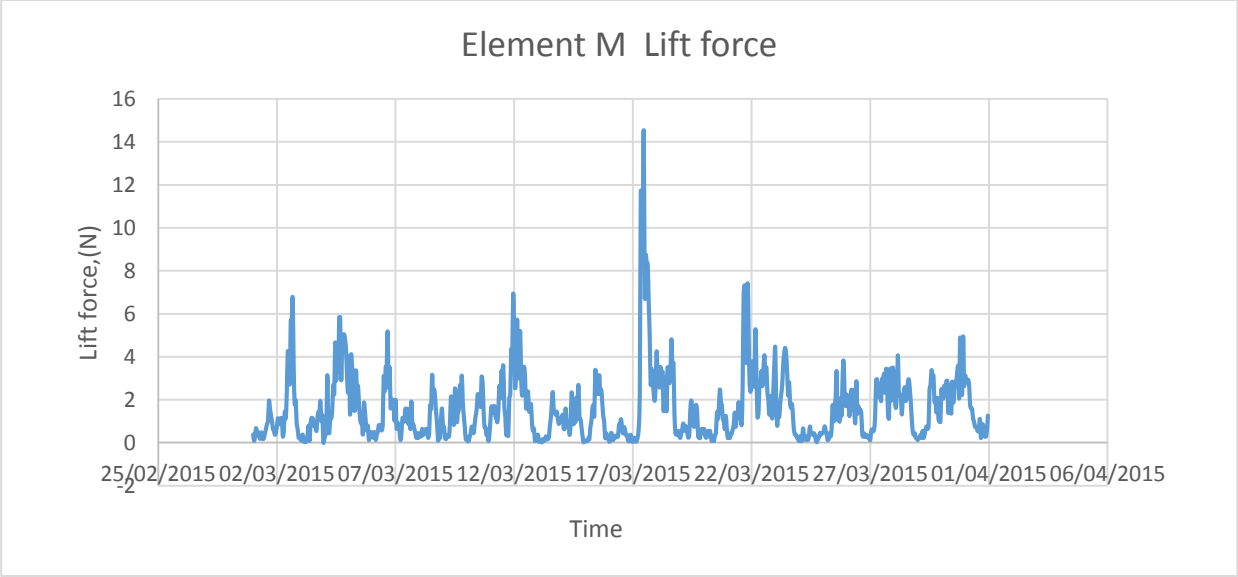

Figure 4.10 Time-history of the lift load on tracker elements for March, 2015.

The above time-history records of the lift and drag forces, which were determined based on the measured weather data for the months of February 2015 and March 2015, and based on the nominal area determined for each element of the tracker for corresponding elevation and azimuth angles, were used for conducting the Finite Element Analysis (FEA), by loading each member of the modeled solar tracker with a different loading pattern. The responses obtained from the static analysis were considered only for the maximum value of the drag and lift loadings as presented in Tables 4.8, 4.9 and 4.10 as presented in detail in the following chapters.

Chapter 5 Structural Response of PV Solar Tracker

5.1 Finite Element Simulation

The analytical procedural steps followed for modelling the dual-axis PV solar tracker installed on the rooftop of the Mann Parking building of the University of Ottawa, were highlighted and explained in Chapter 4 of this thesis. The critical structural elements of the investigated solar tracker are considered as the elements 'K', 'M' and 'A', because the calculation of the drag and lift forces for each of the trackers members, except for the PV solar panels shell, showed that these were subjected to the highest wind loads with reference to different inclination angles 45^0, 50^0, 55^0, 60^0, 65^0, 70^0, 75^0 and 78^0; thus these cases were analysed under the effect of the 16.11 m/s wind speed, as recorded at the weather station. Moreover, for the purpose of determining the critical response of the solar tracker, wind speeds higher than the weather data records were used in the Finite Element Analysis (FEA). The response of the critical elements under the effect of the wind speeds of 22 m/s and 33 m/s, and for the angles of attack from 45^0 to 75^0, corresponding to the operational angles of attack of the tracker during the day between 9:00 a.m. and 5:00 p.m. are reported in the following sections. Also a discussion regarding the response of the tracker for the angle of 78^0 which refers to the stow (parking) position which is considered the safest, and therefore is deployed at night between 5:00 p.m. and 9:00 a.m. has been formulated. The element 'M' is the steel circular beam which carries and orients the PV frame modules which rests on four horizontal frame members (elements 'K1' to 'K4') Elements 'A' are the two vertical legs of the structure which are the truss elements symmetrically supporting the element 'M' at 500 mm from both ends. The response of these elements were determined based on a static analysis, considering the simulated static drag and lift wind loads for determining their structural behaviour along both the horizontal and vertical directions. The time-history analysis was also considered for the critical wind forces and the frequency study showed the variation of the modal response for higher vibration modes.

5.2 Effect of the Wind Speed on the dual-axis PV solar tracker elements

Solar trackers are slender structures installed outdoors, at the terrestrial level or on the rooftop of medium-rise building, therefore they are exposed to wind speed variations; also the support frame of the trackers must be specifically designed to increase the efficiency of PV solar panels they

carry, by orienting the panels towards the sunlight at all times, during the day. Due to this reason, the solar tracker structure must be designed to resist the environmental loads that could affect their stability. In other to determine the effect of wind speed intensity on the tracker structure, its supporting members namely the elements; 'M', 'K' and 'A', were analysed specially for the attack angle 45^0, which proved to be the most critical inclination, under the increased wind speed of 16.11 m/s (as measured), 22 m/s and 33 m/s. The results from the static and modal analyses were obtained, to ascertain the critical responses of the elements as presented in the sections below.

5.2.1. Element M

As described in Chapter 3 , the element 'M 'is the hollow steel circular beam of 4.012 meter length and 0.15 m diameter, which conveys and rotates the upper and lower arms of the PV module frames (Elements 'K1', 'K2', 'K3', 'K4'). This is supported by the two truss elements 'A' each placed at a distance of 500 mm from both ends of member 'M'. The critical response of this element was established by subjecting it to critical wind-induced loads in the horizontal and vertical directions with reference to several attack angles determined for incrementally varied wind speeds as presented in Chapter 4 of this thesis .The analytical results presented in Tables 5.1 below depict the displacements of the element M in 3 different directions: horizontal, transverse and vertical direction, which are denoted as U1, U2 and U3 accordingly. Regardless of the angle of attack, the wind loads were calculated and were de-composed on the main two directions vertical and horizontal as recommended in most of the wind engineering design codes and research papers, therefore the displacements along these two directions, corresponding to U1 and U3 are of interest and are extensively discussed in the current chapter. Also, the vertical displacement U3 was reported as a negative value because the vertical axis was considered with the positive sign convention along the gravitational acceleration vector (downwards). The element 'M' was greatly displaced in horizontal direction as it yielded the maximum values of translational displacements of 0.65 mm, 1.43 mm and 2.35 mm with respect to wind speeds of 16.11 m/s, 22 m/s and 33 m/s respectively. However, the high increase in wind speed did not have any significant effect on the vertical displacement of the element as the values of the vertical displacement were lower than the 1mm as shown in Figure 5.1(b).

Test Case 1: 45^0 Inclination under 16.11 m/s wind speed

In the first case, the element was inclined at $45^0$and rotated at 30^0 to determine its response under the effect of the wind speed intensity of 16.11 m/s. Table 5.1 (a) presents the translational displacements in three different directions denoted as U1, U2 and U3 for the horizontal, transversal and vertical directions. Node 41 displayed critical response to the applied wind speed as it produced the maximum displacement of 0.065 mm and downwards displacement of 0.28 mm for the horizontal and vertical directions.

Table 5.1(a) Displacements of member 'M' for 45° at 16.11 m/s

Joint number	Node number	U1	U2	U3
		m	m	m
1	7	0.000509	2.26E-08	-0.000916
2	8	0.000509	2.83E-08	-0.000916
3	41	0.000651	1.72E-08	-0.000277
4	96	0.000596	1.84E-08	-0.000404
5	97	0.000597	2.58E-08	-0.000404

Test Case 2:45^0 inclination under 22 m/s wind speed

The element M was subjected to the increased wind speed of 22 m/s at the same inclination angle of 45°, for determining further response of this element. However, the displacement results shown in Table 5.1(c) revealed that the element was symmetrically loaded in the vertical direction with Node 41 situated at the middle of element M, having a maximum displacement of 0.29 mm. Exterior nodes 7 and 8, on one side, and 96 and 97 on the other side of element M had similar responses, with the same displacement values.

Table 5.1(b) Displacements of member ‘M’ for 45° at 22 m/s

Joint Identity	Joint	U1	U2	U3
		m	m	m
1	7	0.001431	-2.10E-08	-0.000775
2	8	0.00143	8.06E-08	-0.000775
3	41	0.001331	2.14E-08	-0.000288
4	96	0.001342	6.06E-08	-0.000372
5	97	0.001342	-7.93E-09	-0.000372

Test Case 3: 45^0 inclination under 33m/s wind speed

The wind speed was increased to 33m/s for verifying the critical response of the element M, which sustains the PV solar panels modules. It was observed from table 5.1(c) that the node 41 which is the centre of the element is prone to achieving structural instability in horizontal direction, under wind speed of 33 m/s registering a displacement of 2.0 mm, while the adjacent nodes 7 and 8 responded with approximately the same displacements in both vertical and horizontal direction; this might lead to possible shear rupture near the middle of the element M.

Table 5.1 (c) Displacements of member ‘M’ for 45° at 33 m/s

Joint Identity	Joint	U1	U2	U3
		m	m	m
1	7	0.002353	-6.47E-08	-0.000634
2	8	0.002352	1.33E-07	-0.000634
3	41	0.002012	2.56E-08	-0.000298
4	96	0.002088	1.03E-07	-0.000341
5	97	0.002088	-4.16E-08	-0.000341

From the Tables 5.1 a) to c), it can be noticed that the horizontal, transverse and vertical displacements increased for higher wind speeds; there is increase in vertical displacements at all joints and the displacement patterns are uniform for all wind speeds. However, the central joint (node 41) experienced more deformation as the highest value of the vertical displacement was recorded at each wind speed.

a) (b)

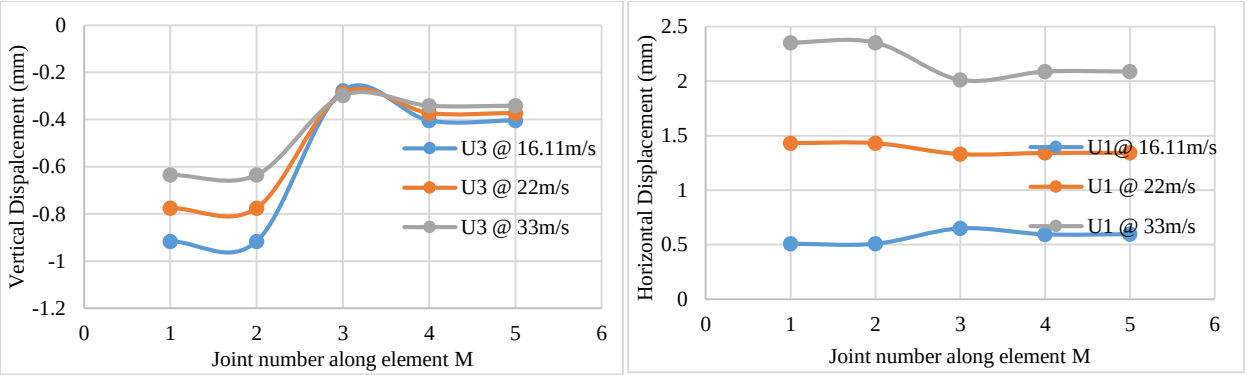

Figure 5.1 a) Vertical and b) horizontal displacement of the element M at different wind speeds

According to Figures 5.1 a) and b), the element M suffered more deformation in horizontal direction as the wind load increases from 16.11m/s to 33m/s, due to the fact that it was more exposed to drag wind load, as compared to vertical lift direction where it was partially shield by the PV solar panel mounted on top. However, the two exterior nodes at both ends of the element M registered similar horizontal displacements. Also it was observed that only at the maximum wind load, the exterior nodes 7 and 8 are the most critical of this element having the same horizontal displacement value of 2.35 mm, followed by the nodes 96 and 97 with the same value of horizontal displacement 2.09 mm, while the least critical is node 41 with horizontal displacement value of 2.01mm.

5.2.2. Element A

The two elements ‘A1’ and ‘A2’ are the non-inclined trusses supporting elements that provide full structural support to the rotating element ‘M’. In other words, ‘A’ elements are the vertical legs of the solar tracker connecting the upper and lower parts of the tracker. Therefore this element has two components A1 and A2, and they form the main body of the tracker which connects the rotating upper beam (element M) as shown in figure 3.1, to the fixed frame connected to the circular rack located at the base of the tracker. This element was investigated at inclination angle of 45° for determining the critical response at different wind speeds of 16.11 m/s, 22 m/s and 33m/s presented in Case 1, Case 2 and Case 3 respectively. The horizontal and vertical displacements at the three nodes situated along the element A 35, 87 and 36 were recorded for element A1 and nodes 79, 94 and 01 for element A2, as shown in table 5.2 (a,) (b) and (c). In general, this element

was only affected by the intensity of the wind speed in the horizontal direction as it is shield by the rack at the bottom end and the element M at the top for the vertical direction. Therefore the A elements were less affected for the vertical displacement direction. Significant horizontal displacements of 1.14 mm were noticed at higher wind speed of 33 m/s as shown in Table 5.2.c) and in Figure 5, with the minimum horizontal displacement of 0.3 mm at the low wind speed of 16.11 m/s. However, The A element was slightly affected by the wind load in the vertical direction as the maximum vertical displacement at gust wind speed is 0.05 mm. It is considered that the 'A' element is one of the most important elements of the tracker and must be able to resist the loads induced by the environmental wind forces during the operation positions and the stow position of the solar tracker.

Test Case 1: Element 'A' response at 45^0 inclination and 16.11 m/s wind speed

This element appeared to be the most critical element of the dual-axis tracker, in the sense that any deformation caused by the wind load would surely damage the upper and lower parts of the structure, as it indirectly impacts the main body of the tracker. Therefore, this element was analysed at different wind loads to ascertain the critical nodes where failure could be encountered. Because of the symmetric geometry, it was observed that the three nodes of each sub element A1 and A2 produced the same vertical and horizontal displacements at each wind speed as shown in table 5.2 (a) and (b). In this regard, only the analytical results for the sub-element 'A1' were presented in detail, to avoid repetitive results, since the members A1 and A2 have same dimensions, material properties and same boundary conditions.

Table 5.2. (a) Displacements of member 'A1' for 45° at 16.11 m/s

	Joint	U1	U2	U3
Node Identity		m	m	m
1	35	0.000297	0.000138	-0.000366
2	87	0.000296	0.000138	-0.000328
3	36	0.000296	0.000135	-0.000288

Table 5.2 (b): Displacements of member 'A2' for 45° at 16.11 m/s

	Joint	U1	U2	U3
Node Identity		m	m	m
1	79	0.000297	-0.000138	-0.000366
2	94	0.000296	-0.000138	-0.000328
3	1	0.000296	-0.000135	-0.000288

Comparing the results obtained for each of the three nodes at the bottom, middle and higher parts of the sub-elements A1 and A2, it was noticed that they behaved similarly, as both produced same value of displacements along the three directions. In general the element A had higher displacements in horizontal direction, of maximum values of 0.29 mm recorded in both frames A1 and A2.

Case 2: Element 'A' response at 45° inclination and 22 m/s wind speed

Since the nodes of the elements A1 and A2 responded symmetrically to the same applied wind load, as shown for the case 1, for the other two cases, only the displacement of the element A1 was presented, as representative for both sub-elements A1 and A2. The A1 element was subjected to higher wind loads in both X and Y directions by increasing the wind speed from 16.11m/s to 22 m/s. The results shown in Table 5.2 (c) revealed that the elements registered higher displacements in both directions. However, higher horizontal displacement was recorded for case 2, as compared to case 1 which had lower wind speed. Interestingly, all the 3 nodes yielded same displacement along the horizontal direction. So, it could be concluded that all nodes behaved similarly in horizontal direction irrespective of the wind load and wind speed**.**

Table 5.2 (b) Displacements of member 'A1' for 45° at 22 m/s

	Joint	U1	U2	U3
Node Identity		m	m	m
1	35	0.000718	0.000123	-0.000363
2	87	0.000718	0.000106	-0.00024
3	36	0.000718	0.000089	-0.000119

Case 3: Element 'A' response at 45 ° inclination and 33 m/s wind speed

When the element 'A' was subjected to higher wins speeds of 33 m/s, except for the node 35, situated at the bottom of the A element, where the vertical displacements remained the same for all the three investigated cases, Case 1, Case 2, and Case 3, the nodes 87 and 36 registered increased vertical displacements, with the increase of the wind speed, as shown in Figure 5.2 (a) below. Maximum vertical displacements of 0.05 mm occurred at the maximum wind speed of 33 m/s for node 36.

Table 5.2(c): Displacements of member 'A1' for 45° at 33 m/s

	Joint	U1	U2	U3
Node Identity		m	m	m
1	35	0.00114	0.000109	-0.00036
2	87	0.00114	0.000075	-0.000151
3	36	0.001139	0.000043	0.00005

a) b)

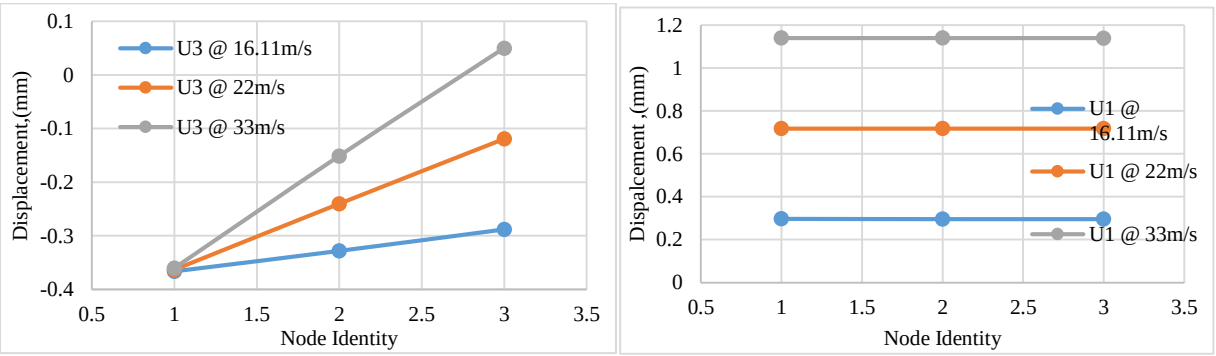

Figure 5.2 a): Vertical and b) horizontal displacements of element A at different wind speeds

However, the element is prone to register more displacement in horizontal direction as the minimum displacement in this direction is even greater than maximum vertical displacement recorded above. As presented in Figure 5.2 (b), all the nodes had equal horizontal displacement for each wind speed tested. Nevertheless, the element maximum displacement was recorded to be uniform for all joints with respect to maximum wind speed of 33 m/s.

5.2.3. Element K

The element K is the surrounding frame which directly supports the PV module installed at the top part of the solar tracker. There are two rows of PV solar panels, and there are two K frames elements on each of the PV module rows, which added to a total number of four K elements denoted as: K1, K2, K3 and K4, as shown in the Table 5.3 below. These elements were analysed at 45^0 angle of attack, with various drag and lift wind loads determined based on the distributed load acting on the two rows of the PV solar modules. From Figure 5.3 (d) below, it can be noticed that the element K4 was more displaced as compared to elements K2 and K3. However, the element K1 also registered significant displacements in both X and Y directions, with respect to intensity of the wind speed, because it directly faced the dominant wind direction where the loads were applied. Moreover, because of the fact that elements K2 and K3 were shielded by the other elements, they were less influenced by the wind load acting both X and Y directions. At maximum wind speed of 33m/s, element K1 had the biggest horizontal displacement of 2.45 mm while the vertical displacement was 0.34 mm at normal wind speed of 16.11 m/s.

Static Analysis of Element 'K'

Element K is an aluminium frame sub-divided into sub-elements K1, K2, K3, and K4, where K1 and K2 are the elements that support the lower arm of the PV solar panels, while K3 and K4 support the upper arm of the PV solar panel module. There are 7 nodes in each of the sub- elements, as shown in Table 5.2. Each element was analysed at 45° with respect to various wind speeds of 16.11 m/s, 22 m/s and 33 m/s aiming at estimating the critical response of the frame K. Table 5.3 (a) presents Case 1 analytical results for K1, (b) Case 2 analytical results for K2, (c) Case 3 analytical results for K3 and Case 4 for K4 at wind speed of 16.11m/s.

Case 1: Element K at 45° inclination angle and wind speed of 16.11m/s

Element K1

Table 5.3 (a): Element K1 Node displacements Element K1

		U1	U2	U3
Serial number	Node Identity	m	m	m
1	333	-0.000055	-0.000033	-0.000881
2	332	0.000235	0.000154	-0.000411
3	335	0.000213	0.000139	-0.000378
4	343	0.000204	0.000132	-0.000351
5	329	0.000213	0.000138	-0.000378
6	328	0.000236	0.000152	-0.000411
7	327	-0.000053	-0.000037	-0.000881

From table 5.3 (a) it was noticed that due to the symmetrical loading of the element K1, the exterior nodes 333 and 327 registered the same vertical displacements, the nodes 332 and 328 had same vertical displacement, while nodes 335 and 329 yielded the same vertical displacement. The node at the centre of the element produced highest vertical displacement. Similar behaviour was noticed for the aforementioned nodes, except that the maximum horizontal displacement did not occur at the centre of the element K, but at extremity nodes 322 and 328 with equal value of 0.24 mm**.**

Element K2

As discussed in the above paragraph for element K1, the K2 element has the same symmetrical properties for the exterior nodes 334 and 330, 400 and 326, and for the interior nodes 401 and 331, and these registered same displacement in vertical direction, as shown in Table 5.3 (b). However, for the horizontal direction, the displacements were different, as each node yielded different value in this direction.

Table 5.3(b): Element K2 Node displacements

		U1	U2	U3
Serial number	**Node Identity**	m	m	m
1	334	-0.0001	-0.000097	-0.000758
2	400	-2.00E-06	-0.000021	-1.80E-06
3	401	-1.77E-06	-9.58E-06	0.000013
4	342	-1.59E-06	-1.04E-06	-1.31E-06
5	331	-6.77E-06	7.04E-06	0.000013
6	326	-0.000013	0.000016	-1.80E-06
7	330	-0.000129	-0.000052	-0.000758

Element K3

As presented in Table 5.3(c), the exterior nodes 322 and 316, 315 and 314 yielded the same displacement in the vertical direction, with the interior joints 325 and 317 having the same displacement; also the maximum displacement recorded at the mid span of element K3 (node 336) was noticed for the vertical direction**.**

Table 5.3(c): Element K3 Node displacements

		U1	U2	U3
Serial number	**Node Identity**	m	m	m
1	322	-0.000109	-0.000038	-0.000742
2	315	-0.000013	0.000016	-1.56E-06
3	325	-0.000018	-7.99E-07	-0.000022
4	336	-1.59E-06	-1.04E-06	-1.31E-06
5	317	-8.88E-06	-0.000017	-0.00002
6	314	9.38E-06	-0.000018	-1.56E-06
7	316	-0.000079	-0.000084	-0.000742

Element K4

Same symmetrical properties of the element K3 above are employed for the element K4 as well, therefore it was noticed that the exterior and the interior nodes produced very similar values for the displacement in the vertical direction. However, the maximum displacement in this direction occurred at exterior nodes 321 and 320, with the minimum displacement registered at the outer nodes as shown in Table 5.2 (d).

Table 5.3(d): Element K4 Node displacements

		U1	U2	U3
Serial number	Node Identity	m	m	m
1	323	-0.000125	-0.000084	-0.000696
2	321	0.000133	0.000084	-0.000279
3	324	0.000148	0.000095	-0.000314
4	337	0.000149	0.000097	-0.000304
5	319	0.000147	0.000096	-0.000314
6	320	0.000131	0.000087	-0.000279

Case 2: Element K at 45° with wind speed of 22mm/s

Another case was considered whereby the wind load was increased by applying 22 m/s, to determine if the element would maintain the response similar to the case of 16.11 m/s, or higher displacements in vertical and horizontal directions would be registered. Sub-elements K1, K2, K3 and K4 were analysed under the applied increased load and the vertical and horizontal displacements are presented in Table 5.4(a). (b), (c) and (d) respectively. Elements K1 and K4 exhibited symmetrical loading of the element, and each produced same displacements for the exterior nodes in both vertical and horizontal direction with the maximum displacements recorded for the vertical direction only. Elements K2 and K3 only produced same displacement at aforementioned nodes in the vertical direction but they are different from the horizontal displacements, as detailed below.

Element K1

Table 5.4(a) Element K1 Node displacements for 22 m/s

		U1	U2	U3
Serial number	**Node Identity**	m	m	m
1	333	0.001367	0.000889	-0.001755
2	332	0.001473	0.000958	-0.001297
3	335	0.00149	0.000969	-0.000991
4	343	0.001432	0.00093	-0.000871
5	329	0.00149	0.000967	-0.000991
6	328	0.001474	0.000956	-0.001297
7	327	0.001368	0.000887	-0.001755

Element K2

Table 5.4(b) Element K2 Node displacements for 22 m/s

		U1	U2	U3
Serial number	**Node Identity**	m	m	m
1	333	0.001289	0.00076	-0.001532
2	332	0.001407	-0.000059	-0.000791
3	335	0.001435	-0.000027	-0.000465
4	343	0.001102	0.000715	-0.0003
5	329	0.001189	0.000804	-0.000465
6	328	0.001148	0.000816	-0.000791
7	327	0.001218	0.000869	-0.001532

Element K3

Table 5.4(c) Element K3 Node displacements for 22 m/s

		U1	U2	U3
Serial number	**Node Identity**	m	m	m
1	333	0.001261	0.000897	-0.001499
2	332	0.001186	0.000841	-0.000761
3	335	0.001214	0.000821	-0.000439
4	343	0.00113	0.000734	-0.000278
5	329	0.001241	0.000774	-0.000434
6	328	0.00125	0.000741	-0.000761
7	327	0.001332	0.000786	-0.001499

Element K4

Table 5.4(d) Element K4 Node displacements for 22 m/s

		U1	U2	U3
Serial number	**Node Identity**	m	m	m
1	333	0.001215	0.000788	-0.00136
2	332	0.001271	0.000824	-0.000877
3	335	0.001328	0.000862	-0.000619
4	343	0.001268	0.000823	-0.000554
5	329	0.001328	0.000863	-0.000619
6	328	0.001269	0.000826	-0.000877
7	327	0.001214	0.00079	-0.001361

Case 3: Element K at 45° with wind speed of 33m/s

The structural impact of higher wind load on the same element K described in Case 2 was investigated by subjecting the elements K1 to K4 to 33 m/s wind speed. In this case, the four different displacements tables were presented corresponding to the displacements reported for K1, K2, K3 and K4, in horizontal and vertical directions. Similar with Case 2, the elements K1 and K4 exhibited same structural properties as each produced same displacements at the outer exterior nodes, and interior nodes, in both vertical and horizontal directions. The maximum displacements were registered at the mid span nods. Element K2 and K3 behaved differently, as the nodes are not symmetrical in this case, hence different displacements were registered for outer exterior, and interior nodes as shown in Tables 5.5 (b) and (c).

Element K1

Table 5.5(a) Element K1 Node displacements for 33 m/s

		U1	U2	U3
Serial number	**Node Identity**	m	m	m
1	333	0.002452	0.001592	-0.001872
2	332	0.002409	0.001564	-0.001566
3	335	0.002315	0.001503	-0.001371
4	343	0.002176	0.001413	-0.001326
5	329	0.002314	0.001502	-0.001371
6	328	0.002408	0.001564	-0.001565
7	327	0.002451	0.001592	-0.001872

Element K2

Table 5.5(b) Element K2 Node displacements for 33 m/s

		U1	U2	U3
Serial number	**Node Identity**	m	m	m
1	333	0.002185	0.001342	-0.001302
2	332	0.002276	-0.000059	-0.000685
3	335	0.002163	-0.000027	-0.000453
4	343	0.001623	0.001054	-0.000349
5	329	0.001799	0.0012	-0.000453
6	328	0.001876	0.001289	-0.000685
7	327	0.002114	0.00145	-0.001302

Element K3

Table 5.5(c) Element K3 Node displacements for 33 m/s

		U1	U2	U3
Serial number	**Node Identity**	m	m	m
1	333	0.002239	0.001533	-0.001204
2	332	0.002004	0.001372	-0.000586
3	335	0.001912	0.001274	-0.000352
4	343	0.001751	0.001137	-0.00025
5	329	0.001938	0.001227	-0.000347
6	328	0.002068	0.001273	-0.000586
7	327	0.00231	0.001422	-0.001205

Element K4

Table 5.5(d) Element K4 Node displacements for 33 m/s

		U1	U2	U3
Serial number	**Node Identity**	m	m	m
1	333	0.002005	0.001303	-0.000721
2	332	0.001896	0.001231	-0.000344
3	335	0.001824	0.001185	-0.00016
4	343	0.00168	0.001092	-0.00014
5	329	0.001824	0.001184	-0.00016
6	328	0.001895	0.001231	-0.000344
7	327	0.002005	0.001302	-0.000722

The wind speed variation effect on the element K is presented in Figures 5.3 a) to h). From Figure 5.3 a), it was observed that the increase in the wind speed has significant impact on the element K1 in horizontal direction, as all the nodes produced higher displacements at higher wind speed. However, at increased wind load, the displacement shown did not have similar pattern, because the node 343 (centre node) was situated in the middle of edge of the PV solar panel module which is vulnerable to damage. Contrarily, all displacements followed the same pattern for the vertical

direction, and the centre node produced maximum displacement, followed by the exterior nodes, for each wind speed effect was as shown in Figure 5.3 (b). Although, no significant impact of higher wind load was recorded in vertical direction, however, the element K1 is more displaced at the corners therefore is vulnerable to more damage at exterior nodes. The element K2 is vulnerable to more damage at higher wind loads, as this was confirmed in Figure 5.3 c), where all nodes had higher displacements at wind speed of 33 m/s as compared to the displacements at wind speed of 22 m/s. At higher wind speeds, the centre node had the lowest deformation, probably because this was not exposed to significant wind load in this direction. In other word, the element was shielded by other element. In the vertical direction, all nodes registered small deformation as shown in Figure 5.3 d), irrespective of the wind load, and the maximum displacement in this direction is far less than unity, as compared with 2.28 mm recorded in horizontal direction. However, the deformation patterns are uniform in both horizontal and vertical directions for higher wind loads.

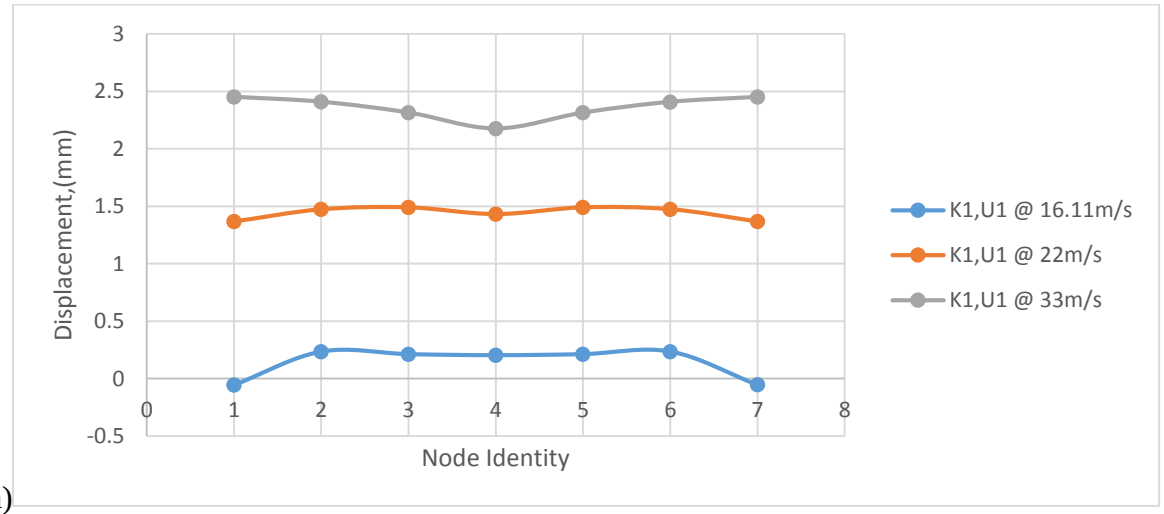

a)

Figure 5.3. a)Vertical and b) Horizontal displacement of element K1 with respect to wind speed.

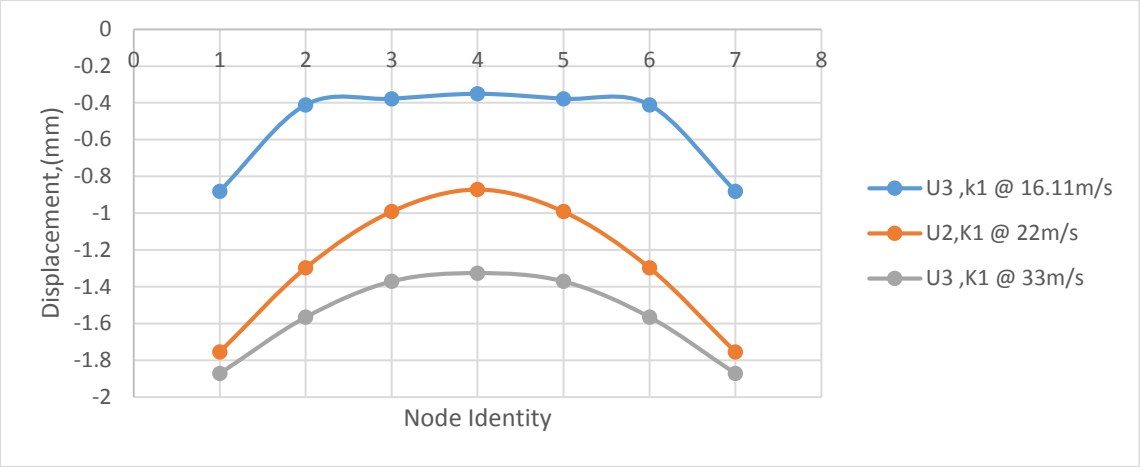

b)

Figure 5.3. a) Vertical and b) Horizontal displacement of element K1 with respect to wind speed.

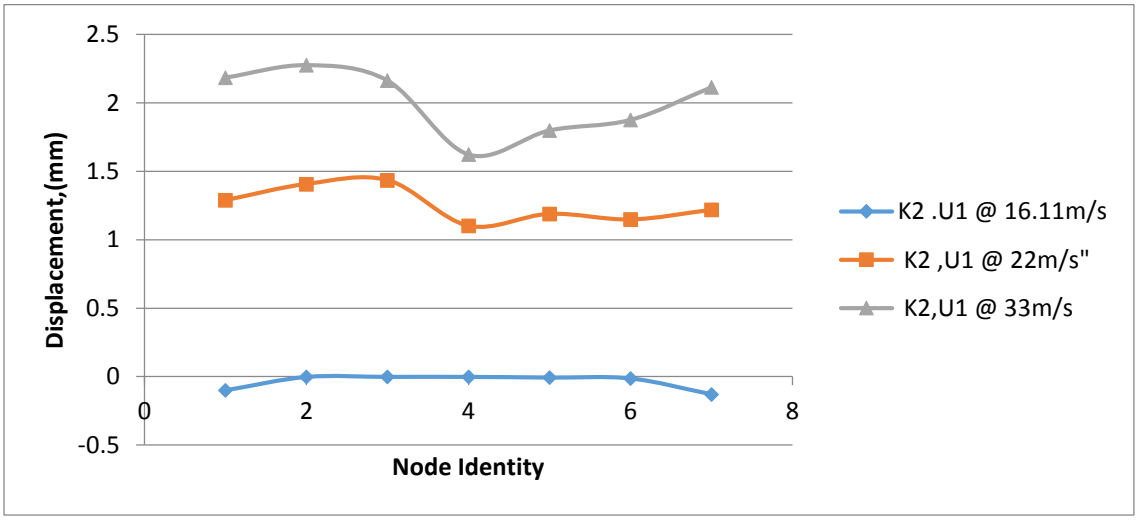

c)

Figure 5.3. c) Vertical and d) Horizontal displacement of element K2 with respect to wind speed.

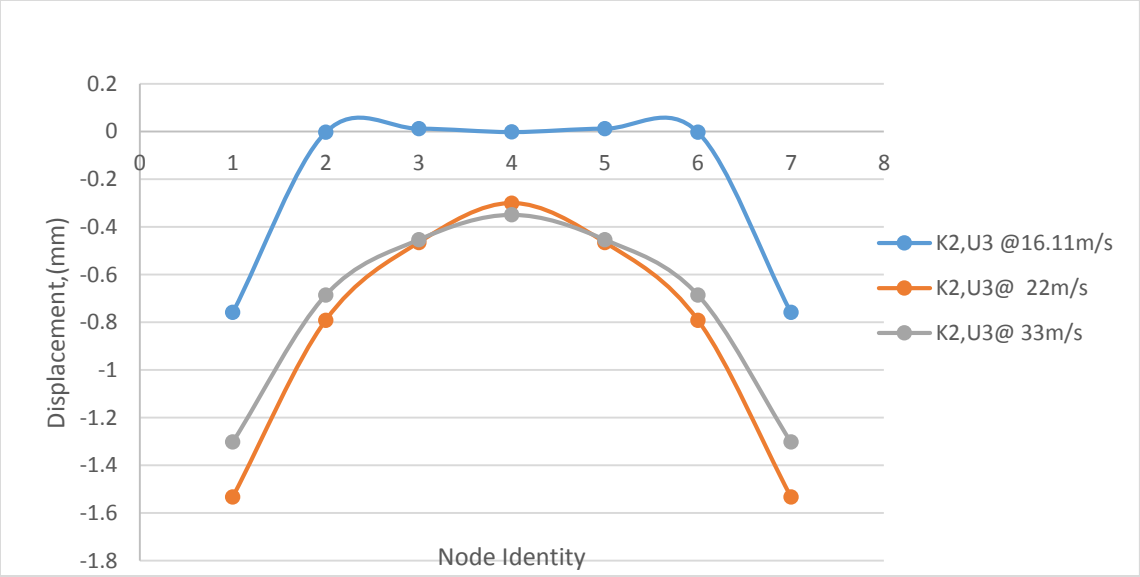

d)

Figure 5.3. c) Vertical and d) Horizontal displacement of element K2 with respect to wind speed.

At higher wind speeds, the element K3 produced maximum displacements for the outer exterior nodes, with the lowest displacement at the centre node as shown in Figure 5.3 e). Although, the deformation patterns did not appear the same for the lower wind load, as the centre load proved to be the most critical node for the horizontal direction. The nodes deformation patterns at 22 mm/s and at 16.11 m/s wind speeds determined the same displacement in vertical direction with most critical joints at the mid span. Therefore the exterior joints are considered the most critical nodes, under the applied medium wind speed of 16.11 m/s.

e)

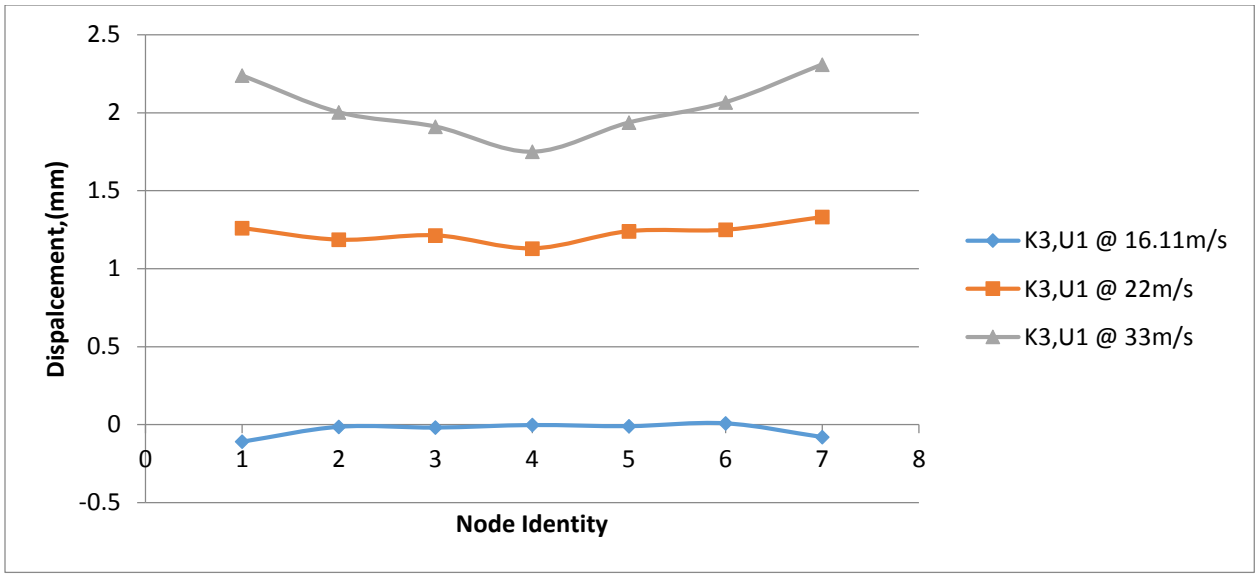

f)

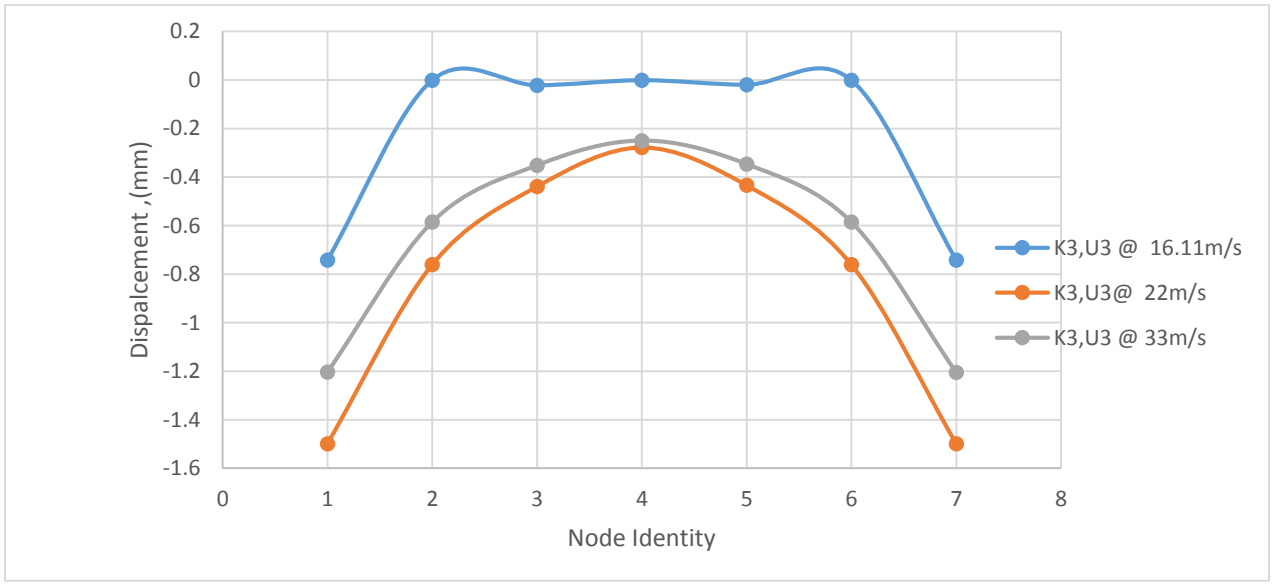

Figure 5.3. e) Vertical and f) Horizontal displacement of element K3 with respect to wind speed.

For the horizontal direction, the 2 outer exterior nodes of the K4 element exposed to the highest wind speed of 33 m/s were the most critical points, with the middle nodes as lower displacement.

However, the element K4 suffered less deformation at 16.11 m/s wind speed as compared to the higher wind speed of 22 m/s. However, the deformation patterns were not the same for each wind load, due to that fact that the element K4 is exposed to more wind damaged at higher wind loads. The interior and the centre nodes of this element, at higher wind speed were greatly affected with higher displacement values recorded in vertical direction at these joints.

g)

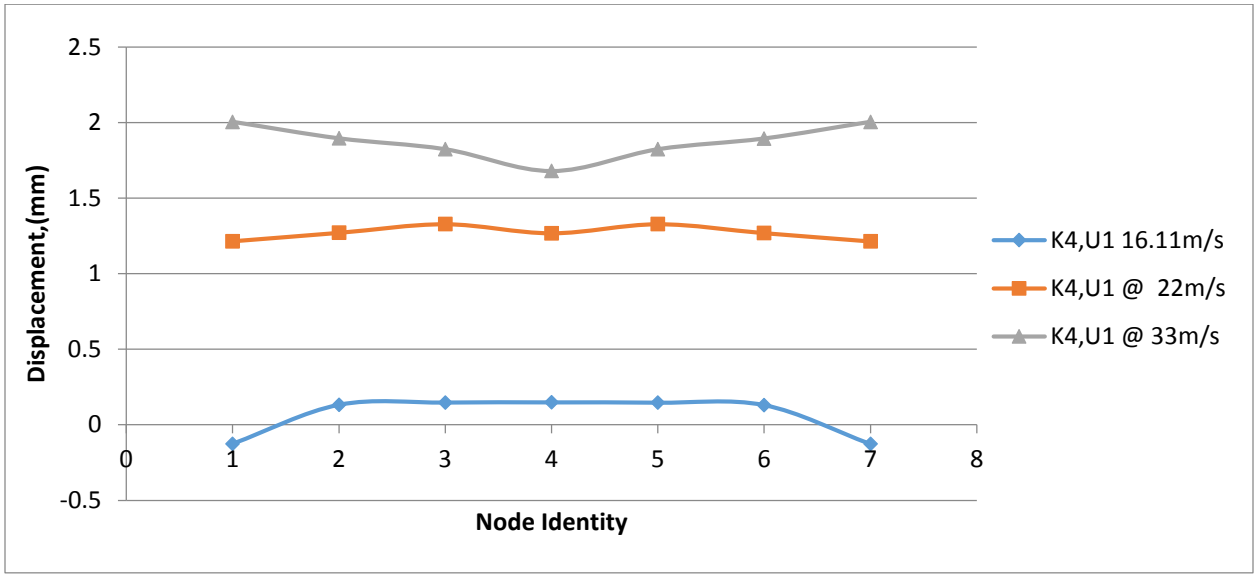

h)

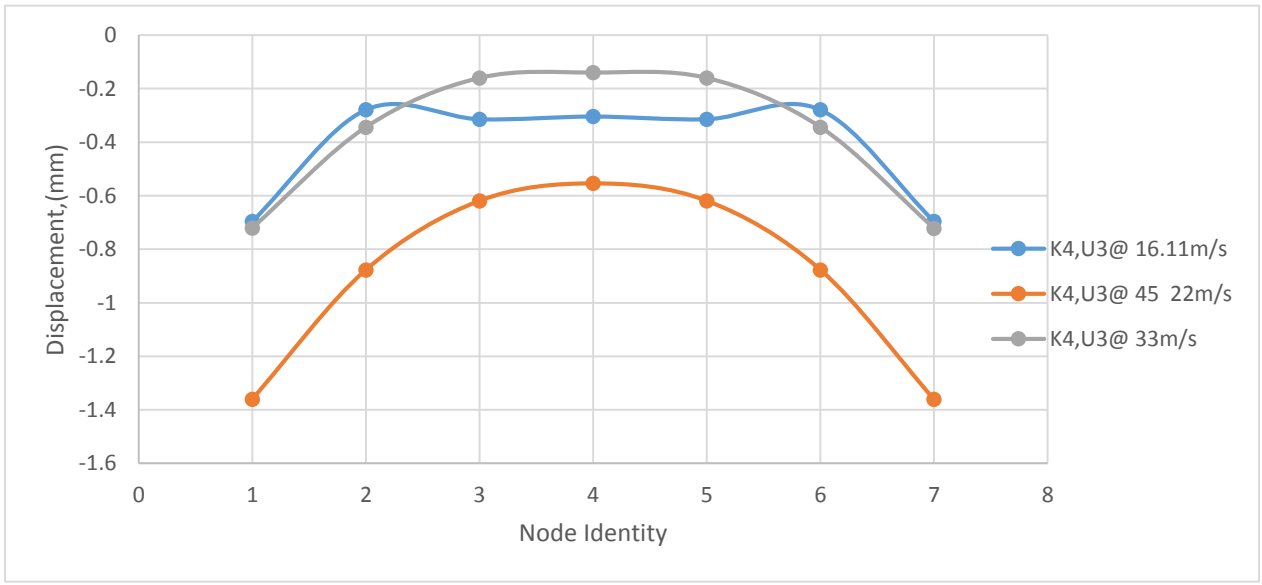

Figure 5.3.g) Vertical and h) Horizontal displacement of element K4 with respect to wind speed.

Generally speaking, due to higher displacement values recorded, the K1 element appeared to be the most critical in correlation with the fact that it was mostly exposed to the direction of wind speed irrespective of the wind load, thus it suffered more deformation.

5.3. Effect of Inclination Angle on the Solar Tracker

5.3.1 Element A

The main body of the dual-axis solar tracker is represented by the two symmetric elements 'A' which connect the top and the bottom parts of the tracker together as previously introduced. Different inclination angles were investigated and analysed with low wind speed of 16.11 m/s at angle of attacks ranging from 45° to 75° at 5° intervals. This investigation was performed to determine the most critical angle of inclination for which the risk of losing the structural stability increases, and such positioning of the tracker during the overnight period. The wind loads were applied along the dominant wind vertical and horizontal directions. The displacements recorded at the three nodes for each case were presented below. As shown Figure 5.4 below, this element was not significantly affected by the wind load in the vertical direction because the nominal area under the lift load was extremely low and equally shielded by the rack element which prevented it from being displaced in this direction. Consequently, the three values reported for the vertical displacements were produced for each angle of attack, as shown on Figure 5.4 and could be concluded that these displacement values were the same at all angles of attack. The critical response was observed for 45° angle of attack, with the maximum vertical displacement of 0.30 mm, recorded for all joints at this inclination angle. All the horizontal displacements for each angle of attack appeared to be same.

Case 1: Element A1 at 45° degree with normal wind speed of 16.11m/s

In this case, maximum wind load generated in chapter four were applied in both vertical and horizontal directions .The Nodes displacement recorded in each direction was presented in table 5.6(a).The horizontal displacement recorded appeared to be the same, meaning that all the 3 nodes responded the same way to the applied wind load but differently in vertical direction. However, maximum displacement was observed in horizontal direction.

Case 2: Element A1 at 50° with low wind speed of 16.11 m/s

As presented in Figure 5.4 all the 3 nodes produced the same horizontal displacement with different values of vertical displacement, thus the element A1 was observed to be more displaced in the horizontal direction, due to higher exposure angle. Also, due to the fact that the element A1 was shielded by the bottom part of the tracker, this was less affected in vertical direction.

Case 3: Element A1 at 55° with wind speed of 16.11 m/s

In this case, the lower horizontal displacement values were observed with almost equal vertical displacements as for the Case 2.

Case 4: Element A1 at 60° degree with normal wind speed of 16.11 m/s

Wind loads were applied with reference to the inclination angle using calm wind speed as previously discussed. The analytical result was presented below in Figure 5.4 below.

Case 5: Element A1 at 70° degree with normal wind speed of 16.11 m/s and Case 6: Element A1 at 75° degree with normal wind speed of 16.11 m/s

Similar interpretation was followed for the rest of the cases 5 and 6 corresponding to the inclination angles 70° and 75°. For each case, the horizontal displacement was recorded for the 3 nodes, but varying with the vertical displacements. The element is vulnerable to more displacement in horizontal direction, having higher values as compared with the vertical displacements, which are constant for each case irrespective of the attack angle.

Figures 5.4 a) and b) present the overall effect of the inclination angles on the element ‘A’. Finally it can be observed that this element is more vulnerable to wind damage at 45° angle of attack for both vertical and horizontal directions. Therefore, it was established that 45° angle of attack is the most critical from all the inclination angles considered. In this regard, if the element A has the highest value of displacement, compared with the other elements of the solar tracker, after the entire analysis it can be concluded that the tracker is not safe at this operational angle of inclination.

a)

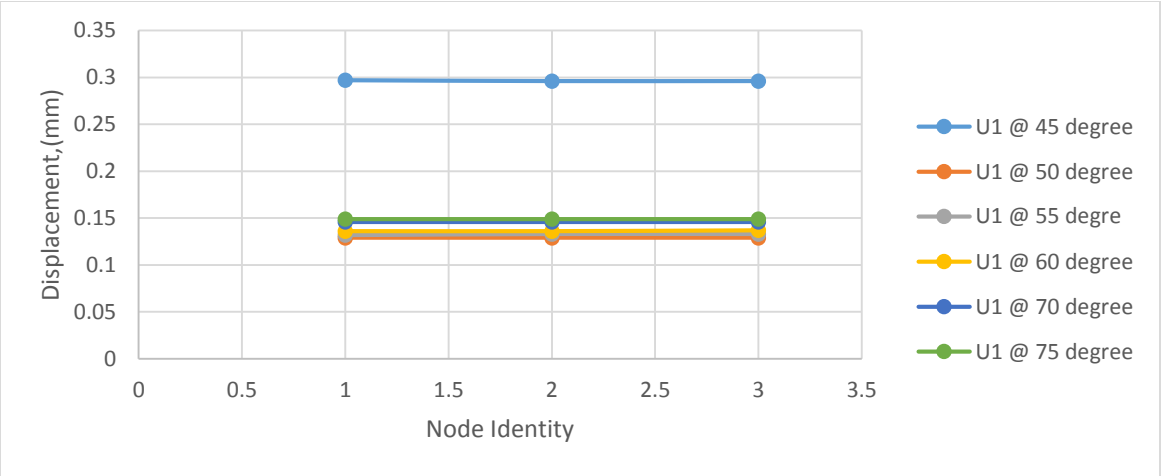

b)

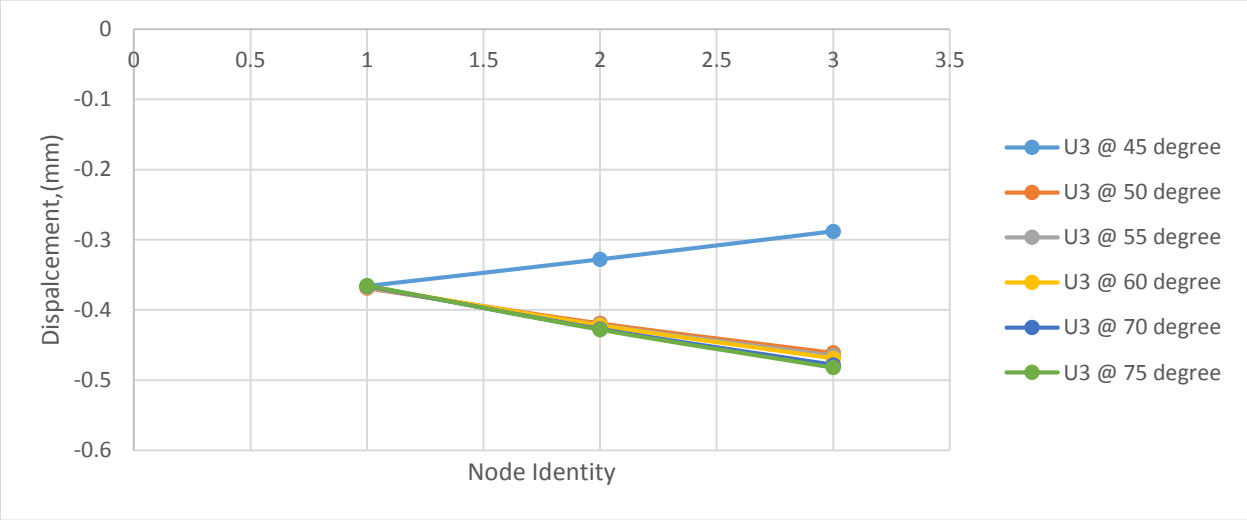

Figure 5.4: Element 'A' a) Horizontal and b) vertical displacement at various angle of attack

5.3.2. Element 'M' with wind speed of 16.11m/s

In order to ascertain more reliability of the structural model during the operation (during the day), further analytical investigation was performed on the structural element 'M' at different angle of attacks: 45^0,50^0,55^0,60^0,65^0,70^0, 75^0 corresponding to operational inclination angles. Similar inclination and wind speed cases were performed as for the element A, however due to the space limitations only the concluding Figures 5.5 a) and b) are discussed below. As previously discussed,

the rotating element K carries and orients the PV modules for better capturing the sunlight to enhance the maximum efficiency of the solar panels. This element consists of 5 nodes as shown in Figure 5.5. The wind loads corresponding to 16.11 m/s were applied to element M in two directions, similar to the other elements, and the nodal displacements generated for each case were presented in Figure 5.5 below.

a)

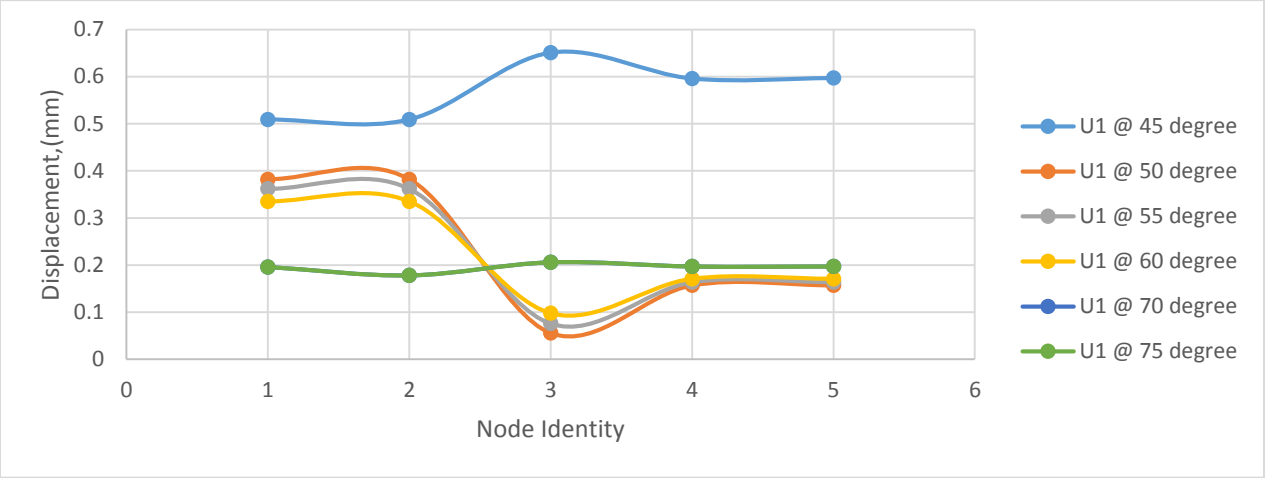

b)

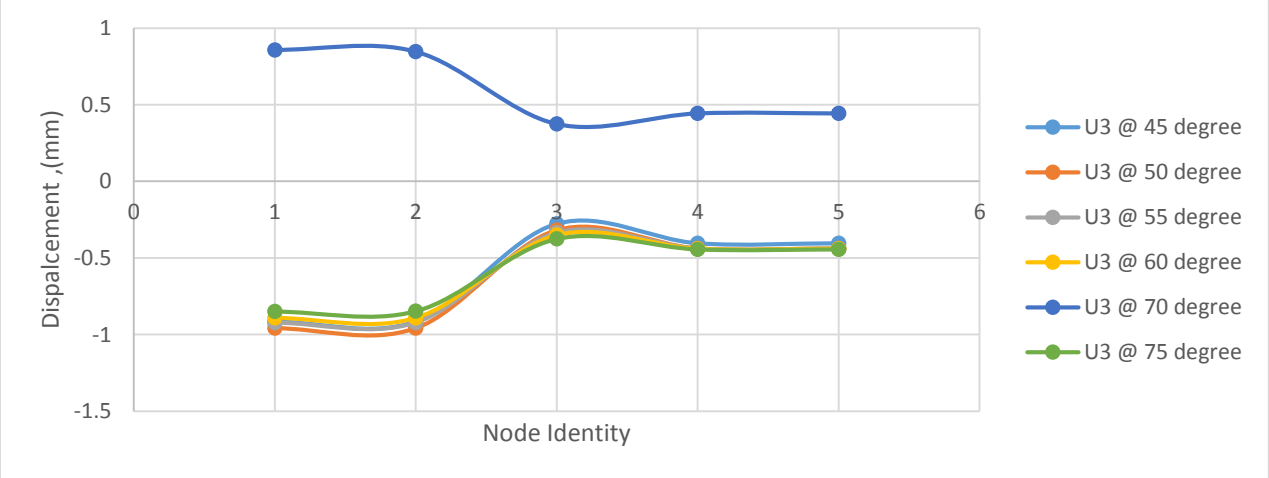

Figure 5.5: Element M Horizontal and vertical displacement at various angles of attack

5.3.3. Element K with wind speed of 16.11m/s

As previously discussed in section 5.1, the element ‘K’ is composed of K1, K2, K3 and K4. These were analysed individually at different angles of attack and the displacements for 16.11 m/s are presented in Figure 5.6 below. It was noticed that the elements K1 and K4 were critical with higher values of horizontal and vertical displacements in both X and Y direction, because of the fact that both were fully exposed to wind flow and not shielded by any element; K2 and K3 elements yielded lower displacement values because of the fact that they were not fully exposed to wind loads as compared to K1 and K4 which are external frames and prone to more displacement by wind load. In this case, sub element K1, K2, K3 and K4 were investigated for critical response whereby the estimated wind load in both directions were applied with respect to inclination angle and the displacements result table in each direction for each sub element was shown in table 5.5 (a-d) respectively**.**

From Figure 5.6 (b) ,element K1 is the most deformed element with highest values of horizontal displacement at inclination of 45 due to the fact that it was fully exposed to wind load as compared to K2 and K3 which are shielded with other elements. On the other hand K2 and K3 yielded more vertical displacement due to concentration area of the solar panel.

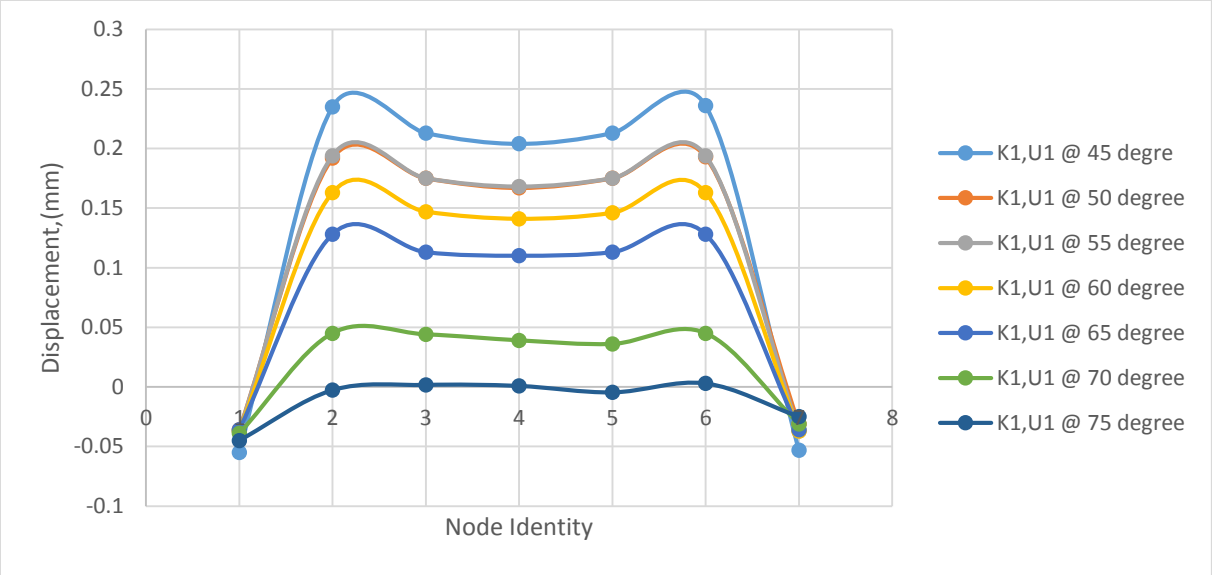

Figure 5.6: a) Horizontal displacements of K1 element for various angle of attack

Moreover, from the above analysis, it was revealed that sub-element K1 and K4 at 45 ° were pruned to more damage by wind load in horizontal direction as these elements directly faced the flow of wind. The displacements obtained for these two elements ranging from inclination angle 45^0 to 78^0 are presented in case 10 and 11 for both horizontal and vertical direction. Figure 5.14 and 5.16 shown below depicted that these two sub element K are only affected by the wind load in horizontal direction with translational displacement of 0.25mm and 0,15mm for K1 and K4 respectively.

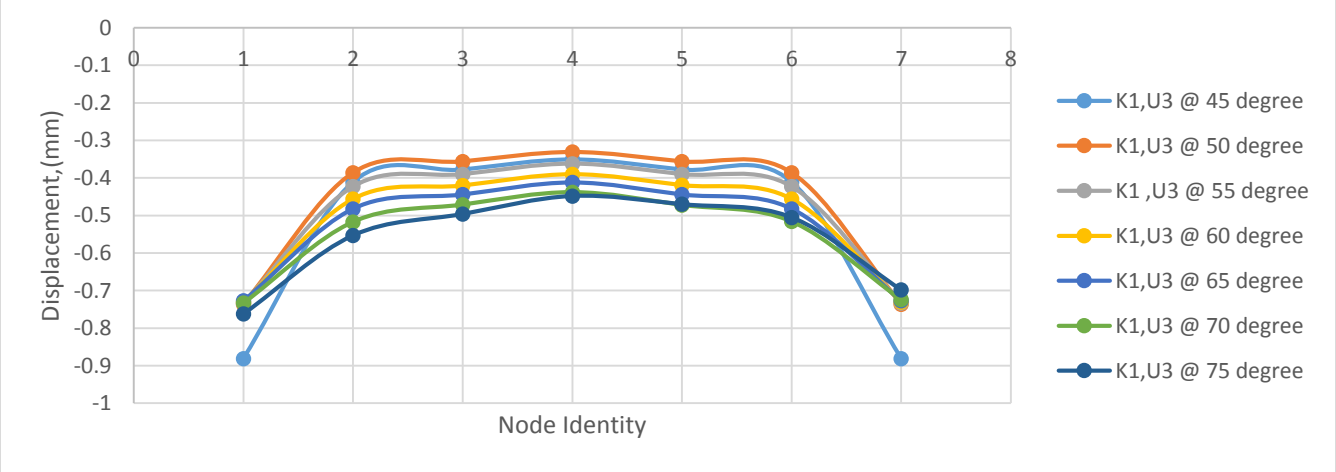

Figure 5.6: b) Vertical displacements of K1 element for various angle of attack

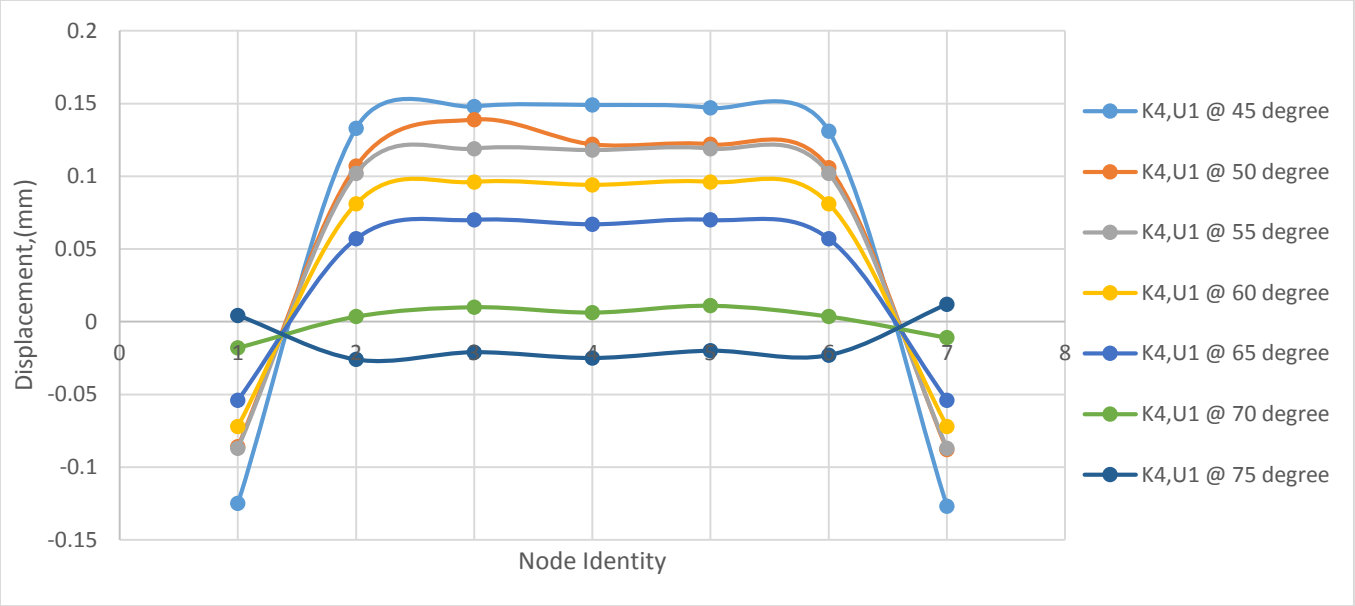

Figure 5.6: c) Horizontal displacements of K4 element for various angle of attack

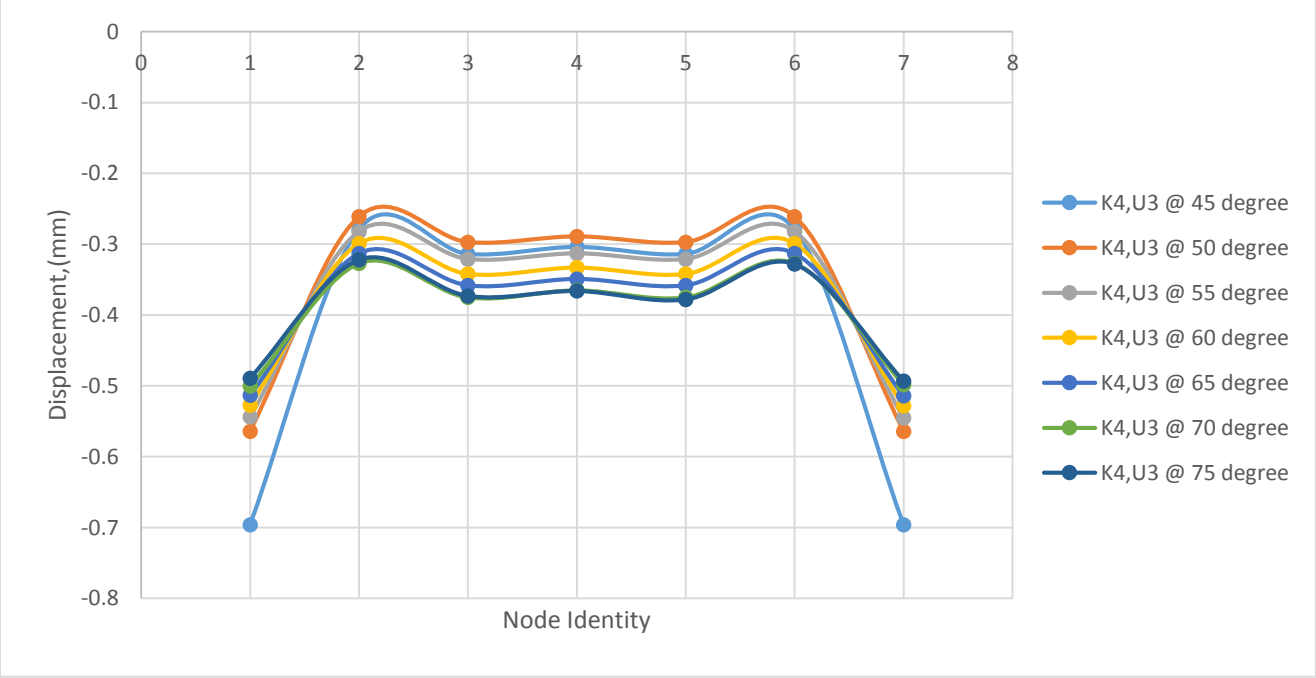

Figure 5.6: d) Vertical displacements of K4 element for various angles of attack

5.4 Modal Analysis

The dynamic wind load would affect the structural response of the structure and the frequencies for different intensities of the drag and lift forces change, especially for higher vibration modes, where the natural frequencies of the structure do not have a dominant contribution. Considering the natural wind speed record for which the maximum wind speed was recorded as 16.11 m/s, the modal analysis of the FE model was conducted for 8 cases of different inclination angles. For a broader interpretation, the 8 cases are reported in Appendix B, while in the current chapter only the modal analysis of the tracker inclined at 45^0 and 78^0 are reported.

Case 1: Stress deformed mode shapes for the tracker at 45^0 and 16.11m/s

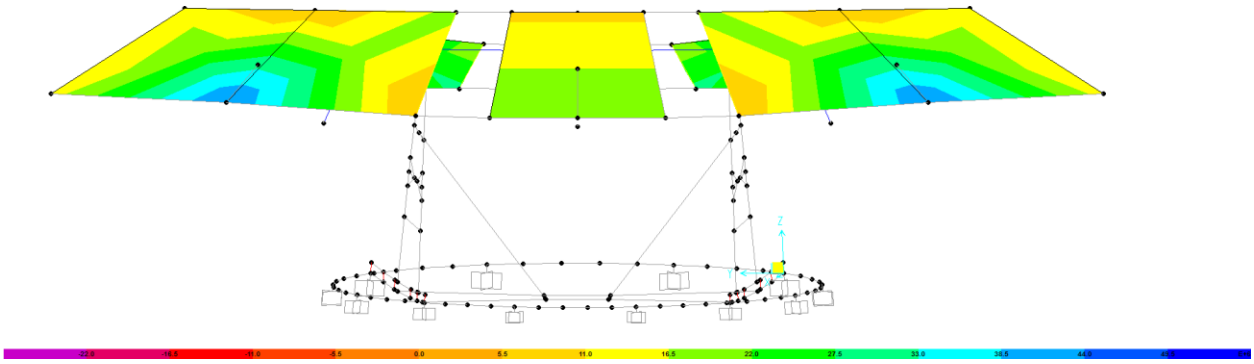

Figure 5.7 First vibration mode (f = 3.99 Hz) for solar tracker at 45^0 and 16.11 m/s

Figure 5.7 represents the vibration mode of the solar tracker inclined at 45^0, under the effect of 16 .11 m/s. Mostly the PV solar panels would respond in the frequency range of 3.99 Hz to 21 Hz, as shown in Table 5.6, and the actual frame of the supporting structure did not show any response for this frequency interval. The deformations of the vibration mode shown in Figure 5.7 are represented for the stress magnitude developed in the PV solar panel.

Table 5.6. Modal properties and frequencies for 45° at 16.11 m/s

StepNum	Period	Frequency	CircFreq	Eigenvalue	Natural frequency
	Sec	Cyc/sec	rad/sec	rad^2/sec^2	Hz
1	0.250825	3.99E+00	2.51E+01	6.28E+02	3.99
2	0.188363	5.31E+00	3.34E+01	1.11E+03	5.31
3	0.161819	6.18E+00	3.88E+01	1.51E+03	6.18
4	0.132368	7.55E+00	4.75E+01	2.25E+03	7.56
5	0.124919	8.01E+00	5.03E+01	2.53E+03	8.01
6	0.10817	9.24E+00	5.81E+01	3.37E+03	9.25
7	0.084325	1.19E+01	7.45E+01	5.55E+03	11.86
8	0.07895	1.27E+01	7.96E+01	6.33E+03	12.67
9	0.073647	1.36E+01	8.53E+01	7.28E+03	13.58
10	0.069863	1.43E+01	8.99E+01	8.09E+03	14.32
11	0.058167	1.72E+01	1.08E+02	1.17E+04	17.20
12	0.046676	2.14E+01	1.35E+02	1.81E+04	21.43

Case 8: Stress deformed mode shapes for the tracker at 78° and 16.11m/s

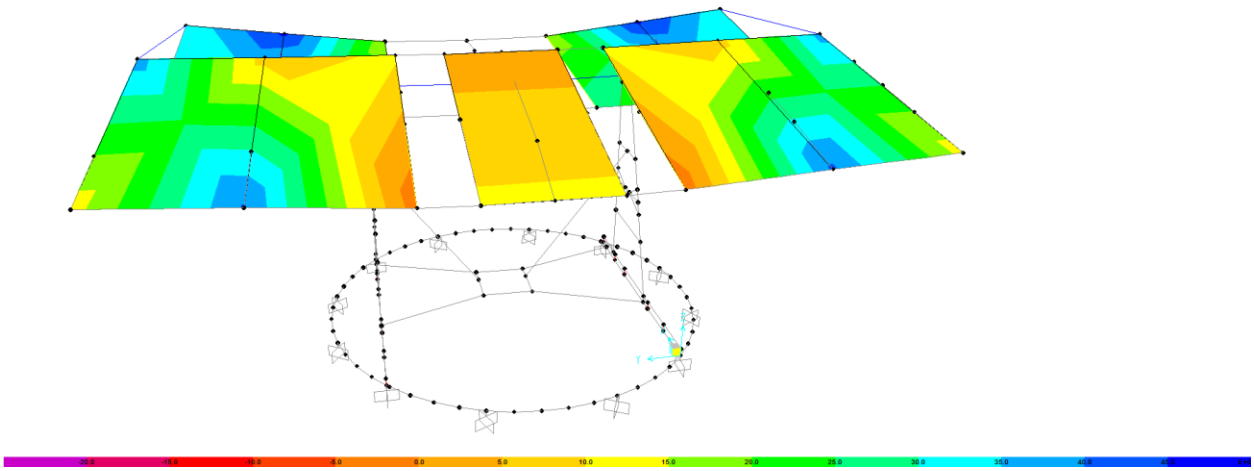

Figure 5.8 First vibration mode (f = 3.93 Hz) for solar tracker at 78° and 16.11 m/s

The case 8 represents the solar panel inclined at 78° and under the effect of 16.11 m/s. The 78° is the closest to the horizontal line and thus parallel to the wind flow; this inclination is considered the safest angle and is employed during the night, when the tracker cannot be controlled. Figure

5.8 shows a similar evolution for the first vibration mode of the solar tracker, however in this case the panels on the second row are more deformed and present higher stresses that nor the case of 45^0. The overall frequencies ranged between the 3.93 Hz and 21.3 Hz.

Table 5.7. Modal properties and frequencies for 78° at 16.11 m/s

StepNum	Period	Frequency	CircFreq	Eigenvalue	Natural frequency
	Sec	Cyc/sec	rad/sec	rad2/sec2	Hz
1	0.254675	3.93E+00	2.47E+01	6.09E+02	3.93
2	0.184893	5.41E+00	3.40E+01	1.15E+03	5.41
3	0.161279	6.20E+00	3.90E+01	1.52E+03	6.20
4	0.133745	7.48E+00	4.70E+01	2.21E+03	7.48
5	0.122798	8.14E+00	5.12E+01	2.62E+03	8.15
6	0.093266	1.07E+01	6.74E+01	4.54E+03	10.73
7	0.089194	1.12E+01	7.04E+01	4.96E+03	11.21
8	0.072008	1.39E+01	8.73E+01	7.61E+03	13.89
9	0.071463	1.40E+01	8.79E+01	7.73E+03	14.00
10	0.067849	1.47E+01	9.26E+01	8.58E+03	14.74
11	0.062494	1.60E+01	1.01E+02	1.01E+04	16.01
12	0.046962	2.13E+01	1.34E+02	1.79E+04	21.30

By identifying the modal properties for all the 8 cases, for angles between 45^0 to 78^0, it could be concluded that the frequency determined by the wind-induced force within the first six vibration modes, was ranging between 3.93 Hz to 11.33 Hz, which are in good agreement with the simulation results for the solar tracker reported by Chih et al (2014), with frequency values ranging between 3.85 Hz and 11.4 Hz.

By comparing the natural frequencies and the mode shapes for all the angles of attack investigated (Figure 5.8 below) it was noticed that in general the first five vibration modes have a constant evolution, probably because the natural vibrations of the solar tracker structure have a dominant contribution for the first vibration modes. Starting with mode six of vibration it was noticed that the higher angles would develop lower frequency of response, especially for the last vibration modes, for which the frequencies increase for angles up to 50^0, and declined thereafter for higher angles up to 78^0. This proves that the angles up to 50^0 can be considered more critical, while the angles between 55^0 to 78^0 can be considered more stable and thus on the within the safety limits.

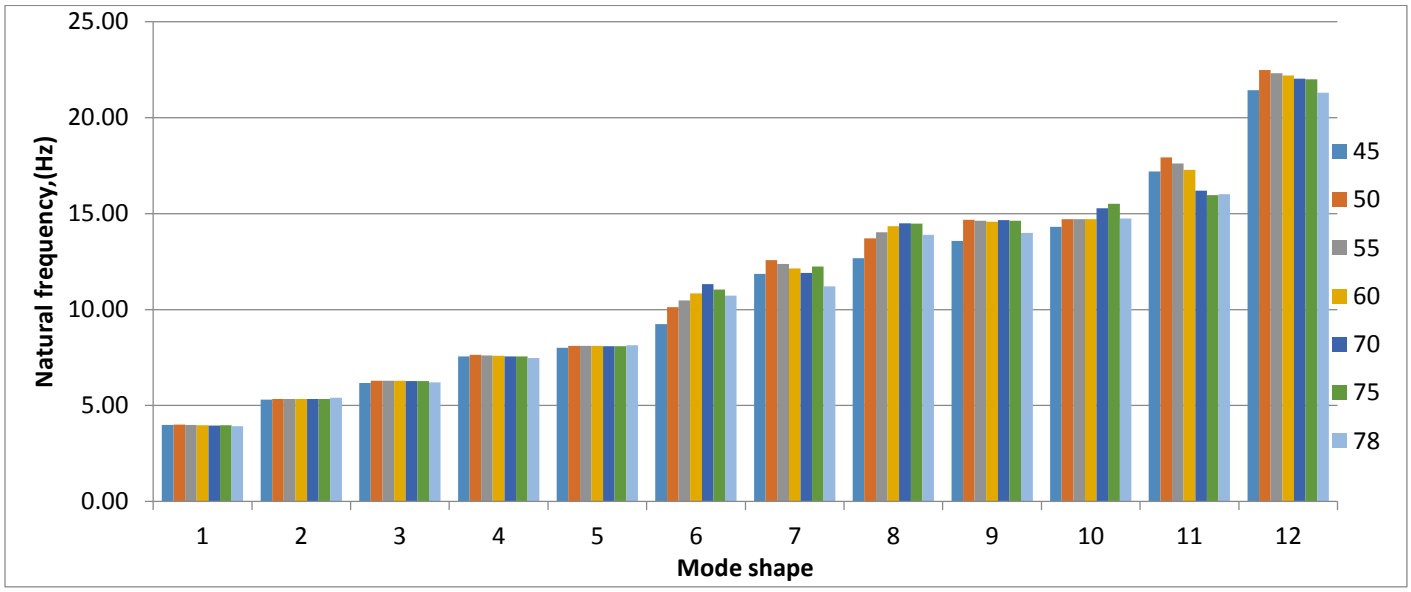

Figure 5.9 Mode shapes and natural frequencies for each angle of attack

5.5 Experimental Investigation Results

In other to determine the wind-induced displacement determined for the dual-axis solar tracker, the upper parts (Elements 'K' and 'M') and the main body of the structure (Element 'A') were instrumented with uniaxial and biaxial strain gauges, at critical locations along these elements. Different cases of inclination angles were tested each day, as shown in the Table 5.9 below to ascertain the effect of wind load directionality on the solar tracker.

Table 5. 8 Experimental Cases Investigated.

Case	**Rotation Angle (^{0})**	**Inclination Angle(^{0})**
Case 1	30	45
Case 2	60	50
Case 3	90	55
Case 4	120	60
Case 5	150	65
Case 6	180	70
Case 7	210	75

The experimental results determined for the instrumented structural elements were discussed in the following section of this thesis, for each critical element.

Element M

The element M of the solar tracker is the steel circular beam with span length of 4.01 meter which, carries and orients the PV panel at desired inclination angles. This element was pivoted on the two elements 'A' at 500 mm from both ends. This was instrumented symmetrically with 2 biaxial strain sensors installed at 600 mm from both ends of element M and 2 uniaxial sensors placed at 1000 m away from each biaxial sensors. Because each of the biaxial sensors produced 2 stress values, a total number of six sensor values were recorded for all the cases. Therefore 7 cases were considered in the experimental investigation with respect to inclination angle ranging from 45^0 to 78^0. For each of these angles, the effect of the same intensity of wind speed at night was also examined for verifying the stability of the safe position. Each case was tested for different wind speeds recorded

at Ottawa international airport and only 3 critical cases were fully discussed here, while the rest of the test cases were presented in Appendix D.

Case 1: Element M at 45º and maximum wind speed of 4.17m/s

The first Case investigated was for the solar tracker placed at 45º inclination angle, with the recorded wind speed of 4.17m/s which occurred on February 10th 2015.The two uniaxial sensors were installed at 60cm from both ends of the element, the first biaxial sensor was installed at distance of 100cm from first uniaxial sensor and last biaxial sensor located 100cm from second uniaxial sensor. From the figure 5.10 below it was noticed that all the stresses imposed by the wind load on the element M at instrumented locations on the element have similar load pattern and there is a high fluctuation in the stresses registered at this angle of attack, depending on the position along the M bar. However, the magnitude of the recorded stress lies between 7.14×10^7E Pa and 7.56×10^7 Pa.

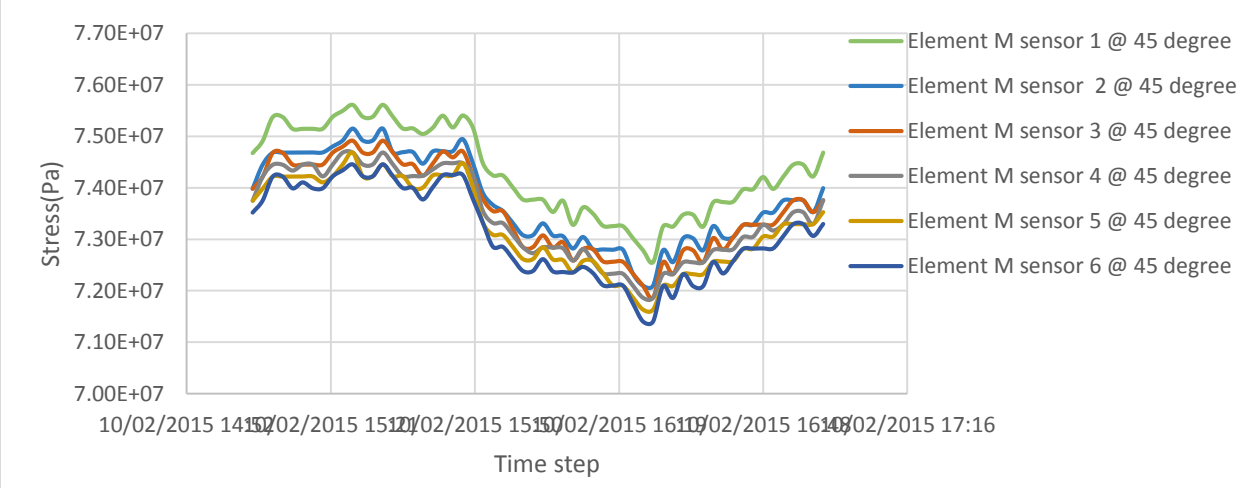

Figure 5.10. Recorded stresses for the element M at 45 and 4.17 m/s

Case 2: Element M at 55º and maximum wind speed of 10.27 m/s

In this case, the element M was also tested with attack angle 55° and for the maximum wind speed of 10.27 m/s as recorded on the day of 12th February 2015. It was observed that this element was prone to more deformation by the aforementioned wind speed, due to the higher stresses recorded by each sensor along the element. Although, all the sensors indicated a similar behaviour of the element M, because they all produced the same stress pattern as shown in Figure 5.11 below. Higher deformation was noticed where the sensor 1 was installed as this position which was close to the actuator of the tracker which enhances the inclination mechanism of the structure, so higher stress was expected at this location. Because of the higher wind speed, also the fluctuations of the stress developed in the element M have increased. The magnitude of the stress at this angle of attack ranges between 7.88 x 10^7 Pa and 6.77 x 10^7 Pa.

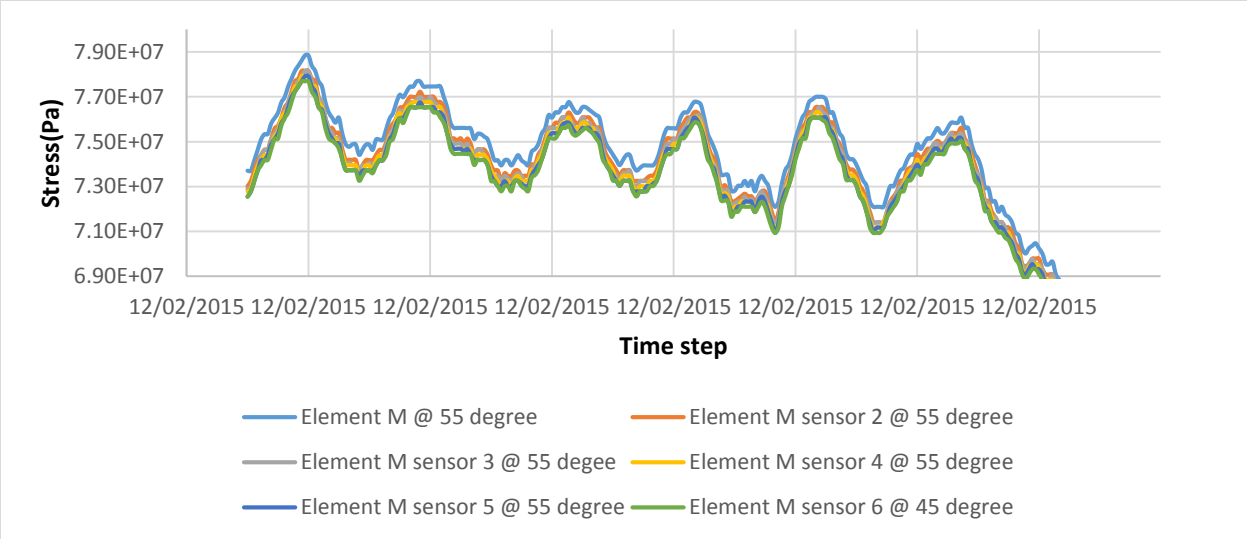

Figure 5.11. Recorded stresses for the element M at 55 and 10.27 m/s

Case 3: Element M at 78º and wind maximum speed of 10.27m/s

Structural stability of element M at stow position was investigated for the maximum wind speed for which the element was tested at 55 degrees. This stow position was believed to be the safest inclination angle, as claimed by the tracker manufacturer, irrespective of the wind intensity and direction of the wind. On the night of 12th February 2015, the tracker was positioned at 78° to ascertain how safe it was under the applied wind speed of 6.15 m/s. Figure 5.12 presented the

stress patterns generated by the sensors installed on this element, with respect to wind intensity at night. However, same stress pattern for all sensors were noticed, high and low fluctuation in stresses observed but only sensor 1 demonstrated the fact that at this location the wind load induced more deformation, because the highest stress values recorded due to load induced by the actuator. The magnitude of the stress for the element at stow position lies between 7.00 x 10^7 Pa and 6.40 x 10^7Pa.

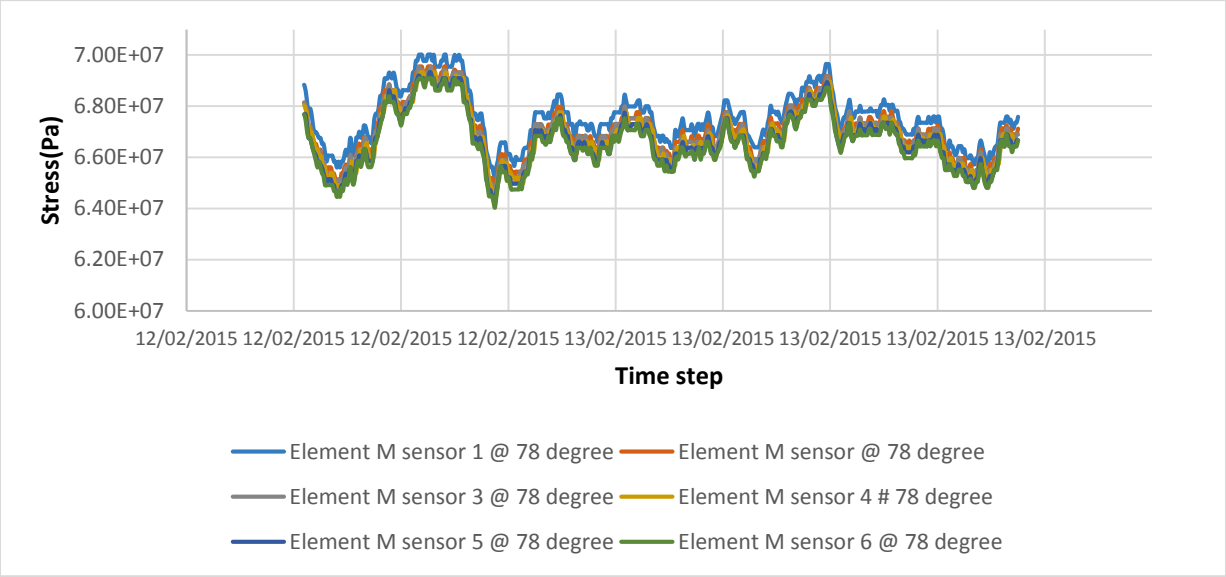

Figure 5.12. Recorded stresses for the element M at 78 and 10.27 m/s

Element A

As previously discussed, elements ‘A’ are the legs which belong to the main part of the tracker that connects both top and bottom part of tracker elements together. This element also provides full structural support to element ‘M’ at 50cm from both top ends. Each of the two elements ‘A’ was instrumented with 2 uniaxial strain gauges located 60cm below the actuator on right and left hand side of the element, making a total of four data points in both elements. The first sensor on element ‘A’ was positioned close to the location of the actuator that performs when the inclined operation of tracker was required. The effect of the wind on the inclination angles were tested.

Case 1: Element A at 45º and maximum wind speed of 4.17 m/s

In this case, the element A was experimented with wind speed of 4.17 m/s, and the stress patterns for all sensors are uniform as shown in figure 5.13 below. It was observed that sensors 3 and 4 on element A produced higher stress values as compared to sensors 1 and 2.The reason behind this is that the element A that was experimented with sensors 3 and 4 was closer to the actuator which impose more stress on this arm, whenever the tracker is inclined and rotated at desire angles. Besides that, despite the fact that the element A was tested under a very low wind speed, still it was not considered a favourable case, due to the inclined angle 45, which also threatens the element's integrity. For sensor 1 and 2, the tress magnitude ranges between 7,38 x 10^7 Pa and 7,07 x 10^7 Pa, while for sensor 3 and 4, the magnitude of stress lies between 7.35 x 10^7 Pa and 7.05 x 10^7 Pa, which are very closer to the stresses registered for element M at a higher wind speed of 10.27 m/s.

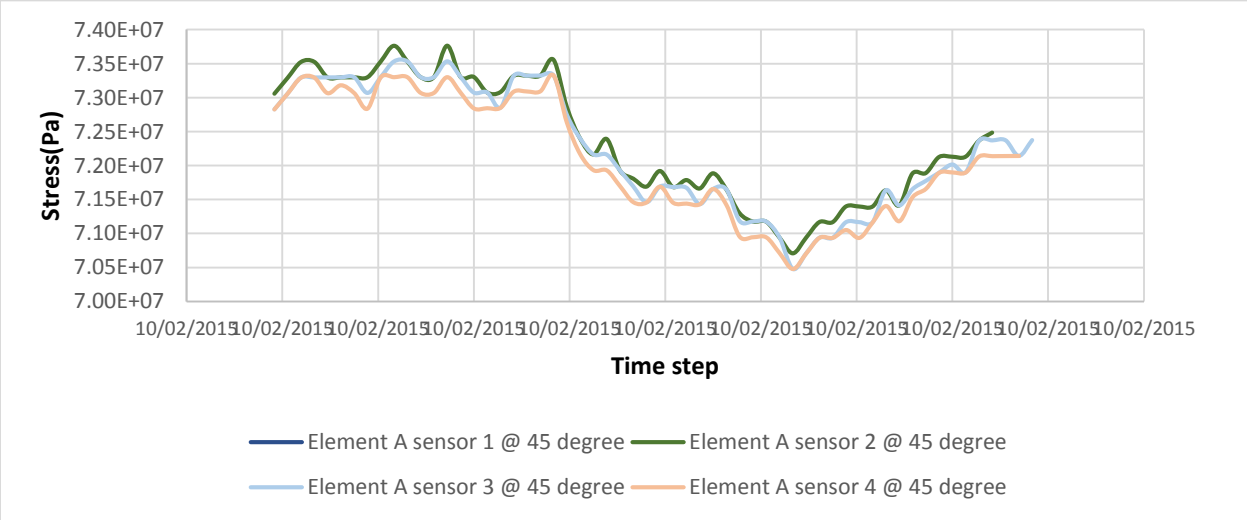

Figure 5.13. Recorded stresses for the element A at 45 and 4.17 m/s

Case 2: Element A at 55º and maximum wind speed of 10.27 m/s

Element A was also experimented at 55 degree inclination due to high wind speed of 10.27 m/s recorded on this day. From the figure 5.14 below, it was noticed that the higher stress values were recorded for all the sensors of the element irrespective of their installed location on the element. Apart from the fact that the element was exposed to high wind speed, the inclination angle also

contributed to the increase in the stress. In other words, this angle added more impact to the high wind speed effect on the element. However, high and low stress fluctuations was recoded with maximum magnitude of 7.70 x 10^7Pa and minimum magnitude of 6.67 x 10^7 Pa.

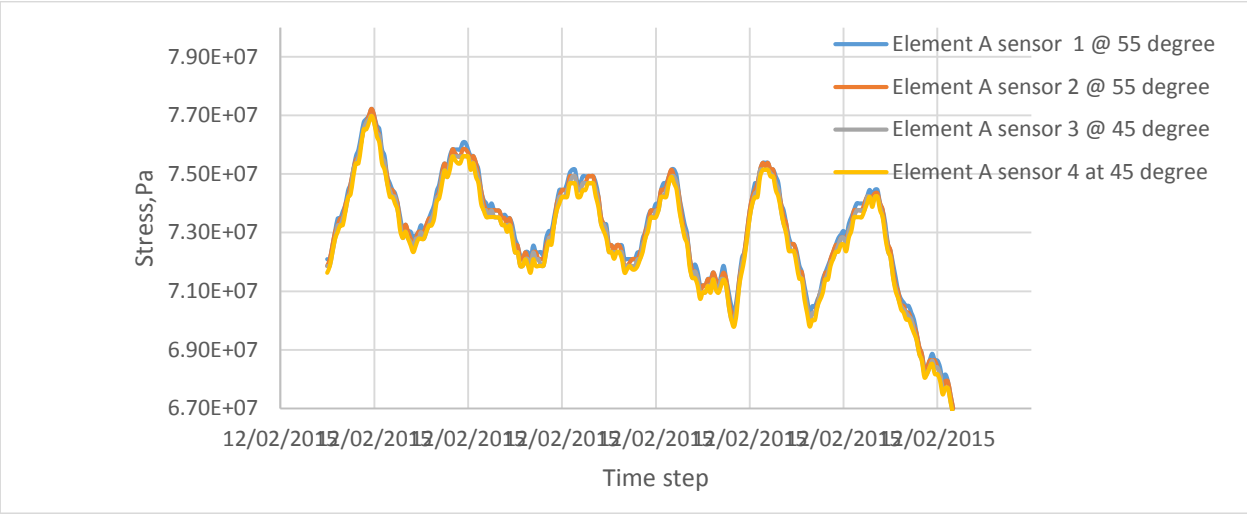

Figure 5.14. Recorded stresses for the element A at 55 and 10.27 m/s

Case 3: Element A at 78º(stow position) and maximum wind speed of 10.27 m/s

At night of the recorded high wind speed mentioned in case 2, the tracker was repositioned from 55° attack angle to stow position (78°) and experimented the same wind speed of 10.27 m/s .It was noticed that the stress recorded under this scenario had a uniform pattern and the magnitude of stress produced by each sensor was greatly reduced under the same wind speed. However, the intensity of wind flow at stow position is minimal as compared to 55° inclination.

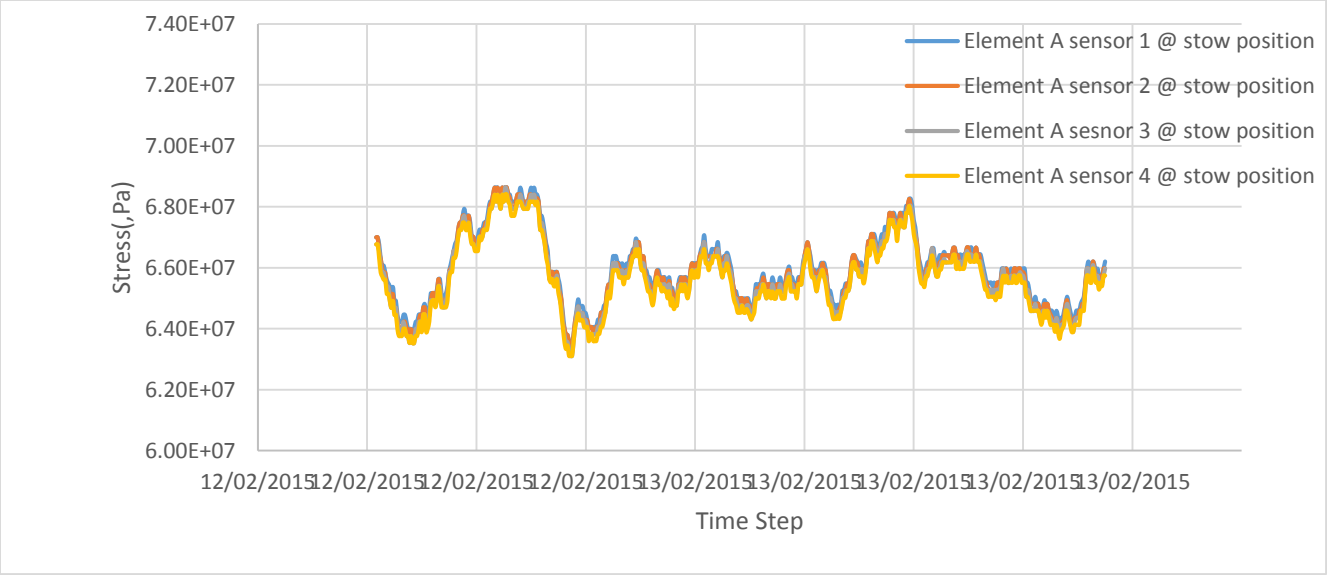

Figure 5.15. Recorded stresses for the element A at 78 and 10.27 m/s

Element K

Element K provides the structural support to the PV module and exists along the upper and lower arms of the suspended solar panel. Each of this elements was instrumented with one uniaxial strain sensor located at 50cm from the left end of each element (dominant wind direction), making a total number of 4 sensors. This element was made of aluminum which was responsible for the reduction changes the Young modulus used for the computation of stress. As presented for other 2 elements, the effect of wind load on attack angle 45°, 55° and 78° were studied and presented.

Case 1: Element K at 45° and maximum wind speed of 4.17 m/s

In the first case, the element was experimented with low wind speed of 4.17 m/s as recorded on February 10th 2015 at inclined angle 45°. It was noticed from figure 5.16 below that all the sensors of this element exhibited the same stress pattern in close range with the stress magnitude between 2.15 x 10^7 Pa and 2.68 x 10^7Pa

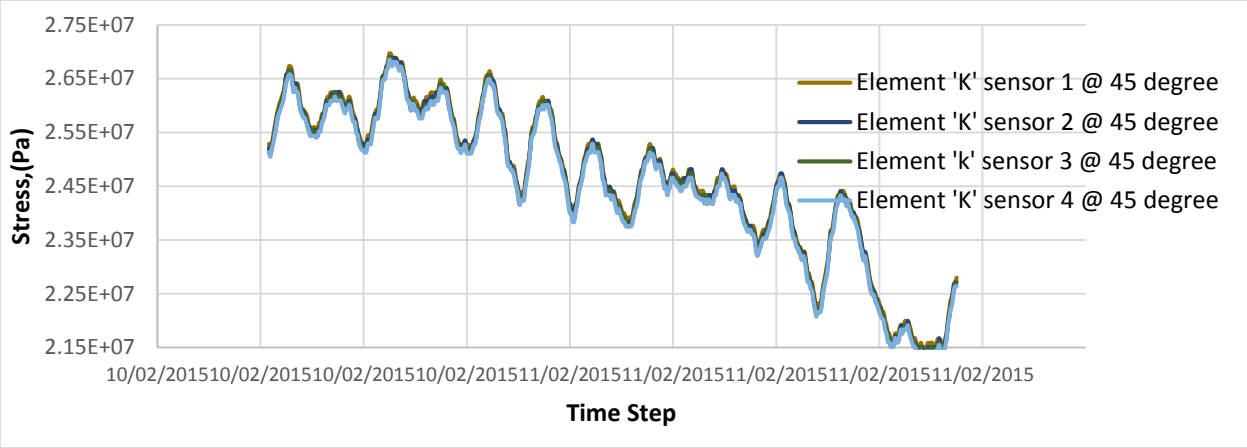

Figure 5.16. Recorded stresses for the element K at 45 and 4.17 m/s

Case 2: Element K at 55° and maximum wind speed of 10.27 m/s

In this case, the element was tested at inclination angle 55° under maximum wind speed as other element described in the above section. It was noticed that this angle imposed more stress on the element as the magnitude of the stress ranges between 2.32 x 10^7 Pa and 2.67 x 10^7Pa . However, the high and low stress fluctuations noticed were uniform as presented in figure 5. 17.

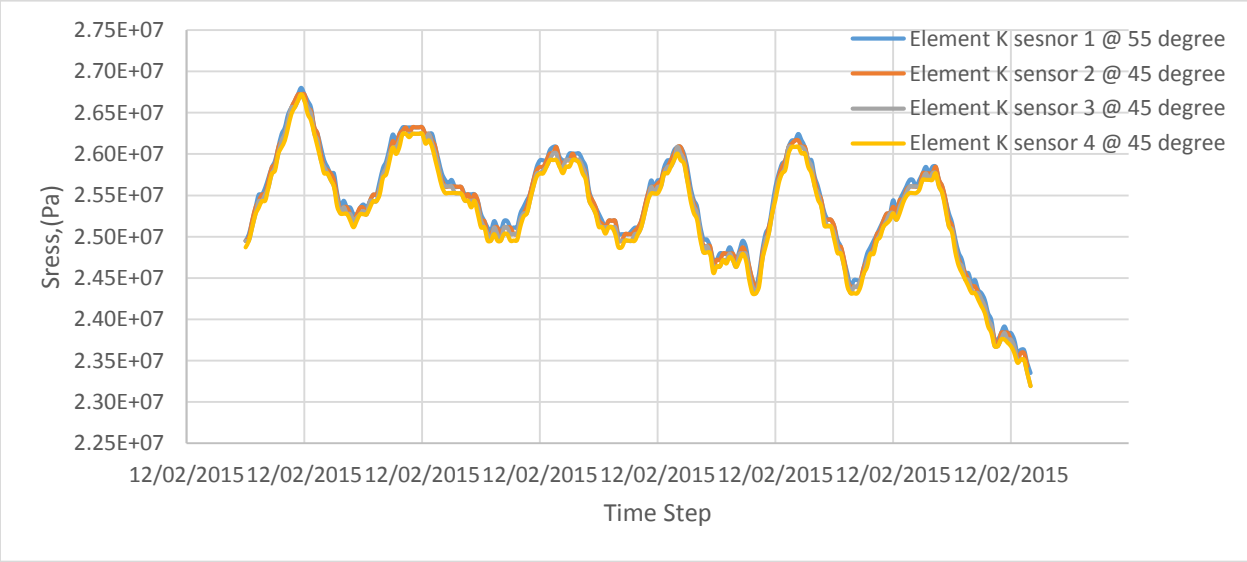

Figure 5.17. Recorded stresses for the element K at 55 and 10.27 m/s

Case 3: Element K at 78º (stow position) and maximum wind speed of 10.27 m/s

In this case, the tracker inclination angle was adjusted to the stow position and was still exposed to high wind speed at night. It was observed that the sensors produced same stress pattern regardless of the location of each sensor and the magnitude of stress recorded with the same high wind speed was lower, as compared to the inclined angle 55° described in case 2. The magnitude of stress in this case spans between 2.19 x 10^7Pa and 2.38 x 10^7 Pa.

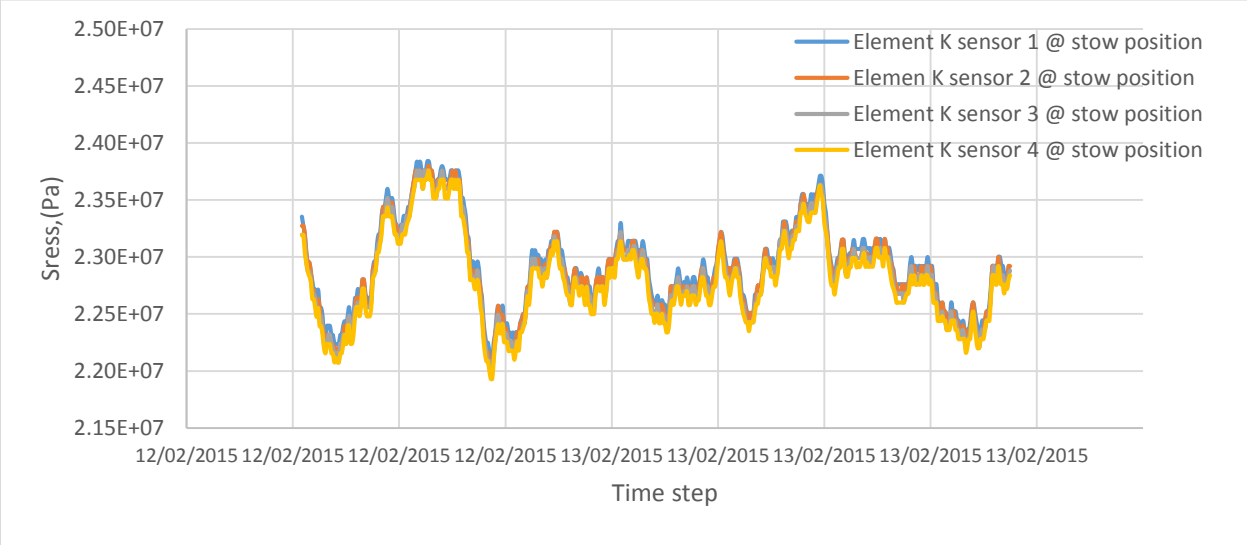

Figure 5.18 Recorded stresses for the element K at 78 and 10.27 m/s

From the above analysis, it was obvious that Element M (circular beam) appeared to be the most critical element of the tracker as it demonstrated high value of the stress regardless of the inclination angle and exposed intensity of wind speed.

5.6. Tracker elements stress analysis

As previously discussed in the above section, the tracker consists of 3 parts: upper part, main body and the lower part. Since we are concerned with the effect of the wind on the structure at different inclination angles, this experimental investigation focused on the wind-induced displacement of the upper and main body of the tracker, which are the important part of tracker vulnerable to wind damage in any direction. In this regard, the upper part of the tracker (element K and M) and main body of the tracker were instrumented with uniaxial and biaxial strain sensors for strain computation and the resulted strain were used in computing the stress along each member. The stress of each element sensors were computed using hook's law

Only 7 cases of inclination angles were investigated on the dual axis tracker as presented in table 5.10, with recorded daily average wind speed presented in table 5. 12, because for the rest of the cases the wind speed was not sufficiently strong, for the tracker to register displacements. The tracker was rotated and inclined at presented days between 9:00 a.m. and 5:00 p.m. with the help of the GS Golden tracker software as described in the previous chapter.

Table 5.9.Experimental Cases Investigated.

Case	**Rotation Angle (°)**	**Inclination Angle(°)**
Case 1	30	45,50.55,60.65.70.75
Case 2	60	45,50.55,60.65.70.75
Case 3	90	45,50.55,60.65.70.75
Case 4	120	45,50.55,60.65.70.75
Case 5	150	45,50.55,60.65.70.75
Case 6	180	45,50.55,60.65.70.75
Case 7	210	45,50.55,60.65.70.75

As stated above, the stress of each element sensors were computed using Hook's law represented by equation 5.1.

$$\sigma = \gamma * \mu\varepsilon \qquad \text{[Eq 5.1]}$$

γ= Young modulus of the material

σ=Stress, (Pa or N/m^2)

$\mu\varepsilon$ = microstrain

Where the Young modulus of the element material and the micro strain computed in the previous chapters were employed. The Young modulus used for each elements differs because of the fact that they are not made of the same material. Element A and M are made of steel and element K was made of aluminum, so the Young modulus of steel and aluminum are 2×10^{11} N/m^2 and 7×10^{10} N/m^2 respectively. Table 5.12 presents the average sensors' stresses of each element with respect to inclination angle.

Table 5.10 Average Wind Speed

Date	Average Wind Speed(m/s)
10-Feb	4.17
11-Feb	4.49
12-Feb	6.15
13-Feb	4.38
14-Feb	4.88
17-Feb	2.19
19-Feb	7.36
20-Feb	6.53

Table 5.11. (a) Element '**M'** Day light Sensors' stresses

	Day light Sensor Stresses(Pa)				
Inclination angle(°)	(Date)2015	1	2	3	4
45	10-Feb	5.72E+07	5.71E+07	5.70E+07	5.69E+07
50	11-Feb	7.09E+07	7.07E+07	7.06E+07	7.05E+07
55	12-Feb	7.31E+07	7.30E+07	7.29E+07	7.28E+07
60	13-Feb	6.42E+07	6.41E+07	6.40E+07	6.39E+07
65	14-Feb	6.70E+07	6.69E+07	6.68E+07	6.66E+07
70	17-Feb	6.60E+07	6.59E+07	6.57E+07	6.56E+07
75	19-Feb	6.49E+07	6.48E+07	6.47E+07	6.45E+07

Elements ‘A1’ and ‘A2’ provides full support to the rotating element ‘M’. Each of elements ‘A’ was instrumented with 2 uniaxial strain gauge. The first element ‘A’ was positioned close to where the actuator that perform the inclined operation of tracker was installed.

Table 5.12 a) presents the result of daylight stress analysis performed on element ‘A’ at different angle of inclinations ranging from 45° to 75°, which represent the operational angle of the tracker element. Resulted strain values from experimental investigation with the young modulus of the steel were employed in the stress computation. It is observed that at all the attack angles, sensor 1 recorded maximum stress value while sensor 4 produced the lowest. Also, sensors 1 and 2 exhibited higher average stress values which might be due to the fact that they are installed at the side where actuator that enhance the inclination of the panel operates, so the actuator imposed more stress on this arm of the element at all the inclination angles. Moreover, the highest stress were recorded at attack angle 55° for all sensors due to the fact that the intensity of wind was high on this day as shown in table 5.11 and the inclined angle imposed more risk to the element A. On 19th of February, much higher wind speed was recorded, as shown in the table 5.11, but because of the fact that the attack angle for this day is closer to the safe position, then smaller stresses were recorded as compared to 12th February, when the average wind speed was 6.15 m/s but the inclination angle posed more treat on the element. However, from Table 5.12 (b), it was shown at all night of considered inclination angles, the element was exposed to more wind intensity at night despite the fact that it was in safe position (78°), and higher values of stress were still recoded.

Table 5.11 (b) Element ‘A’ overnight sensors ‘stresses

		Overnight Sensor Stresses(Pa)			
Inclination angle(°)	(Date)2015	1	2	3	4
45	10-Feb	7.09E+07	7.07E+07	7.06E+07	7.05E+07
50	11-Feb	7.21E+07	7.20E+07	7.19E+07	7.17E+07
55	12-Feb	6.60E+07	6.58E+07	6.57E+07	6.56E+07
60	13-Feb	5.92E+07	5.90E+07	5.89E+07	5.88E+07
65	14-Feb	6.58E+07	6.57E+07	6.56E+07	6.55E+07
70	17-Feb	6.83E+07	6.82E+07	6.81E+07	6.80E+07
75	19-Feb	6.71E+07	6.70E+07	6.68E+07	6.67E+07

Element ‘K’ directly provides support to the PV modules, 2 of this element support the upper and lower arms of the PV panels mounted on n top of the solar tracker and each of this elements was

instrumented with one uniaxial strain sensor. Since this element is made of aluminium, lower stress values were recorded for each angle of attack as compared to the element 'A' which was made of steel due to the influence of young modulus of the material. As presented in table 5.12 (c), Sensors 1 and 2 produced higher stress values at all angles because they are located at dominant wind direction as compared to sensor 3 and 4. Moreover, the maximum wind speed was recorded on 12th of February at inclined angle 55^{0}, this higher wind intensity during the day have great impact on the element because the stresses on this day were noticed to be the highest among all inclination angle cases tested, which shows that the element at this inclination angle is vulnerable to damage induced by wind load. However, the element registered more stresses at stow position, at night as shown in table 5.11d) despite the fact that the stow position is considered safe.

Table 5.11 (c) Element 'K' Day light Sensors' stresses

	Day light Sensor Stresses(Pa)				
Inclination angle(^{o})	(Date)2015	1	2	3	4
45	10-Feb	1.99E+07	1.99E+07	1.98E+07	1.98E+07
50	11-Feb	2.46E+07	2.46E+07	2.45E+07	2.45E+07
55	12-Feb	2.54E+07	2.54E+07	2.53E+07	2.53E+07
60	13-Feb	2.23E+07	2.23E+07	2.22E+07	2.22E+07
65	14-Feb	2.33E+07	2.32E+07	2.32E+07	2.32E+07
70	17-Feb	2.29E+07	2.29E+07	2.29E+07	2.28E+07
75	19-Feb	2.25E+07	2.25E+07	2.25E+07	2.24E+07

Table 5.11d) Element ‘K’ overnight sensors ‘stresses

		Overnight Sensor Stresses(Pa)			
Inclination angle(°)	(Date)2015	1	2	3	4
45	10-Feb	2.46E+07	2.46E+07	2.45E+07	2.45E+07
50	11-Feb	2.50E+07	2.50E+07	2.50E+07	2.49E+07
55	12-Feb	2.29E+07	2.29E+07	2.28E+07	2.28E+07
60	13-Feb	2.06E+07	2.05E+07	2.05E+07	2.05E+07
65	14-Feb	2.29E+07	2.28E+07	2.28E+07	2.27E+07
70	17-Feb	2.37E+07	2.37E+07	2.37E+07	2.36E+07
75	19-Feb	2.33E+07	2.33E+07	2.32E+07	2.32E+07

Element M

The element M is the steel circular beam with span length of 4.01 m, which rotates vertically to orient the PV panels mounted on top, at the optimum inclination angle. This element was pivoted on element ‘A’ at 500 mm from both ends. The 2 biaxial strain sensors installed at 600 mm from both ends and the 2 uniaxial sensors placed at 1 m away from each biaxial sensors recorded the stress for all investigated cases, as shown in table 5.11 (e). A number of 7 cases were considered for reporting the experimental results for inclination angle ranging from 45° to 78°. For each of these cases, the effect of the wind speed intensity at night was also examined for analysing the stability of the stow position. It was noticed that at angle 50°, the element experienced more deformation during the day, despite the fact that the wind speed was considerably low but thus this angle was not stable enough to resist even low wind velocities. However, at 55° angle of attack, the element was highly vulnerable to wind damaged because of higher stresses determined by the wind speeds recorded on this. Additionally, on 19th of February, a higher wind intensity was recorded which also determined the higher value of the stress but this did not have significant impact on the element as compared to angle 50°.

Table 5.11 e) Element 'M' Day light Sensors' stresses

Inclination angle(°)	(Date)2015	Day light Sensor Stresses(Pa)					
		1	2	3	4	5	6
45	10-Feb	5.86E+07	5.82E+07	5.81E+07	5.80E+07	5.79E+07	5.78E+07
50	11-Feb	7.26E+07	7.20E+07	7.19E+07	7.18E+07	7.16E+07	7.15E+07
55	12-Feb	7.48E+07	7.43E+07	7.41E+07	7.40E+07	7.39E+07	7.37E+07
60	13-Feb	6.58E+07	6.53E+07	6.52E+07	6.50E+07	6.49E+07	6.48E+07
65	14-Feb	6.87E+07	6.81E+07	6.80E+07	6.78E+07	6.77E+07	6.76E+07
70	17-Feb	6.77E+07	6.72E+07	6.70E+07	6.69E+07	6.68E+07	6.66E+07
75	19-Feb	6.65E+07	6.59E+07	6.58E+07	6.57E+07	6.56E+07	6.55E+07

Table 5.11 f) Element M overnight Sensors 'stresses

Inclination angle(°)	(Date)2015	Overnight Sensor Stresses(Pa)					
		1	2	3	4	5	6
45	10-Feb	7.26E+07	7.21E+07	7.19E+07	7.18E+07	7.16E+07	7.15E+07
50	11-Feb	7.38E+07	7.32E+07	7.29E+07	7.29E+07	7.28E+07	7.27E+07
55	12-Feb	6.75E+07	6.71E+07	6.69E+07	6.68E+07	6.67E+07	6.66E+07
60	13-Feb	6.08E+07	6.03E+07	6.02E+07	6.00E+07	5.99E+07	5.98E+07
65	14-Feb	6.74E+07	6.69E+07	6.67E+07	6.66E+07	6.65E+07	6.64E+07
70	17-Feb	7.00E+07	6.95E+07	6.93E+07	6.92E+07	6.91E+07	6.89E+07
75	19-Feb	6.86E+07	6.82E+07	6.80E+07	6.79E+07	6.78E+07	6.77E+07

5.7 Effect of the Inclination Angle on the Elements

From the above section, it was established that for the lower angles the range between 45° and 65° appeared to be the worst scenario angles in term of tracker safety and stability; even at lower wind speeds, these inclination angles threaten to be unsafe as higher stress values were recorded compared to attach angles of 70°,75° and 78°. In the light of this remark, critical inclination angles 45° and 55° for each element were examined in detail.

Case 1: 45° angle of attack

From the figure 5.17 below, it was noticed that at attack angle 45°, both elements 'A' and 'M' have same stress pattern for the same inclination angles. However, the element M is more affected by the wind damage during the day, because all the computed stresses at each instrumented points are higher as compared to element A. The magnitude of stresses on element M ranges between 5.86×10^7 Pa and 5.78×10^7 Pa, while the magnitude of element A stress lies between 5.72×10^7 Pa and 5.69×10^7Pa. Unexpectedly, during the night, for the stow position, the increase in stresses for both elements were observed, as the magnitude of element A ranges between 7.09×10^7 Pa and 7.05×10^7 Pa, while that of element M lies between 7.26×10^7 Pa and 7.15×10^7 Pa.

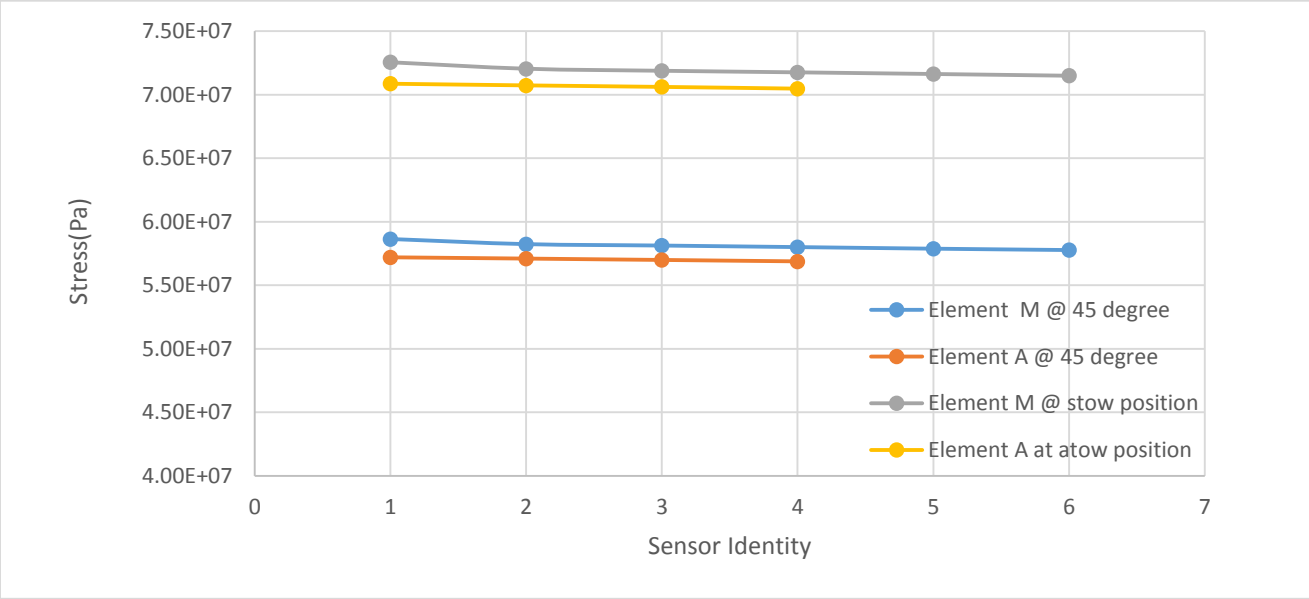

Figure 5.19 Recorded stresses for the elements A and M at 45° and 78°

Moreover, the inclination angle 55° seems to be most dangerous for the tracker positioning according to figure 5.18 below, because both elements produced higher stresses at the instrumented points, which are even greater than that of 45°. Element M produced stress values ranging from 7.48 x 10^7 Pa to 7.37 x 10^7 Pa while element A has higher value of 7.31 x 10^7 Pa and lower value of 7.28 x 10^7 Pa. Figure 5.18 below showed that at 78° which is considered the safe angle, both elements are less affected by the wind load, due to reduction in stress values ranging from 6.75×10^7 Pa to 7.37×10^7 Pa for element M, while these values were greatly reduced in element A with magnitude ranging between 6.60×10^7 Pa and 6.56×10^7 Pa.

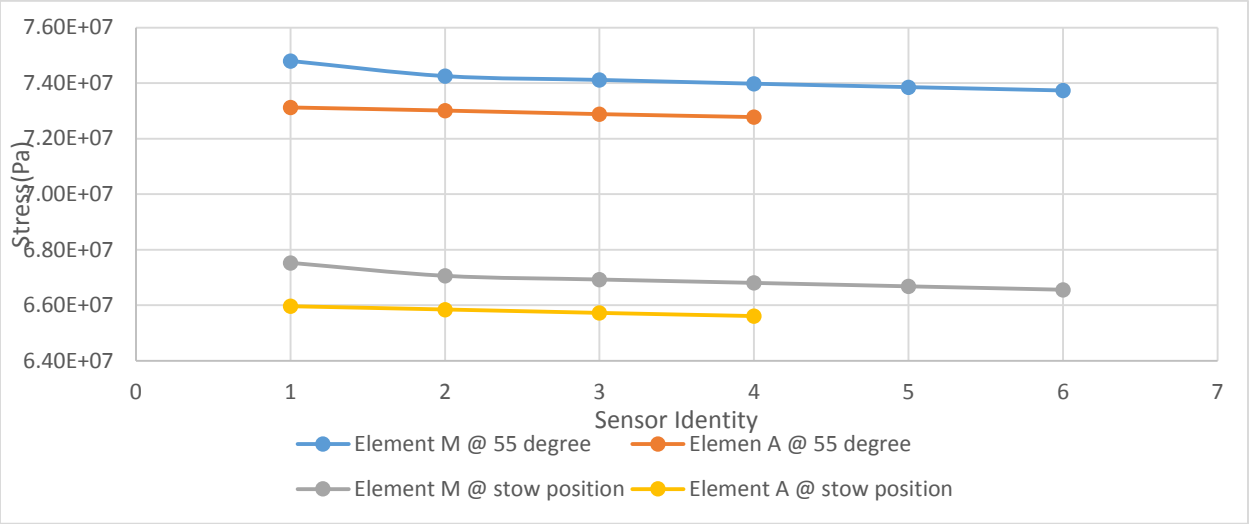

a)

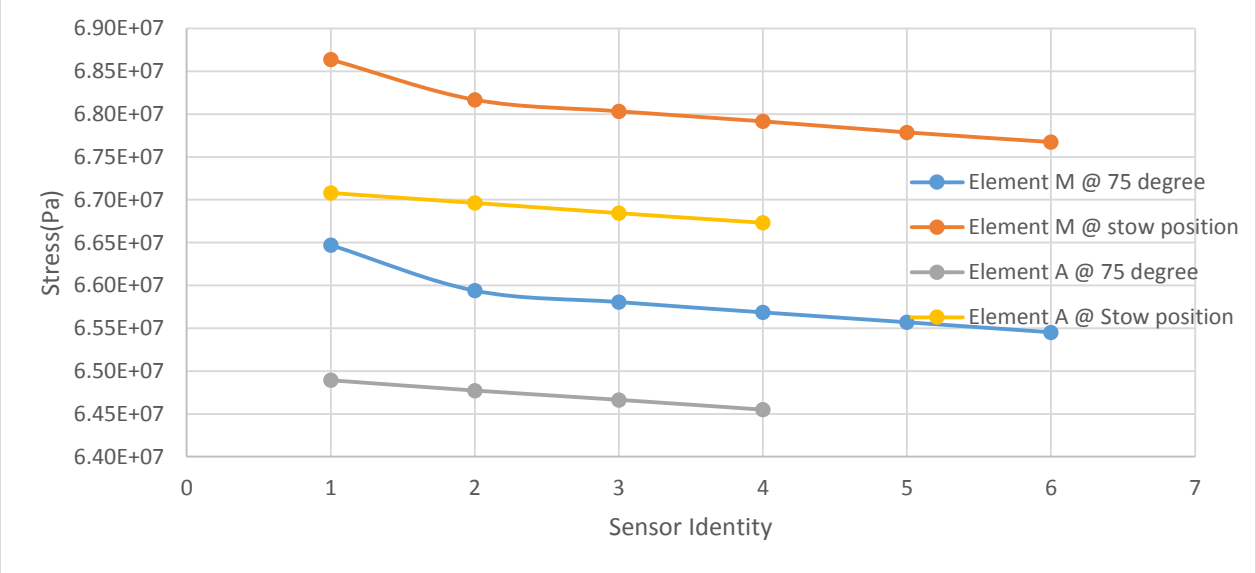

b)

Figure 5.20 Recorded stresses for a) Elements A and b) Element M at 55°, 75° and 78°

As previously discussed, the element K produced lower stress values due to its Young modulus which is considerably lower than those of element A and M. Even though, the element produced the same stress pattern during the day and overnight but it is more vulnerable to wind effect at

night due to higher stress computed with magnitude ranging from 2.46 x 10^7 Pa to 2.45 x 10^7 Pa as shown in figure 5.19 below.

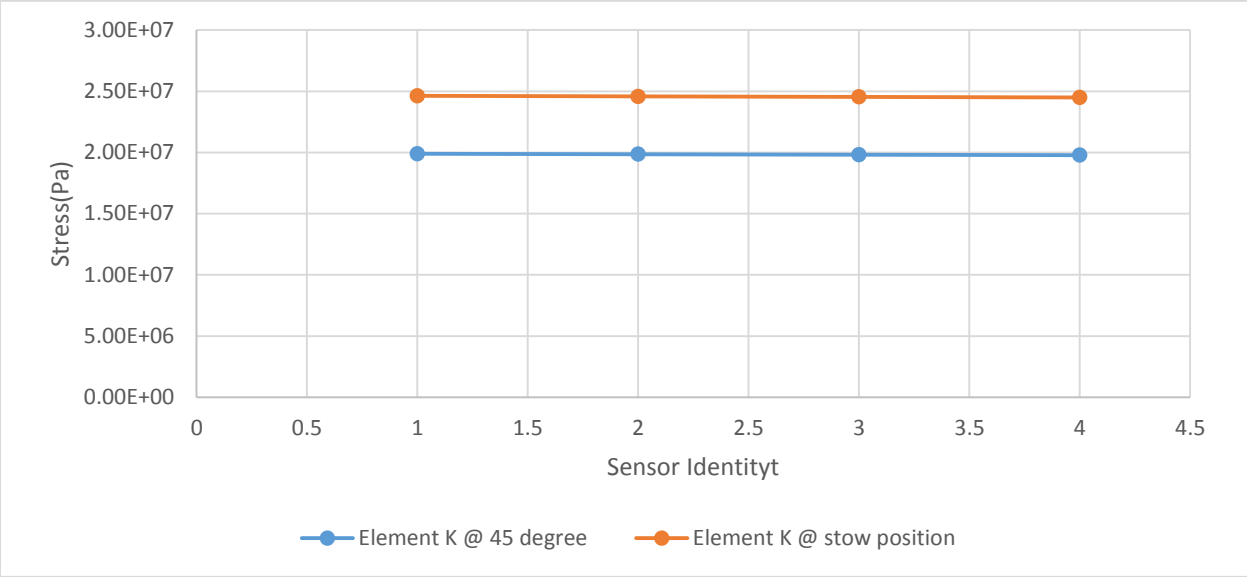

Figure 5.21(a) Recorded stresses for the elements K at 45° and 78°

Higher stress values were recorded for element K at 55° angle of attack due to higher wind speeds of 6.15 m/s recorded on this day as noticed from figure 5.18. However, the element produced same stress trend for both day (55°) and overnight (78°). It is noticed that this element is prone to more wind effect during the day because the magnitude of the stress ranging between 2.53 x 10^7 Pa and 2.54 x 10^7 Pa, while at stow position it produced less stress values ranging from 2.29E+07 Pa to 2.28 x 10^7 Pa.

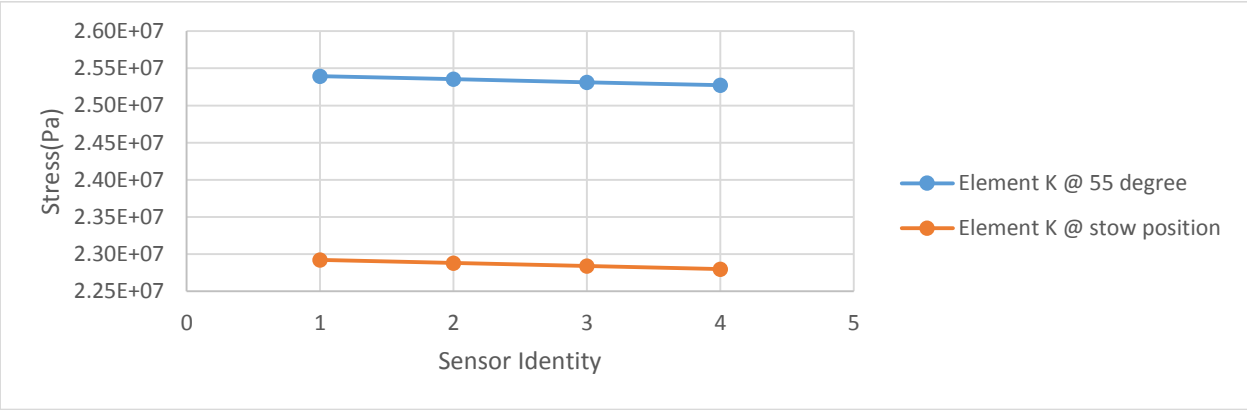

Figure 5.21 (b) Recorded stresses for the elements K at 55° and 78°

Inclination angle of 75° degree is very close to the stow position (78^0) and this angle demonstrated the same safe property of the 78° inclination because it yielded lower stress values despite the fact that it was exposed to high wind speeds of 7.36 m/s recorded on this day as presented in the above table 5.11. The element K exhibited the same stress pattern at stow position with the maximum stress value of 2.25 x 10^7 Pa and minimum value of 2.24 x 10^7 Pa. As shown in the figure 5.20 below, it is observed that the stress values of this element produced at both 75^0 and 78^0 inclination angles are very close, therefore these two angles might be considered as a safe inclination angle for the solar tracker.

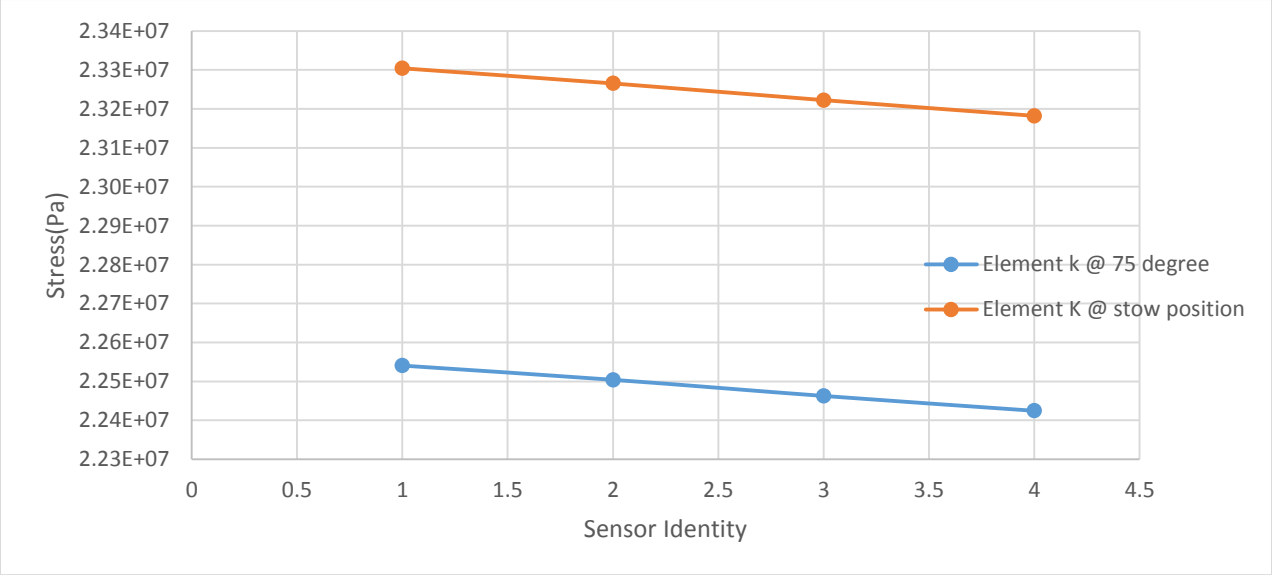

Figure 5.22 Recorded stresses for the elements K at 75° and 78°

Finally from the Table 5.12 (a) to (f) , it is observed that the element 'M' can be considered to be the most critical element because it produced highest stress values at most of the inclination angles investigated 50^0, 55^0, 65^0, 70^0, 75^0 and 78^0(stow position), regardless of the wind intensity and rotation angle.

Chapter 6 Conclusions and Recommendations

Photovoltaic (PV) solar panels installed on dual-axis mobile enable the most efficient collection of solar radiation by continuously turning the structure so it should achieve an optimum exposure to the sunlight. These devices however became the research object for the structural engineers, due to their requirement of withstanding environmental-induced loads such as snow loading and wind loading. With the main focus on the wind loading effect on a dual-axis structure, an experiment was conducted as part of the current study, to measure the strain induced by various wind loads on the solar tracker installed on the Mann Parking Building in the University of Ottawa campus. The effect of the elevation and azimuth angles was investigated by turning and tilting the entire structure for a different angles combination each day. However, many of the measured days during the February-March 2015 did not exhibit high winds, therefore some of the measured cases could not be fully documented in the current thesis. The experiment was performed in two stages; daylight (between 9.a.m and 5.p.m) and overnight (between 5.p.m and 9.a.m). For the azimuth angle 7 cases were considered for each rotation angle corresponding to the daily operational angles. A total of 49 different cases of azimuth, elevations and stow positions were measured, however the data from only 20 cases could be used for determining the high wind load effect on the solar tracker structure. The PV tracker critical elements 'A', 'K' and 'M' were instrumented with 16 strain gauges in quarter Wheatstone bridge arrangements, at selected locations. The strain gauge sensors were connected to a multiplexer which in turn it was connected to CR 1000 datalogger that measures the strain at every 2 minutes.

Because the highest wind speeds measured at the site were only 16.11 m/s, which do not determine very high drag and lift wind loads for the investigated solar tracker, a finite element (FE) model of the solar tracker was developed, and static and dynamic analyses were performed at different inclination angles ranging from 45^0 to 78^0 (stow position), by the aid of the structural SAP 2000 software. In this regard, mechanical properties were defined and the structure was divided into a smaller number of elements. Lift and drag coefficients were selected based on the structural element shape and the direction of wind speed and angle of attack, by consulting the available literature. Two components of the wind-induced force, the drag and the lift forces, for each

structural element of the tracker were computed with respect to recorded weather parameters such as temperature, relative humidity, station pressure, direction of wind, wind speed and the exposed nominal area of the element for every hour between February and March 2015. Exposure to incremental wind speed at considered angle of attacks have impact on structural deformations of the tracker under the application of drag and lift loads.

High records of induced-wind speed by data acquisition system for every two minutes depicted the intensity and dominated direction of wind load on each structural element. Dynamic loading at every one hour was computed for each element, using the weather data recorded at the International Airport, because the weather station equipment at the tracker site was malfunctioning and did not provide weather characteristics due to a mechanical problem. The hourly loading function was introduced in the time-history analysis.

Both static and modal analyses were performed for better studying the tracker behaviour under the application of wind load. For the static analysis, maximum values of the drag and lift loads determined with respect to angle of attack were applied to each element for critical response. At maximum wind load, induced wind frequency of the tracker at different angle of attacks was verified to ensure it does not coincide with the frequency of the installed tracker. The impact of angle attack was well understood through the FEA, as the tracker deformed differently with respect to the wind speed variation. The horizontal and vertical displacements were obtained from the wind load applied to the modeled tracker at different inclinations. The obtained analytical result shows that at 45^0 angle of attack, all the tracker's elements are prone to higher displacement, thus the chances of losing the structural integrity increase, regardless of the wind speed intensity, as compared to other angles of attack. At stow position, the tracker is more exposed to the lift force, although, the tracker is considered within the safety limits, during the operation and at stow position between 0 m/s and 33 m/s

Moreover, the variation of the response of the tracker with respect to wind speed was verified experimentally during February-March 2015. The measured output voltage resulted from quarter bridge of each strain gauge sensor by datalogger, was used to compute the micro-strain. By employing the equations provided in the guide book of the strain gauges, the recorded data was corrected with the calculated gauge factor as specified in the datalogger manual. Using the Young

modulus of steel and aluminum, the stress at two minutes interval for each sensor was computed using Hook's law.

The effect of the inclination angle was well understood through the numerical study performed by employing the FE model, from case 6 to case 8, as all the tracker elements exhibited lower displacements at inclination angle between 65^0 and 75^0, while for case 1 to case 5 the tracker elements were at lower inclination between 45^0 and 60^0, and much higher horizontal displacements were recorded for all the elements. This also reveals that when the tracker elements are inclined at higher angles and is getting closer to the stow position, the tracker can be considered safer for wind speed of 16.11 m/s and lower. At higher wind speeds of 22 m/s and 33 m/s, the reported displacement were higher which shows that when the tracker is exposed to greater wind load, and it might be prone to more damage. The elements K, on the edge of the suspended solar panels, was exposed to wind loads similar to elements 'M', the rotating upper bar and 'A', the legs of the tracker, however, this experienced less stress for all the elements due to its reduced Young modulus. From the performed simulation it was noticed that the elements 'K' are the most critical elements reporting higher displacement values irrespective of the inclination angle thus always the edge of the PV solar panel will be vulnerable to more displacement induced by wind forces.

From the experiment, it was obvious that the magnitude of the wind load determines the extent of the deformation of the tracker, due to the fact that on Feb 12^{th}, when the higher wind speed was recorded, though the tracker (element 'M') was inclined at 55^0, which is considered a safer angle, still higher stress of 7.48×10^7 Pa was recorded as compared to the day of Feb 19^{th} when the same wind intensity of 10.27 m/s yielded lower stresses of 6.65×10^7 Pa at 75^0 inclination.

For the element K, the stress obtained from the experiment ranged between 1.02×10^7 Pa and 2.18×10^7 Pa, while the magnitude of the stress from the simulation lies within 2.84×10^7 Pa and 3.63×10^7 Pa. From the experiment, the maximum axial force registered by element 'M' was 881 N while 6291 N was the axial force obtained from the FEM analysis. Also, the FEM simulation results were compared with the previous research carried out by Fatech et al, (2014) where the maximum displacement recorded at 50^0 inclination was 1.18 mm and this occurred at the aluminum frame supporting the PV panel of the dual-axis tracker, at critical wind speeds of 36 m/s, while the tracker element 'K' yielded maximum displacement of 2.50 mm at 45^0 angle of

attack which shows that the element is vulnerable to more damage at increased wind speed as established in both cases. Moreover, tracker might be considered as structurally safe and stable at wind speed between 0 m/s and 33 m/s depending on the position of the tracker.

The wind-induced frequency, obtained from the simulation of the first six vibration modes, for angles between 45^0 to 78^0, was ranging between 3.93 Hz to 11.33 Hz, which are in close agreement with the simulation results of the solar tracker performed by Chih et al (2014), with frequency values ranging between 3.85 Hz and 11.4 Hz.

Finally the behaviour of the experimental results were in agreement with the FE simulation result as the stress obtained ranged between 1.02×10^7 Pa and 7.88×10^7 Pa. The obtained results showed that the supporting structure of the solar tracker can be considered moderately stable between inclination angle 65° to 75° for wind speeds of up to 33 m/s in Ottawa region.

Recommendations for future work

From the experimental point of view, it is suggested that wind tunnel tests should also be conducted on the model of the prototype Photovoltaic solar tracker. The tracker should be subjected to same wind speed experienced on site, for better accuracy of the investigation. The wind tunnel experiments would make possible measuring the wind-induced pressure directly on the surface of the PV solar panels, measurements which were not possible in the current experiments, because sensors could not be installed directly on the surface of the PV panels. This would interfere with the solar energy collection performed by the solar panel, thus it was avoided.

References

[1] Sources of energy classification <http://www.factmonster.com/ipka/A0907040.html>.

[2] Natural resources Canada <http://www.nrcan.gc.ca/earth-sciences/geography/atlas-canada/selected-thematic-Maps/16872>.

[3] Eric Mcamb. (2011). "Fossil fuels and renewable energy resources" <http://www.ecology.com/2011/09/06/fossil-fuels-renewable-energy-resources>

[4] Robert, N., Meroney, and David, E., Neh. (2010). "Wind effects on roof-mounted solar photovoltaic arrays; CFD and Wind-tunnel evaluation' 'journal of international symposium on Computational Wind Engineering, pg 13-22.

[5] Risk,J., Chaiko,Y. (2008)."Solar tracking system: more efficient use of solar panels," International Journal of Electrical, computer, energetic, electronic and communication engineering Vol 2, No 5, pp. 784-786. < http://www.slideshare.net/shasze/abstract-on-solar-energy-tracking-system>.

[6] Single Axis solar tracking system for low power application <http://singledualaxis.blogspot.ca/2012/02/1-definition-of-solar-tracker-what-is.htm>.

[7] Francisco, J., Gomez,G. , De, M., , Pelaez,J., V., and Justo R. (2009) "A review of solar tracker patents in Spain", Electromechanical Engineering Department Burgos University EPS Avda. Cantabria, 09006, Burgos Univ. SPAIN, pp 292-297.

[8] Overview of solar tracker <https://en.wikipedia.org/wiki/Solar_tracker>.

[9] Granda, C., (2010). "Wind storm in northern VT damaged 4 month old PV tracker"

<http://homeenergypros.lbl.gov/photo/after-the-storm?context=user>.

[10] Structural Engineers Association of Califonia (2012)."Wind design for low profile solar photovoltaic arrays on flat roofs ". by Structural Engineers Association of California.

[11] International Electro technical Commission (IEC 62817)(2014)."Design qualification of Solar Tracker. <https://webstore.iec.ch/publication/7442>.

[12] Scaletchi, I., Visa,I., and Veicu,R. (2010). "Modelling wind action on Solar Tracking Platforms", Journal in Bulleting of Transilvania University of Brasor,Vol 3 Pg. 52.

[13] American Society of Civil Engineers (2005),Standard ASCE 7-2005,Minimum Design Loads for buildings and other structures. pp 12-24.

[14] Boggs, D.,W, and Lepage.(2006) "Wind Tunnel test", CPP technical publication, 240: 125-142.

[15] Libra, M., and V., Poulek,V. (2008) "Wind tunnel testing of a new Solar Tracker".Czech Technical University,faculty of mechanical engineering,Pg 1-5.

[16] Robert, N., Meroney, and David, E.,Neh. (2010)."Wind effects on roof-mounted solar photovoltaic arrays: CFD and Wind-tunnel evaluation". Journal of international symposium on computational Wind Engineering, 2010, pp1-8

[17] Swagat., M.(2011). "Wind tunnel Investigation of Wind load on a ground mounted photovoltaic tracker' masters' thesis report, pp. ii-iii.

[18] Hernandez,S., Mendez, J., F, Nieto, J., and Jurado,A.(2009) "Aerodynamic analysis of a Photovoltaic Solar Tracker", Proceedings of EACWE 5 Conference , Florence, Italy.[19] Abdulrahim ,T., Onundi , L,O., and Diso , I,S. (2013.) "An assessment of critical loadings and member sizing for the design of structural support for a solar Tracking Bi-Focal Collector system": International Journal of Science and Tech, Vol 2 No 4.

[20] Chih Kuang Lin, and Chen Yu Dai.(2014)".Structural Analysis of a tracking Photovoltaic system with a Pedestal Solar Tracker", Applied mechanics and material, Vol 492 Pg. 361-366.

[21] Mostafa Mehrtash B., Guillermo Quesada Y., van Dutil, Daniel Rouse, (2012). "Performance Evaluation of sun Tracking Photovoltaic systems in Canada", Proc of the 20th Annual International Conference on Mechanical Engineering-ISME2012, May, Shiraz, Iran.

[22] Helwa, N,H., Bahgat,A,B,G., Shafee,A,M.R.E,L., Shenawy ,E,T ,L.(2010). "Maximum Collectable Solar Energy by different Solar Tracking System".

[23] Rustu ,Eke, and Ali Senturk.(2012)."Performance Comparison of a double-axis sun tracking versus fixed PV system"

[24]Salah,A.(2003).”The effect of Using Sun Tracking systems on the Voltage-Current characteristics and Power generation of plate photovoltaics, Journal in energy and Management Vol 45 Pg. 167—1-1679.

[25] TML strain gauge users’ guide at <www.straingauge.om/2011/pages/straingauge> userguide pdf

[26] Multicomp technical data sheet.

<http://www.datasheetlib.com/datasheet/1069825/mc24323_multicomp/download.html>.

[27] Multicomp technical datasheet.

<http://canada.newark.com/multicomp/mf50-120r/resistor-metal-film-120-ohm-500mw/dp/38K5150>.

[28] Campbell Scientific Instruction manual, AM 16/32B Relay Multiplexer,revision 10/09.

[29] Campbell Scientific Operator’s manual, CR 1000 measurement and Control system.

[30]Operational system of dual axis photovoltaic solar tracker

<http://www.icpdas.com/products/Software/VxComm/vxcomm.htm>.

[31] Brustsaert,W,H., and Reidel,D.(1982). “Evaporation into the atmosphere;theory,history and application” Pg 37-38

[32] National Weather Service of the United States NWS, National Oceanic and Atmospheric Administration of the United State.

[33] Hristo Nedev Hristov. ‘Wind Turbines Introduction’ Technical University of Gabrovo. Engineering week lecture, Pg. 5.

<http://www.hsschmalkalden.de/Engineering+Week/_/wind%20turbines_Introduction%20IEW15.pdf>.

[34]Shane Maxemor.University of South florida,Undergraduate journal of mathematical modelling,(2009).

[35]National Aeronautics and Space Administration. <www.grc.nasa.gov>.

[36]Drag of a body, chapter nine, page 149 <www.mech.pk.edu.pl/nm52/pdf/fm/R_09 pdf>.

[37]Engineering toolbox <www.engineeringtoolbox.com>.

[38] Sadraecy,M,H.,(2009). Air craft performance and analysis, chapter three pg. 1-11

[39]<www.reseachsupporttechnology.com>.

[40]<www.aerospaceweb.org/question/aifoils/qo150b.shtml>.

[41] Historic climate data <Climate.weather.gc.ca>.

[42]SAP 2000, ”Integrated software for structural analysis and design” Analysis reference manual.

[43]Takahashi, H., Matsumoto, K., and Shimoyama,I.(2013) .”Differential pressure distribution Measurement for the development of insect-sized wings”, The University of Tokyo.

[44] Flows outside solid walls, <http://www.slideshare.net/garapatiavinash/9-drag-and-lift>.

Appendix A

Appendix A represents the the CRBasic programming for strain measurement.

```
' Revision History
' 20141129: Adding wheatstone bridge stain guage
' 20110307: Enabled I-V curve measurement routines, changed scan time to 2 minutes,
'                                   and set parameters for 1 string of 10 optics.
' 20110309: Removed optic 10 from individual optic string.
'          Set Keithley current limit to 1.5A
' 20110323: Fixed error in thermocouple type.  Table1 ambient temp was TypeJ, should be TypeT.
' 20110509: Change IV curve sweep to go from 3.2V down to 0V (reverse direction, 0.04V step
size).

Const n_optic_strings = 4      ' Number of double strings for single optic measurement
Const n_cells_total = 33
Dim  n_cells(n_optic_strings)   ' Number of cells in each double string

Public optic_string as Long   ' Count the current string
Public optic_cell as Long     ' Count the current optic in string.

'Variables to hold measured values
Public panel_temp As Float      ' CR1000 panel temperature
Public dni_voltage, gdi_voltage, ghi_voltage, ambient_temp, err_azimuth, err_elevation As Float
Public temp_C(4) as Float
Public mppt_V(4), mppt_I(4) as Float
Public tracker_power(2)as Float
Public tracker_consumption(2) as Float
Public dstring_V(16), dstring_I(16) as Float
Public watt_count As Float
Public IV_curve_V(111) as Float
Public IV_curve_I(111) As Float
```

```
Public  return_string_V As String *50
Public  return_string_I As String *50
Public return_string_relays2 As String *50
Public return_string_relays As String *50
Public return_string_relays3 As String *50
Public return_string_relays4 As String *50
' intermediate variables
Dim i As Long
Dim k As Long
Dim m As Long
Dim output as String * 30
Public RS485_send_string As String * 30
Public RS485_rec_string As String * 30

'%%%%%%%%%%%%%%%%%%%%%%%%%%%%%%%%%%%%%%%%
Public Xs(16) As Float
Public StrainVals(16) As Float
Public X1 As Float
Public R2 As Float
Public R3 As Float
Public R4 As Float
Public Mult(16)={1,1,1,1,1,1,1,1,1,1,1,1,1,1,1,1}
Public Offs(16)={0,0,0,0,0,0,0,0,0,0,0,0,0,0,0,0}
'%%%%%%%%%%%%%%%%%%%%%%%%%%%%%%%%%%%%%%%%


' Define Main datalogging table
DataTable(Table1, 1, -1)
        Sample(1,dni_voltage,IEEE4)                                        '
voltage on pyrheliometer
```

```
        Sample(1,err_azimuth,FP2)                    ' measured
tracking error (azimuth)
        Sample(1,err_elevation,FP2)                  ' measured tracking
error (elevation)
        Sample(1,panel_temp, FP2)                    ' CR1000
Panel temperature
        Sample(1,ambient_temp,FP2)                   ' ambient temp
(thermocouple on datalogger enclosure)
        Sample(4,temp_C(1), FP2)                     ' other
temperatures
        Sample(4,mppt_V(1), FP2)                     ' MPPT input
voltages
        Sample(4,mppt_I(1), FP2)                     ' MPPT input
currents
        Sample(2,tracker_power(1), FP2)      ' tracker power production
        Sample(2,tracker_consumption(1), FP2) ' tracker power consumption
        Sample(16,dstring_V(1), FP2)                 ' Measured voltage on
double strings
        Sample(16,dstring_I(1), FP2)                 ' Measured current on double
strings
EndTable

' Define second datalogging table for I-V curves
DataTable(Table2, 1, 2048)
        Sample(1,dni_voltage,IEEE4)                  '
voltage on pyrheliometer
        Sample(1,panel_temp, FP2)                    ' CR1000
Panel temperature
        Sample(1,ambient_temp,FP2)                   ' ambient temp
(thermocouple on datalogger enclosure)
        Sample(1,optic_string,Long)
```

```
        Sample(1,optic_cell,Long)
        Sample(81,IV_curve_V(1), IEEE4)
        Sample(81,IV_curve_I(1), IEEE4)
EndTable

'Define third datalogging table for pulse count
DataTable(Table3, 1, 200)
        Sample(1,watt_count,IEEE4)
EndTable



'Define fourth table for py
DataTable(Table4, 1, -1)
        Sample(1,ghi_voltage,IEEE4)
EndTable

DataTable(Table5, 1, -1)
        Sample(1,gdi_voltage,IEEE4)
EndTable

DataTable(StrainTable, 1, -1)
  Sample(16,StrainVals,IEEE4)
EndTable



Sub Keithley

        Public asd as Float
        output = ":READ?" + CHR(13) + ""
        SerialFlush(Com1) ' Throw out any characters currently in serial input buffer
        SerialOut(Com1, output, "", 1, 0) ' Trigger I-V curve measurement
```

```
        For k=1 To 81
                SerialIn(return_string_V,       Com1,50,ASCII(","),50)
                IV_curve_V(k) = return_string_V
                SerialIn(return_string_I,       Com1,50,ASCII(","),50)
                IV_curve_I(k) = return_string_I
        Next k
EndSub


Sub SetRelay (dstring, cell)
        ' Relay control modules are on addresses AA=10,11,12,13

        Dim cnt, address, chan As Long

'       cnt = 0
'       For i = 1 To dstring
'               If i < dstring Then
'                   cnt = cnt + n_cells(i)
'               Else
'                   cnt = cnt + cell - 1
'               EndIf
'       Next i

        address = dstring - 1
        chan = cell - 1

        If (chan < 8) Then
                RS485_send_string = "#1" + Hex(address) + "A" + Hex(chan) + "01" + CHR(13)
+ ""
        Else
```

```
            RS485_send_string = "#1" + Hex(address) + "B" + Hex(chan-8) + "01" +
CHR(13)+ ""
        EndIf

  SerialFlush(Com2)
        SerialOut(Com2, RS485_send_string, "", 1, 0)
        SerialIn(return_string_relays2,          Com2, 50, 13, 30)
        SerialOut(Com2, "$1" + Hex(address) + "6" + CHR(13) + "" ,"",  1, 0)
        SerialIn(return_string_relays, Com2, 50, 13, 30)
EndSub

Sub ClearRel (dstring, cell)
        'Clear all relays.
  ' Previously had CHR(10) at end of these strings.  removing them fixed communication problems.
'       output = "#100A00" + CHR(13) + ""
'       SerialOut(Com2, output, "", 1, 0)
'       output = "#100B00" + CHR(13) + ""
'       SerialOut(Com2, output, "", 1, 0)
'       output = "#110A00" + CHR(13) + ""
'       SerialOut(Com2, output, "", 1, 0)
'       output = "#110B00" + CHR(13) + ""
'       SerialOut(Com2, output, "", 1, 0)
'       output = "#120A00" + CHR(13) + ""
'       SerialOut(Com2, output, "", 1, 0)
'       output = "#120B00" + CHR(13) + ""
'       SerialOut(Com2, output, "", 1, 0)
'       output = "#130A00" + CHR(13) + ""
'       SerialOut(Com2, output, "", 1, 0)
'       output = "#130B00" + CHR(13) + ""
'       SerialOut(Com2, output, "", 1, 0)
'       output = "#140A00" + CHR(13) + ""
```

```
'       SerialOut(Com2, output, "", 1, 0)
'       output = "#140B00" + CHR(13) + ""
'       SerialOut(Com2, output, "", 1, 0)

        Dim cnt, address, chan As Long

'       cnt = 0
'       For i = 1 To dstring
'               If i < dstring Then
'                   cnt = cnt + n_cells(i)
'               Else
'                   cnt = cnt + cell - 1
'               EndIf
'       Next i

        address = dstring - 1
        chan = cell - 1

        If (chan < 8) Then
                RS485_send_string = "#1" + Hex(address) + "A" + Hex(chan) + "00" + CHR(13)
+ ""
        Else
                RS485_send_string = "#1" + Hex(address) + "B" + Hex(chan-8) + "00" +
CHR(13)+ ""
        EndIf

  SerialFlush(Com2)
        SerialOut(Com2, RS485_send_string, "", 1, 0)
        SerialIn(return_string_relays4,         Com2, 50, 13, 30)
        SerialOut(Com2, "$1" + Hex(address) + "6" + CHR(13) + "" ,"",  1, 0)
        SerialIn(return_string_relays3,         Com2, 50, 13, 30)
```

```
EndSub

Sub Read_MPPTs ()

'  MPPT Enclosure I/O modules are on AA=21 (8017R-A5) and AA=22 (8018)
'  Read Channel N syntax:  #AAN
        SerialFlush(Com2)
        For k = 0 To 3
          If (k < 3) Then

              RS485_send_string = "#21" + k + CHR(13) + ""
              SerialOut(Com2, RS485_send_string, "", 1, 0)
              SerialIn(RS485_rec_string, Com2, 50, 13, 30)
              SplitStr(mppt_V(k+1),RS485_rec_string,">",1,4)

              RS485_send_string = "#22" + k + CHR(13) + ""
              SerialOut(Com2, RS485_send_string, "", 1, 0)
              SerialIn(RS485_rec_string, Com2, 50, 13, 30)
              SplitStr(mppt_I(k+1),RS485_rec_string,">",1,4)
            Else If (k = 3) Then

              RS485_send_string = "#21" + k + CHR(13) + ""
              SerialOut(Com2, RS485_send_string, "", 1, 0)
              SerialIn(RS485_rec_string, Com2, 50, 13, 30)
              SplitStr(mppt_V(k+1),RS485_rec_string,">",1,4)

              RS485_send_string = "#22" + k + CHR(13) + ""
              SerialOut(Com2, RS485_send_string, "", 1, 0)
              SerialIn(RS485_rec_string, Com2, 50, 13, 30)
              SplitStr(mppt_I(k+1),RS485_rec_string,">",1,4)
              mppt_I(k+1) = mppt_I(k+1)/10
```

```
            End If

        Next k
EndSub

BeginProg
        'number of cells to scan in each string.
        n_cells(1) = 10
        n_cells(2) = 10
        n_cells(3) = 5
        n_cells(4) = 8
        'n_cells(5) = 18



        ' Open RS232 port (Keithley)
        SerialOpen(Com1,57600, 0, 1000, 4096)
        ' Initialize Keithley with test parameters
        output = "*RST" + CHR(13) + ""                          'Reset
        SerialOut(Com1, output, "", 1, 0)
        output = ":ROUTE:TERM REAR" + CHR(13) + ""              'Use Rear Terminals
        SerialOut(Com1, output, "", 1, 100)
        output = ":SYST:RSEN ON" + CHR(13) + ""                     'Remote  4-wire  sense
on
        SerialOut(Com1, output, "", 1, 0)
        output = ":SENS:FUNC:CONC ON" + CHR(13) + ""                'Concurrent       sense
functions on
        SerialOut(Com1, output, "", 1, 0)
        output = ":SOUR:FUNC VOLT" + CHR(13) + ""               'Voltage Source mode
        SerialOut(Com1, output, "", 1, 0)
        output = ":SENS:FUNC 'VOLT','CURR'" + CHR(13) + ""  'Sense voltage and current
```

```
SerialOut(Com1, output, "", 1, 0)
output = ":SENS:CURR:PROT 3.0" + CHR(13) + ""          '3.0A current limit
SerialOut(Com1, output, "", 1, 0)
output = ":SOUR:VOLT:START 3.4" + CHR(13) + ""         'Start sweep at 3.2V
SerialOut(Com1, output, "", 1, 0)
output = ":SOUR:VOLT:STOP 0" + CHR(13) + ""            'Stop sweep at 0V
SerialOut(Com1, output, "", 1, 0)
output = ":SOUR:VOLT:STEP -40E-3" + CHR(13) + ""       '40mV step size
SerialOut(Com1, output, "", 1, 0)
output = ":SOUR:VOLT:MODE SWE" + CHR(13) + ""          'Set sweep mode
SerialOut(Com1, output, "", 1, 0)
output = ":SOUR:SWE:RANG BEST" + CHR(13) + ""          'Auto range source
SerialOut(Com1, output, "", 1, 0)
output = ":SOUR:SWE:SPAC LIN" + CHR(13) + ""           'Use a Linear sweep
SerialOut(Com1, output, "", 1, 0)
output = ":TRIG:COUN 81" + CHR(13) + ""                '81 points per sweep
SerialOut(Com1, output, "", 1, 0)
output = ":SOUR:DEL:AUTO ON" + CHR(13) + ""            'settling time after setting voltage set to auto
SerialOut(Com1, output, "", 1, 0)
output = ":SENS:CURR:NPLC 0.1" + CHR(13) + ""          'Set sense current integration time to 0.1 power line cycles
SerialOut(Com1, output, "", 1, 0)
output = ":SENS:VOLT:NPLC 0.1" + CHR(13) + ""          'Set sense voltage integration time to 0.1 power line cycles
SerialOut(Com1, output, "", 1, 0)
output = ":DISP:DIG 5" + CHR(13) + ""                  'Setting # digits displayed on screen
SerialOut(Com1, output, "", 1, 0)
output = ":FORM:ELEM VOLT,CURR" + CHR(13) + ""         'Output voltage and current.
```

```
        SerialOut(Com1, output, "", 1, 0)
        output = ":SOUR:CLE:AUTO ON" + CHR(13) + ""          'Turn output off automatically
after measurement.
        SerialOut(Com1, output, "", 1, 0)



        ' Open Com Port (Superlogics)
        SerialOpen(Com2, 9600, 0, 0, 100)

'%%%%%%%%%%%%%%%%%%%%%%%%%% Setting the wheatstone bridge resistance
%%%%%%%%%%
        R2= 120 'Ohm
        R3= 120 'Ohm
        R4= 120 'Ohm
'%%%%%%%%%%%%%%%%%%%%%%%%%%%%

        Scan(2, Min, 3, 0)



                VoltDiff(ghi_voltage, 1, mv25, 3, 1, 0, _60Hz, 1, 0)
                CallTable Table4

    VoltDiff(gdi_voltage, 1, mv25, 5, 1, 0, _60Hz, 1, 0)
                CallTable Table5



                VoltDiff(dni_voltage, 1, mV25, 1, 1, 0, _60Hz, 1, 0)
                err_azimuth = 0
                err_elevation = 0
```

```
        PanelTemp(panel_temp, _60Hz)
        TCDiff(ambient_temp, 1, mV2_5C, 2, TypeT, panel_temp, True, 0, _60Hz, 1, 0)
        temp_C(1) = 0
        temp_C(2) = 0
        temp_C(3) = 0
        temp_C(4) = 0

        Call Read_MPPTs()
    '   Call Read_DStrings()
        CallTable Table1


        PulseCount (watt_count,1,1 ,2,0,1.0,0)
        CallTable Table3
        'PulseCountReset

'%%%%%%%%%%%%%%%%%%%%%%%%%%%%%%%%%%%%%%%
'This gathers the strain gauge data. Interfaces with the AM16/32B multiplexer

'Assuming COM4 is being used C7 and C8.
  PortSet(6,1)  'Set Reset to high
  Delay(0,15,mSec) 'Function=0 to affect the PortSet. RST is set to high for 15ms. RST high for at least 9ms is suggested to put MUX into mode A
  PortSet(6,0)
'Turn AM16/32 Multiplexer On
        PortSet(5,1)   'Set the appropriate output port
        Delay(0,2,mSec)
        k=1
        SubScan(0,uSec,16)
            'Switch to next AM16/32 Multiplexer channel
            PulsePort(5,1000)
```

```
            'Generic Full Bridge measurements 'FullBR()' on the AM16/32 Multiplexer
            BrFull(Xs(k),1,mV2500C,1,1,1,2500,True,True,0,_60Hz,Mult(k),Offs(k))
            X1= ((-1*Xs(k))/1000)+(R3/(R3+R4))
            StrainVals(k)=(R2*(1-X1))/X1
            k=k+1
        NextSubScan
        'Turn AM16/32 Multiplexer Off
        PortSet(5,0)
        Delay(0,2,mSec)
'Call Data Tables and Store Data
CallTable StrainTable

'%%%%%%%%%%%%%%%%%%%%%%%%%%%%%%%%%%%%%%%%%'


    optic_cell = 1
    optic_string = 1
    SubScan(0,Sec, 33)

        VoltDiff(dni_voltage, 1, mV25, 1, 1, 0, _60Hz, 1, 0)
        PanelTemp(panel_temp, _60Hz)
        TCDiff(ambient_temp, 1, mV2_5C, 2, TypeT, panel_temp,True, 0, _60Hz, 1, 0)

        SetRelay(optic_string, optic_cell)
        Keithley()
     ClearRel(optic_string, optic_cell)
        CallTable Table2

        ' increment cell and string number for next subscan.
        If optic_cell < n_cells(optic_string) Then
            optic_cell = optic_cell + 1
```

```
            Else
              optic_string = optic_string + 1
              optic_cell = 1
            EndIf

        NextSubScan
        NextScan
EndProg
```

APPENDIX B

Modal Analysis

Case 1: 45^0 Stress Deformed mode shape number 12 at wind speed of 11m/s

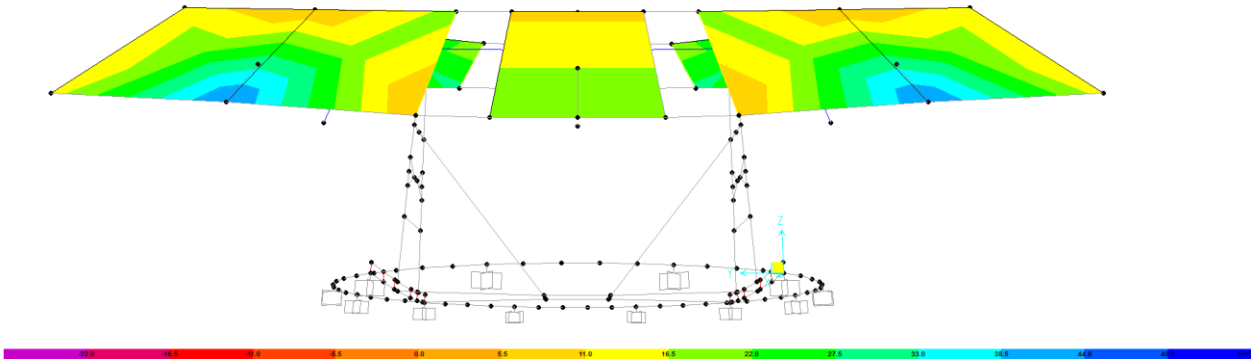

Table 4.1(a) : **45^0 : Modal Periods And Frequencies**

OutputCase	StepType	StepNum	Period	Frequency	CircFreq	Eigenvalue	Natural frequency
			Sec	Cyc/sec	rad/sec	rad2/sec2	Hz
MODAL	Mode	1	0.250825	3.99E+00	2.51E+01	6.28E+02	3.99
MODAL	Mode	2	0.188363	5.31E+00	3.34E+01	1.11E+03	5.31
MODAL	Mode	3	0.161819	6.18E+00	3.88E+01	1.51E+03	6.18
MODAL	Mode	4	0.132368	7.55E+00	4.75E+01	2.25E+03	7.56
MODAL	Mode	5	0.124919	8.01E+00	5.03E+01	2.53E+03	8.01
MODAL	Mode	6	0.10817	9.24E+00	5.81E+01	3.37E+03	9.25
MODAL	Mode	7	0.084325	1.19E+01	7.45E+01	5.55E+03	11.86
MODAL	Mode	8	0.07895	1.27E+01	7.96E+01	6.33E+03	12.67
MODAL	Mode	9	0.073647	1.36E+01	8.53E+01	7.28E+03	13.58
MODAL	Mode	10	0.069863	1.43E+01	8.99E+01	8.09E+03	14.32

MODAL	Mode	11	0.058167	1.72E+01	1.08E+02	1.17E+04	17.20
MODAL	Mode	12	0.046676	2.14E+01	1.35E+02	1.81E+04	21.43

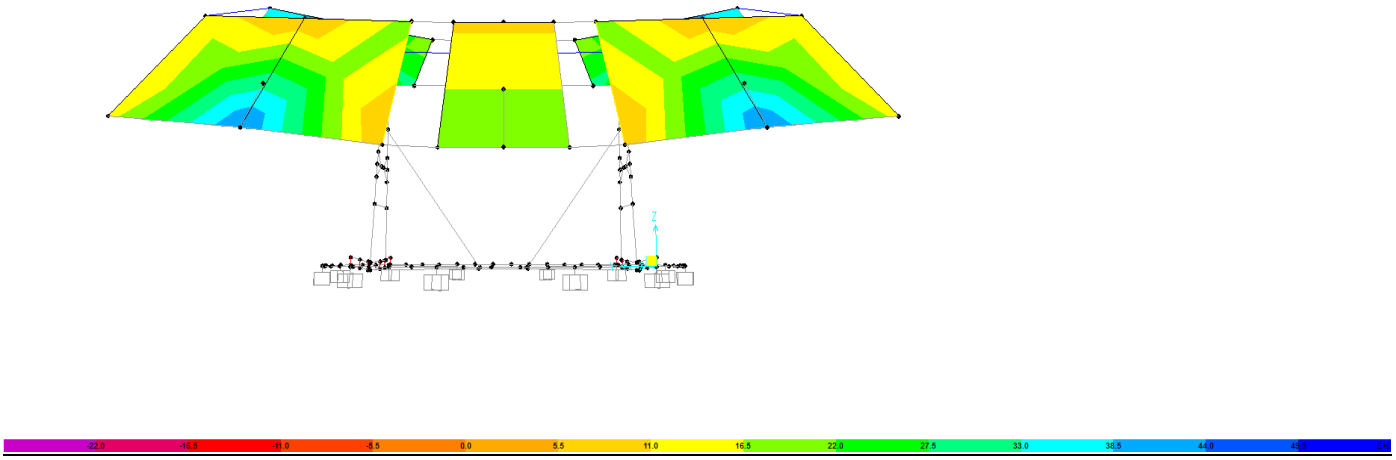

Table 4.1(b) : **45^0: Modal Periods And Frequencies at wind speed of 22m/s**

OutputCase	StepType	StepNum	Period	Frequency	CircFreq	Eigenvalue	Natural frequency
			Sec	Cyc/sec	rad/sec	rad2/sec2	Hz
MODAL	Mode	1	0.250825	3.99E+00	2.51E+01	6.28E+02	3.99
MODAL	Mode	2	0.188363	5.31E+00	3.34E+01	1.11E+03	5.31
MODAL	Mode	3	0.161819	6.18E+00	3.88E+01	1.51E+03	6.18
MODAL	Mode	4	0.132368	7.55E+00	4.75E+01	2.25E+03	7.56
MODAL	Mode	5	0.124919	8.01E+00	5.03E+01	2.53E+03	8.01
MODAL	Mode	6	0.10817	9.24E+00	5.81E+01	3.37E+03	9.25
MODAL	Mode	7	0.084325	1.19E+01	7.45E+01	5.55E+03	11.86
MODAL	Mode	8	0.07895	1.27E+01	7.96E+01	6.33E+03	12.67
MODAL	Mode	9	0.073647	1.36E+01	8.53E+01	7.28E+03	13.58
MODAL	Mode	10	0.069863	1.43E+01	8.99E+01	8.09E+03	14.32
MODAL	Mode	11	0.058167	1.72E+01	1.08E+02	1.17E+04	17.20
MODAL	Mode	12	0.046676	2.14E+01	1.35E+02	1.81E+04	21.43

Case 2: 50^0 Stress Deformed mode shape number 12 at wind speed of 11m/s

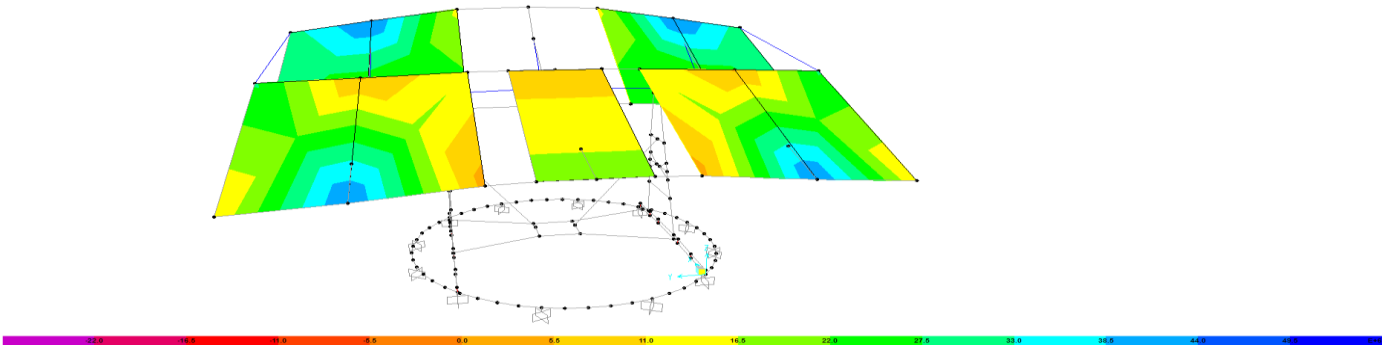

Table 4.2 : **50^0: Modal Periods And Frequencies**

OutputCase	StepType	StepNum	Period	Frequency	CircFreq	Eigenvalue	Natural frequency
			Sec	Cyc/sec	rad/sec	rad2/sec2	Hz
MODAL	Mode	1	0.249143	4.01E+00	2.52E+01	6.36E+02	4.01
MODAL	Mode	2	0.187023	5.35E+00	3.36E+01	1.13E+03	5.35
MODAL	Mode	3	0.159093	6.29E+00	3.95E+01	1.56E+03	6.29
MODAL	Mode	4	0.130939	7.64E+00	4.80E+01	2.30E+03	7.64

MODAL	Mode	5	0.123402	8.10E+00	5.09E+01	2.59E+03	8.11
MODAL	Mode	6	0.0988	1.01E+01	6.36E+01	4.04E+03	10.12
MODAL	Mode	7	0.079512	1.26E+01	7.90E+01	6.24E+03	12.58
MODAL	Mode	8	0.072957	1.37E+01	8.61E+01	7.42E+03	13.71
MODAL	Mode	9	0.06819	1.47E+01	9.21E+01	8.49E+03	14.67
MODAL	Mode	10	0.067966	1.47E+01	9.24E+01	8.55E+03	14.72
MODAL	Mode	11	0.05579	1.79E+01	1.13E+02	1.27E+04	17.93
MODAL	Mode	12	0.0445	2.25E+01	1.41E+02	1.99E+04	22.48

Case 3: 55^0 Stress Deformed mode shape number 12 at wind speed of 11m/s

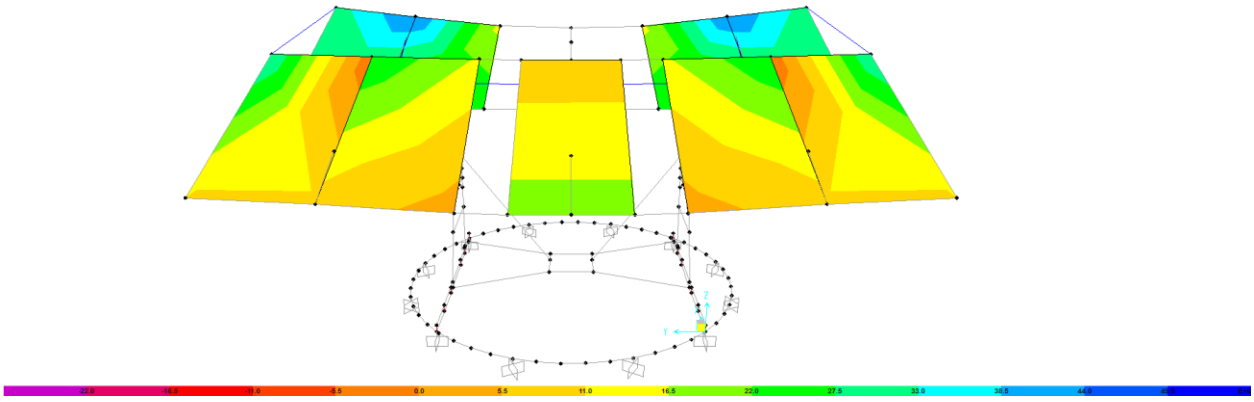

Table 4.3 : **55^0: Modal Periods And Frequencies**

OutputCase	StepType	StepNum	Period	Frequency	CircFreq	Eigenvalue	Natural frequency(Hz)
			Sec	Cyc/sec	rad/sec	rad2/sec2	Hz
MODAL	Mode	1	0.250713	3.99E+00	2.51E+01	6.28E+02	3.99
MODAL	Mode	2	0.187082	5.35E+00	3.36E+01	1.13E+03	5.35
MODAL	Mode	3	0.159094	6.29E+00	3.95E+01	1.56E+03	6.29
MODAL	Mode	4	0.131343	7.61E+00	4.78E+01	2.29E+03	7.62
MODAL	Mode	5	0.12343	8.10E+00	5.09E+01	2.59E+03	8.10
MODAL	Mode	6	0.095463	1.05E+01	6.58E+01	4.33E+03	10.48
MODAL	Mode	7	0.080831	1.24E+01	7.77E+01	6.04E+03	12.38
MODAL	Mode	8	0.07135	1.40E+01	8.81E+01	7.75E+03	14.02
MODAL	Mode	9	0.068411	1.46E+01	9.18E+01	8.44E+03	14.62
MODAL	Mode	10	0.067981	1.47E+01	9.24E+01	8.54E+03	14.71
MODAL	Mode	11	0.0568	1.76E+01	1.11E+02	1.22E+04	17.61
MODAL	Mode	12	0.044824	2.23E+01	1.40E+02	1.96E+04	22.32

Case 4: 60^0 Stress Deformed mode shape number 12 at wind speed of 11m/s

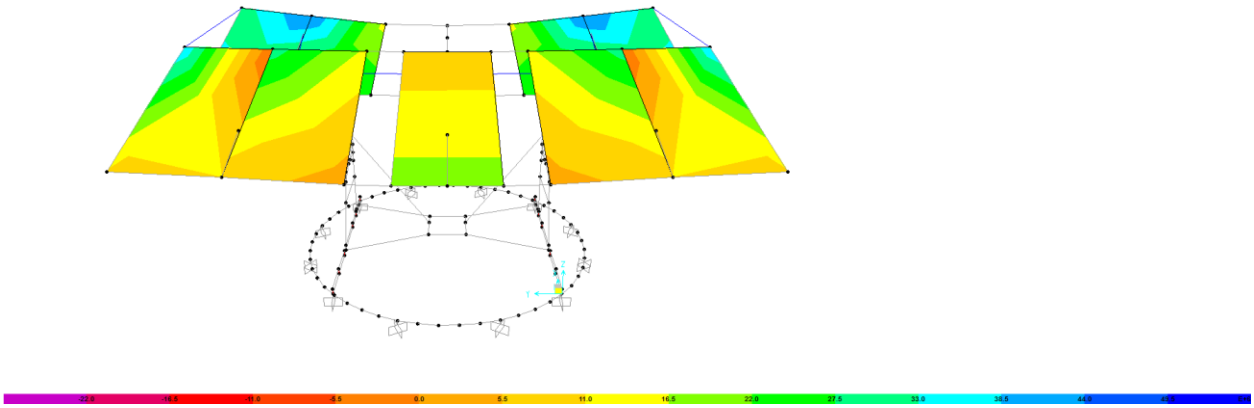

Table 4.4 : 60^0: Modal Periods And Frequencies

OutputCase	StepType	StepNum	Period	Frequency	CircFreq	Eigenvalue	Natural frequency(Hz)
			Sec	Cyc/sec	rad/sec	rad2/sec2	Hz
MODAL	Mode	1	0.251851	3.97E+00	2.49E+01	6.22E+02	3.97
MODAL	Mode	2	0.187154	5.34E+00	3.36E+01	1.13E+03	5.34
MODAL	Mode	3	0.159125	6.28E+00	3.95E+01	1.56E+03	6.29
MODAL	Mode	4	0.131682	7.59E+00	4.77E+01	2.28E+03	7.60
MODAL	Mode	5	0.12346	8.10E+00	5.09E+01	2.59E+03	8.10
MODAL	Mode	6	0.092305	1.08E+01	6.81E+01	4.63E+03	10.84
MODAL	Mode	7	0.082351	1.21E+01	7.63E+01	5.82E+03	12.15
MODAL	Mode	8	0.069757	1.43E+01	9.01E+01	8.11E+03	14.34
MODAL	Mode	9	0.068605	1.46E+01	9.16E+01	8.39E+03	14.58
MODAL	Mode	10	0.067983	1.47E+01	9.24E+01	8.54E+03	14.71
MODAL	Mode	11	0.057917	1.73E+01	1.08E+02	1.18E+04	17.27
MODAL	Mode	12	0.045068	2.22E+01	1.39E+02	1.94E+04	22.20

Case 5: 65^0 Stress Deformed mode shape number 12 at wind speed of 11m/s

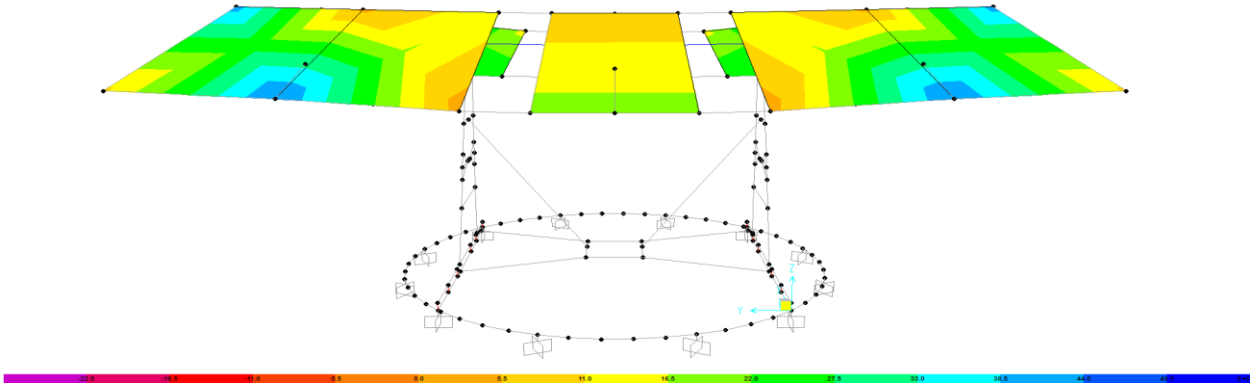

Case 6: 70^0 Stress Deformed mode shape number 12 at wind speed of 11m/s

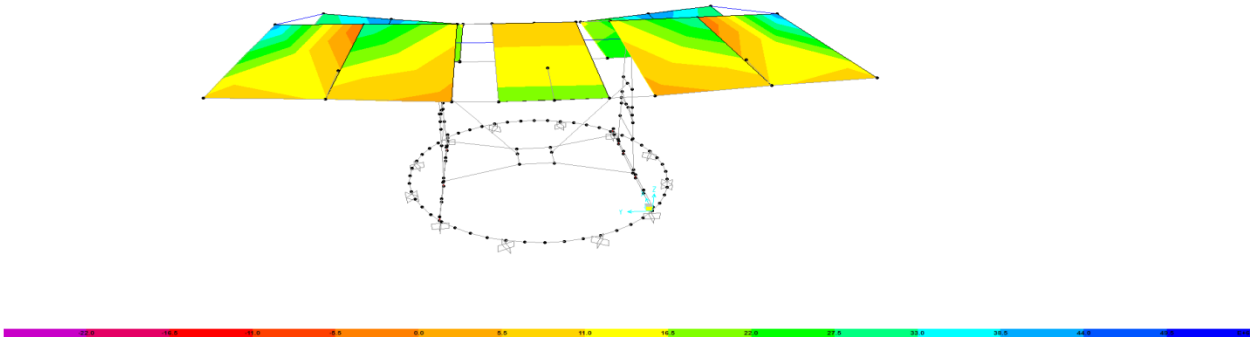

Table 4.6 : 70^0: Modal Periods And Frequencies

OutputCase	StepType	StepNum	Period	Frequency	CircFreq	Eigenvalue
			Sec	Cyc/sec	rad/sec	rad2/sec2
MODAL	Mode	1	0.252475	3.96E+00	2.49E+01	6.19E+02

MODAL	Mode	2	0.187416	5.34E+00	3.35E+01	1.12E+03
MODAL	Mode	3	0.159378	6.27E+00	3.94E+01	1.55E+03
MODAL	Mode	4	0.132254	7.56E+00	4.75E+01	2.26E+03
MODAL	Mode	5	0.123592	8.09E+00	5.08E+01	2.58E+03
MODAL	Mode	6	0.088271	1.13E+01	7.12E+01	5.07E+03
MODAL	Mode	7	0.08405	1.19E+01	7.48E+01	5.59E+03
MODAL	Mode	8	0.069032	1.45E+01	9.10E+01	8.28E+03
MODAL	Mode	9	0.068259	1.47E+01	9.21E+01	8.47E+03
MODAL	Mode	10	0.06551	1.53E+01	9.59E+01	9.20E+03
MODAL	Mode	11	0.061801	1.62E+01	1.02E+02	1.03E+04
MODAL	Mode	12	0.045404	2.20E+01	1.38E+02	1.92E+04

Case 7: 75^0 Stress Deformed mode shape number 12 at wind speed of 11m/s

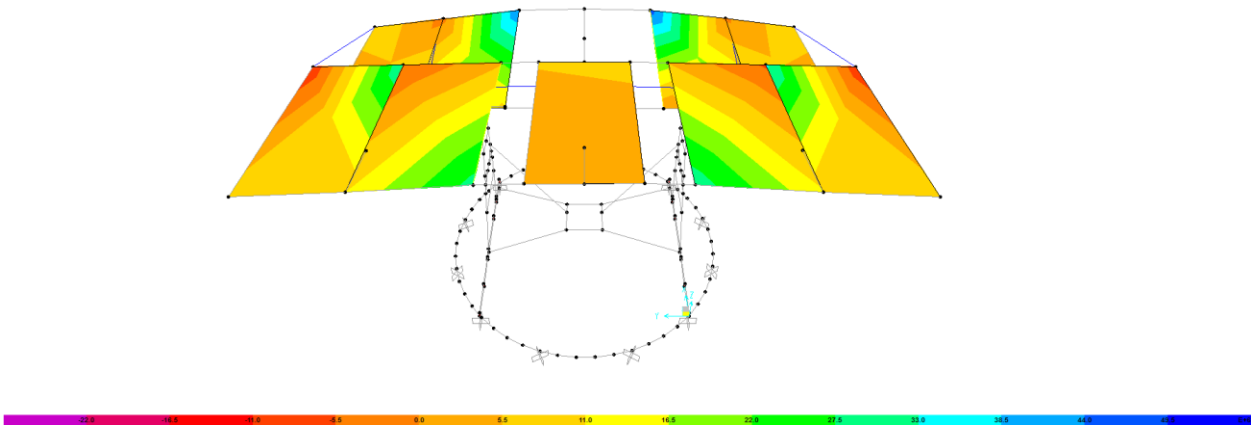

Table 4.7 : 75^0: Modal Periods And Frequencies

OutputCase	StepType	StepNum	Period	Frequency	CircFreq	Eigenvalue	Natural frequency
			Sec	Cyc/sec	rad/sec	rad2/sec2	Hz
MODAL	Mode	1	0.251807	3.97E+00	2.50E+01	6.23E+02	3.97
MODAL	Mode	2	0.187587	5.33E+00	3.35E+01	1.12E+03	5.33
MODAL	Mode	3	0.159508	6.27E+00	3.94E+01	1.55E+03	6.27
MODAL	Mode	4	0.132305	7.56E+00	4.75E+01	2.26E+03	7.56

MODAL	Mode	5	0.123676	8.09E+00	5.08E+01	2.58E+03	8.09
MODAL	Mode	6	0.090599	1.10E+01	6.94E+01	4.81E+03	11.04
MODAL	Mode	7	0.081745	1.22E+01	7.69E+01	5.91E+03	12.24
MODAL	Mode	8	0.06913	1.45E+01	9.09E+01	8.26E+03	14.47
MODAL	Mode	9	0.068402	1.46E+01	9.19E+01	8.44E+03	14.62
MODAL	Mode	10	0.064476	1.55E+01	9.75E+01	9.50E+03	15.51
MODAL	Mode	11	0.062653	1.60E+01	1.00E+02	1.01E+04	15.96
MODAL	Mode	12	0.045468	2.20E+01	1.38E+02	1.91E+04	22.00

Case 8: 78^0 Stress Deformed mode shape number 12 at wind speed of 11m/s

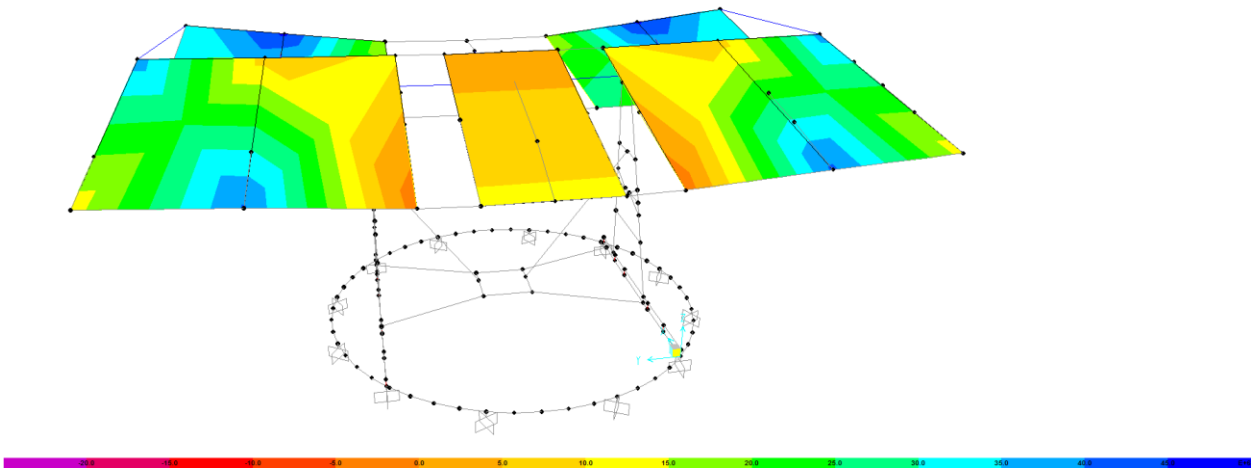

Table 4.8: **78^0: Modal Periods And Frequencies**

OutputCase	StepType	StepNum	Period	Frequency	CircFreq	Eigenvalue	Natural frequency
			Sec	Cyc/sec	rad/sec	rad2/sec2	Hz
MODAL	Mode	1	0.254675	3.93E+00	2.47E+01	6.09E+02	3.93
MODAL	Mode	2	0.184893	5.41E+00	3.40E+01	1.15E+03	5.41
MODAL	Mode	3	0.161279	6.20E+00	3.90E+01	1.52E+03	6.20
MODAL	Mode	4	0.133745	7.48E+00	4.70E+01	2.21E+03	7.48
MODAL	Mode	5	0.122798	8.14E+00	5.12E+01	2.62E+03	8.15
MODAL	Mode	6	0.093266	1.07E+01	6.74E+01	4.54E+03	10.73
MODAL	Mode	7	0.089194	1.12E+01	7.04E+01	4.96E+03	11.21
MODAL	Mode	8	0.072008	1.39E+01	8.73E+01	7.61E+03	13.89
MODAL	Mode	9	0.071463	1.40E+01	8.79E+01	7.73E+03	14.00
MODAL	Mode	10	0.067849	1.47E+01	9.26E+01	8.58E+03	14.74
MODAL	Mode	11	0.062494	1.60E+01	1.01E+02	1.01E+04	16.01
MODAL	Mode	12	0.046962	2.13E+01	1.34E+02	1.79E+04	21.30

Appendix C

This Appendix C presents the calculation involved in elements Induced drag and Lift Area.

- **Element B**

Drag Length =1.5443m

Drag Breadth=0.061m

Drag Area of Element B=1.5443m× 0.061m=0.094m^2

Lift Area of Element B= 1.5443m× 0.061m=0.094m^2

The angle of attack does not affect this element as it does not move like upper parts of the tracker

- **Element D**

  Length =1.642m

  Diameter of the circular beam=0.05m

  Projected Lift Area =length×Diameter of the beam×cos 78°

  1.642×0.05×0.2079

  0.017m^2

  Projected Drag Area= length×Diameter of the beam×Sin 78°

  1.642×0.05×0.9781

  0.080m^2

- **Element E**

  Length of the beam=2.219m

  Diameter= 0.05m

  Projected Lift Area= length×Diameter of the beam×cos 78°

  2.219m×0.05m× cos 78°

$0.023m^2$

Projected Drag Area== length×Diameter of the beam×Sin 78°

2.219m×0.05m× Sin 78°

2.219m×0.05×0.9781

$0.108m^2$

- **Element F**

Length of the element=2.0879m

Width of the element=0.061m

Angle of attack=78°

Projected Lift Area of the element=2.0879m×0.061m×cos 78°

$0.026m^2$

Projected Drag Area of the Element=2.0879m×0.061m×Sin 78°

0.1246m^2

- **Element G**

Length of the element=2.0879m

Width of the element=0.061m

Angle of attack=78°

Projected Lift Area of the element=2.0879m×0.061m×cos 78°

$0.026m^2$

Projected Drag Area of the Element=2.0879m×0.061m×Sin 78°

$0.1246m^2$

- **Element I**

Length of the element=0.3048m

Width of the element=0.061m

Angle of attack=78°

Projected Lift Area of the element=0.3048m×0.061m × cos 78°

$0.004m^2$

Projected Drag Area of the element=0.3048m×0.061m × sin 78°

$0.018m^2$

- **Element J**

Length =1.642m

Diameter of the circular beam=0.05m

Projected Lift Area =length×Diameter of the beam×cos 78°

1.642×0.05×0.2079

$0.017m^2$

Projected Drag Area= length×Diameter of the beam×Sin 78°

1.642×0.05×0.9781

$0.080m^2$

- **Element K**

Length of the element=1.8471m

Width of the element =0.061m

Angle of attack=78°

Projected Lift Area=1.8471m×0.061m×Cos 78°

0.023m^2

Projected Drag Area=1.8471m×0.061m×Sin 78°

0.110m^2

Drag force:

These below equations present how Drag and Lift forces for each element are estimated

$F_{DD}=\frac{1}{2}C_{DD}\rho A_{DD}V_{max}^2$=1/2× 1.2×0.080 × ρV_{max}^2

$F_{DE}=\frac{1}{2}C_{DE}\rho A_{DE}V_{max}^2$=1/2× 1.2× 0.108× ρV_{max}^2

$F_{DF}=\frac{1}{2}C_{DF}\rho A_{DF}V_{max}^2$=1/2× 2.2×0.125 × ρV_{max}^2

$F_{DG}=\frac{1}{2}C_{DG}\rho A_{DG}V_{max}^2$=1/2× 2.2×0.125 × ρV_{max}^2

$F_{DH}=\frac{1}{2}C_{DH}\rho A_{DH}V_{max}^2$=1/2× 2.2×0.018 × ρV_{max}^2

$F_{DI}=\frac{1}{2}C_{DI}\rho A_{DI}V_{max}^2$=1/2× 2.2×0.018 × ρV_{max}^2

Lift force:

$F_{LD}=\frac{1}{2}C_{LD}\rho A_{LD}V_{max}^2$=1/2× 1.2×0.017 × ρV_{max}^2

$F_{LE}=\frac{1}{2}C_{LE}\rho A_{LE}V_{max}^2$=1/2× 1.2×0.023 × ρV_{max}^2

$F_{LF}=\frac{1}{2}C_{LF}\rho A_{LF}V_{max}^2$=1/2× 2.2× 0.026× ρV_{max}^2

$F_{LG}=\frac{1}{2}C_{LG}\rho A_{LG}V_{max}^2$=1/2× 2.2×0.026 × ρV_{max}^2

$F_{LH}=\frac{1}{2}C_{LH}\rho A_{LH}V_{max}^2$=1/2× 2.2× 0.004× ρV_{max}^2

$F_{LI}=\frac{1}{2}C_{LI}\rho A_{LI}V_{max}^2$=1/2× 2.2×0.004 × ρV_{max}^2

Table A1: Drag forces for elements G to M at stow position (78°) using corresponding wind speed and humid air density.

		Elements						
Date/Time	**Wind speed(m/s)**	**G**	**H**	**I**	**J**	**K**	**L**	**M**
01/02/2015 0:00	2.7778	1.4369	0.2069	0.2069	0.5016	1.2645	1.2645	2.1651
01/02/2015 1:00	2.7778	1.4346	0.2066	0.2066	0.5008	1.2624	1.2624	2.1615
01/02/2015 2:00	2.7778	1.4385	0.2071	0.2071	0.5022	1.2658	1.2658	2.1674
01/02/2015 3:00	5.0000	4.6797	0.6739	0.6739	1.6336	4.1181	4.1181	7.0512
01/02/2015 4:00	5.0000	4.7168	0.6792	0.6792	1.6466	4.1508	4.1508	7.1071
01/02/2015 5:00	4.1667	3.2920	0.4740	0.4740	1.1492	2.8970	2.8970	4.9603
01/02/2015 6:00	8.0556	12.2593	1.7653	1.7653	4.2796	10.7882	10.7882	18.4719
01/02/2015 7:00	7.2222	9.9258	1.4293	1.4293	3.4650	8.7347	8.7347	14.9559
01/02/2015 8:00	7.2222	9.9738	1.4362	1.4362	3.4818	8.7770	8.7770	15.0282
01/02/2015 9:00	5.8333	6.5156	0.9382	0.9382	2.2745	5.7337	5.7337	9.8174

The figures below represents the intensity of drag load of each element in February 2015.

The time-history of the wind-induced drag and lift loads for the most critical elements:

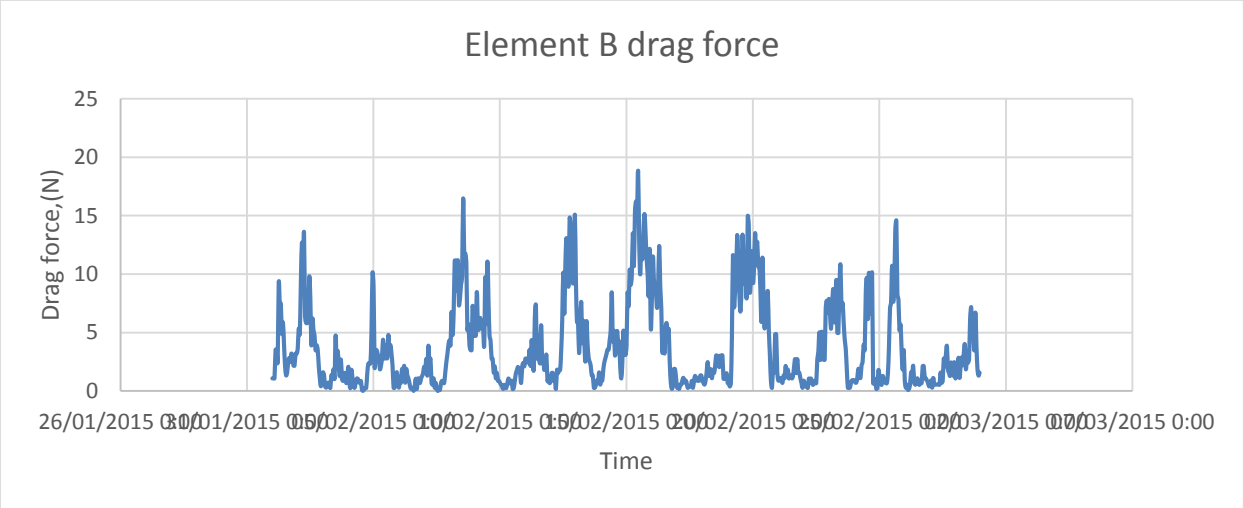

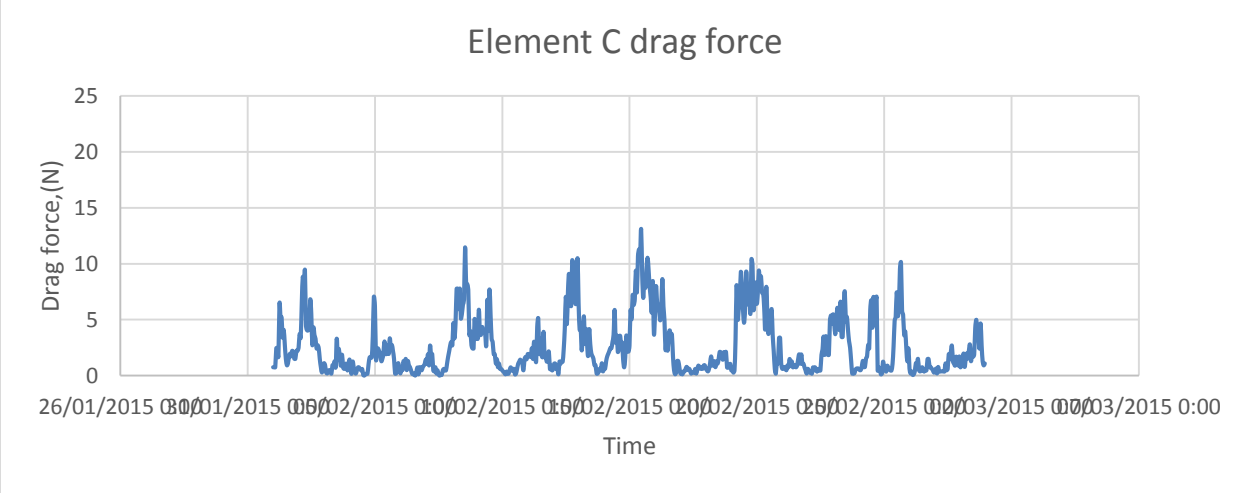

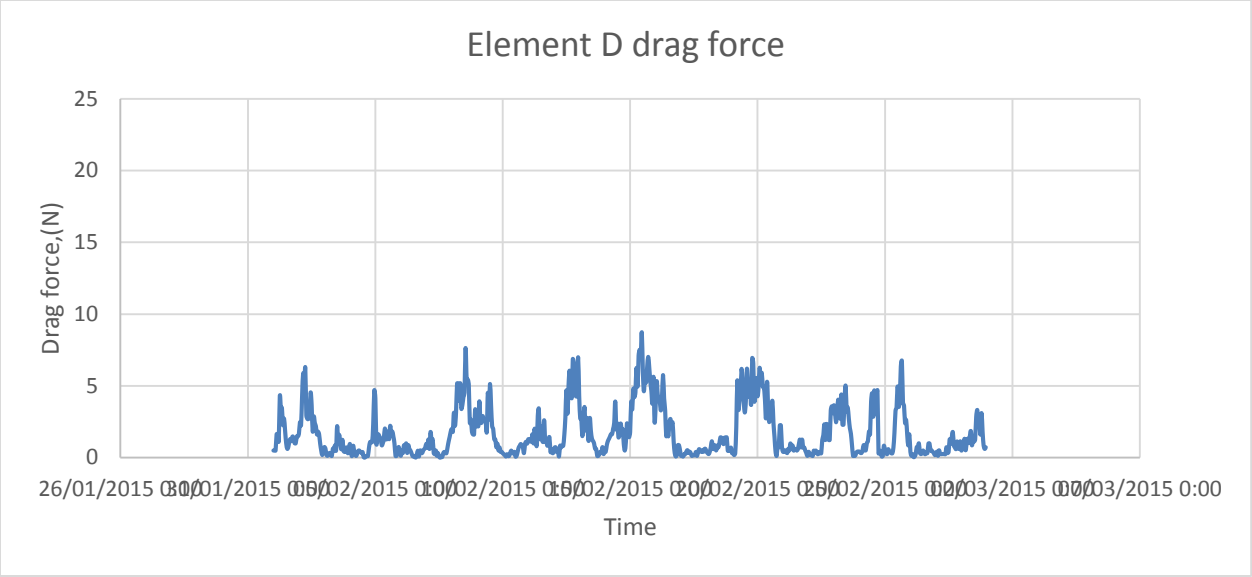
Element D drag force
Drag force,(N)
25
20
15
10
5
0
26/01/2015 0:00
30/01/2015 0:00
05/02/2015 0:00
10/02/2015 0:00
15/02/2015 0:00
20/02/2015 0:00
25/02/2015 0:00
02/03/2015 0:00
07/03/2015 0:00
Time

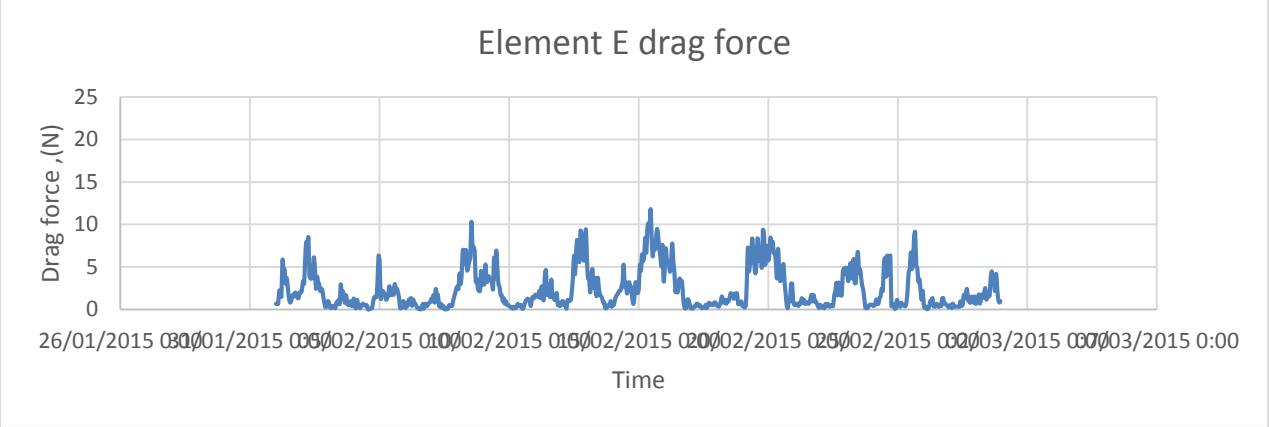
Element E drag force
Drag force ,(N)
25
20
15
10
5
0
26/01/2015 0:00
30/01/2015 0:00
05/02/2015 0:00
10/02/2015 0:00
15/02/2015 0:00
20/02/2015 0:00
25/02/2015 0:00
02/03/2015 0:00
07/03/2015 0:00
Time

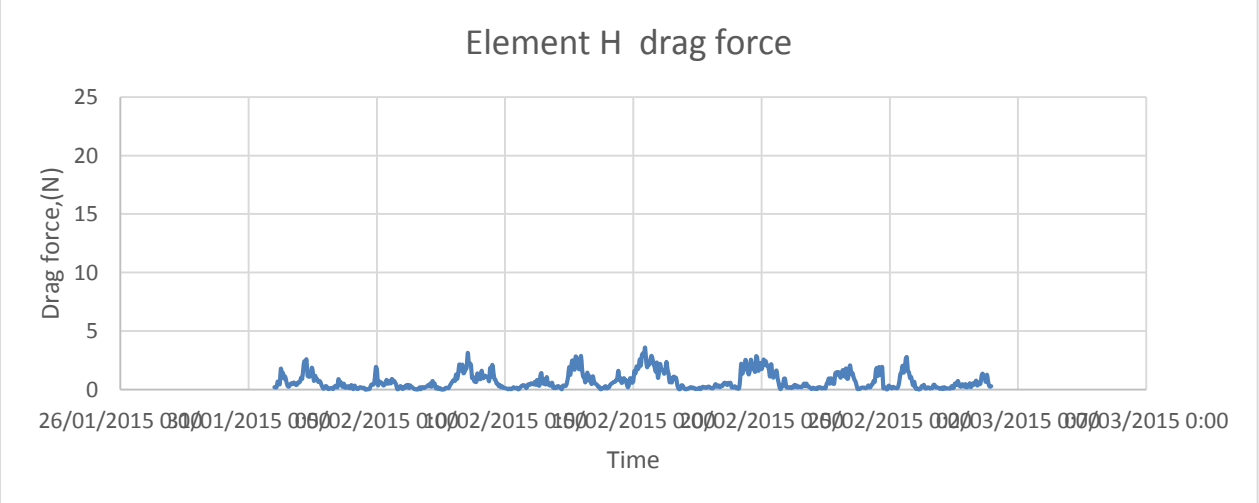
Element H drag force
Drag force,(N)
25
20
15
10
5
0
26/01/2015 0:00
30/01/2015 0:00
05/02/2015 0:00
10/02/2015 0:00
15/02/2015 0:00
20/02/2015 0:00
25/02/2015 0:00
02/03/2015 0:00
07/03/2015 0:00
Time

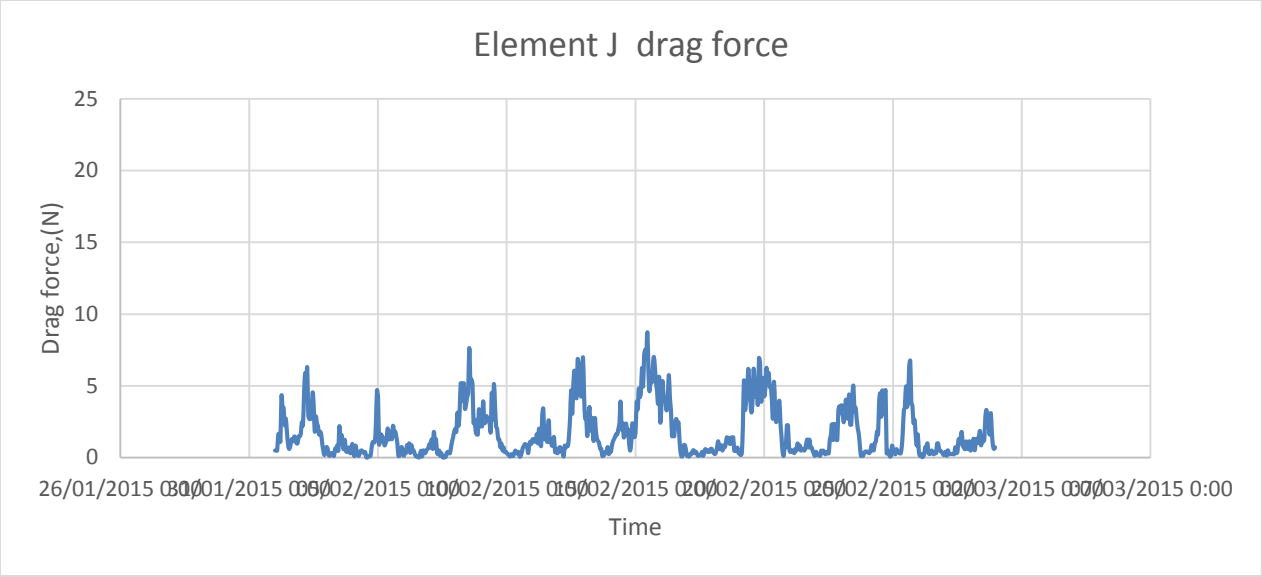

Figure C1.1 Time-history of the drag force on tracker element in February 2015.

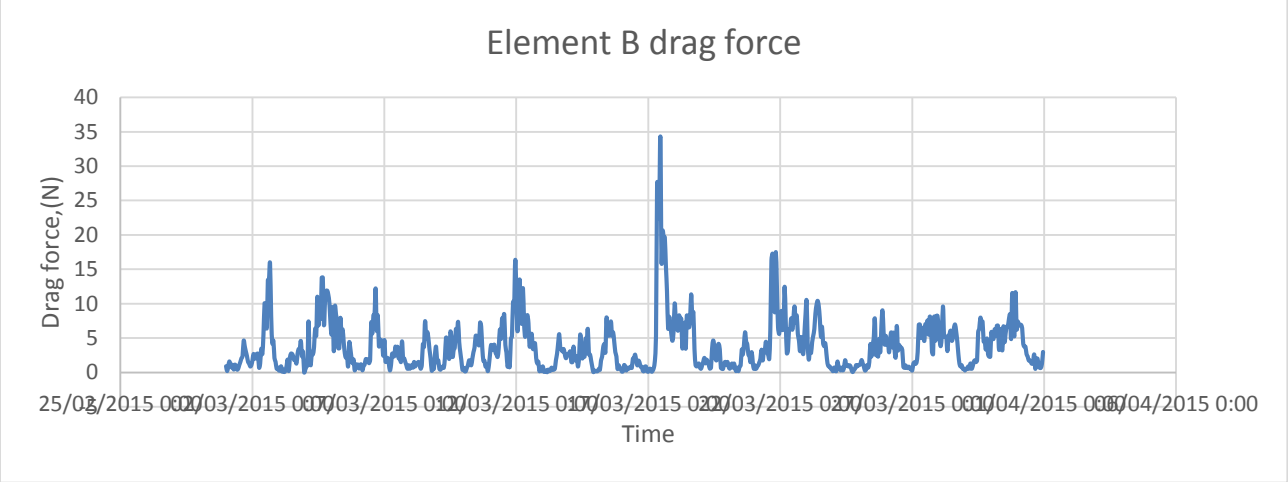

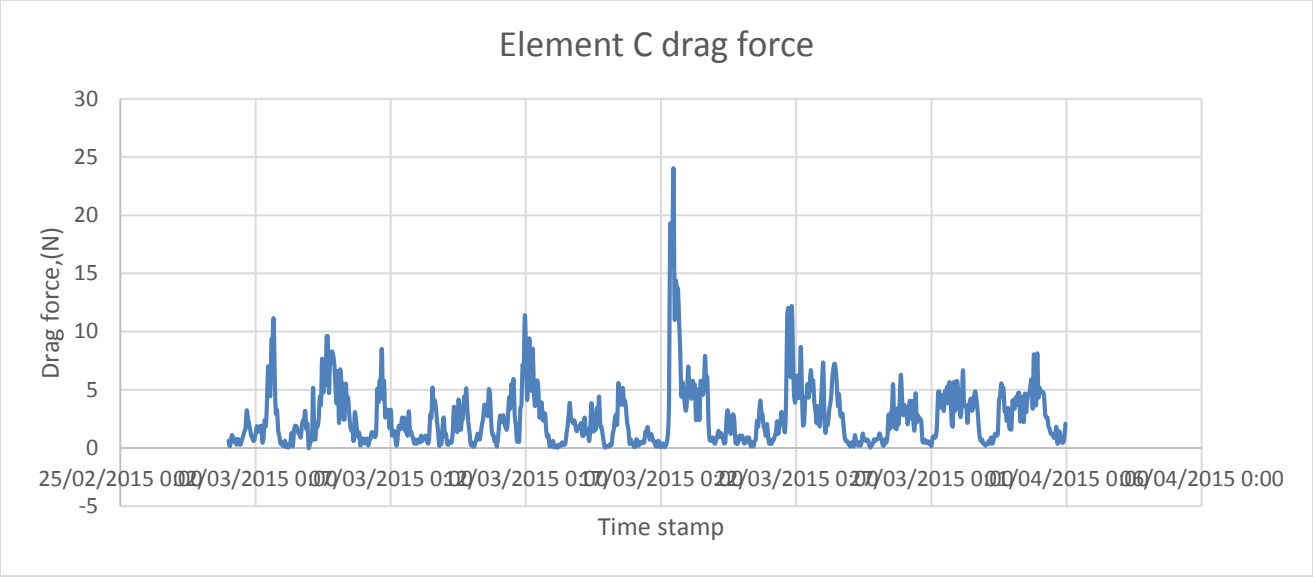
Element C drag force
Drag force,(N)
30
25
20
15
10
5
0
-5
25/02/2015 0:00
02/03/2015 0:00
07/03/2015 0:00
12/03/2015 0:00
17/03/2015 0:00
22/03/2015 0:00
27/03/2015 0:00
01/04/2015 0:00
06/04/2015 0:00
Time stamp

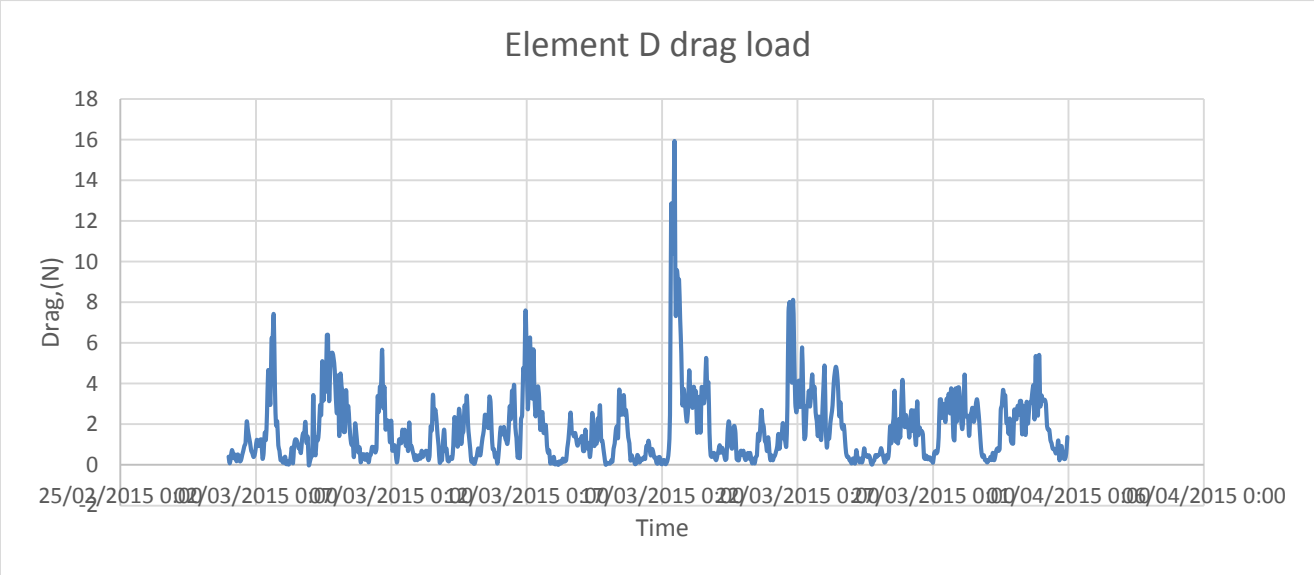
Element D drag load
Drag,(N)
18
16
14
12
10
8
6
4
2
0
-2
25/02/2015 0:00
02/03/2015 0:00
07/03/2015 0:00
12/03/2015 0:00
17/03/2015 0:00
22/03/2015 0:00
27/03/2015 0:00
01/04/2015 0:00
06/04/2015 0:00
Time

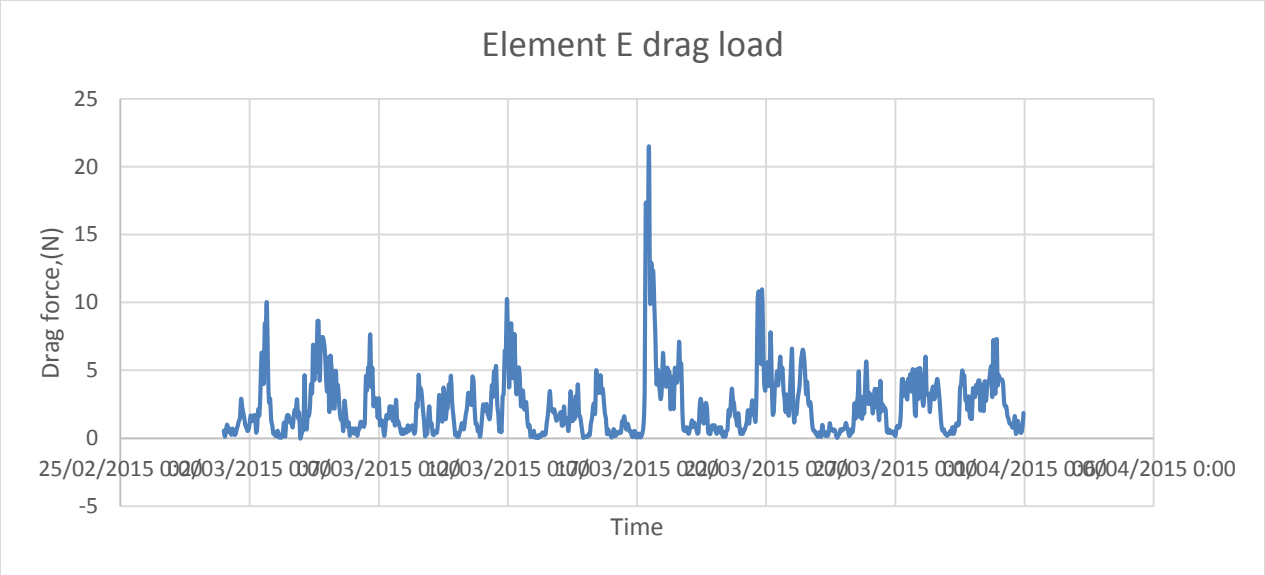
Element E drag load
Drag force,(N)
25
20
15
10
5
0
-5
25/02/2015 0:00
02/03/2015 0:00
07/03/2015 0:00
12/03/2015 0:00
17/03/2015 0:00
22/03/2015 0:00
27/03/2015 0:00
01/04/2015 0:00
06/04/2015 0:00
Time

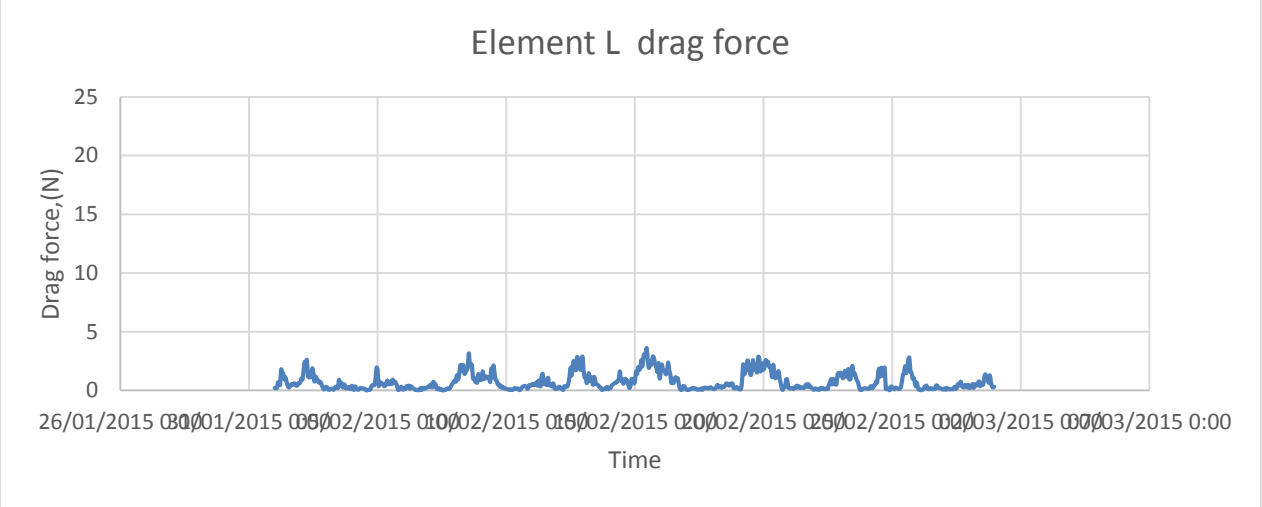
Element L drag force
Drag force,(N)
25
20
15
10
5
0
26/01/2015 0:00
31/01/2015 0:00
05/02/2015 0:00
10/02/2015 0:00
15/02/2015 0:00
20/02/2015 0:00
25/02/2015 0:00
02/03/2015 0:00
07/03/2015 0:00
Time

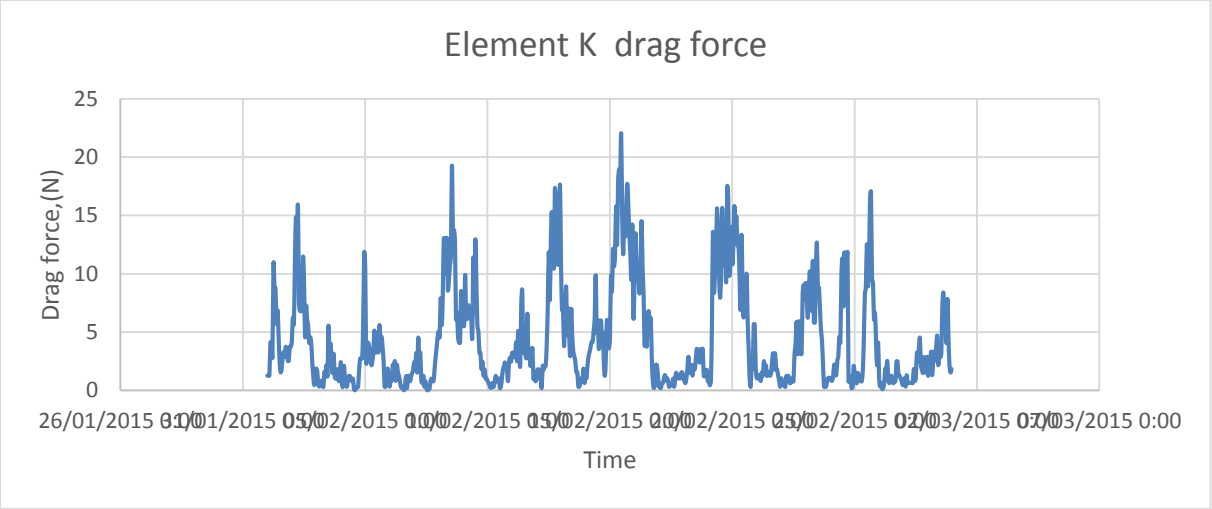
Element K drag force
Drag force,(N)
25
20
15
10
5
0
26/01/2015 0:00
01/02/2015 0:00
05/02/2015 0:00
10/02/2015 0:00
15/02/2015 0:00
20/02/2015 0:00
25/02/2015 0:00
02/03/2015 0:00
07/03/2015 0:00
Time

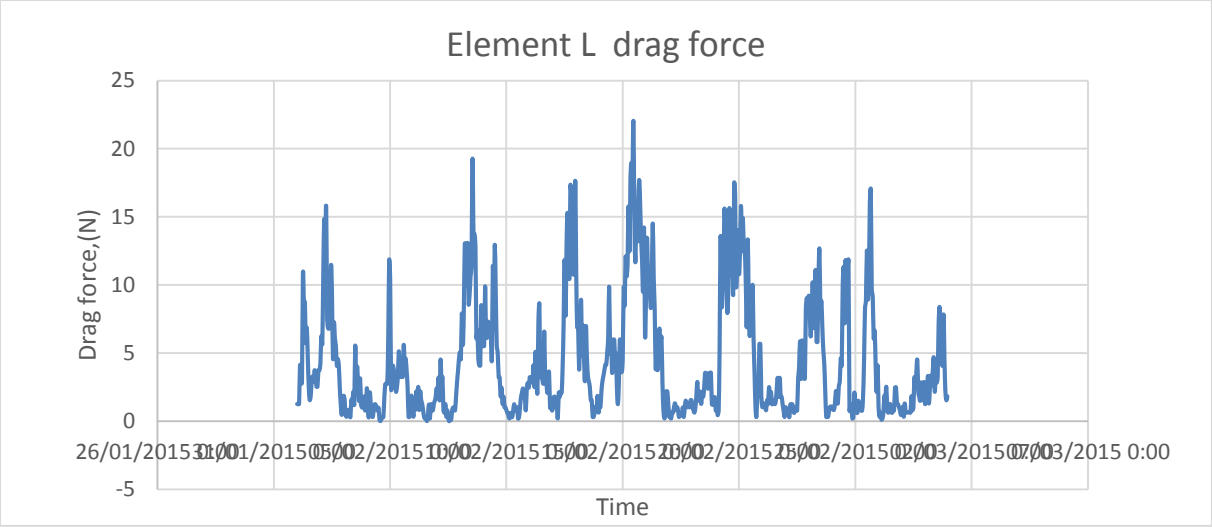
Element L drag force
Drag force,(N)
25
20
15
10
5
0
-5
26/01/2015 0:00
01/02/2015 0:00
05/02/2015 0:00
10/02/2015 0:00
15/02/2015 0:00
20/02/2015 0:00
25/02/2015 0:00
02/03/2015 0:00
07/03/2015 0:00
Time

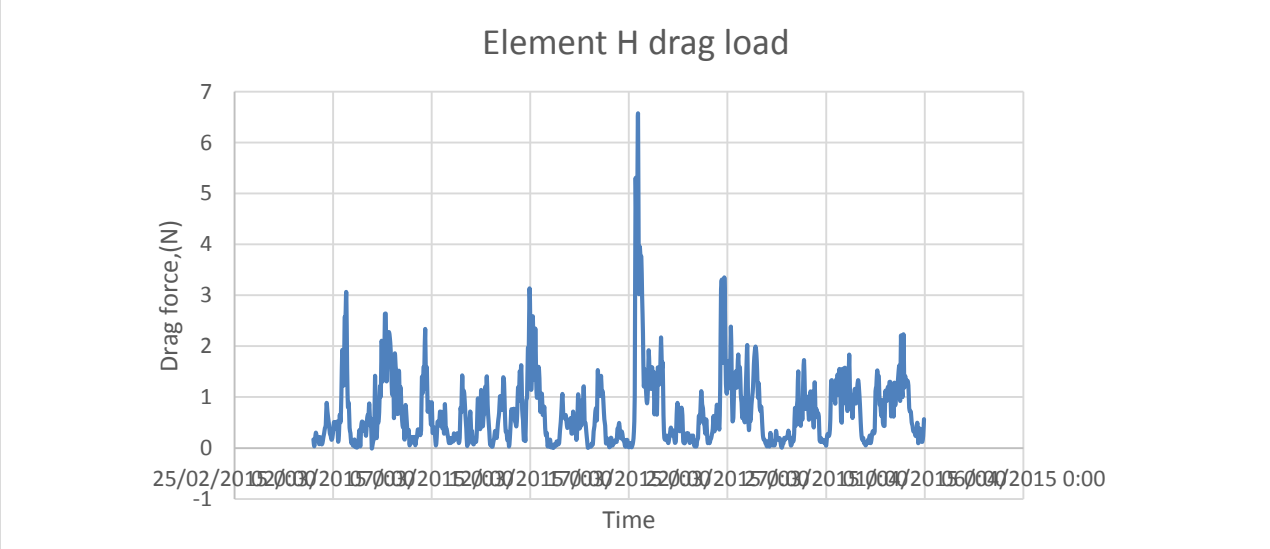
Element H drag load
Drag force,(N)
7
6
5
4
3
2
1
0
-1
25/02/2015 0:00
Time

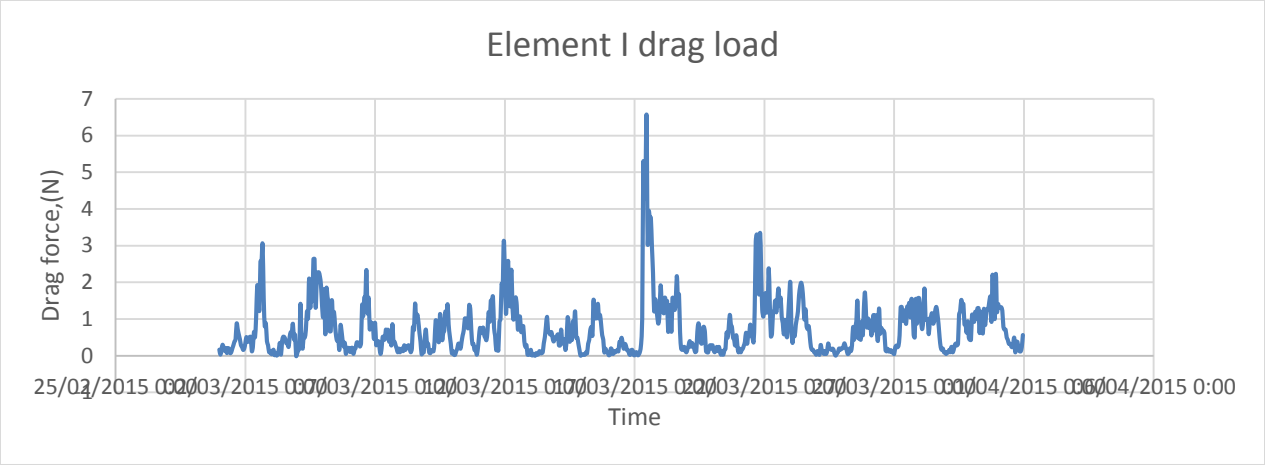
Element I drag load
Drag force,(N)
7
6
5
4
3
2
1
0
-1
25/02/2015 0:00
02/03/2015 0:00
07/03/2015 0:00
12/03/2015 0:00
17/03/2015 0:00
22/03/2015 0:00
27/03/2015 0:00
01/04/2015 0:00
06/04/2015 0:00
Time

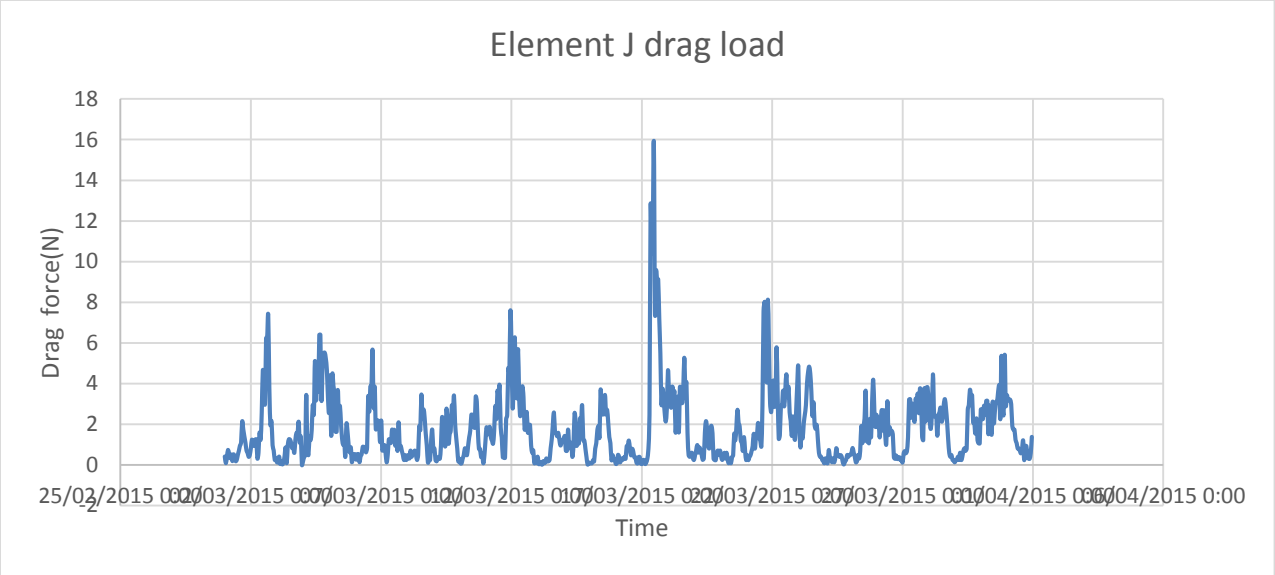
Element J drag load
Drag force(N)
18
16
14
12
10
8
6
4
2
0
-2
25/02/2015 0:00
02/03/2015 0:00
07/03/2015 0:00
12/03/2015 0:00
17/03/2015 0:00
22/03/2015 0:00
27/03/2015 0:00
01/04/2015 0:00
06/04/2015 0:00
Time

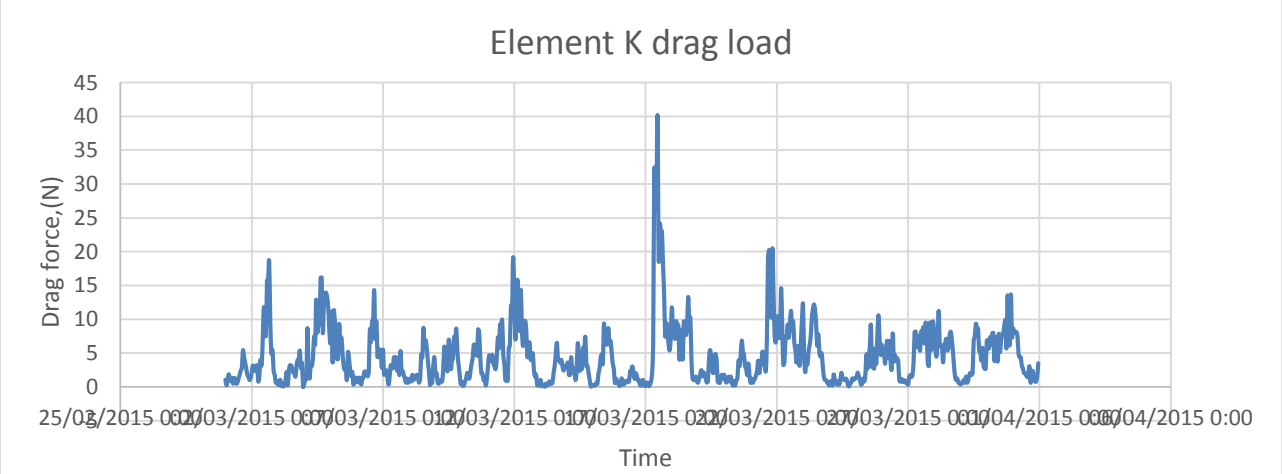
Element K drag load
Drag force,(N)
45
40
35
30
25
20
15
10
5
0
-5
25/02/2015 0:00
02/03/2015 0:00
07/03/2015 0:00
12/03/2015 0:00
17/03/2015 0:00
22/03/2015 0:00
27/03/2015 0:00
01/04/2015 0:00
06/04/2015 0:00
Time

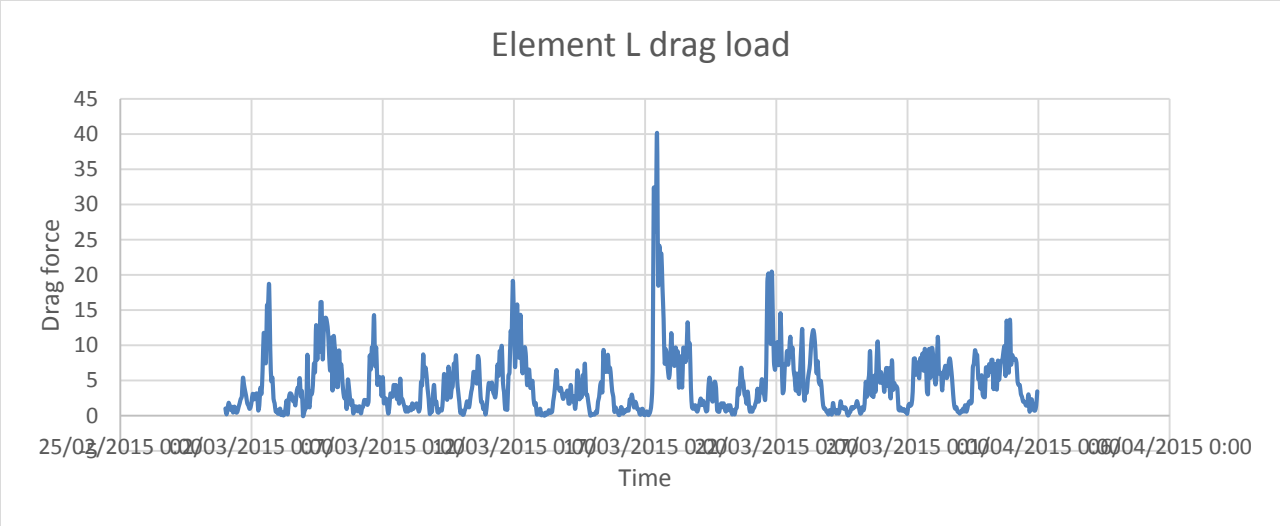

Figure C1.2 Time-history of the drag force on tracker elements in March, 2015.

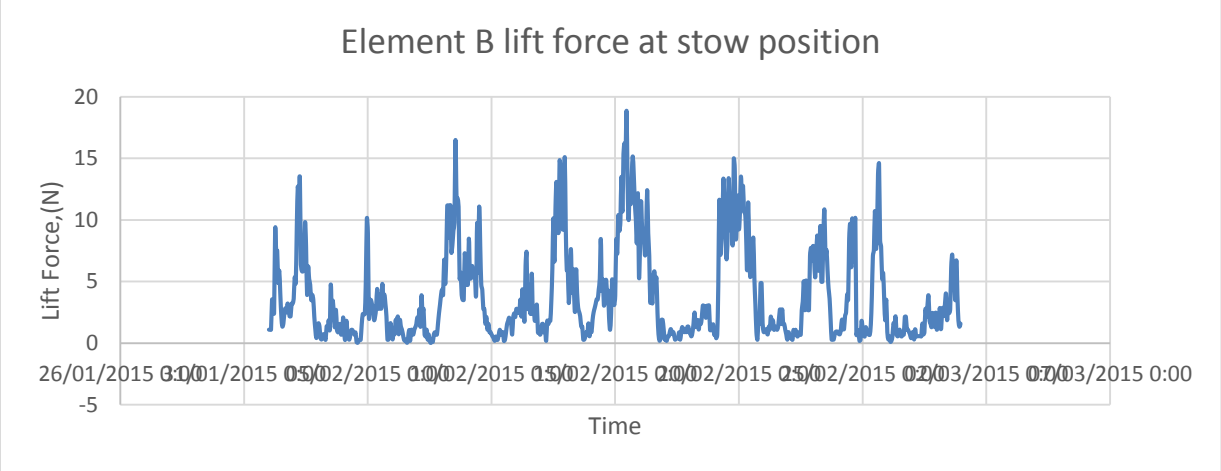

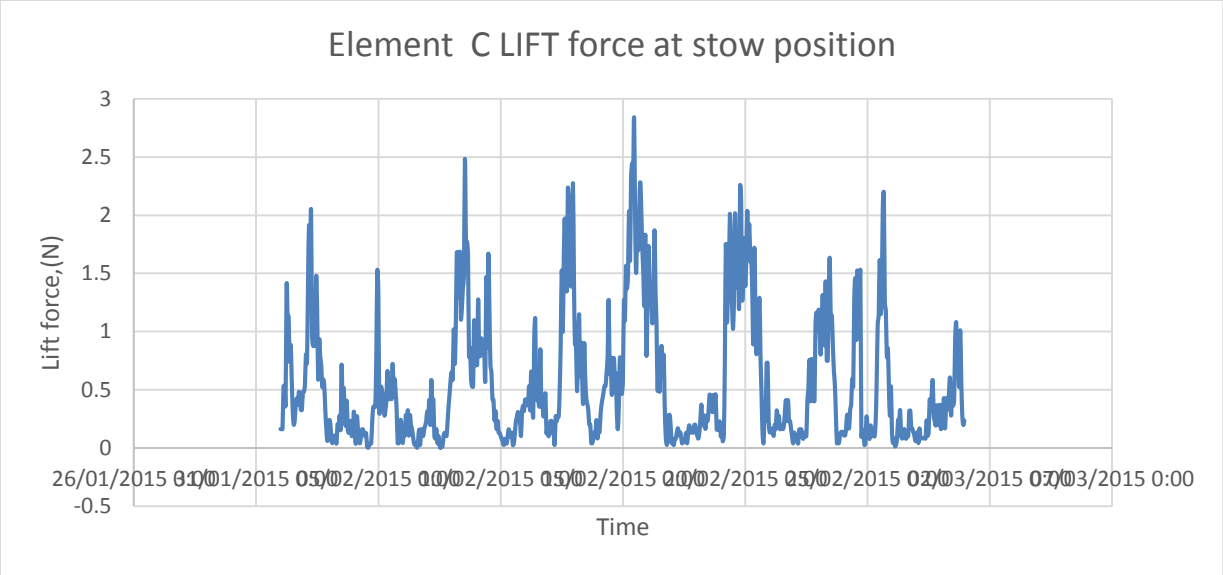
Element C LIFT force at stow position
Lift force,(N)
3
2.5
2
1.5
1
0.5
0
-0.5
26/01/2015 0:00
31/01/2015 0:00
05/02/2015 0:00
10/02/2015 0:00
15/02/2015 0:00
20/02/2015 0:00
25/02/2015 0:00
02/03/2015 0:00
07/03/2015 0:00
Time

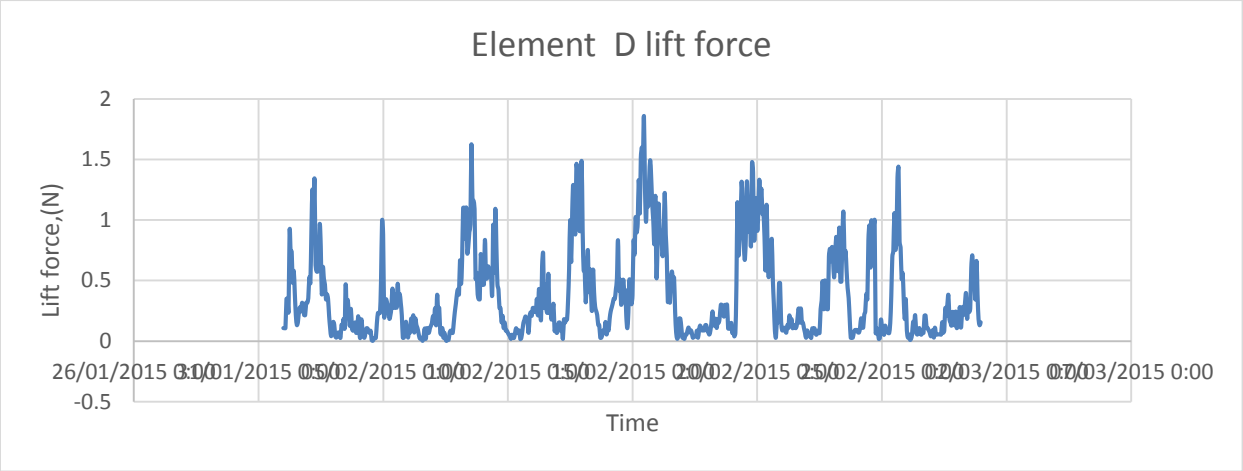
Element D lift force
Lift force,(N)
2
1.5
1
0.5
0
-0.5
26/01/2015 0:00
31/01/2015 0:00
05/02/2015 0:00
10/02/2015 0:00
15/02/2015 0:00
20/02/2015 0:00
25/02/2015 0:00
02/03/2015 0:00
07/03/2015 0:00
Time

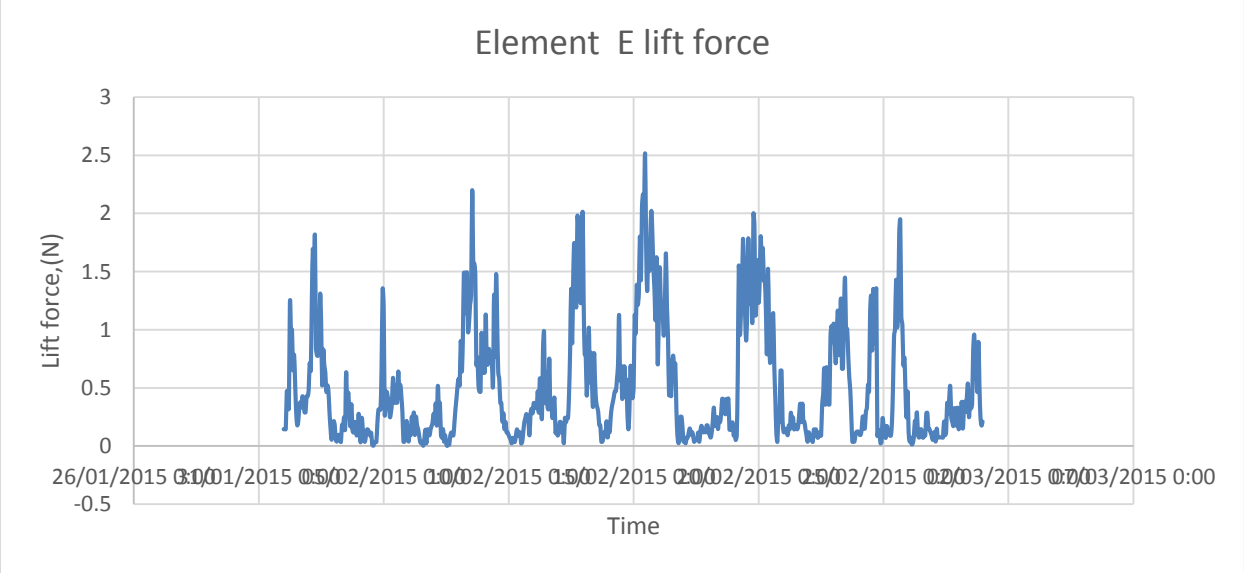
Element E lift force
Lift force,(N)
3
2.5
2
1.5
1
0.5
0
-0.5
26/01/2015 0:00
31/01/2015 0:00
05/02/2015 0:00
10/02/2015 0:00
15/02/2015 0:00
20/02/2015 0:00
25/02/2015 0:00
02/03/2015 0:00
07/03/2015 0:00
Time

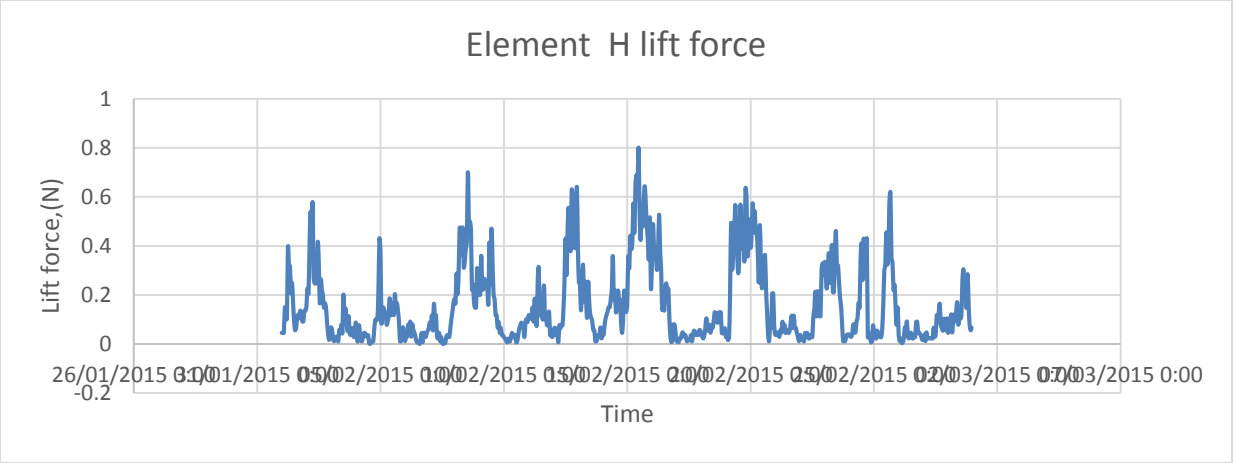
Element H lift force
Lift force,(N)
1
0.8
0.6
0.4
0.2
0
-0.2
26/01/2015 0:00
31/01/2015 0:00
05/02/2015 0:00
10/02/2015 0:00
15/02/2015 0:00
20/02/2015 0:00
25/02/2015 0:00
02/03/2015 0:00
07/03/2015 0:00
Time

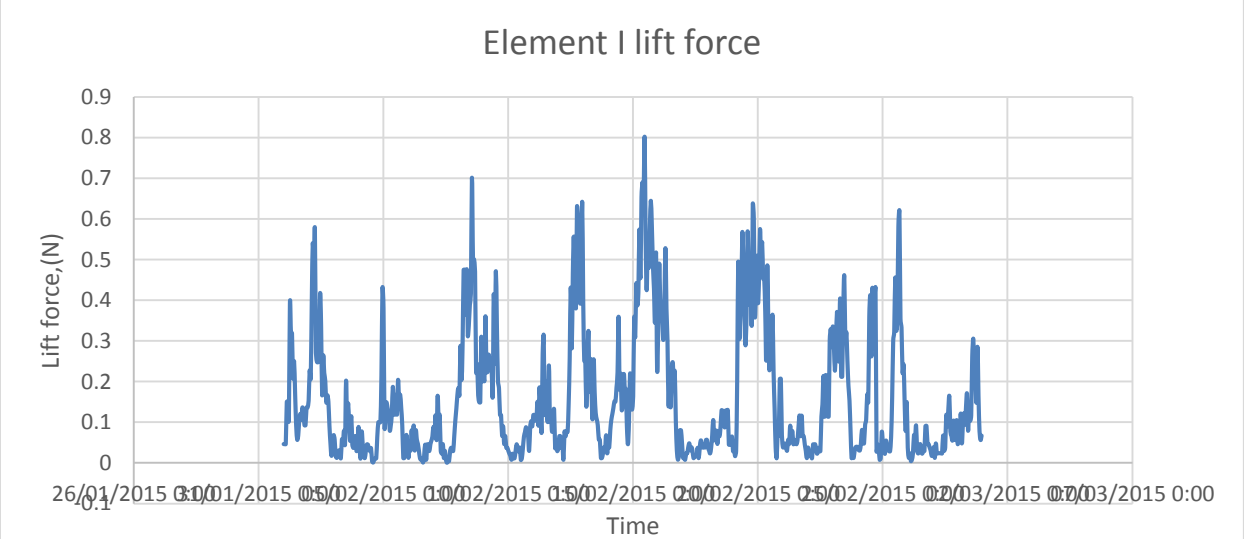
Element I lift force
Lift force,(N)
0.9
0.8
0.7
0.6
0.5
0.4
0.3
0.2
0.1
0
-0.1
26/01/2015 0:00
31/01/2015 0:00
05/02/2015 0:00
10/02/2015 0:00
15/02/2015 0:00
20/02/2015 0:00
25/02/2015 0:00
02/03/2015 0:00
07/03/2015 0:00
Time

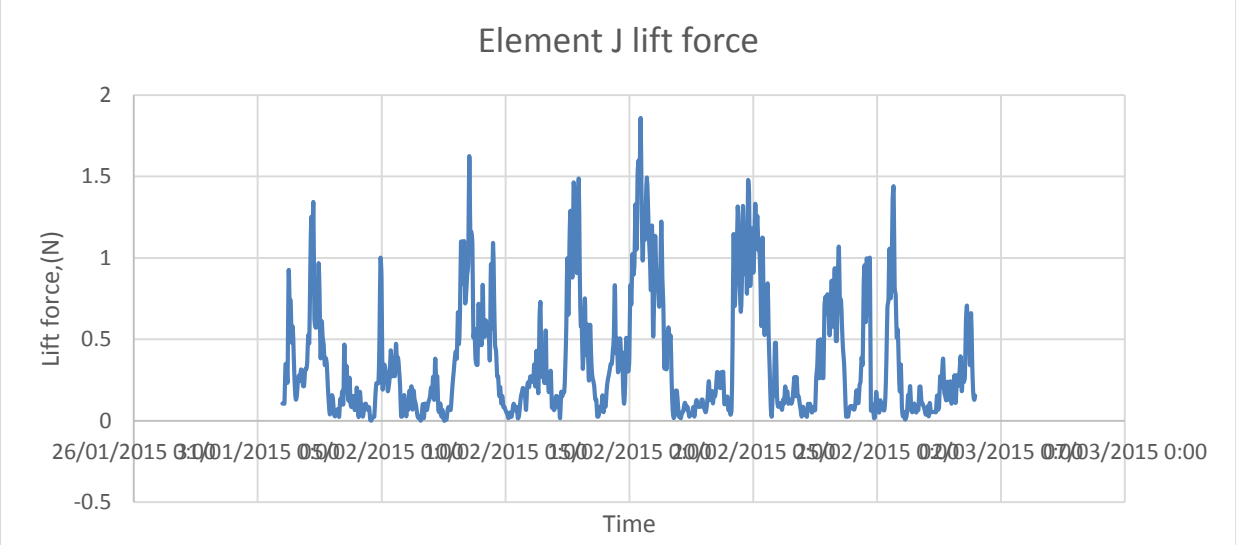
Element J lift force
Lift force,(N)
2
1.5
1
0.5
0
-0.5
26/01/2015 0:00
31/01/2015 0:00
05/02/2015 0:00
10/02/2015 0:00
15/02/2015 0:00
20/02/2015 0:00
25/02/2015 0:00
02/03/2015 0:00
07/03/2015 0:00
Time

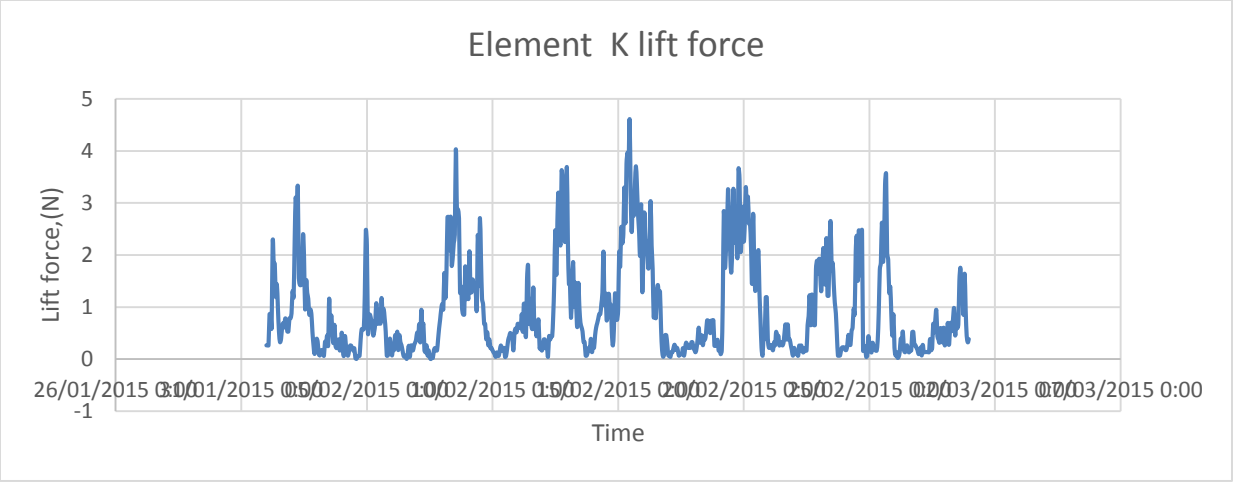
Element K lift force
Lift force,(N)
5
4
3
2
1
0
-1
26/01/2015 0:00
31/01/2015 0:00
05/02/2015 0:00
10/02/2015 0:00
15/02/2015 0:00
20/02/2015 0:00
25/02/2015 0:00
02/03/2015 0:00
07/03/2015 0:00
Time

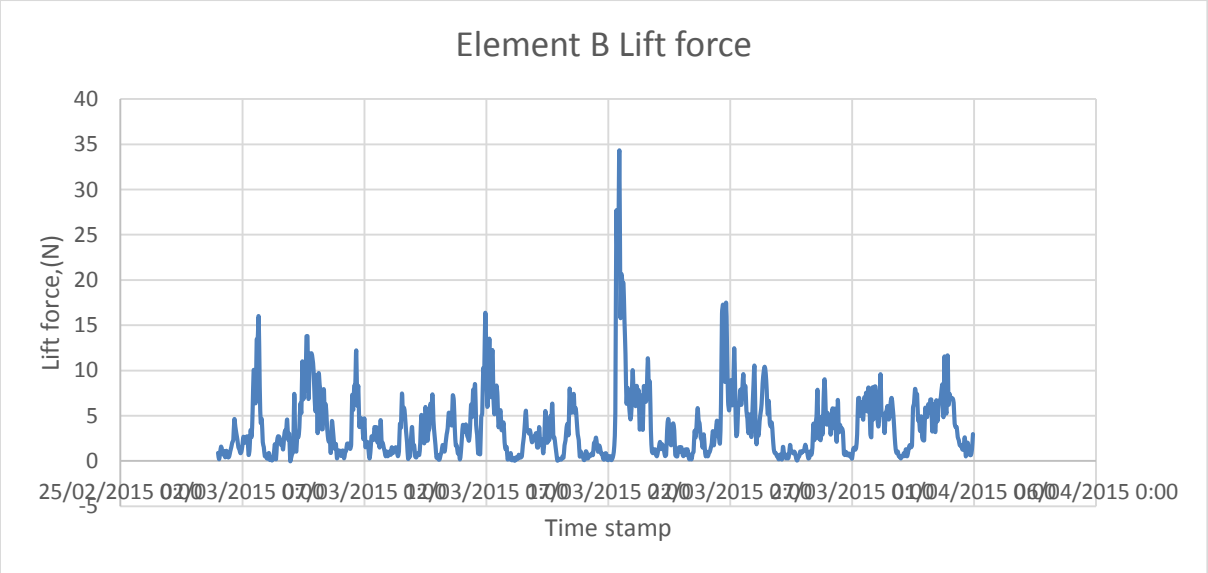
Element B Lift force
Lift force,(N)
40
35
30
25
20
15
10
5
0
-5
25/02/2015 0:00
02/03/2015 0:00
07/03/2015 0:00
12/03/2015 0:00
17/03/2015 0:00
22/03/2015 0:00
27/03/2015 0:00
01/04/2015 0:00
06/04/2015 0:00
Time stamp

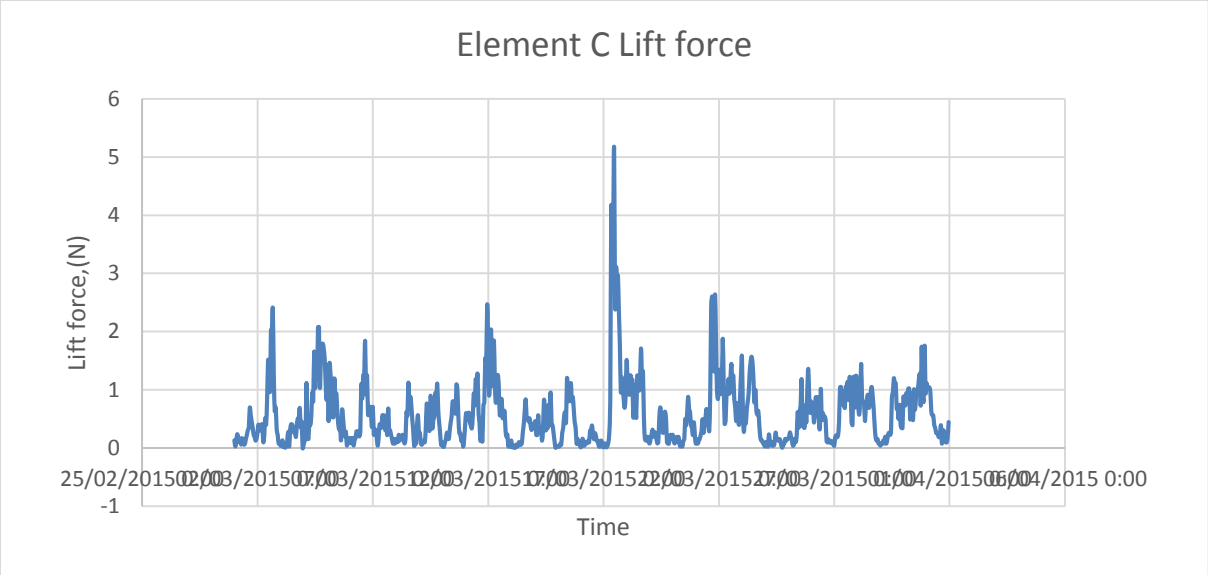
Element C Lift force
Lift force,(N)
Time
6
5
4
3
2
1
0
-1
25/02/2015 0:00
02/03/2015 0:00
07/03/2015 0:00
12/03/2015 0:00
17/03/2015 0:00
22/03/2015 0:00
27/03/2015 0:00
01/04/2015 0:00
06/04/2015 0:00

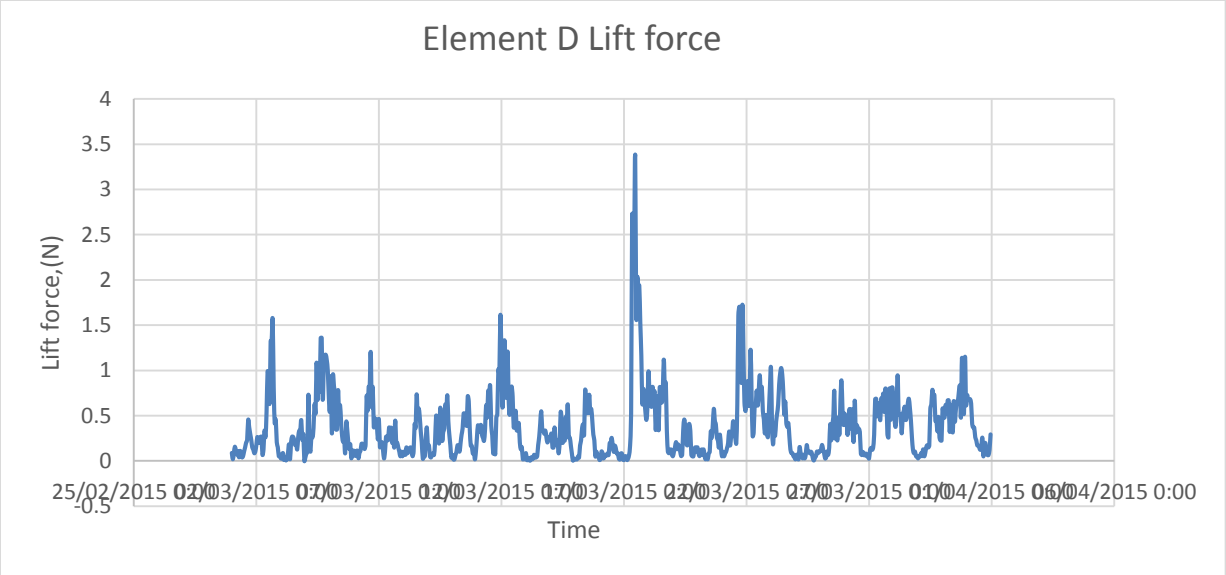
Element D Lift force
Lift force,(N)
Time
4
3.5
3
2.5
2
1.5
1
0.5
0
-0.5
25/02/2015 0:00
02/03/2015 0:00
07/03/2015 0:00
12/03/2015 0:00
17/03/2015 0:00
22/03/2015 0:00
27/03/2015 0:00
01/04/2015 0:00
06/04/2015 0:00

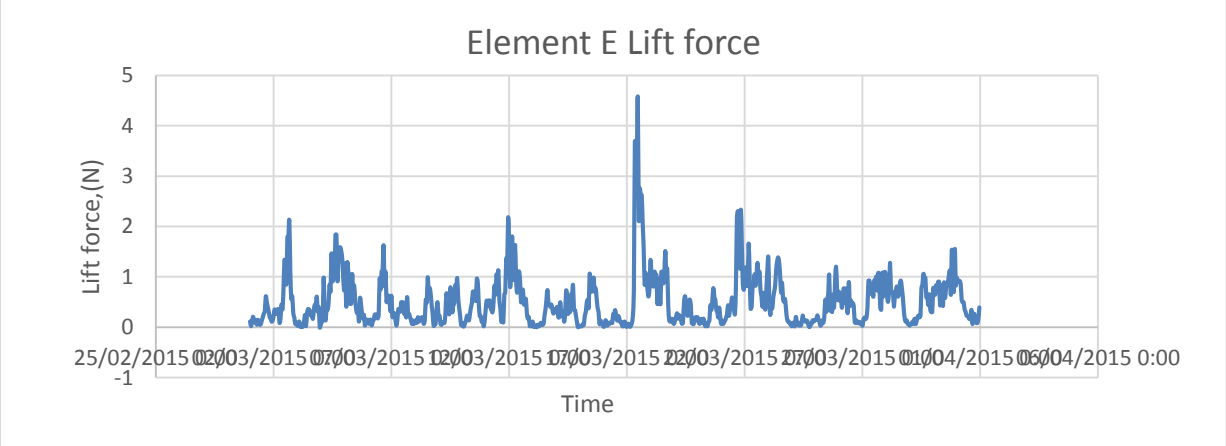
Element E Lift force
Lift force,(N)
Time
5
4
3
2
1
0
-1
25/02/2015 0:00
02/03/2015 0:00
07/03/2015 0:00
12/03/2015 0:00
17/03/2015 0:00
22/03/2015 0:00
27/03/2015 0:00
01/04/2015 0:00
06/04/2015 0:00

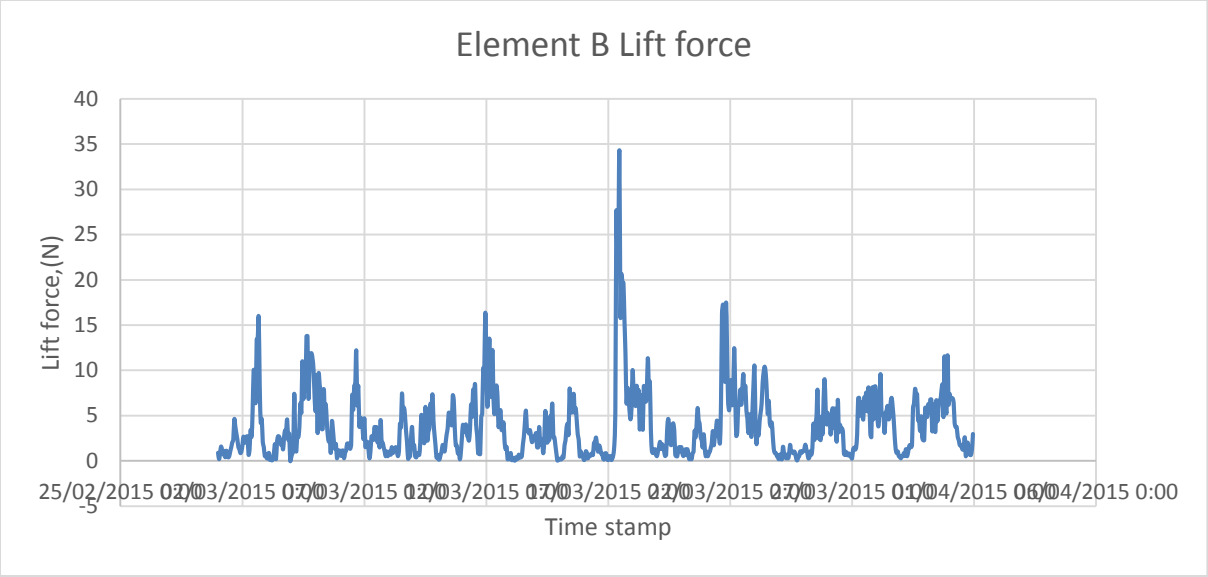
Element B Lift force
Lift force,(N)
40
35
30
25
20
15
10
5
0
-5
25/02/2015 0:00
02/03/2015 07:00
07/03/2015 12:00
12/03/2015 17:00
17/03/2015 22:00
22/03/2015 03:00
27/03/2015 08:00
01/04/2015 13:00
06/04/2015 0:00
Time stamp

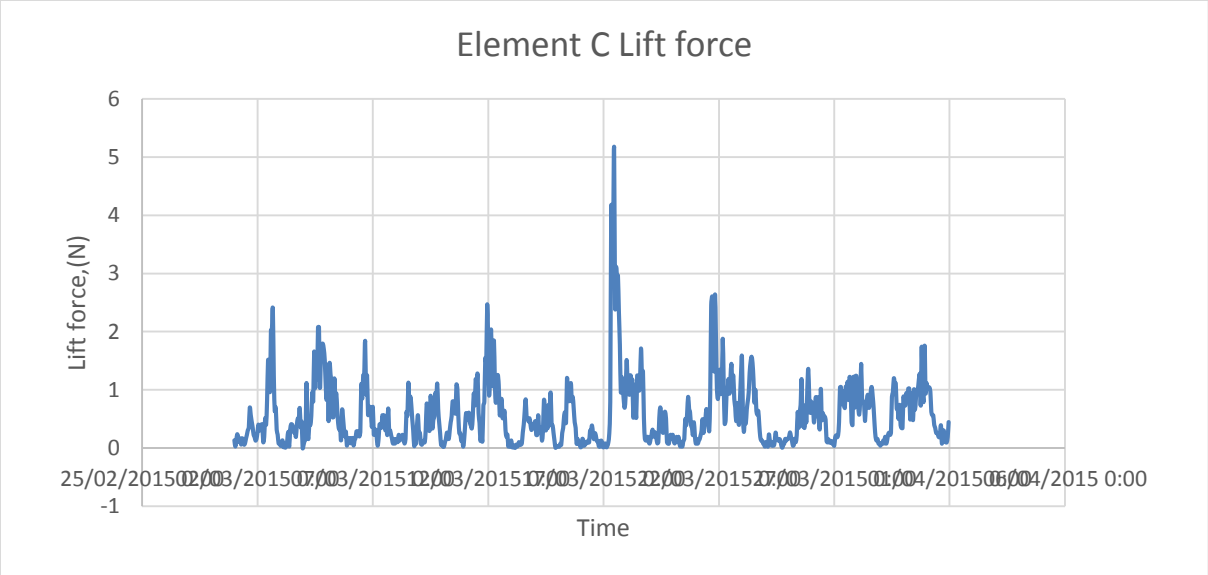
Element C Lift force
Lift force,(N)
6
5
4
3
2
1
0
-1
25/02/2015 0:00
02/03/2015 07:00
07/03/2015 12:00
12/03/2015 17:00
17/03/2015 22:00
22/03/2015 03:00
27/03/2015 08:00
01/04/2015 13:00
06/04/2015 0:00
Time

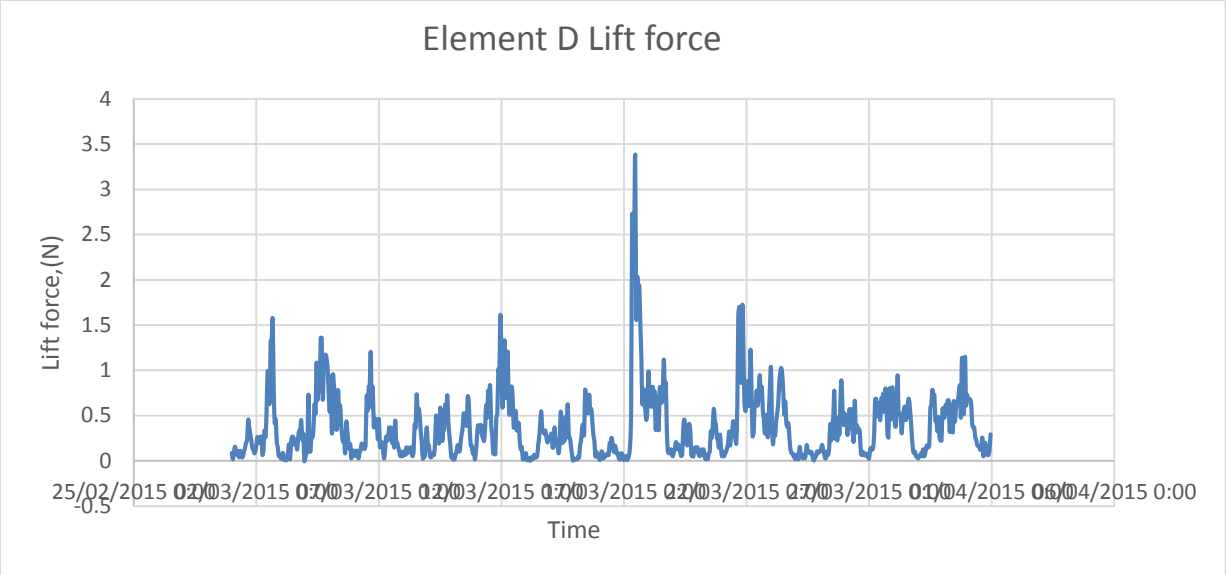
Element D Lift force
Lift force,(N)
4
3.5
3
2.5
2
1.5
1
0.5
0
-0.5
25/02/2015 0:00
02/03/2015 0:00
07/03/2015 0:00
12/03/2015 0:00
17/03/2015 0:00
22/03/2015 0:00
27/03/2015 0:00
01/04/2015 0:00
06/04/2015 0:00
Time

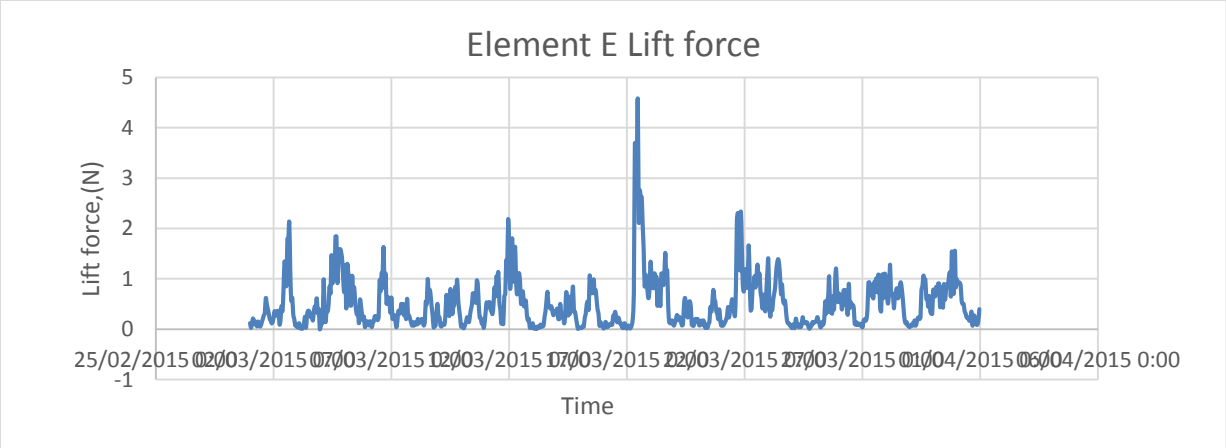
Element E Lift force
Lift force,(N)
5
4
3
2
1
0
-1
25/02/2015 0:00
02/03/2015 0:00
07/03/2015 0:00
12/03/2015 0:00
17/03/2015 0:00
22/03/2015 0:00
27/03/2015 0:00
01/04/2015 0:00
06/04/2015 0:00
Time

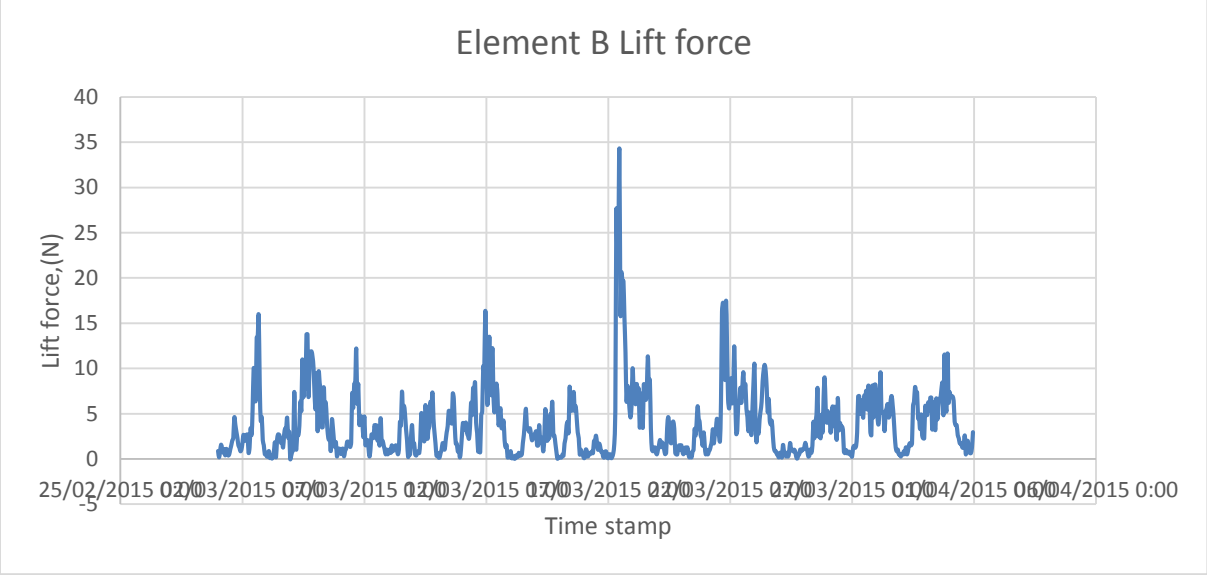
Element B Lift force
Lift force,(N)
40
35
30
25
20
15
10
5
0
-5
25/02/2015 0:00
02/03/2015 0:00
07/03/2015 0:00
12/03/2015 0:00
17/03/2015 0:00
22/03/2015 0:00
27/03/2015 0:00
01/04/2015 0:00
06/04/2015 0:00
Time stamp

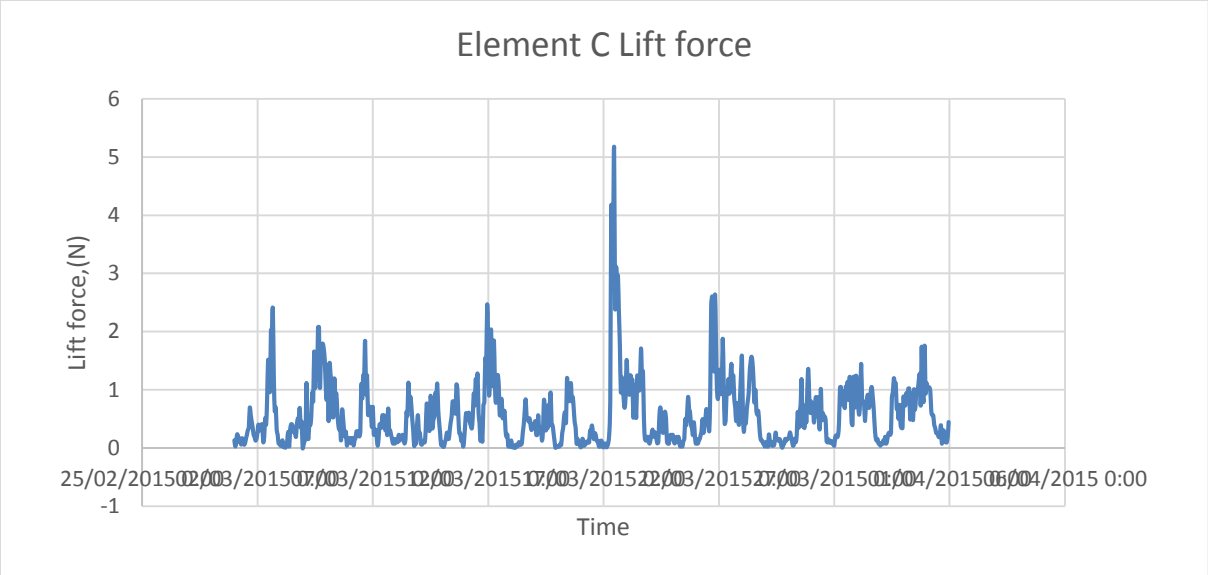
Element C Lift force
Lift force,(N)
Time

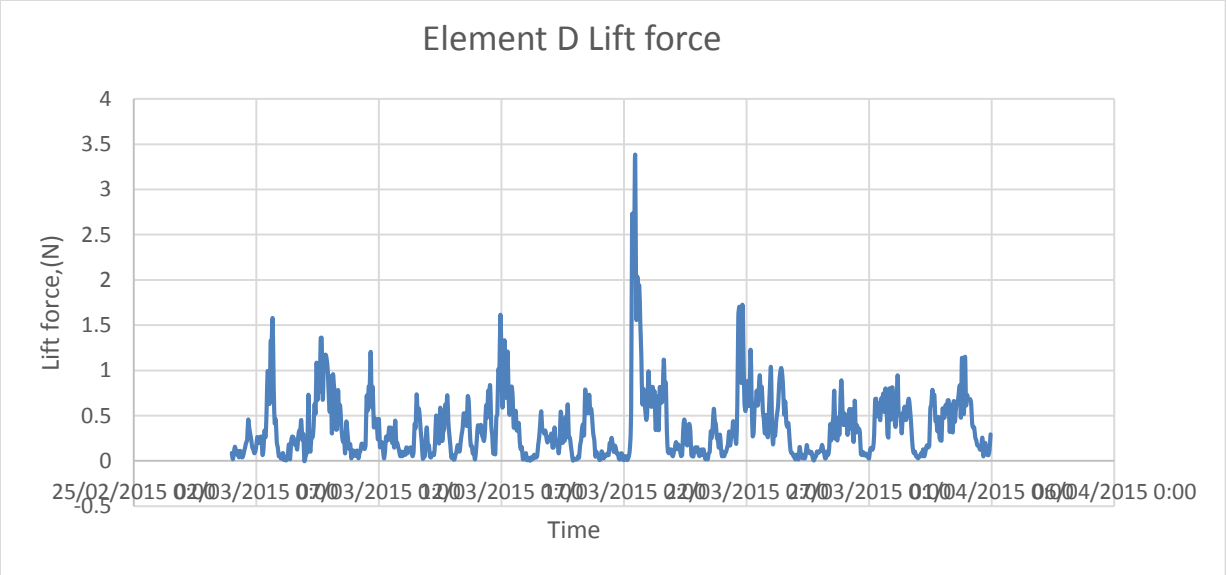
Element D Lift force
Lift force,(N)
Time

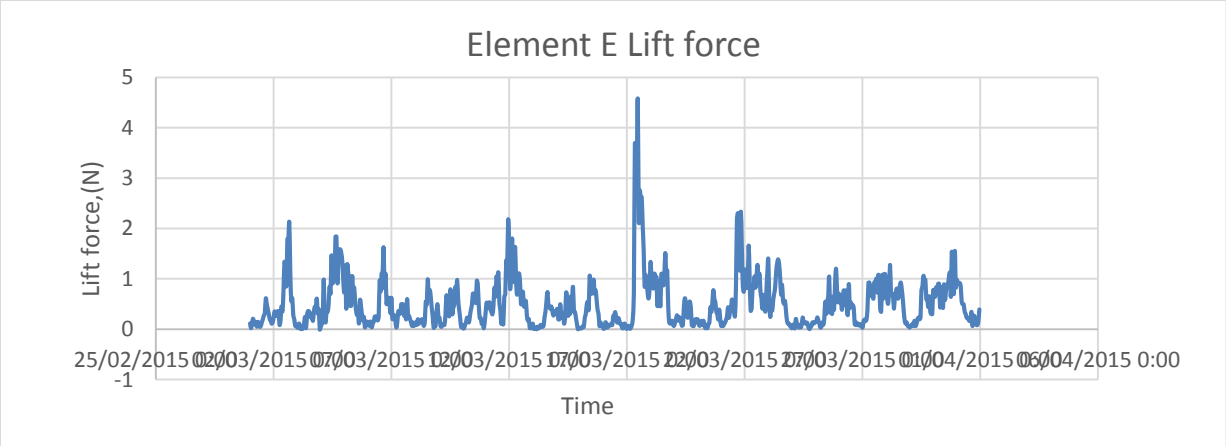
Element E Lift force
Lift force,(N)
Time

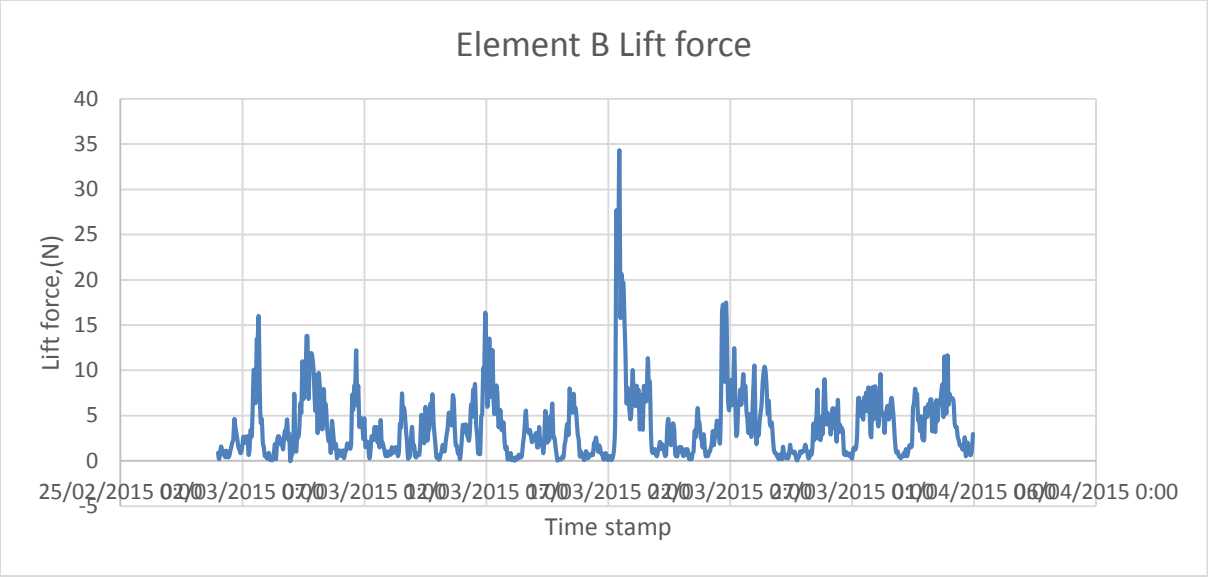
Element B Lift force
Lift force,(N)
40
35
30
25
20
15
10
5
0
-5
25/02/2015 0:00
02/03/2015 07:00
07/03/2015 12:00
12/03/2015 17:00
17/03/2015 22:00
22/03/2015 03:00
27/03/2015 08:00
01/04/2015 13:00
06/04/2015 0:00
Time stamp

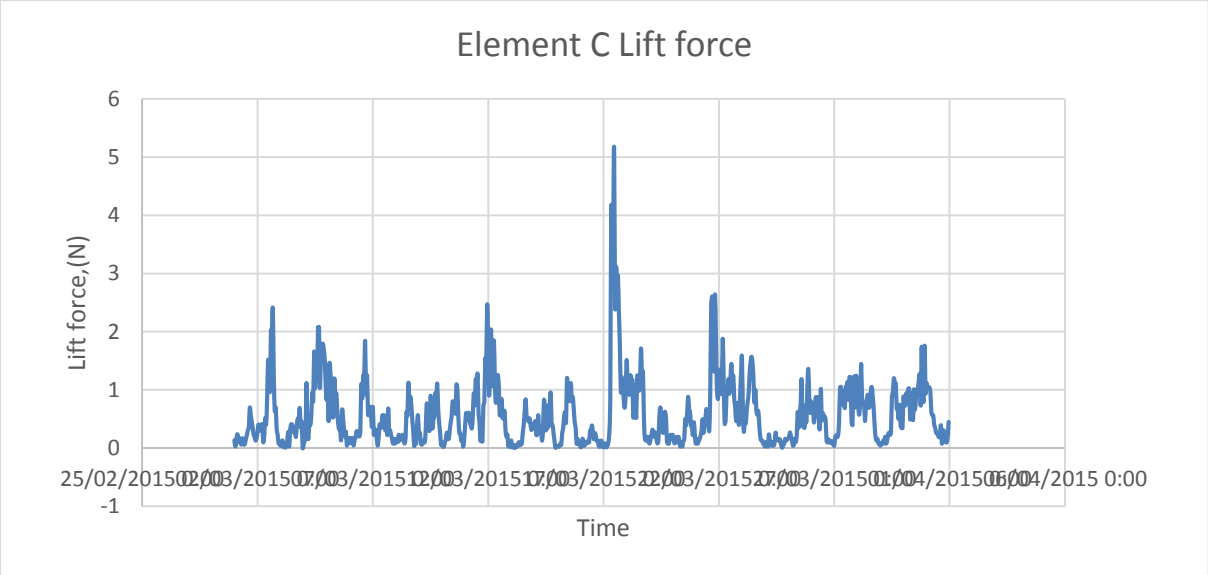
Element C Lift force
Lift force,(N)
6
5
4
3
2
1
0
-1
25/02/2015 0:00
02/03/2015 07:00
07/03/2015 12:00
12/03/2015 17:00
17/03/2015 22:00
22/03/2015 03:00
27/03/2015 08:00
01/04/2015 13:00
06/04/2015 0:00
Time

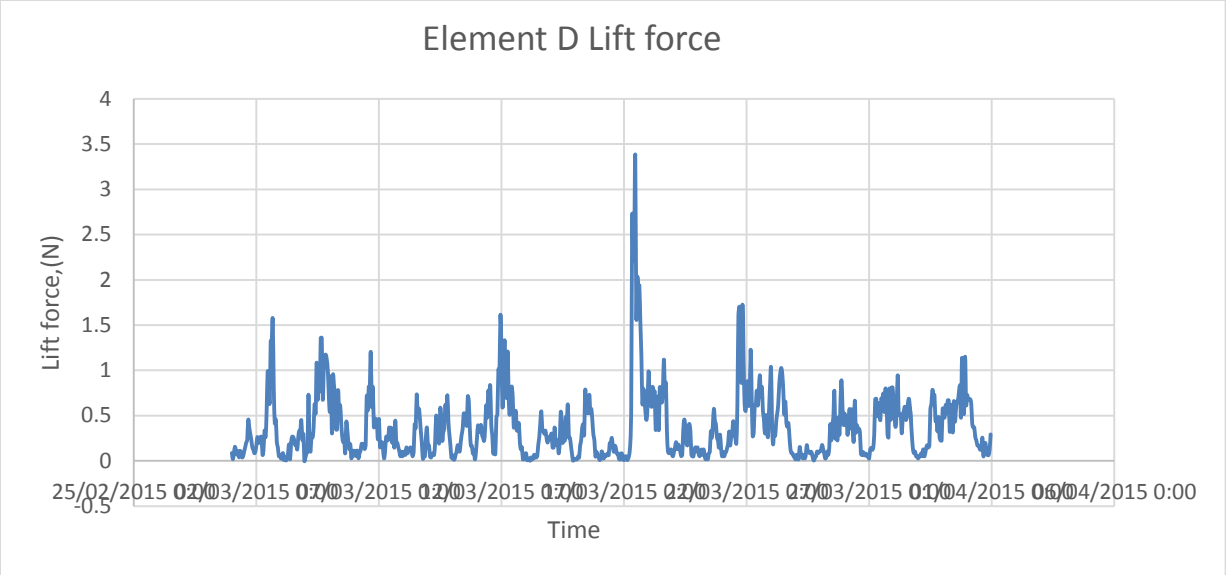
Element D Lift force
Lift force,(N)
4
3.5
3
2.5
2
1.5
1
0.5
0
-0.5
25/02/2015 0:00
02/03/2015 0:00
07/03/2015 0:00
12/03/2015 0:00
17/03/2015 0:00
22/03/2015 0:00
27/03/2015 0:00
01/04/2015 0:00
06/04/2015 0:00
Time

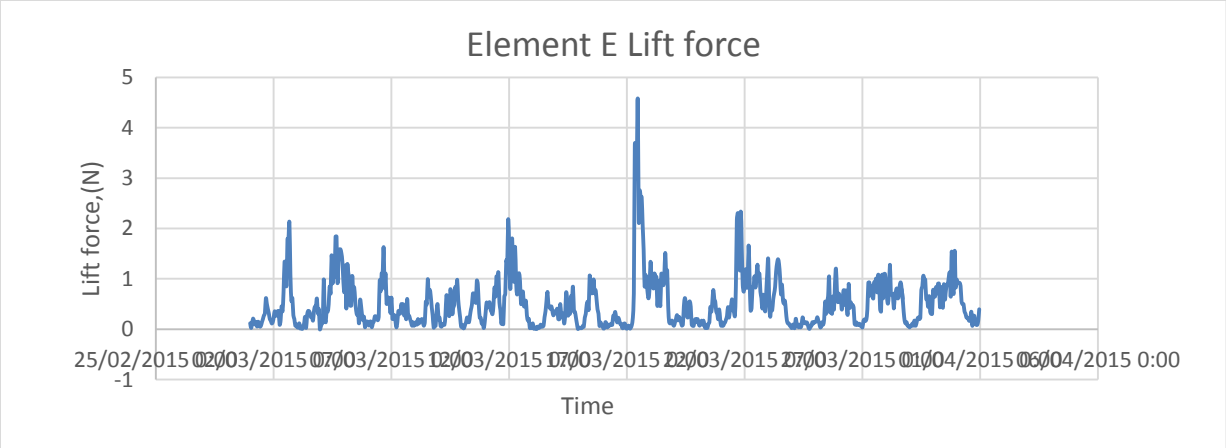
Element E Lift force
Lift force,(N)
5
4
3
2
1
0
-1
25/02/2015 0:00
02/03/2015 0:00
07/03/2015 0:00
12/03/2015 0:00
17/03/2015 0:00
22/03/2015 0:00
27/03/2015 0:00
01/04/2015 0:00
06/04/2015 0:00
Time

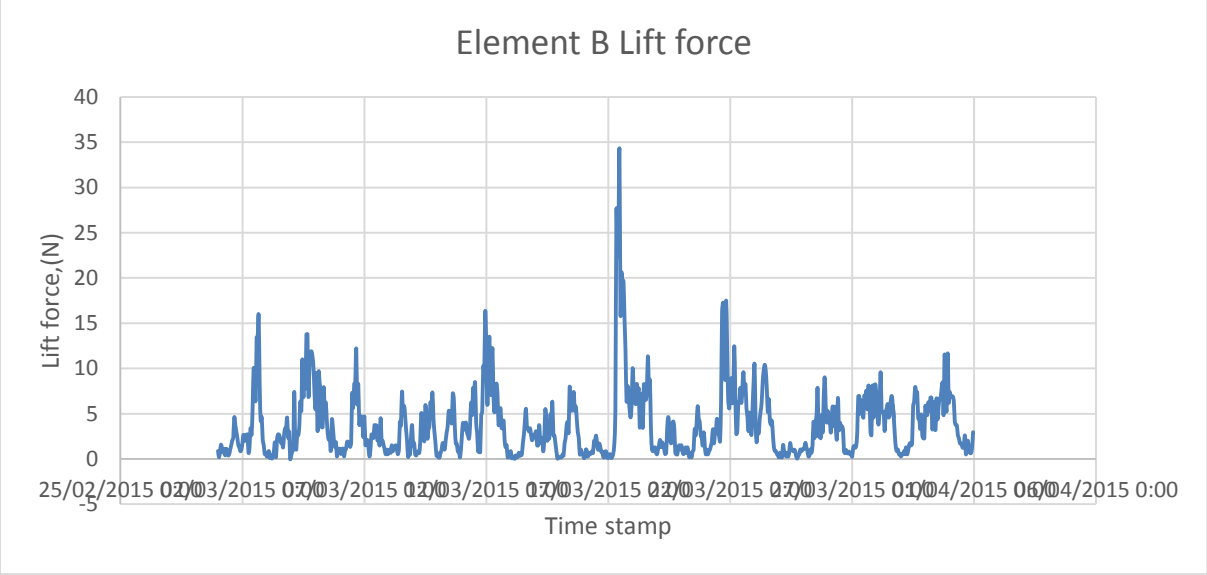
Element B Lift force
Lift force,(N)
40
35
30
25
20
15
10
5
0
-5
25/02/2015 0:00
02/03/2015 0:00
07/03/2015 0:00
12/03/2015 0:00
17/03/2015 0:00
22/03/2015 0:00
27/03/2015 0:00
01/04/2015 0:00
06/04/2015 0:00
Time stamp

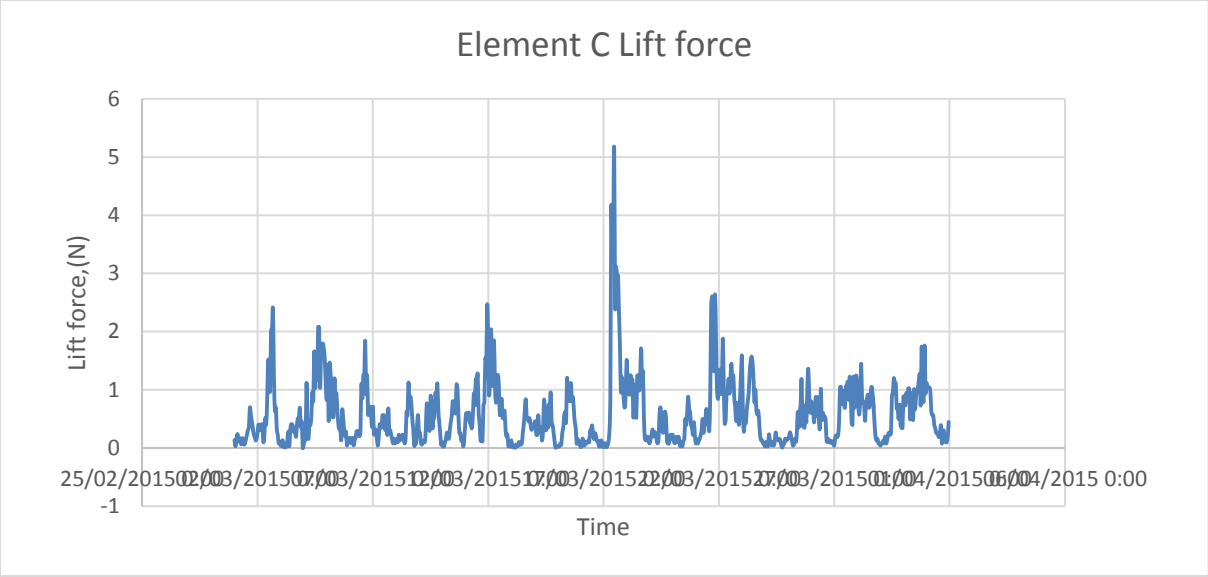
Element C Lift force
Lift force,(N)
6
5
4
3
2
1
0
-1
25/02/2015 0:00
02/03/2015 0:00
07/03/2015 0:00
12/03/2015 0:00
17/03/2015 0:00
22/03/2015 0:00
27/03/2015 0:00
01/04/2015 0:00
06/04/2015 0:00
Time

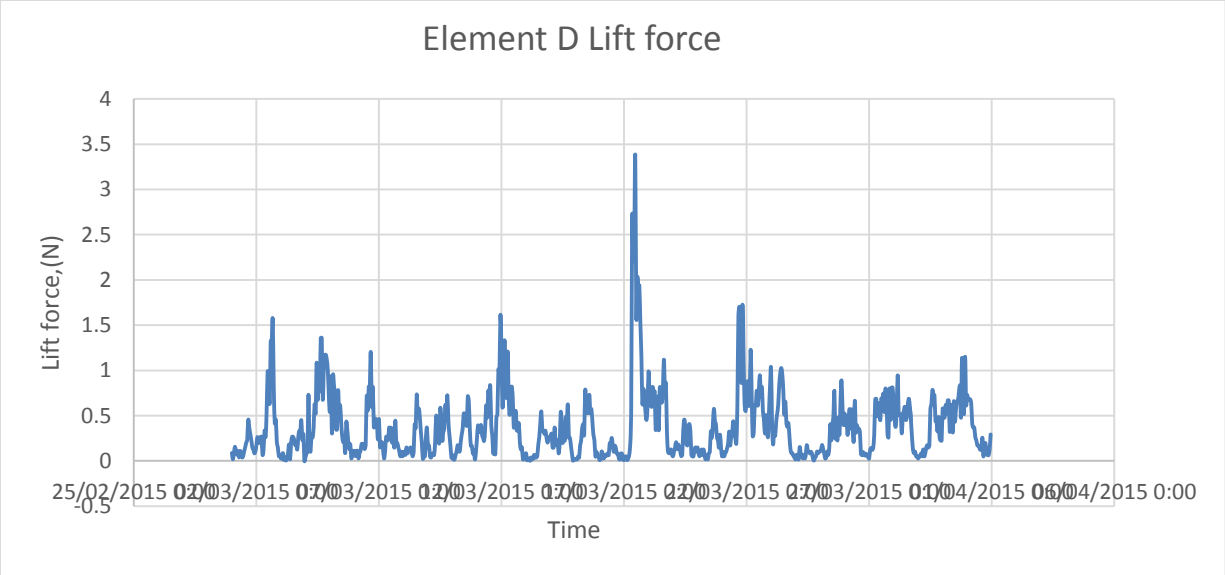
Element D Lift force
Lift force,(N)
4
3.5
3
2.5
2
1.5
1
0.5
0
-0.5
25/02/2015 0:00
02/03/2015 0:00
07/03/2015 0:00
12/03/2015 0:00
17/03/2015 0:00
22/03/2015 0:00
27/03/2015 0:00
01/04/2015 0:00
06/04/2015 0:00
Time

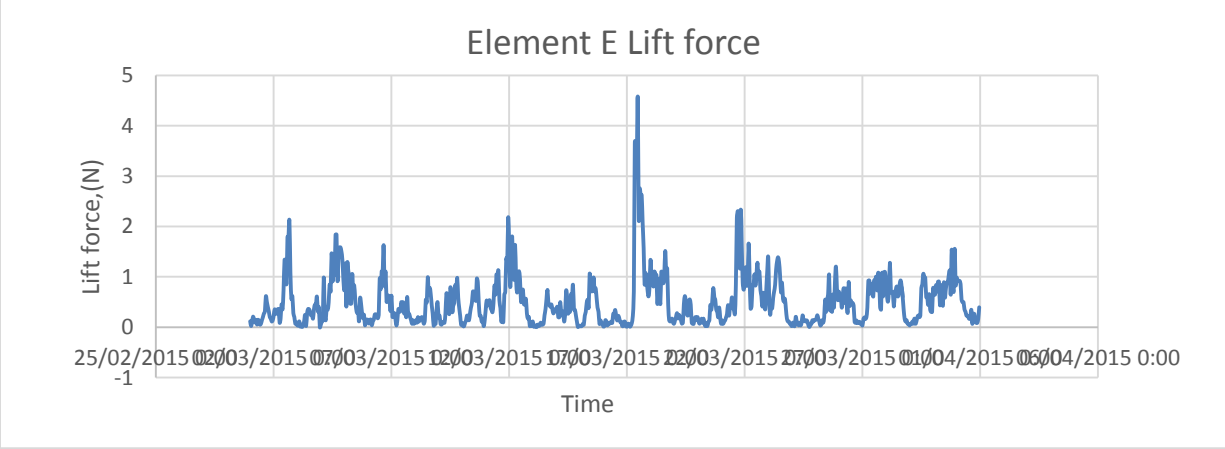
Element E Lift force
Lift force,(N)
5
4
3
2
1
0
-1
25/02/2015 0:00
02/03/2015 0:00
07/03/2015 0:00
12/03/2015 0:00
17/03/2015 0:00
22/03/2015 0:00
27/03/2015 0:00
01/04/2015 0:00
06/04/2015 0:00
Time

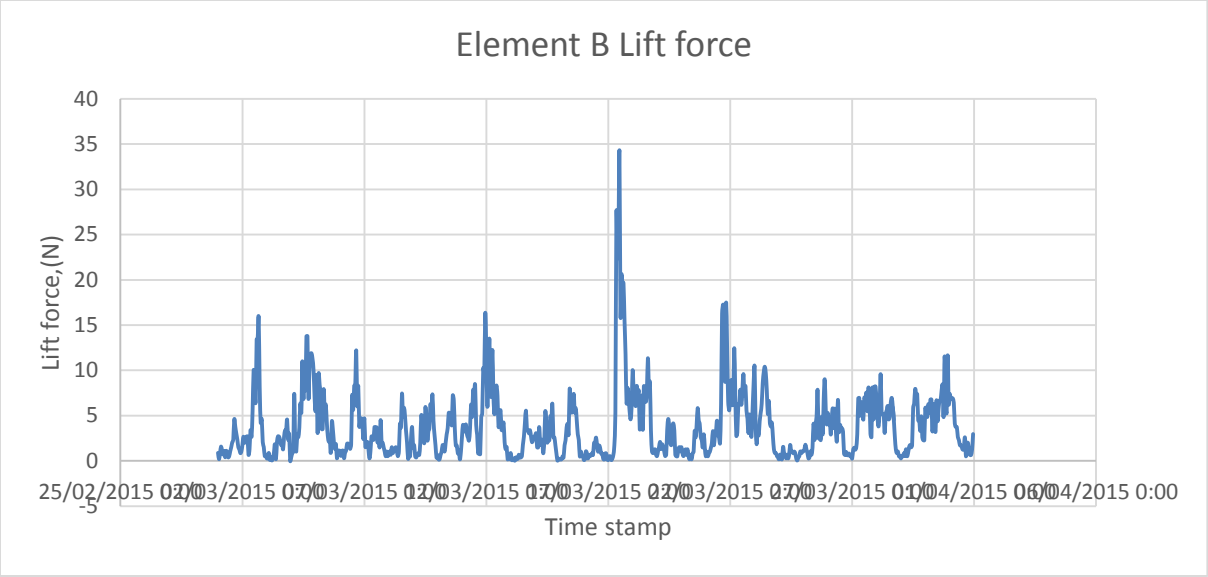
Element B Lift force
Lift force,(N)
40
35
30
25
20
15
10
5
0
-5
25/02/2015 0:00
02/03/2015 07:00
07/03/2015 12:00
12/03/2015 17:00
17/03/2015 22:00
22/03/2015 03:00
27/03/2015 08:00
01/04/2015 13:00
06/04/2015 0:00
Time stamp

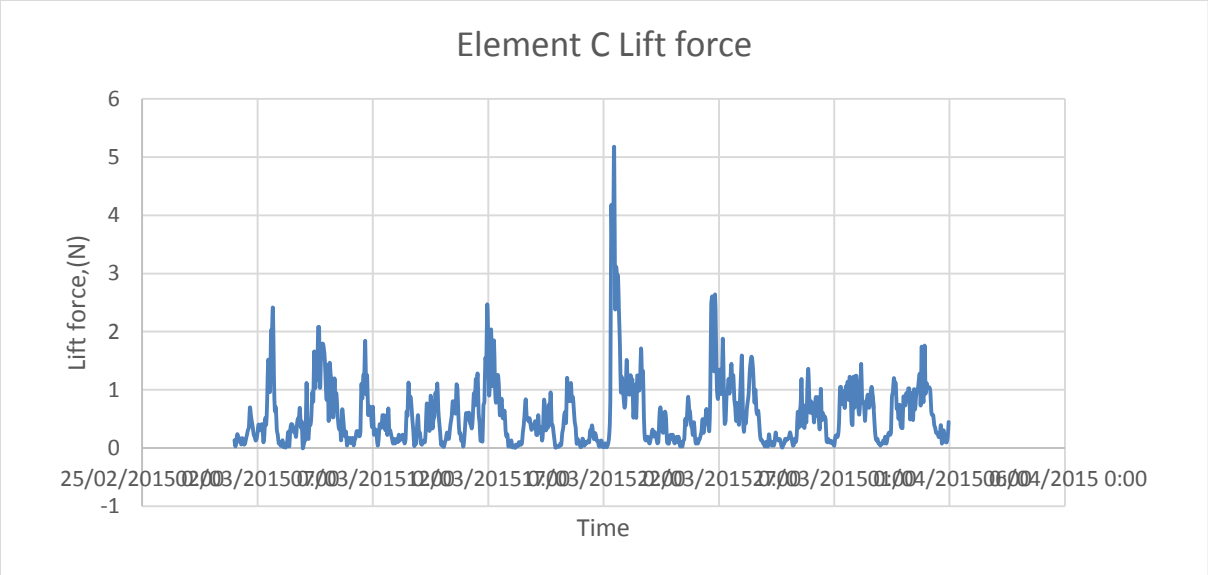
Element C Lift force
Lift force,(N)
6
5
4
3
2
1
0
-1
25/02/2015 0:00
02/03/2015 07:00
07/03/2015 12:00
12/03/2015 17:00
17/03/2015 22:00
22/03/2015 03:00
27/03/2015 08:00
01/04/2015 13:00
06/04/2015 0:00
Time

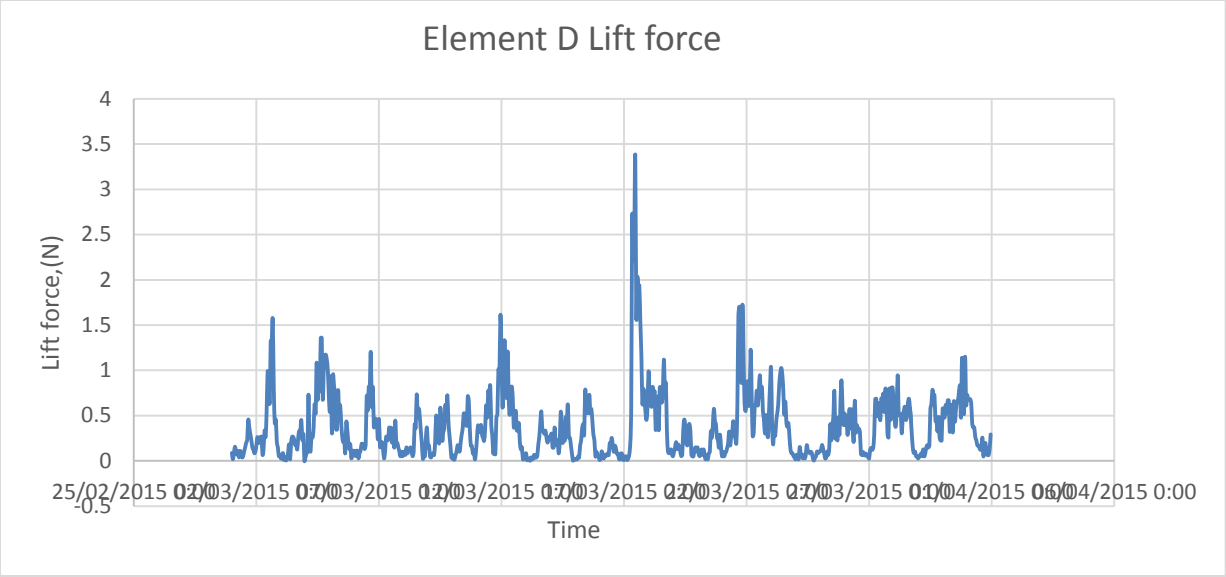
Element D Lift force
Lift force,(N)
4
3.5
3
2.5
2
1.5
1
0.5
0
-0.5
25/02/2015 0:00
02/03/2015 0:00
07/03/2015 0:00
12/03/2015 0:00
17/03/2015 0:00
22/03/2015 0:00
27/03/2015 0:00
01/04/2015 0:00
06/04/2015 0:00
Time

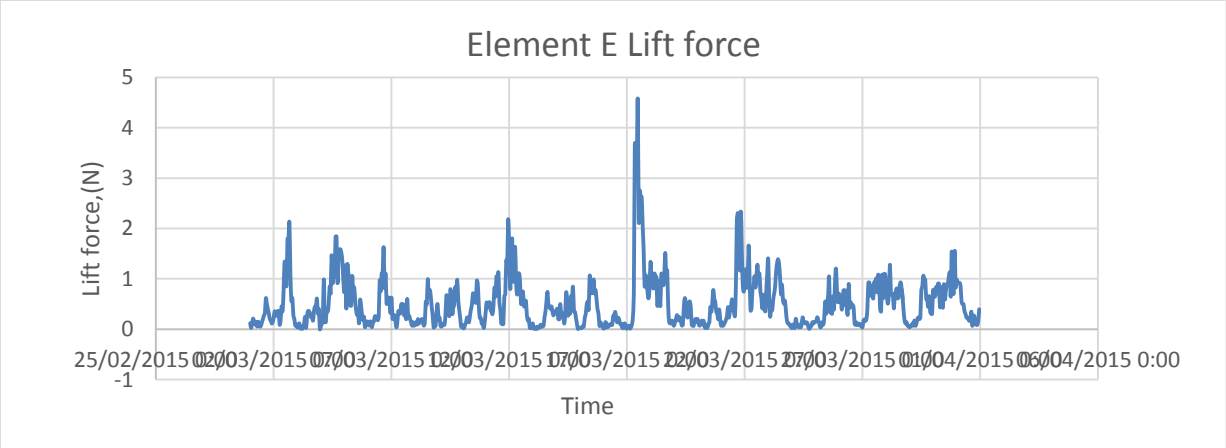
Element E Lift force
Lift force,(N)
5
4
3
2
1
0
-1
25/02/2015 0:00
02/03/2015 0:00
07/03/2015 0:00
12/03/2015 0:00
17/03/2015 0:00
22/03/2015 0:00
27/03/2015 0:00
01/04/2015 0:00
06/04/2015 0:00
Time

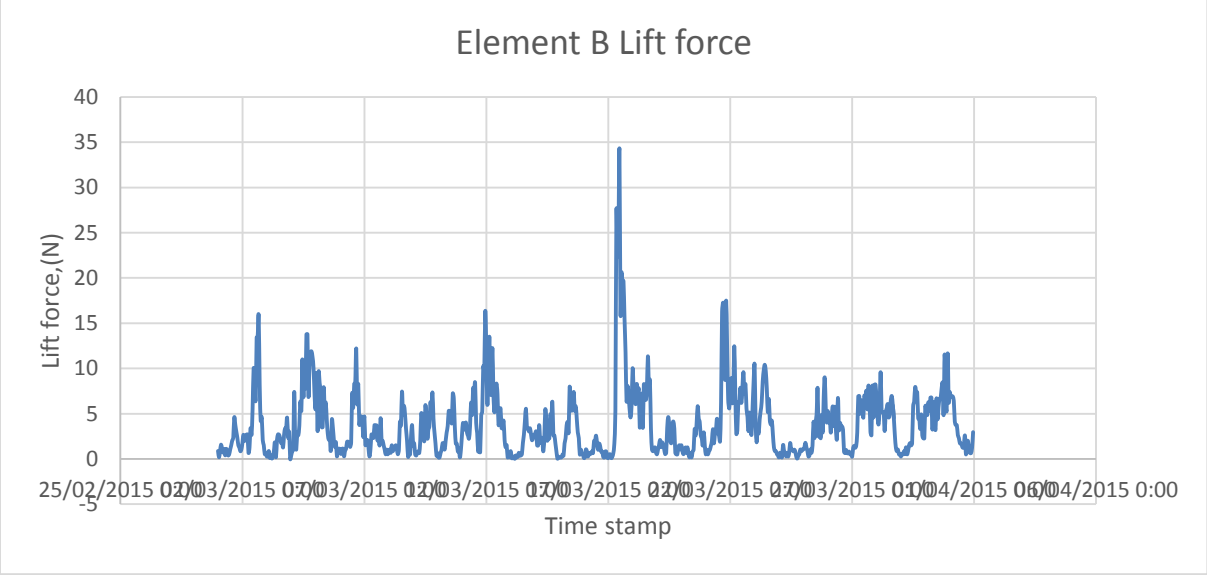
Element B Lift force
Lift force,(N)
40
35
30
25
20
15
10
5
0
-5
25/02/2015 0:00
02/03/2015 0:00
07/03/2015 0:00
12/03/2015 0:00
17/03/2015 0:00
22/03/2015 0:00
27/03/2015 0:00
01/04/2015 0:00
06/04/2015 0:00
Time stamp

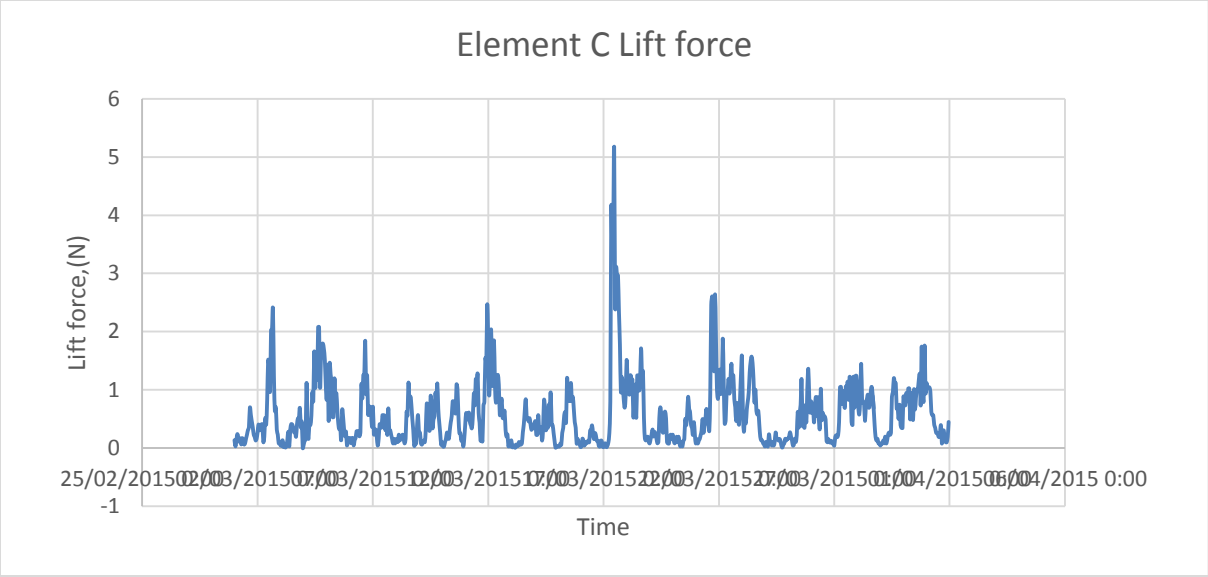
Element C Lift force
Lift force,(N)
Time

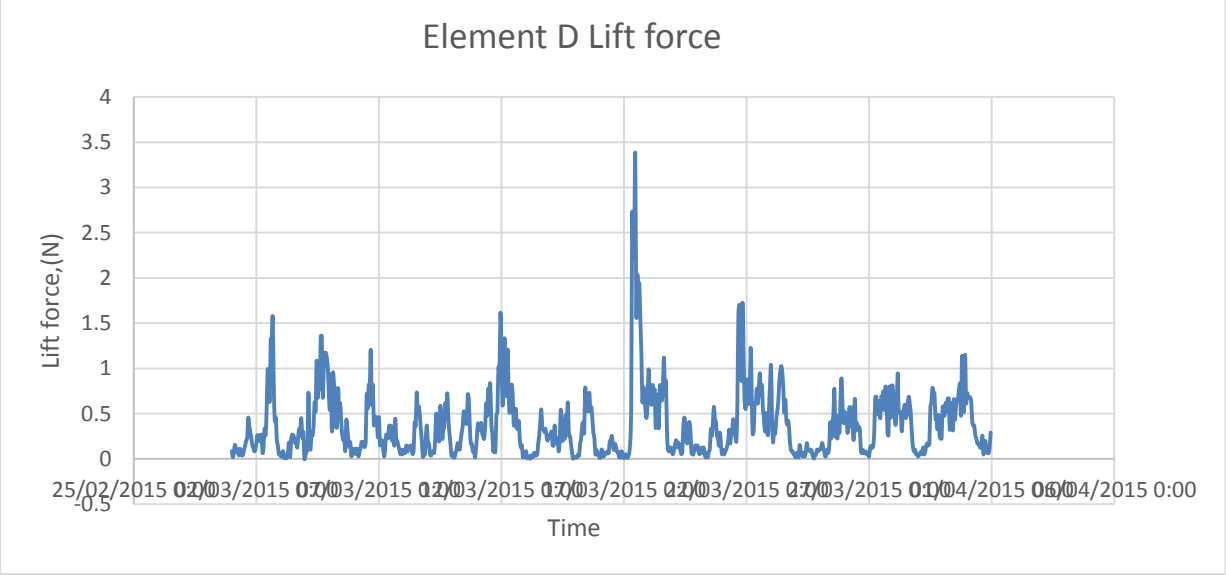
Element D Lift force
Lift force,(N)
Time

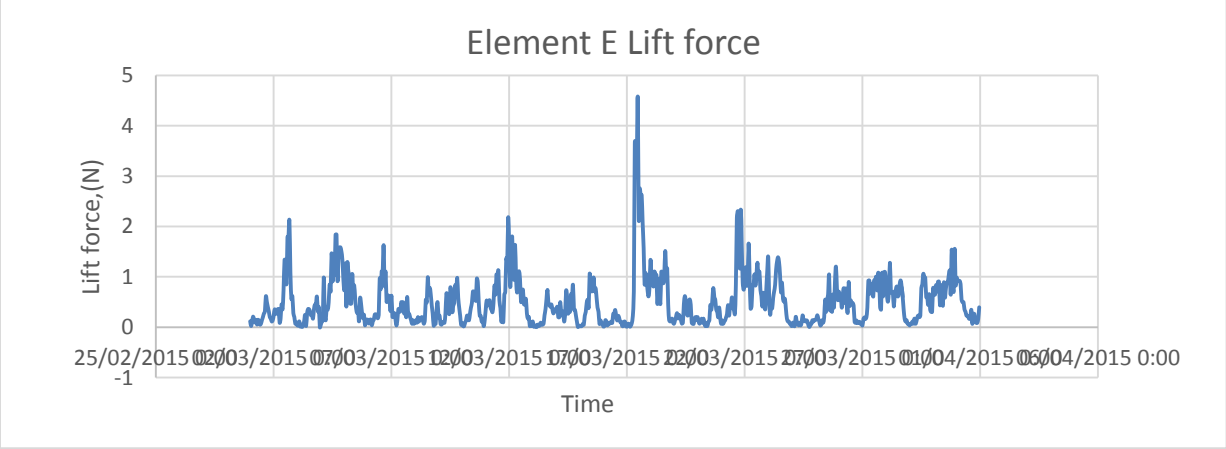
Element E Lift force
Lift force,(N)
Time

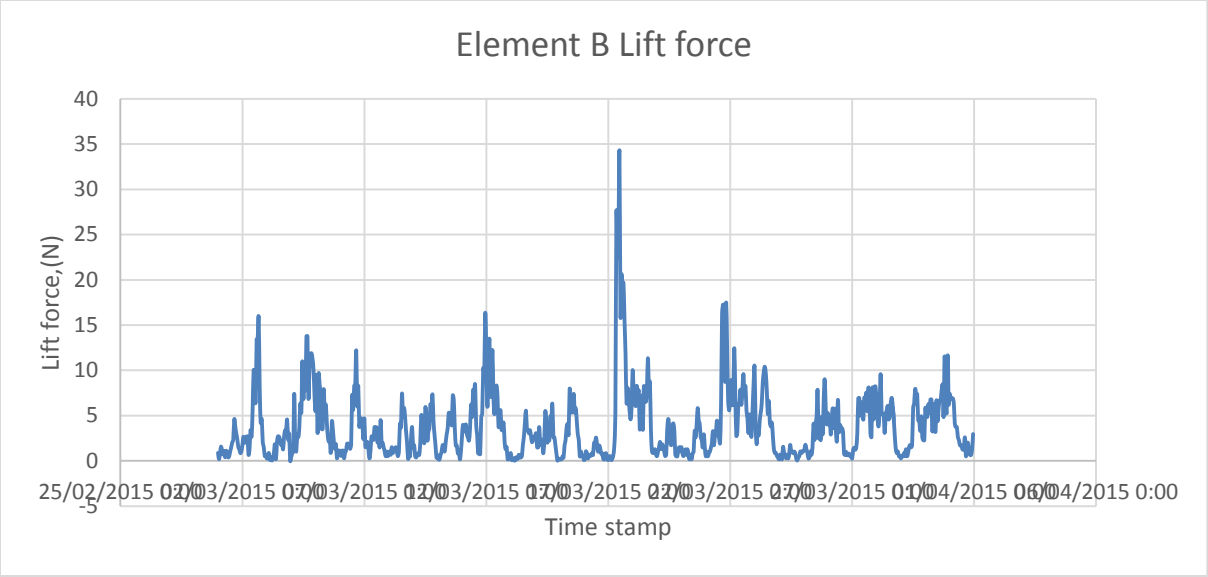
Element B Lift force
Lift force,(N)
40
35
30
25
20
15
10
5
0
-5
25/02/2015 0:00
02/03/2015 0:00
07/03/2015 0:00
12/03/2015 0:00
17/03/2015 0:00
22/03/2015 0:00
27/03/2015 0:00
01/04/2015 0:00
06/04/2015 0:00
Time stamp

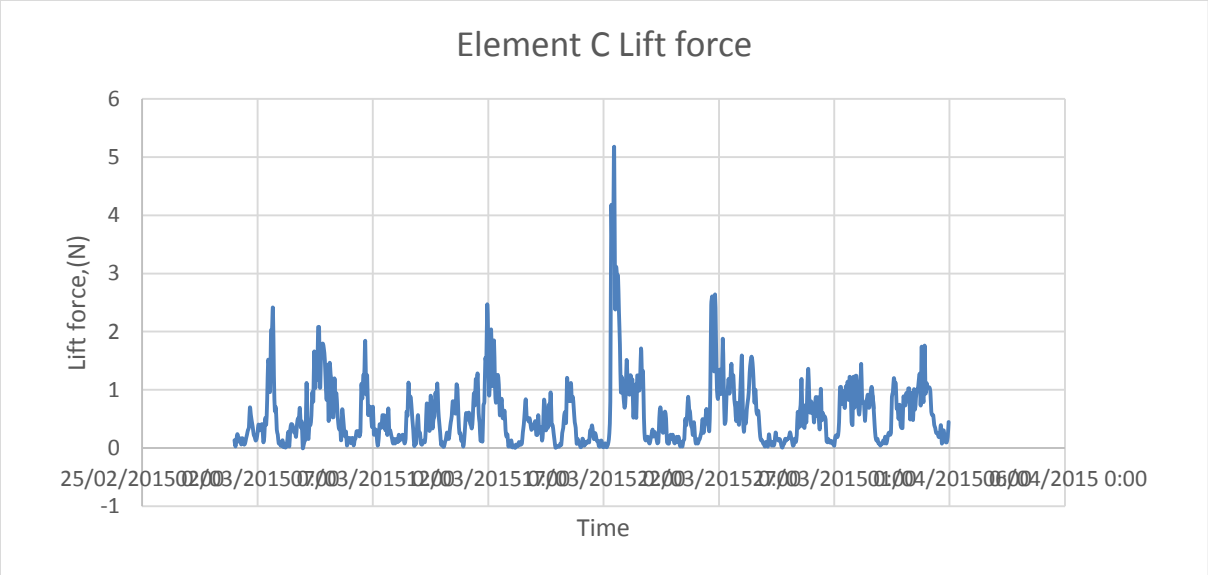
Element C Lift force
Lift force,(N)
6
5
4
3
2
1
0
-1
25/02/2015 0:00
02/03/2015 0:00
07/03/2015 0:00
12/03/2015 0:00
17/03/2015 0:00
22/03/2015 0:00
27/03/2015 0:00
01/04/2015 0:00
06/04/2015 0:00
Time

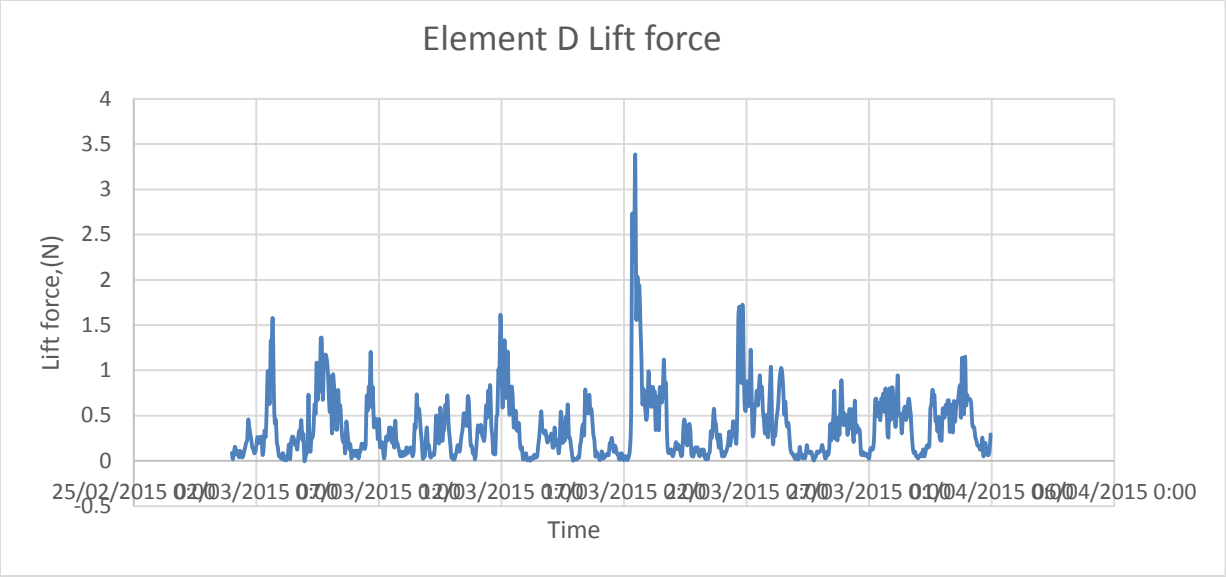
Element D Lift force
Lift force,(N)
4
3.5
3
2.5
2
1.5
1
0.5
0
-0.5
25/02/2015 0:00
02/03/2015 0:00
07/03/2015 0:00
12/03/2015 0:00
17/03/2015 0:00
22/03/2015 0:00
27/03/2015 0:00
01/04/2015 0:00
06/04/2015 0:00
Time

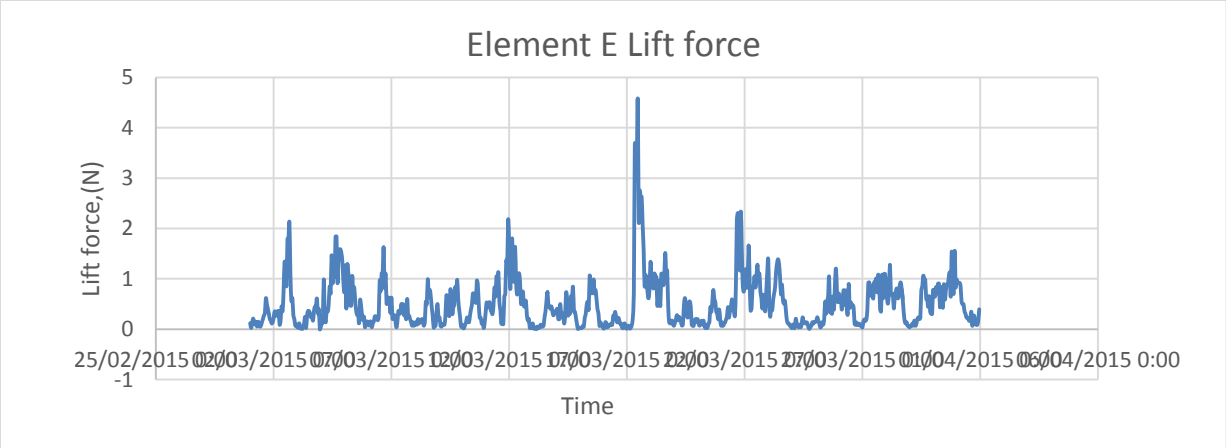
Element E Lift force
Lift force,(N)
5
4
3
2
1
0
-1
25/02/2015 0:00
02/03/2015 0:00
07/03/2015 0:00
12/03/2015 0:00
17/03/2015 0:00
22/03/2015 0:00
27/03/2015 0:00
01/04/2015 0:00
06/04/2015 0:00
Time

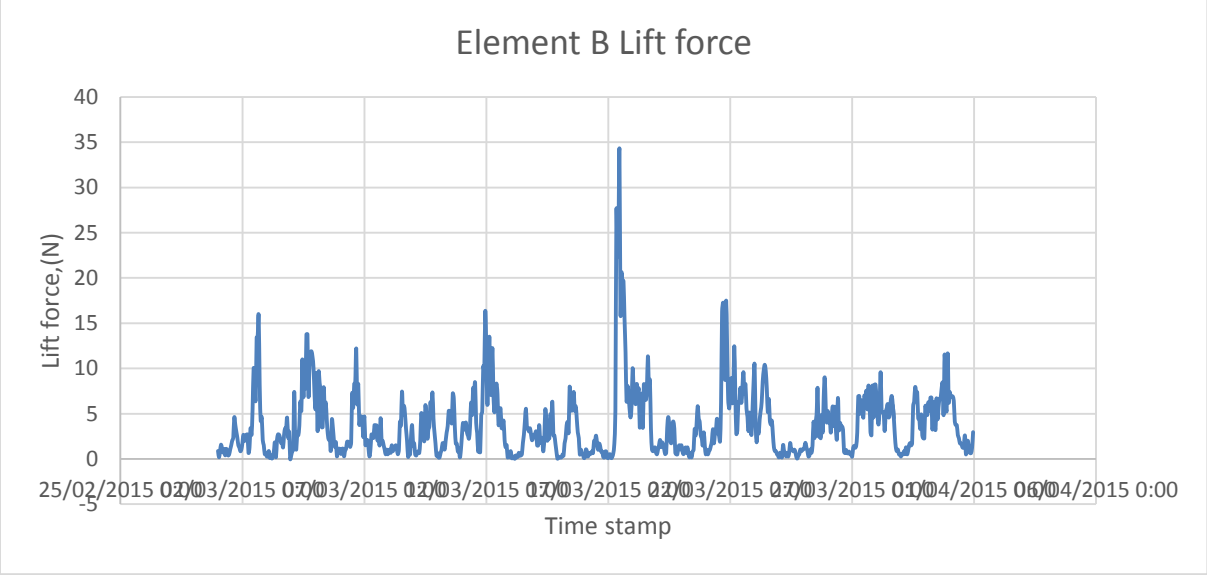
Element B Lift force
Lift force,(N)
40
35
30
25
20
15
10
5
0
-5
25/02/2015 0:00
02/03/2015 0:00
07/03/2015 0:00
12/03/2015 0:00
17/03/2015 0:00
22/03/2015 0:00
27/03/2015 0:00
01/04/2015 0:00
06/04/2015 0:00
Time stamp

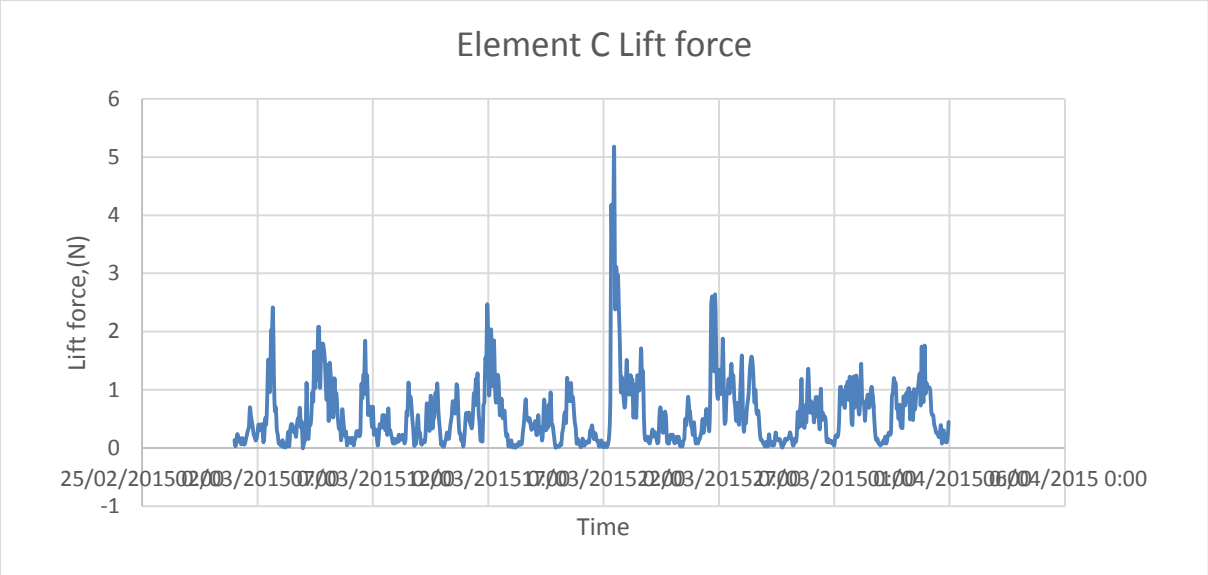
Element C Lift force
Lift force,(N)
6
5
4
3
2
1
0
-1
25/02/2015 0:00
02/03/2015 0:00
07/03/2015 0:00
12/03/2015 0:00
17/03/2015 0:00
22/03/2015 0:00
27/03/2015 0:00
01/04/2015 0:00
06/04/2015 0:00
Time

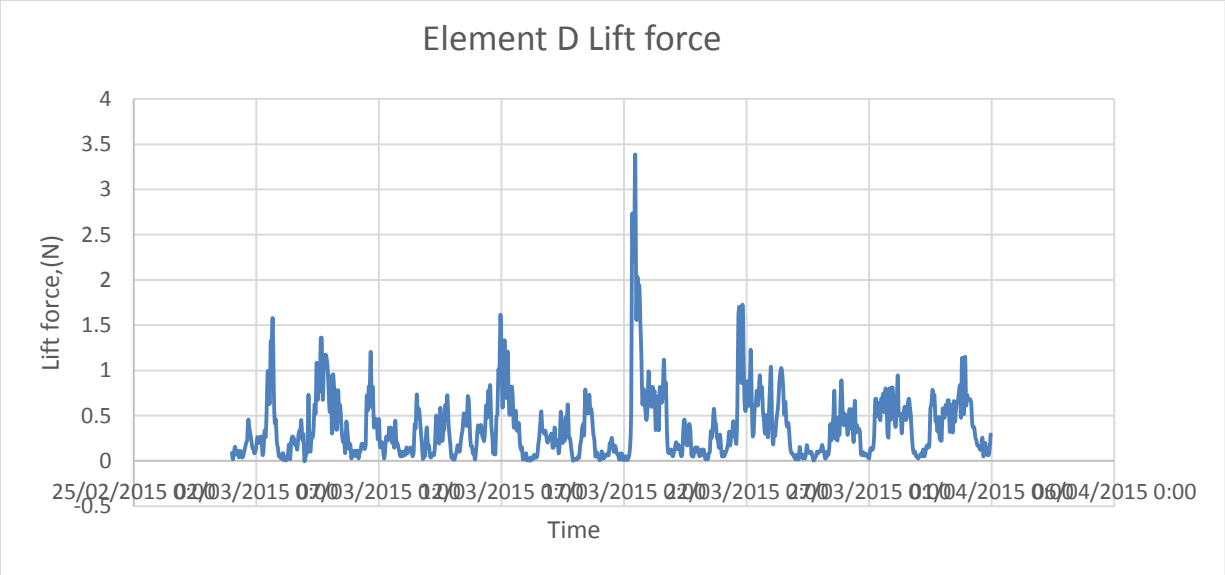
Element D Lift force
Lift force,(N)
4
3.5
3
2.5
2
1.5
1
0.5
0
-0.5
25/02/2015 0:00
02/03/2015 0:00
07/03/2015 0:00
12/03/2015 0:00
17/03/2015 0:00
22/03/2015 0:00
27/03/2015 0:00
01/04/2015 0:00
06/04/2015 0:00
Time

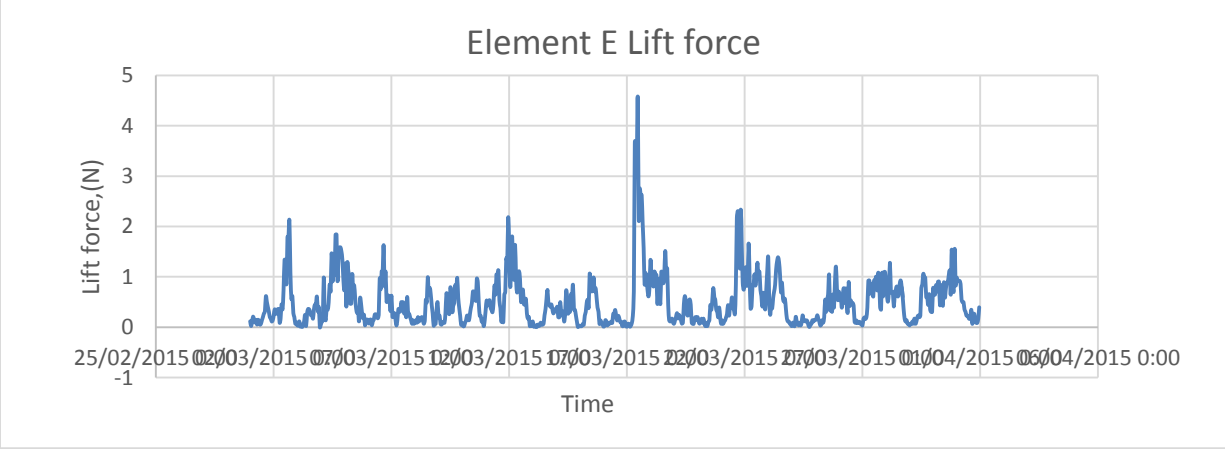
Element E Lift force
Lift force,(N)
5
4
3
2
1
0
-1
25/02/2015 0:00
02/03/2015 0:00
07/03/2015 0:00
12/03/2015 0:00
17/03/2015 0:00
22/03/2015 0:00
27/03/2015 0:00
01/04/2015 0:00
06/04/2015 0:00
Time

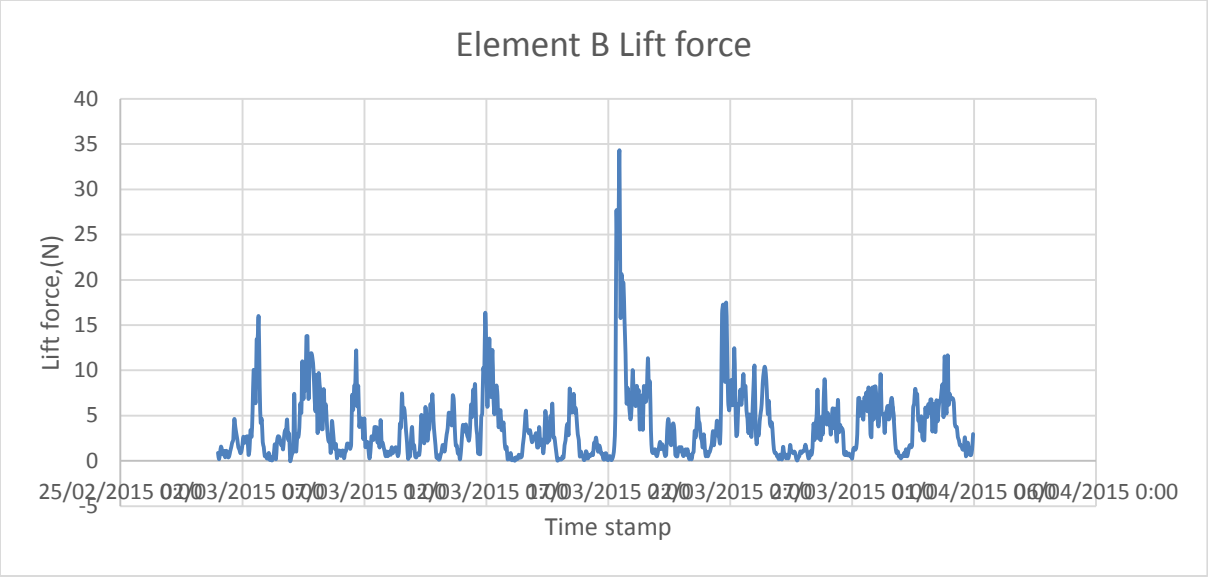
Element B Lift force
Lift force,(N)
40
35
30
25
20
15
10
5
0
-5
25/02/2015 0:00
02/03/2015 07:00
07/03/2015 12:00
12/03/2015 17:00
17/03/2015 22:00
22/03/2015 03:00
27/03/2015 08:00
01/04/2015 13:00
06/04/2015 0:00
Time stamp

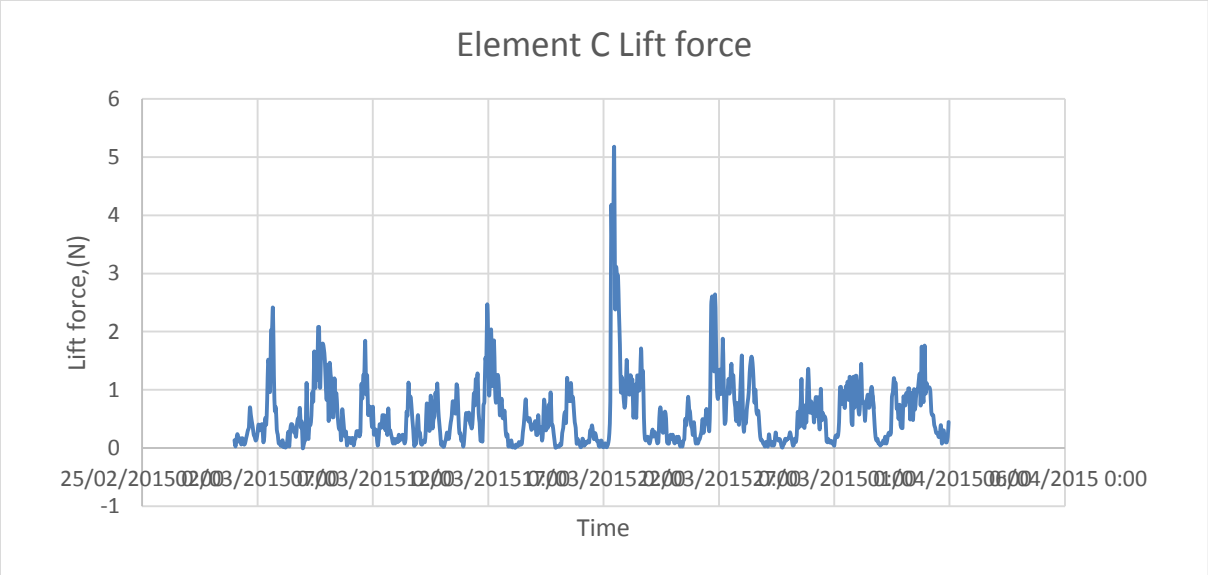
Element C Lift force
Lift force,(N)
6
5
4
3
2
1
0
-1
25/02/2015 0:00
02/03/2015 07:00
07/03/2015 12:00
12/03/2015 17:00
17/03/2015 22:00
22/03/2015 03:00
27/03/2015 08:00
01/04/2015 13:00
06/04/2015 0:00
Time

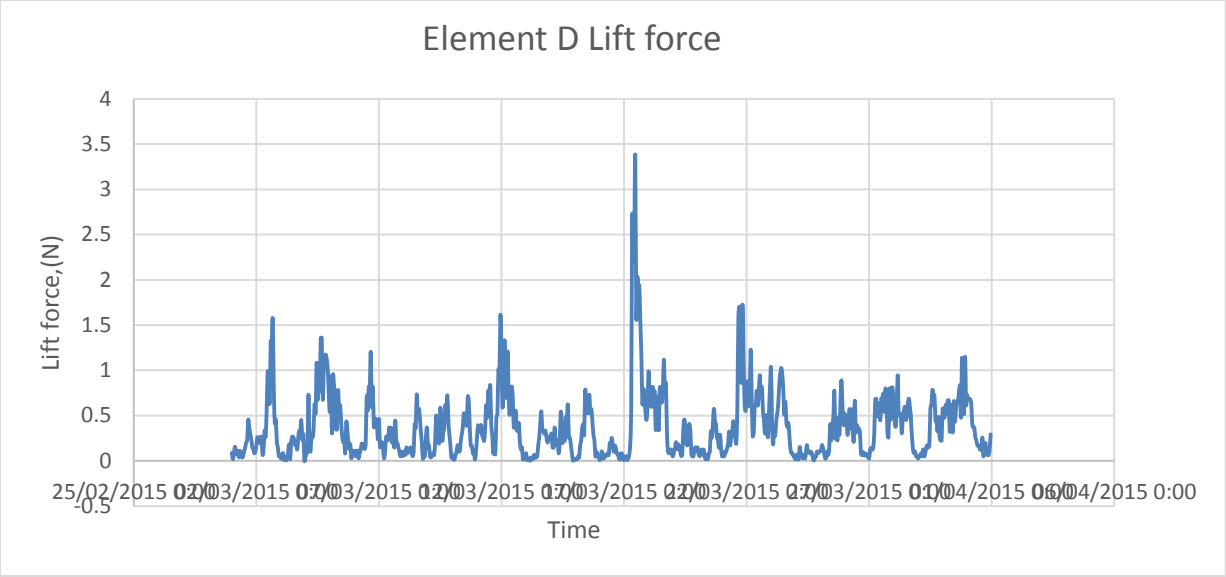
Element D Lift force
Lift force,(N)
4
3.5
3
2.5
2
1.5
1
0.5
0
-0.5
25/02/2015 0:00
02/03/2015 0:00
07/03/2015 0:00
12/03/2015 0:00
17/03/2015 0:00
22/03/2015 0:00
27/03/2015 0:00
01/04/2015 0:00
06/04/2015 0:00
Time

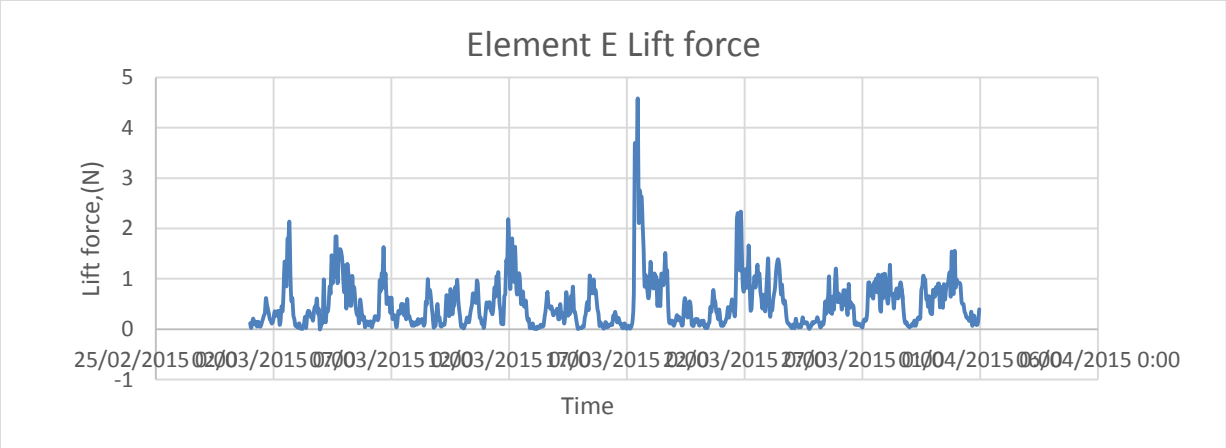
Element E Lift force
Lift force,(N)
5
4
3
2
1
0
-1
25/02/2015 0:00
02/03/2015 0:00
07/03/2015 0:00
12/03/2015 0:00
17/03/2015 0:00
22/03/2015 0:00
27/03/2015 0:00
01/04/2015 0:00
06/04/2015 0:00
Time

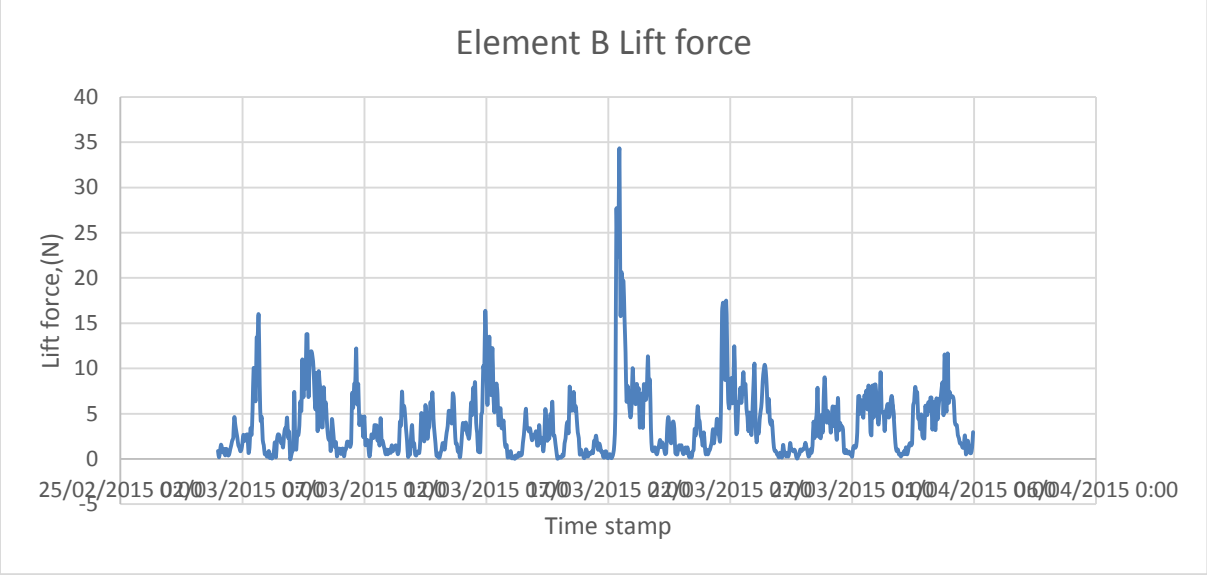
Element B Lift force
Lift force,(N)
40
35
30
25
20
15
10
5
0
-5
25/02/2015 0:00
02/03/2015 0:00
07/03/2015 0:00
12/03/2015 0:00
17/03/2015 0:00
22/03/2015 0:00
27/03/2015 0:00
01/04/2015 0:00
06/04/2015 0:00
Time stamp

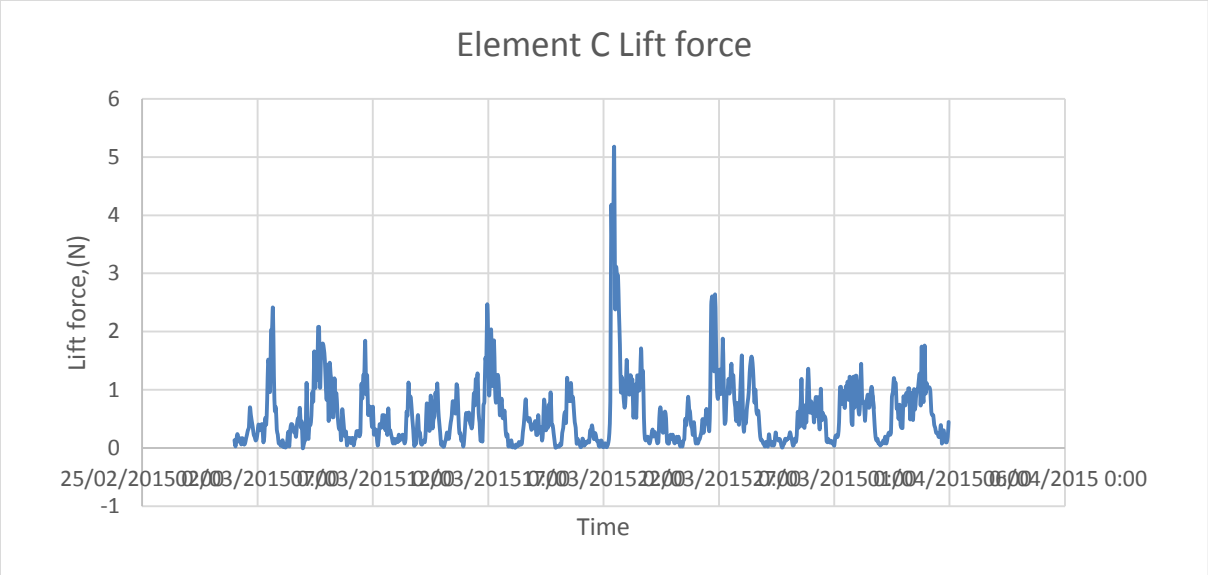
Element C Lift force
Lift force,(N)
6
5
4
3
2
1
0
-1
25/02/2015 0:00
02/03/2015 0:00
07/03/2015 0:00
12/03/2015 0:00
17/03/2015 0:00
22/03/2015 0:00
27/03/2015 0:00
01/04/2015 0:00
06/04/2015 0:00
Time

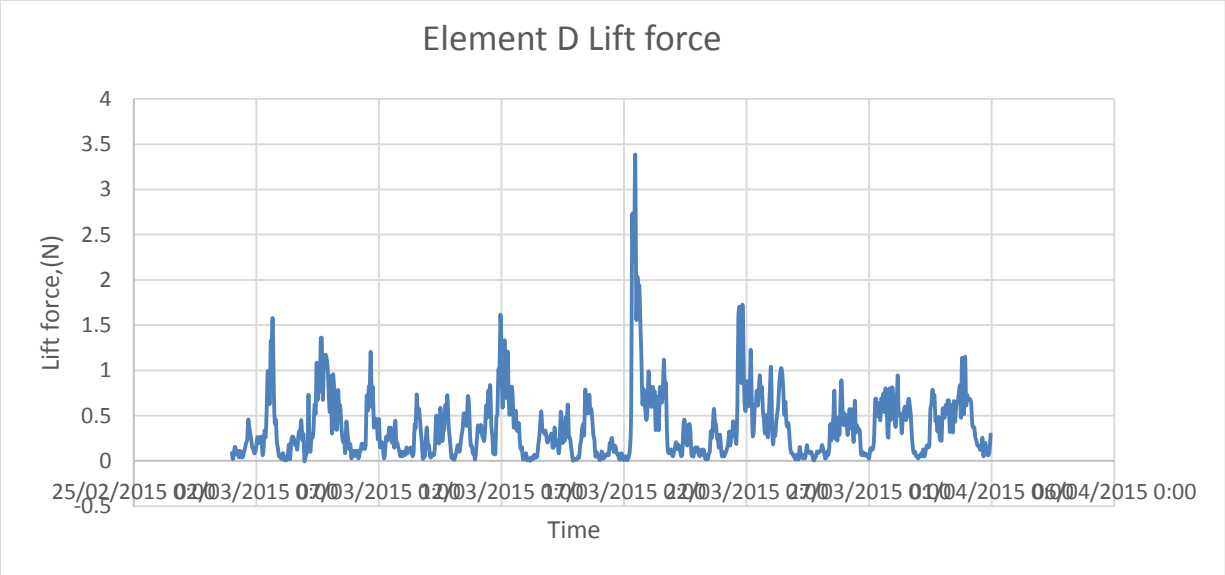
Element D Lift force
Lift force,(N)
4
3.5
3
2.5
2
1.5
1
0.5
0
-0.5
25/02/2015 0:00
02/03/2015 0:00
07/03/2015 0:00
12/03/2015 0:00
17/03/2015 0:00
22/03/2015 0:00
27/03/2015 0:00
01/04/2015 0:00
06/04/2015 0:00
Time

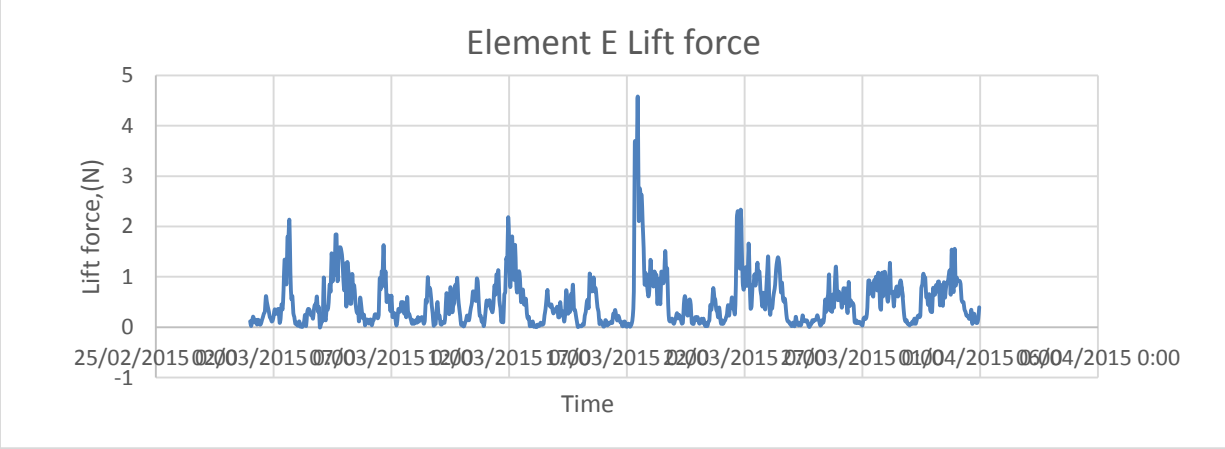
Element E Lift force
Lift force,(N)
5
4
3
2
1
0
-1
25/02/2015 0:00
02/03/2015 0:00
07/03/2015 0:00
12/03/2015 0:00
17/03/2015 0:00
22/03/2015 0:00
27/03/2015 0:00
01/04/2015 0:00
06/04/2015 0:00
Time

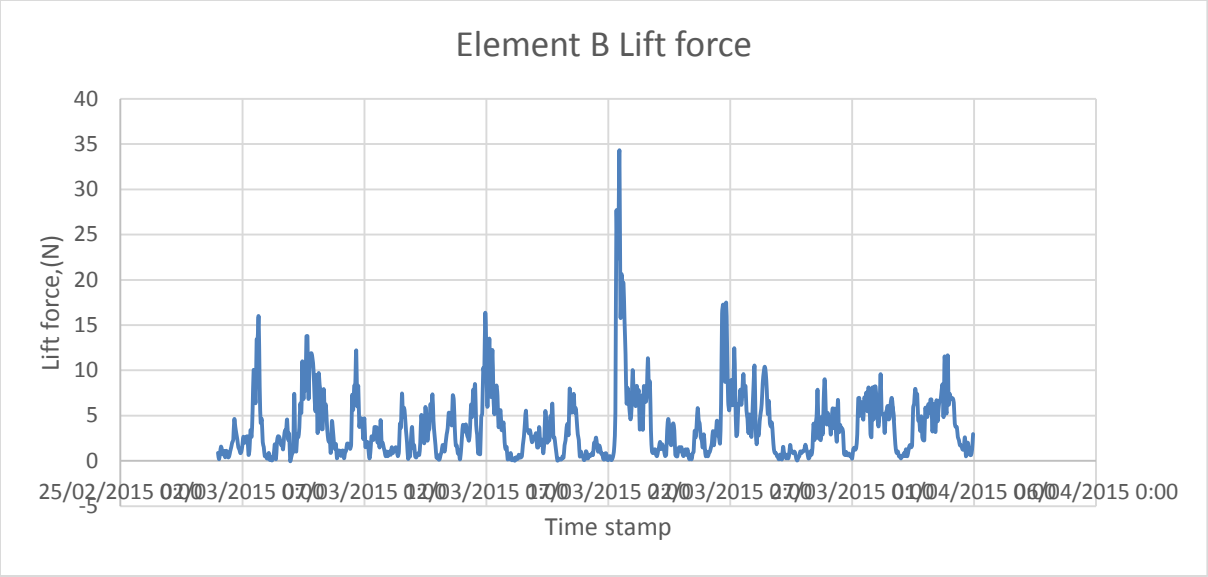
Element B Lift force
Lift force,(N)
40
35
30
25
20
15
10
5
0
-5
25/02/2015 0:00
02/03/2015 07:00
07/03/2015 12:00
12/03/2015 17:00
17/03/2015 22:00
22/03/2015 03:00
27/03/2015 08:00
01/04/2015 13:00
06/04/2015 0:00
Time stamp

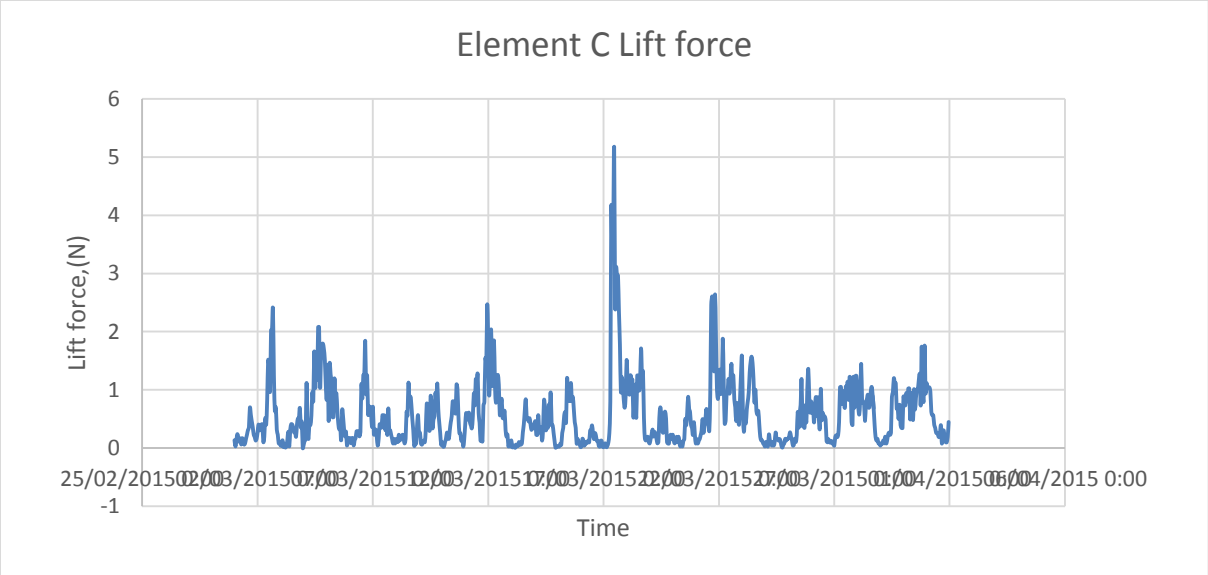
Element C Lift force
Lift force,(N)
6
5
4
3
2
1
0
-1
25/02/2015 0:00
02/03/2015 07:00
07/03/2015 12:00
12/03/2015 17:00
17/03/2015 22:00
22/03/2015 03:00
27/03/2015 08:00
01/04/2015 13:00
06/04/2015 0:00
Time

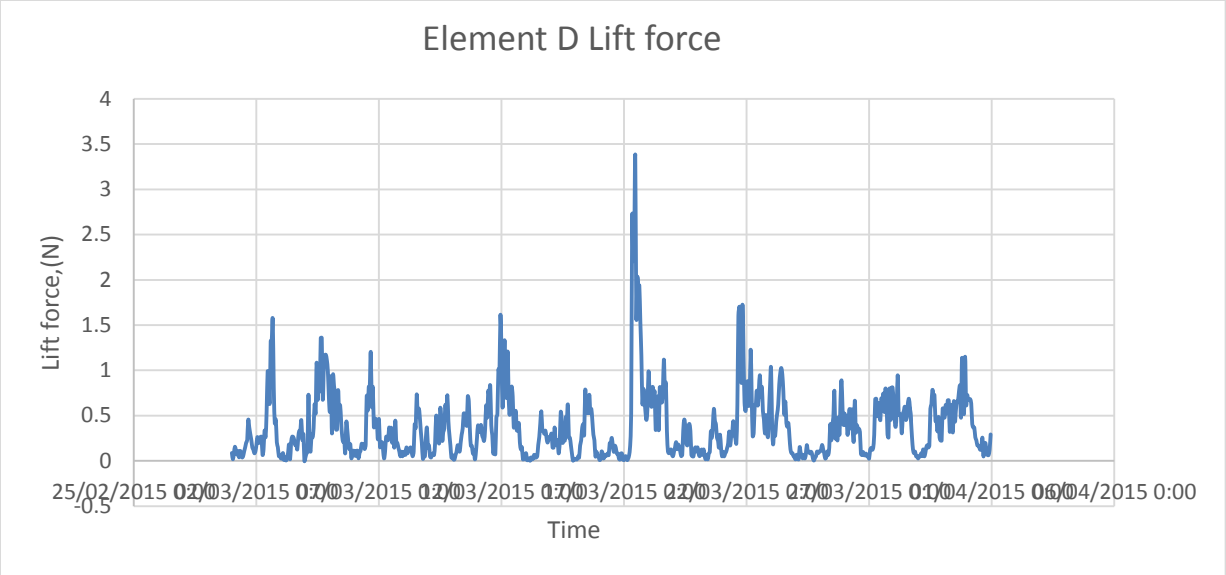
Element D Lift force
Lift force,(N)
4
3.5
3
2.5
2
1.5
1
0.5
0
-0.5
25/02/2015 0:00
02/03/2015 0:00
07/03/2015 0:00
12/03/2015 0:00
17/03/2015 0:00
22/03/2015 0:00
27/03/2015 0:00
01/04/2015 0:00
06/04/2015 0:00
Time

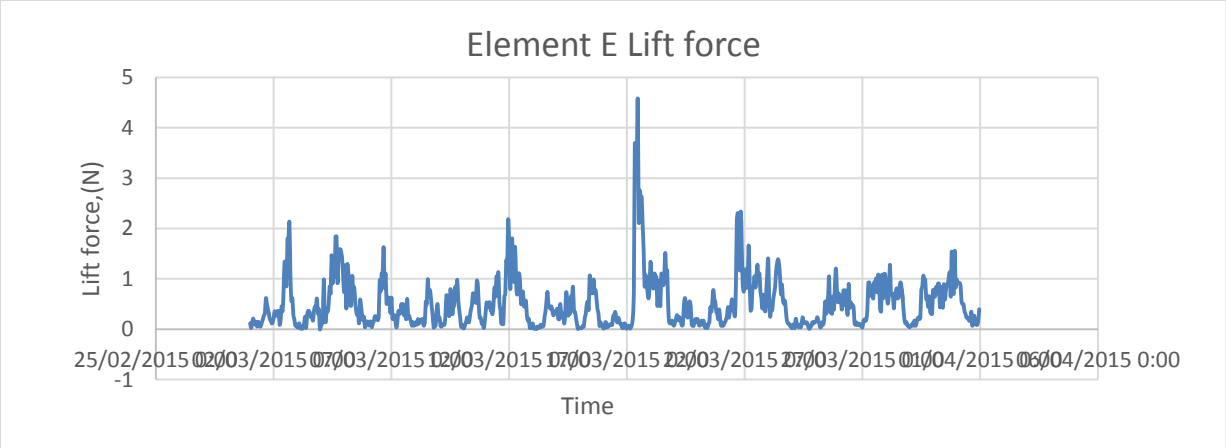
Element E Lift force
Lift force,(N)
5
4
3
2
1
0
-1
25/02/2015 0:00
02/03/2015 0:00
07/03/2015 0:00
12/03/2015 0:00
17/03/2015 0:00
22/03/2015 0:00
27/03/2015 0:00
01/04/2015 0:00
06/04/2015 0:00
Time

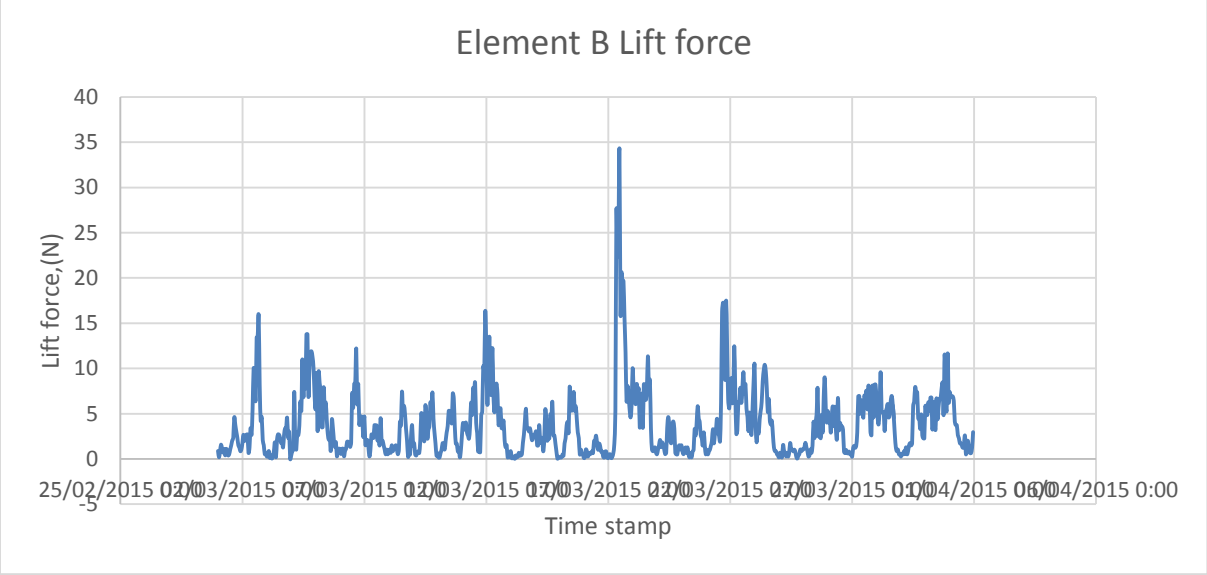
Element B Lift force
Lift force,(N)
40
35
30
25
20
15
10
5
0
-5
25/02/2015 0:00
02/03/2015 0:00
07/03/2015 0:00
12/03/2015 0:00
17/03/2015 0:00
22/03/2015 0:00
27/03/2015 0:00
01/04/2015 0:00
06/04/2015 0:00
Time stamp

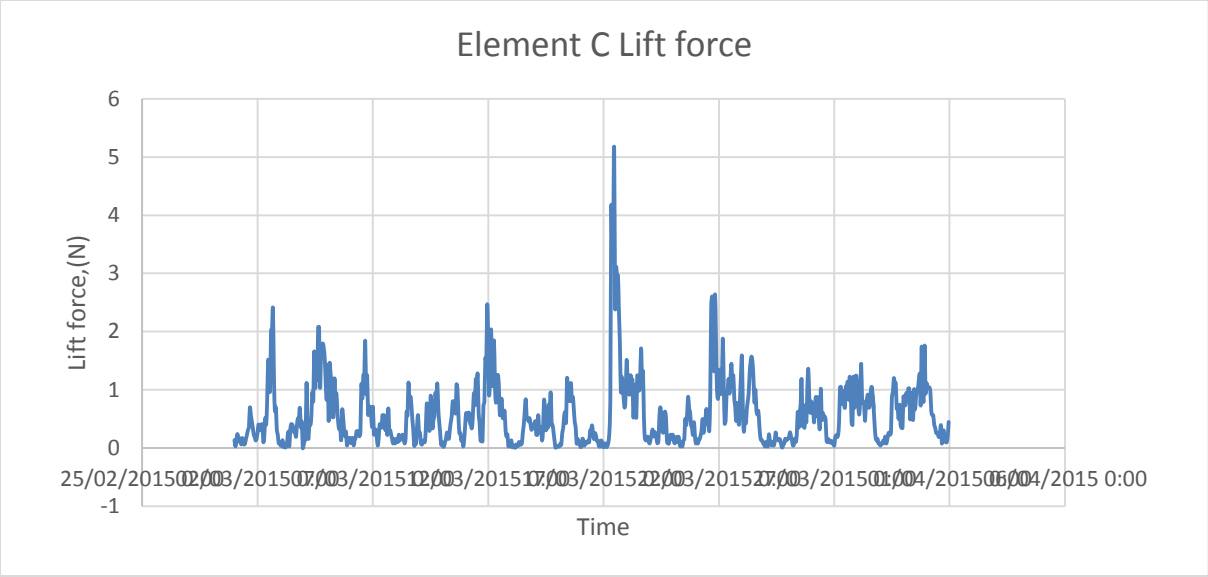
Element C Lift force
Lift force,(N)
Time

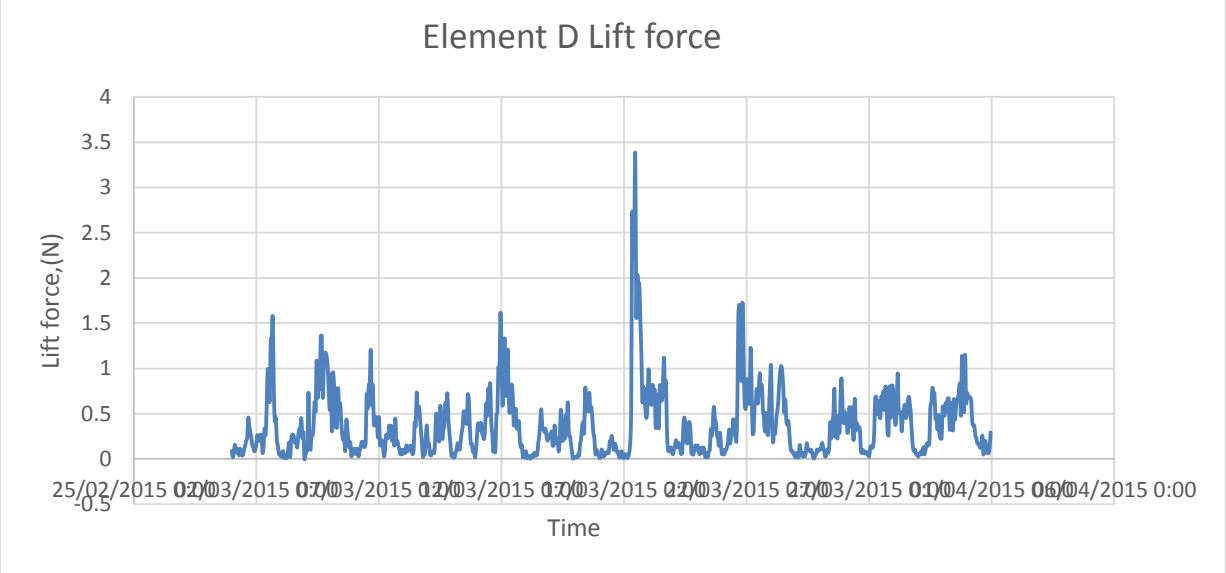
Element D Lift force
Lift force,(N)
Time

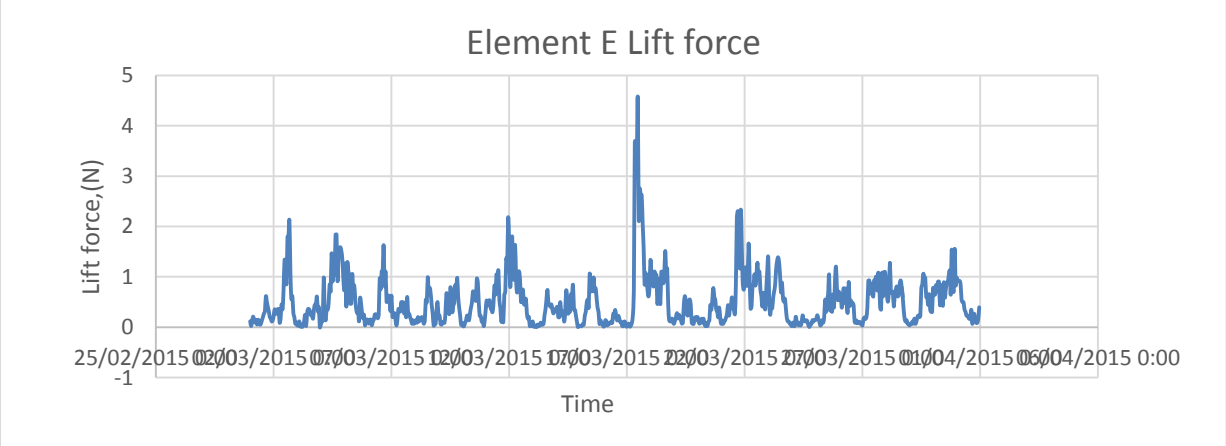
Element E Lift force
Lift force,(N)
Time

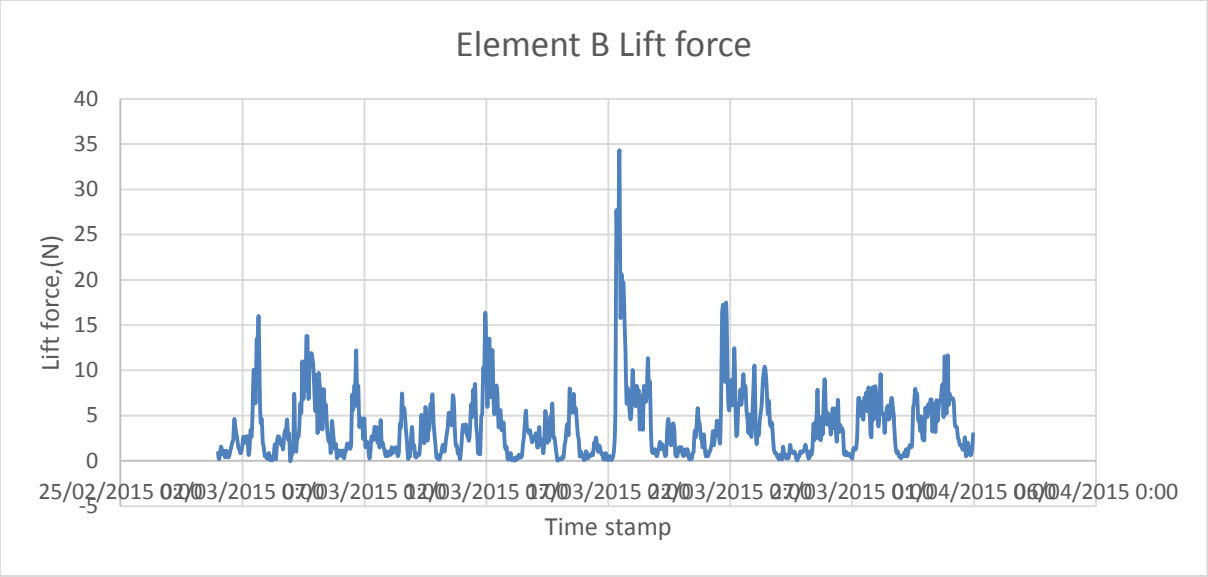
Element B Lift force
Lift force,(N)
40
35
30
25
20
15
10
5
0
-5
25/02/2015 0:00
02/03/2015 07:00
07/03/2015 12:00
12/03/2015 17:00
17/03/2015 22:00
22/03/2015 03:00
27/03/2015 08:00
01/04/2015 13:00
06/04/2015 0:00
Time stamp

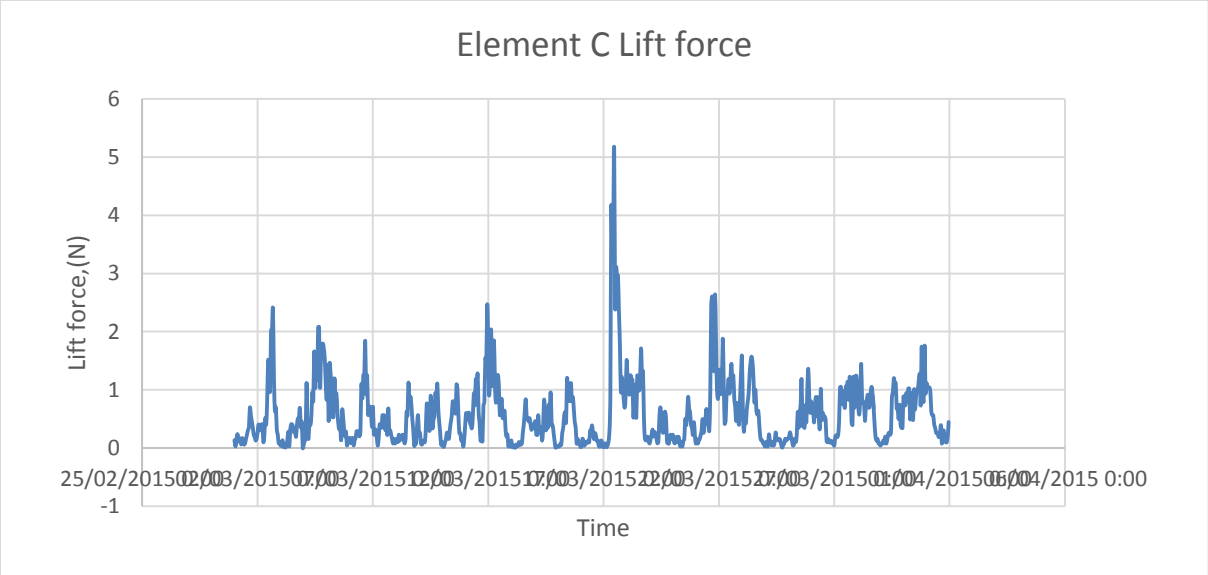
Element C Lift force
Lift force,(N)
6
5
4
3
2
1
0
-1
25/02/2015 0:00
02/03/2015 07:00
07/03/2015 12:00
12/03/2015 17:00
17/03/2015 22:00
22/03/2015 03:00
27/03/2015 08:00
01/04/2015 13:00
06/04/2015 0:00
Time

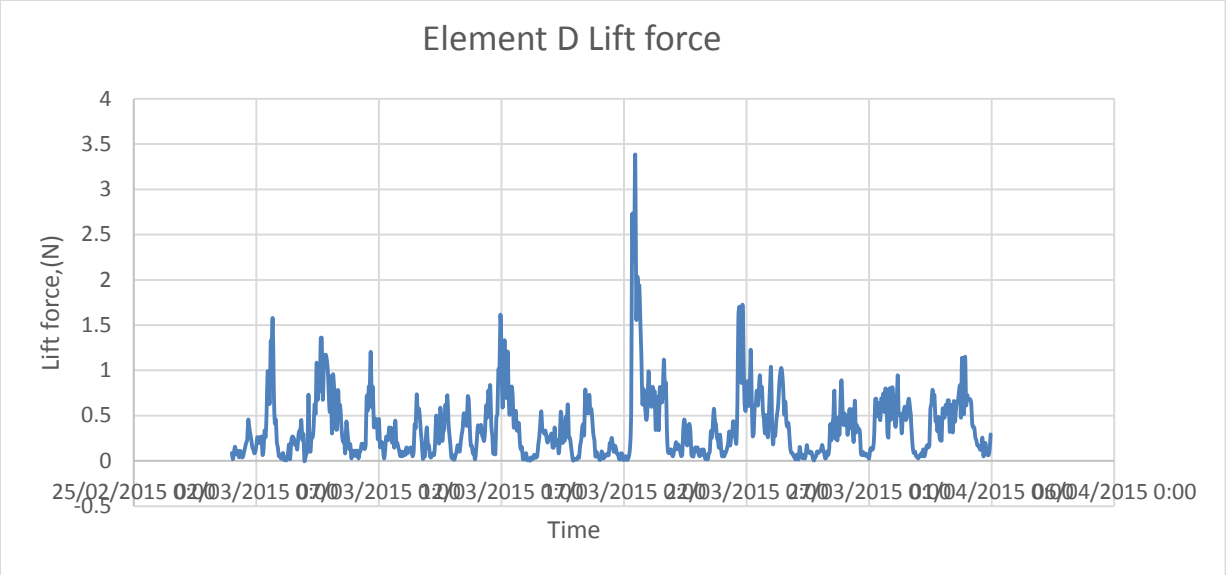
Element D Lift force
Lift force,(N)
4
3.5
3
2.5
2
1.5
1
0.5
0
-0.5
25/02/2015 0:00
02/03/2015 7:00
07/03/2015 12:00
12/03/2015 17:00
17/03/2015 22:00
22/03/2015 3:00
27/03/2015 8:00
01/04/2015 13:00
06/04/2015 0:00
Time

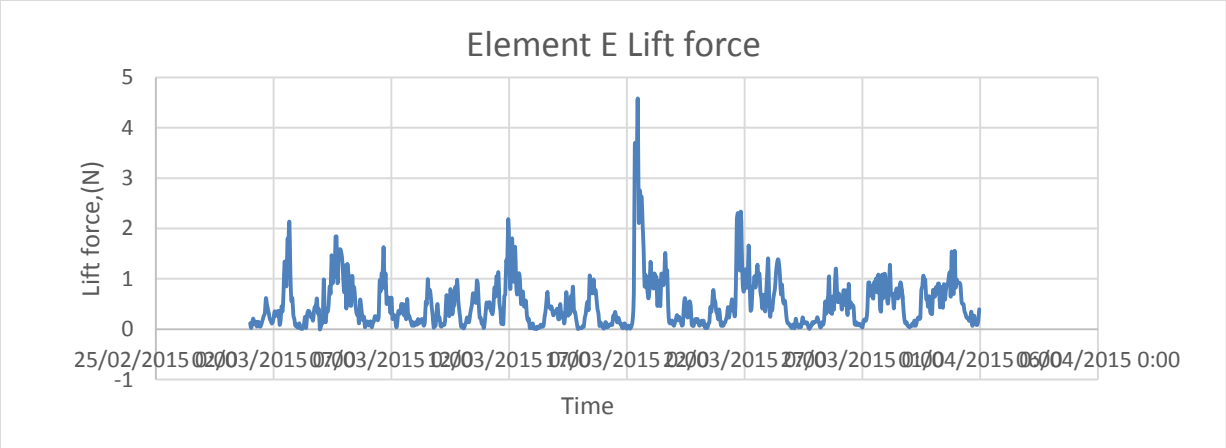
Element E Lift force
Lift force,(N)
5
4
3
2
1
0
-1
25/02/2015 0:00
02/03/2015 7:00
07/03/2015 12:00
12/03/2015 17:00
17/03/2015 22:00
22/03/2015 3:00
27/03/2015 8:00
01/04/2015 13:00
06/04/2015 0:00
Time

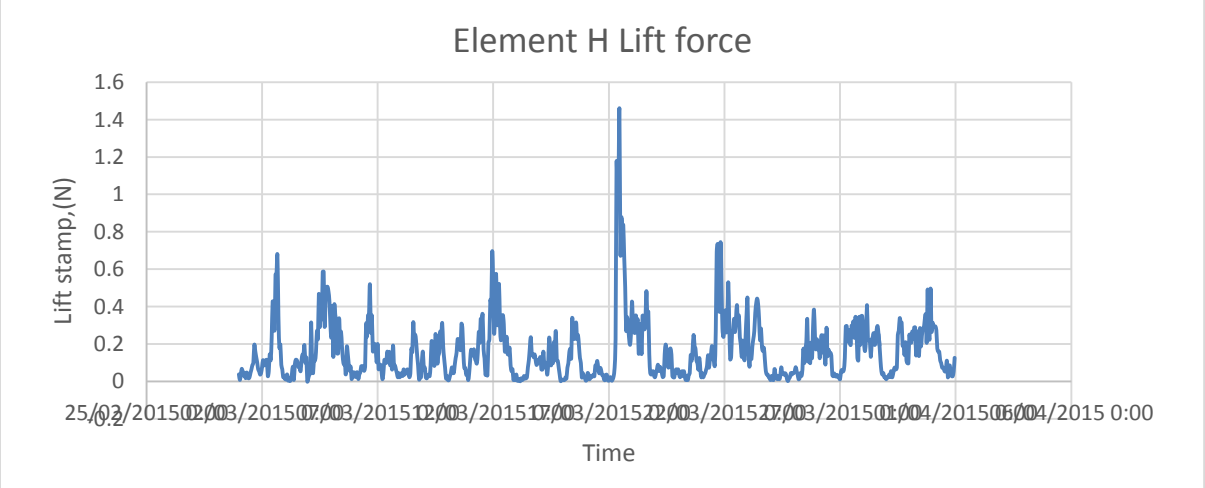
Element H Lift force
Lift stamp,(N)
1.6
1.4
1.2
1
0.8
0.6
0.4
0.2
0
-0.2
25/02/2015 0:00
02/03/2015 7:00
07/03/2015 12:00
12/03/2015 17:00
17/03/2015 22:00
22/03/2015 3:00
27/03/2015 8:00
01/04/2015 13:00
06/04/2015 0:00
Time

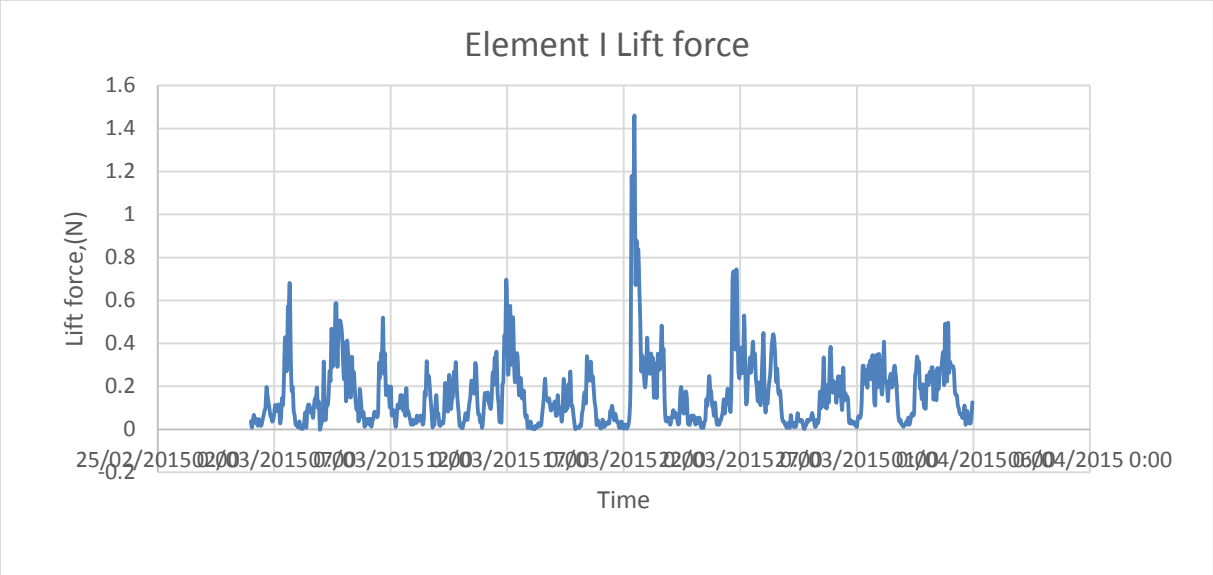
Element I Lift force
Lift force,(N)
1.6
1.4
1.2
1
0.8
0.6
0.4
0.2
0
-0.2
25/02/2015 0:00
02/03/2015 0:00
07/03/2015 0:00
12/03/2015 0:00
17/03/2015 0:00
22/03/2015 0:00
27/03/2015 0:00
01/04/2015 0:00
06/04/2015 0:00
Time

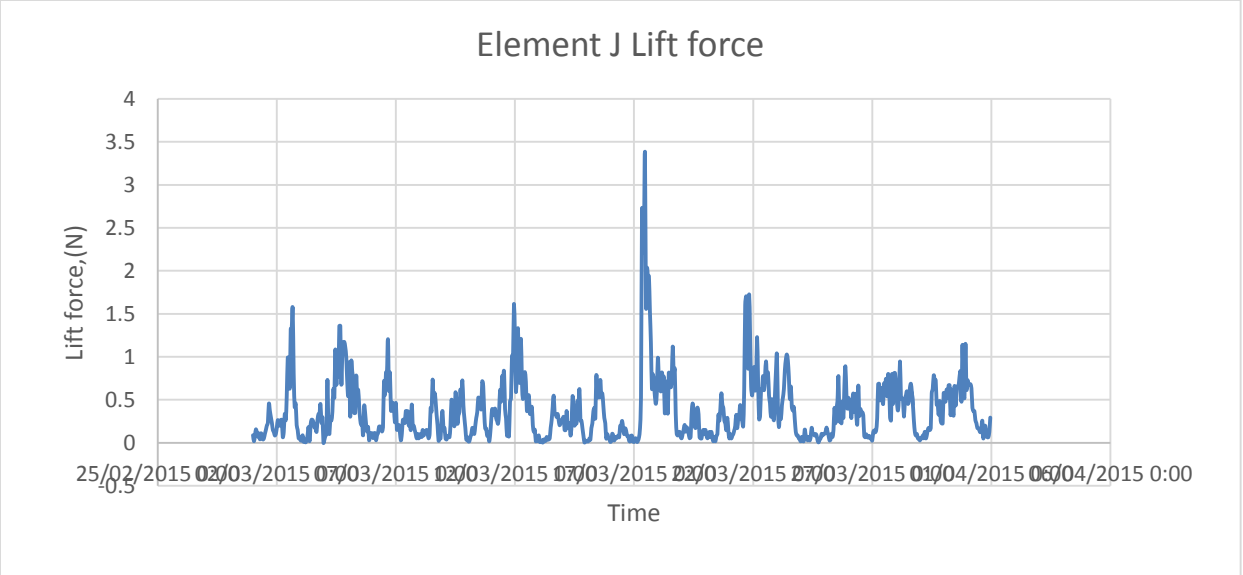
Element J Lift force
Lift force,(N)
4
3.5
3
2.5
2
1.5
1
0.5
0
-0.5
25/02/2015 0:00
02/03/2015 0:00
07/03/2015 0:00
12/03/2015 0:00
17/03/2015 0:00
22/03/2015 0:00
27/03/2015 0:00
01/04/2015 0:00
06/04/2015 0:00
Time

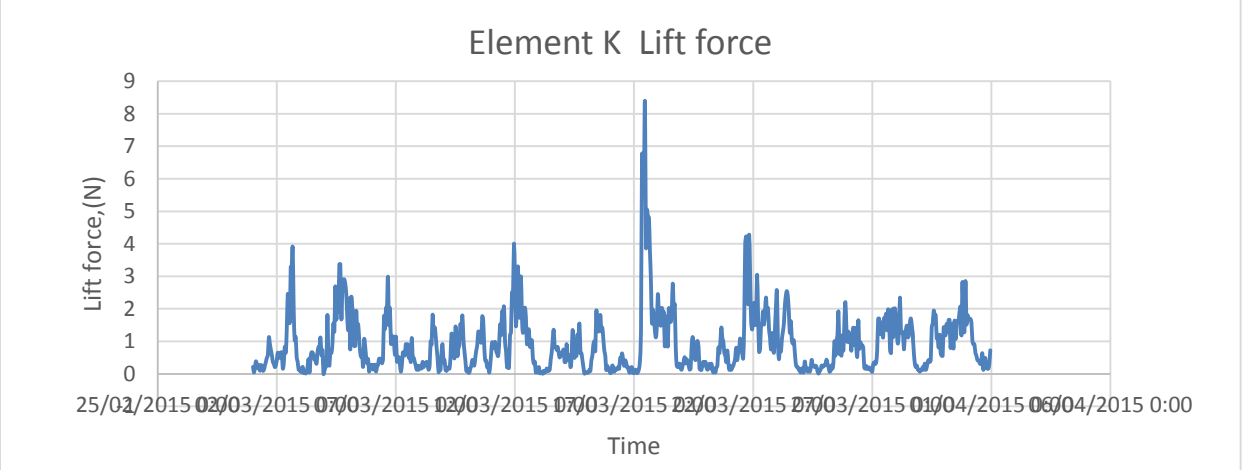
Element K Lift force
Lift force,(N)
9
8
7
6
5
4
3
2
1
0
-1
25/02/2015 0:00
02/03/2015 0:00
07/03/2015 0:00
12/03/2015 0:00
17/03/2015 0:00
22/03/2015 0:00
27/03/2015 0:00
01/04/2015 0:00
06/04/2015 0:00
Time

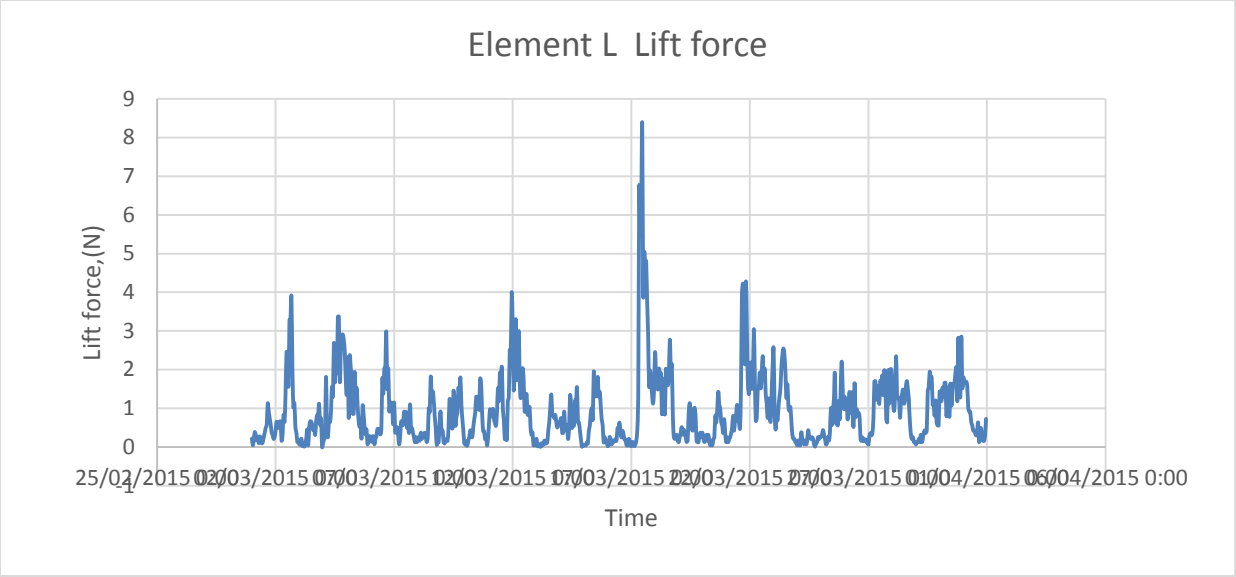
Element L Lift force
Lift force,(N)
9
8
7
6
5
4
3
2
1
0
-1
25/02/2015 0:00
02/03/2015 0:00
07/03/2015 0:00
12/03/2015 0:00
17/03/2015 0:00
22/03/2015 0:00
27/03/2015 0:00
01/04/2015 0:00
06/04/2015 0:00
Time